

<sup>1</sup>

©Copyright 2021

<sup>2</sup>

Sean Gasiorowski

<sup>3</sup> Searches for pair production of Higgs bosons in the  $b\bar{b}b\bar{b}$  final state  
<sup>4</sup> using the ATLAS detector, or: How I Learned to Stop Worrying  
<sup>5</sup> and Love the QCD Background

<sup>6</sup> Sean Gasiorowski

<sup>7</sup> A dissertation  
<sup>8</sup> submitted in partial fulfillment of the  
<sup>9</sup> requirements for the degree of

<sup>10</sup> Doctor of Philosophy

<sup>11</sup> University of Washington

<sup>12</sup> 2021

<sup>13</sup> Reading Committee:

<sup>14</sup> Anna Goussiou, Chair

<sup>15</sup> Jason Detwiler

<sup>16</sup> Shih-Chieh Hsu

<sup>17</sup> David Kaplan

<sup>18</sup> Henry Lubatti

<sup>19</sup> Thomas Quinn

<sup>20</sup> Gordon Watts

<sup>21</sup> Program Authorized to Offer Degree:  
<sup>22</sup> Physics

23

University of Washington

24

## Abstract

25

Searches for pair production of Higgs bosons in the  $b\bar{b}b\bar{b}$  final state using the ATLAS  
detector, or: How I Learned to Stop Worrying and Love the QCD Background

27

Sean Gasiorowski

28

Chair of the Supervisory Committee:

29

Professor Anna Goussiou

30

Physics

This thesis discusses searches for pair production of Higgs bosons in the  $b\bar{b}b\bar{b}$  final state using data recorded by the ATLAS detector from  $\sqrt{s} = 13$  TeV proton-proton ( $pp$ ) collisions during the full period of LHC Run 2. It develops two separate analysis strategies: one targeting resonant pair production of Higgs bosons, in which Beyond the Standard Model resonances are produced which subsequently decay to two Higgs bosons, and one targeting non-resonant pair production of Higgs bosons, which is sensitive to Standard Model  $HH$  production as well as to variations of the Higgs trilinear self-coupling. In the resonant searches, no significant excesses are seen, and upper limits on cross section are set on both spin-0 and spin-2 resonant hypotheses. Such limits are competitive with other leading ATLAS full Run 2 searches, and represent a significantly stronger statement than previous, beating the early Run 2 combined ATLAS results above 350 GeV and leading the ATLAS full Run 2 sensitivity above 700 GeV. In the non-resonant, no evidence of Standard Model  $HH$  production is seen, but upper limits on cross section of  $pp \rightarrow HH$  via gluon-gluon fusion are set to be 4.4 (5.9) observed (expected) times the value predicted by the Standard Model. Such limits represent a significant improvement in sensitivity over the early Run 2  $b\bar{b}b\bar{b}$  results, achieving a 30 (40) % additional gain in sensitivity beyond that predicted from a pure increase in dataset size. These limits are competitive with other leading ATLAS full Run 2 searches. Cross section

<sup>48</sup> limits are additionally set for a range of values of the Higgs self coupling, parametrized via  
<sup>49</sup> its ratio to the value predicted by the Standard Model,  $\kappa_\lambda = \lambda_{HHH}/\lambda_{HHH}^{SM}$ . This is restricted  
<sup>50</sup> to have values  $-4.9 \leq \kappa_\lambda \leq 14.4$  observed ( $-3.9 \leq \kappa_\lambda \leq 10.9$  expected). An excess of data  
<sup>51</sup> over background is seen for values of  $\kappa_\lambda \geq 5$ , with maximum local significance of  $3.8\sigma$  at  
<sup>52</sup>  $\kappa_\lambda = 6$ . Such an excess is demonstrated to be due to low mass, where the  $b\bar{b}b\bar{b}$  channel has  
<sup>53</sup> limited sensitivity, and is not seen in more sensitive channels in this region. Results on the  
<sup>54</sup> development of two methods for the improvement of hadronic shower modeling in ATLAS  
<sup>55</sup> fast calorimeter simulation are also presented.

## TABLE OF CONTENTS

	Page
57 List of Figures . . . . .	iv
58 Preface . . . . .	xxi
59 Chapter 1: The Standard Model of Particle Physics . . . . .	1
60    1.1 Introduction: Particles and Fields . . . . .	1
61    1.2 Quantum Electrodynamics . . . . .	4
62    1.3 An Aside on Group Theory . . . . .	9
63    1.4 Quantum Chromodynamics . . . . .	11
64    1.5 The Weak Interaction . . . . .	14
65    1.6 The Higgs Potential and the SM . . . . .	20
66    1.7 The Standard Model: A Summary . . . . .	26
67    1.8 Experimental Review and Outlook . . . . .	27
68 Chapter 2: Di-Higgs Phenomenology and Physics Beyond the Standard Model . . . . .	31
69    2.1 Intro to Di-Higgs . . . . .	31
70    2.2 Resonant $HH$ Searches . . . . .	32
71    2.3 Non-resonant $HH$ Searches . . . . .	34
72 Chapter 3: Experimental Apparatus . . . . .	38
73    3.1 The Large Hadron Collider . . . . .	38
74    3.2 The ATLAS Experiment . . . . .	41
75 Chapter 4: Simulation . . . . .	51
76    4.1 Event Generation . . . . .	51
77    4.2 Detector Simulation . . . . .	54
78    4.3 Correlated Fluctuations in FastCaloSim . . . . .	56

79	<b>4.4 Outlook</b>	65
80	<b>Chapter 5: Reconstruction</b>	66
81	<b>5.1 Jets</b>	66
82	<b>5.2 Flavor Tagging</b>	68
83	<b>Chapter 6: Setting up the <math>HH \rightarrow b\bar{b}b\bar{b}</math> Analysis</b>	78
84	<b>6.1 Data and Monte Carlo Simulation</b>	80
85	<b>6.2 Triggers</b>	82
86	<b>Chapter 7: Analysis Selection</b>	86
87	<b>7.1 Analysis Selection</b>	86
88	<b>7.2 Background Reduction and Top Veto</b>	94
89	<b>7.3 Kinematic Region Definition</b>	97
90	<b>7.4 Discriminating Variable</b>	101
91	<b>Chapter 8: Background Estimation</b>	104
92	<b>8.1 The Two Tag Region</b>	105
93	<b>8.2 Kinematic Reweighting</b>	105
94	<b>Chapter 9: Uncertainties and Validation</b>	138
95	<b>9.1 Statistical Uncertainties and Bootstrapping</b>	138
96	<b>9.2 Background Shape Uncertainties</b>	143
97	<b>9.3 Signal Uncertainties</b>	146
98	<b>9.4 Background Validation</b>	148
99	<b>Chapter 10: Results</b>	151
100	<b>10.1 <math>m_{HH}</math> Distributions</b>	151
101	<b>10.2 Statistical Analysis</b>	163
102	<b>10.3 Results</b>	167
103	<b>Chapter 11: Comparisons with Other Channels</b>	175
104	<b>Chapter 12: Conclusions</b>	178
105	<b>Appendix A: Overview of Other <math>b\bar{b}b\bar{b}</math> Channels</b>	196

106	Appendix B: Future Ideas for $HH \rightarrow b\bar{b}b\bar{b}$	200
107	B.1 pairAGraph: A New Method for Jet Pairing	200
108	B.2 Background Estimation with Mass Plane Interpolation	205
109	Appendix C: Kinematic Reweighting for the 2018 Validation Region	220

## LIST OF FIGURES

Figure Number		Page
111	1.1 Diagram of the elementary particles described by the Standard Model [6]. . . . .	3
112	2.1 Representative diagrams for the gluon-gluon fusion production of spin-0 ( $X$ ) 113 and spin-2 ( $G_{KK}^*$ ) resonances which decay to two Standard Model Higgs 114 bosons. The spin-0 resonance considered for this thesis is a generic narrow 115 width resonance which may be interpreted in the context of two Higgs doublet 116 models [23], whereas the spin-2 resonance is considered as a Kaluza-Klein 117 graviton within the bulk Randall-Sundrum (RS) model [24, 25]. . . . .	32
118	2.2 Dominant contributing diagrams for non-resonant gluon-gluon fusion produc- 119 tion of $HH$ . $\kappa_\lambda$ and $\kappa_t$ represent ratios of the Higgs self-coupling and coupling 120 to top quarks respectively, relative to the values predicted by the Standard 121 Model. . . . .	33
122	2.3 Illustration of dominant $HH$ branching ratios. $HH \rightarrow b\bar{b}b\bar{b}$ is the most common 123 decay mode, representing 34 % of all $HH$ events produced at the LHC. . . . .	34
124	2.4 Monte Carlo generator level $m_{HH}$ distributions for various values of $\kappa_\lambda$ , demon- 125 strating the impact of the interference between the two diagrams of Figure 2.2 126 on the resulting $m_{HH}$ distribution. For $\kappa_\lambda = 0$ there is no triangle diagram con- 127 tribution, demonstrating the shape of the box diagram contribution, whereas 128 for $\kappa_\lambda = 10$ , the triangle diagram dominates, with a strong low mass peak. 129 The interplay between the two is quite evident for other values, resulting in, 130 e.g., the double peaked structure present for $\kappa_\lambda = 2$ (near maximal destructive 131 interference) and $\kappa_\lambda = -5$ . At $\kappa_\lambda = 5$ , the interference leads to a deficit at 132 high $m_{HH}$ , resulting in a narrower distribution (and thus a more pronounced 133 low mass peak) than the $\kappa_\lambda = 10$ case. [26] . . . . .	36
134	3.1 Diagram of the ATLAS detector [48] . . . . .	41
135	3.2 Cross section of the ATLAS detector showing how particles interact with 136 various detector components [50] . . . . .	43
137	3.3 2D projections of the ATLAS coordinate system . . . . .	44

138	3.4 Illustration of electromagnetic showering. Repeated bremsstrahlung and				
139	electron-positron pair production result in a shower structure in which the				
140	number of particles approximately doubles every radiation length, $X_0$ . Figure				
141	taken from [8]. . . . .				48
142	4.1 Schematic diagram of the Monte Carlo simulation of a hadron-hadron collision.				
143	The incoming hadrons are the green blobs with the arrows on the left and				
144	right, with the red blob in the center representing the hard scatter event,				
145	and the purple representing a secondary hard scatter. Radiation from both				
146	incoming and outgoing particles is shown, and the light green blobs represent				
147	hadronization, with the outermost dark green circles corresponding to the final				
148	state hadrons. Yellow lines are radiated photons. [65] . . . . .				53
149	4.2 The projected ATLAS computational requirements for Run 3 and the HL-LHC				
150	relative to the projected computing budget. Aggressive R&D is required to				
151	keep resources within budget [68]. $y$ -axis units are in MHS06 · years, where				
152	HS06 is a high energy physics specific CPU performance benchmark [69]. . .				55
153	4.3 Example average lateral shower shape for a 265 GeV photon in the range				
154	$0.55 <  \eta  < 0.60$ in the second layer of the EM barrel. The binning shown				
155	here is in polar $\alpha - R$ coordinates in a local plane tangential to the surface of				
156	the calorimeter system. Such a histogram is used as a probability distribution,				
157	from which a finite number of “hits” are drawn [71]. . . . .				57
158	4.4 Energy and variable weta2, defined as the energy weighted lateral width of a				
159	shower in the second electromagnetic calorimeter layer, for 16 GeV photons				
160	with full simulation (G4) and FastCaloSimV2 (FCSV2) [71]. . . . .				58
161	4.5 Example of photon and pion average shapes in $5 \times 5$ calorimeter cells. The				
162	left column shows the average shape over a sample of 10000 events, while the				
163	right column shows the energy ratio, in each cell, of single GEANT4 events				
164	with respect to this average. The photon ratios are all close to 1, while the				
165	pion ratios show significant deviation from the average. . . . .				59
166	4.6 Distribution of the ratio of voxel energy in single events to the corresponding				
167	voxel energy in the average shape, with GEANT4 events in blue and Gaussian				
168	model events in orange, for 65 GeV central pions in EMB2. Moving top to				
169	bottom corresponds to increasing $\alpha$ , left to right corresponds to increasing $R$ ,				
170	with core voxels numbered 1, 10, 19, .... Agreement is quite good across all				
171	voxels. Results are similar for the VAE method. . . . .				61

172	4.7	Correlation coefficient of ratios of voxel energy in single events to the corresponding voxel energy in the average shape, examined between the core bin from $\alpha = 0$ to $2\pi/8$ and each of the other voxels. The periodic structure represents the binning in $\alpha$ , and the increasing numbers in each of these periods correspond to increasing $R$ , where the eight points with correlation coefficient 1 are the eight core bins. Both the Gaussian and VAE generated toy events are able to reproduce the major correlation structures for 65 GeV central pions in EMB2. . . . .	62
180	4.8	Comparison of the RMS fluctuations about the average shape with the Gaussian fluctuation model (red), the VAE fluctuation model (green), and without correlated fluctuations (blue) for a range of pion energies, $\eta$ points, and layers. . . . .	63
183	4.9	Comparison of the Gaussian fluctuation model to the default FCSV2 version and to G4 simulation, using pions of 65 GeV energy and $0.2 <  \eta  < 0.25$ . Variables shown relate to calorimeter clusters, three-dimensional spatial groupings of cells [76] which provide powerful insight on the structure of energy deposits in the calorimeter. Variables considered include number and energy of clusters, the 2nd moment in lambda, ( $\langle \lambda^2 \rangle$ ), which describes the square of the longitudinal extension of a cluster, where $\lambda$ is the distance of a cell from the shower center along the shower axis, and a cluster moment is defined as $\langle x^n \rangle = \frac{\sum E_i x_i}{\sum E_i}$ , and the distance $\Delta R$ , between the cluster and the true pion. With the correlated fluctuations, variables demonstrate improved modeling relative to default FastCaloSimV2. . . . .	64
194	5.1	Illustration of an interaction producing two light jets and one $b$ -jet in the transverse plane. While the light jets decay “promptly”, coinciding with the primary vertex of the proton-proton interaction, the longer lifetime of $B$ hadrons leads to a secondary decay vertex, displaced from the primary vertex by length $L_{xy}$ . This is typically a few mm, and therefore is not directly visible in the detector, but leads to a large transverse impact parameter, $d_0$ , for the resulting tracks. [85] . . . . .	71
201	5.2	Performance of the various low and high level flavor tagging algorithms in $t\bar{t}$ simulation, demonstrating the tradeoff between $b$ -jet efficiency and light and $c$ -jet rejection. The high level taggers demonstrate significantly better performance than any of the individual low level taggers, with DL1 offering slight improvements over MV2 due to the inclusion of additional input variables. . . . .	75

206	5.3 Performance of the MV2, DL1, and DL1r algorithms in $t\bar{t}$ simulation, demon-		
207	strating the tradeoff between $b$ -jet efficiency and light and $c$ -jet rejection. $f_c$		
208	controls the importance of $c$ -jet rejection in the discriminating variable, and		
209	values shown have been optimized separately for each DL1 configuration. DL1r		
210	demonstrates a significant improvement in both light and $c$ jet rejection over		
211	MV2 and DL1. [90] . . . . .	76	
212	6.1 Example distributions in invariant mass of the reconstructed di-Higgs system		
213	for a variety of spin-0 resonances ( $m(X)$ ) compared to the Standard Model		
214	non-resonant signal (SM HH). Both are presented in their respective signal		
215	regions, after all corresponding analysis selections. The resonant signals are		
216	sharply peaked at values near their respective resonance masses, whereas the		
217	non-resonant signal is much more broad. The different character of these		
218	different signals informs the analysis design. . . . .	85	
219	7.1 Comparison of $m_{H_1}$ vs $m_{H_2}$ planes for the full Run 2 2 $b$ dataset with different		
220	pairings, where $m_{H_1}$ and $m_{H_2}$ are the invariant masses of the leading and		
221	subleading Higgs candidates. As evidenced, this choice significantly impacts		
222	where events fall in this plane, and therefore which events fall into the various		
223	kinematic regions defined in this plane (see Section 7.3). The signal regions		
224	for the resonant/early Run 2 analysis are shown for reference for the BDT and		
225	$D_{HH}$ pairings, while the the min $\Delta R$ signal region shifted is shifted slightly		
226	up and to the right to match the non-resonant selection. Note that the band		
227	structure around 80 GeV in both $m_{H_1}$ and $m_{H_2}$ is introduced by the top veto		
228	described in Section 7.2. . . . .	92	
229	7.2 Comparison of signal distributions in the respective signal regions for the		
230	min $\Delta R$ and $D_{HH}$ pairing for various values of the Higgs trilinear coupling.		
231	The distributions are quite similar at the Standard Model point, but for other		
232	variations, min $\Delta R$ does not pick up the low mass features. . . . .	93	
233	7.3 <b>Resonant search:</b> Illustration of the impact of the top veto on $t\bar{t}$ Monte Carlo		
234	for the resonant analysis, with representative scalar signals shown for reference.		
235	The cut value used is 1.5, shown in the dashed black, and events below this		
236	value are discarded. This top veto clearly removes the bulk of $t\bar{t}$ events, and		
237	the value of the cut is chosen to retain analysis sensitivity, particularly for low		
238	mass. . . . .	95	

239	7.4	<b>Non-resonant search:</b> Illustration of the impact of the top veto on $t\bar{t}$ Monte Carlo for the non-resonant analysis, with the Standard Model signal shown for reference. The cut value used is 1.5, shown in the dashed black, and events below this value are discarded. This top veto clearly removes the bulk of $t\bar{t}$ events. While this plot may seem to motivate a more aggressive cut on $X_{Wt}$ , increasing the value of the cut was found to reduce analysis sensitivity. . . . .	96
245	7.5	Regions used for the resonant search, shown on the $2b$ data mass plane. The outermost region (the “control region”) is used for derivation of the nominal background estimate. The innermost region is the signal region, where the signal extraction fit is performed. The region in between (the “validation region”) is used for the assessment of an uncertainty. . . . .	98
250	7.6	Regions used for the non-resonant search. The “top” and “bottom” quadrants together comprise the control region, in which the nominal background estimate is derived. The “left” and “right” quadrants together comprise the validation region, which is used to assess an uncertainty. The signal region, in the center, is where the signal extraction fit is performed. . . . .	100
255	7.7	Acceptance times efficiency for the respective analysis selections for spin-0, spin-2, and $4b$ Standard Model signals. The Standard Model acceptance times efficiency is roughly consistent with the resonant signals in the mass range near the Standard Model peak (near 400 to 600 GeV). Acceptance times efficiency at low mass is mostly limited by the trigger, whereas for higher masses, the jets start to merge together, and the efficiency for reconstructing four $b$ -tagged jets decreases. The spin-2 signal has a higher low mass acceptance times efficiency than spin-0 due to the broader signal distributions of this variable, which leads to a distortion of this distribution towards higher mass values. The increase in acceptance times efficiency at very low mass reflects the impact of the kinematic threshold of 250 GeV. . . . .	102
266	7.8	Impact of the $m_{HH}$ correction on a range of spin-0 resonant signals. The corrected $m_{HH}$ distributions (solid lines) are much sharper and more centered on the corresponding resonance masses than the uncorrected $m_{HH}$ distributions (dashed). . . . .	103
270	8.1	<b>Resonant Search:</b> Distributions of $\Delta R$ between the closest Higgs Candidate jets, $\Delta R$ between the other two, and average absolute value of HC jet $\eta$ before (left) and after (right) CR derived reweighting for the 2018 Control Region. . . . .	111
273	8.2	<b>Resonant Search:</b> Distributions of $p_T$ of the 2nd and 4th leading Higgs Candidate jets and the $p_T$ of the di-Higgs system before (left) and after (right) CR derived reweighting for the 2018 Control Region. . . . .	112

276	<b>8.3 Resonant Search:</b> Distributions of the number of jets before (left) and after (right) CR derived reweighting for the 2018 Control Region. A minimum of 4 jets is required in each event in order to form Higgs candidates. . . . .	113
277		
278		
279	<b>8.4 Resonant Search:</b> Distributions of $p_T$ of the 1st and 3rd leading Higgs Candidate jets and $\Delta R$ between Higgs candidates before (left) and after (right) CR derived reweighting for the 2018 Control Region. . . . .	114
280		
281		
282	<b>8.5 Resonant Search:</b> Distributions of $\eta$ of the 1st, 2nd, and 3rd leading Higgs Candidate jets before (left) and after (right) CR derived reweighting for the 2018 Control Region. . . . .	115
283		
284		
285	<b>8.6 Resonant Search:</b> Distributions of $\eta$ of the 4th leading Higgs Candidate jet and the $p_T$ of the leading and subleading Higgs candidates before (left) and after (right) CR derived reweighting for the 2018 Control Region. . . . .	116
286		
287		
288	<b>8.7 Resonant Search:</b> Distributions of mass of the leading and subleading Higgs candidates and of the di-Higgs system before (left) and after (right) CR derived reweighting for the 2018 Control Region. . . . .	117
289		
290		
291	<b>8.8 Resonant Search:</b> Distributions of $\Delta\phi$ between jets in the leading and subleading Higgs candidates before (left) and after (right) CR derived reweighting for the 2018 Control Region. . . . .	118
292		
293		
294	<b>8.9 Resonant Search:</b> Distributions of the top veto variable, $X_{Wt}$ , before (left) and after (right) CR derived reweighting for the 2018 Control Region. Reweighting is done after the cut on this variable is applied . . . . .	119
295		
296		
297	<b>8.10 Non-resonant Search (4b):</b> Distributions of $\Delta R$ between the closest Higgs Candidate jets, $\Delta R$ between the other two, and average absolute value of HC jet $\eta$ before (left) and after (right) CR derived reweighting for the 2018 4b Control Region. . . . .	120
298		
299		
300		
301	<b>8.11 Non-resonant Search (4b):</b> Distributions of $p_T$ of the 2nd and 4th leading Higgs Candidate jets and the $p_T$ of the di-Higgs system before (left) and after (right) CR derived reweighting for the 2018 4b Control Region. . . . .	121
302		
303		
304	<b>8.12 Non-resonant Search (4b):</b> Distributions of the number of jets before (left) and after (right) CR derived reweighting for the 2018 4b Control Region. A minimum of 4 jets is required in each event in order to form Higgs candidates. . . . .	122
305		
306		
307	<b>8.13 Non-resonant Search (4b):</b> Distributions of $p_T$ of the 1st and 3rd leading Higgs Candidate jets and $\Delta R$ between Higgs candidates before (left) and after (right) CR derived reweighting for the 2018 4b Control Region. . . . .	123
308		
309		
310	<b>8.14 Non-resonant Search (4b):</b> Distributions of $\eta$ of the 1st, 2nd, and 3rd leading Higgs Candidate jets before (left) and after (right) CR derived reweighting for the 2018 4b Control Region. . . . .	124
311		
312		

313	<b>8.15 Non-resonant Search (4b):</b> Distributions of $\eta$ of the 4th leading Higgs Candidate jet and the $p_T$ of the leading and subleading Higgs candidates before (left) and after (right) CR derived reweighting for the 2018 4b Control Region.	125
317	<b>8.16 Non-resonant Search (4b):</b> Distributions of mass of the leading and sub-leading Higgs candidates and of the di-Higgs system before (left) and after (right) CR derived reweighting for the 2018 4b Control Region.	126
320	<b>8.17 Non-resonant Search (4b):</b> Distributions of $\Delta\phi$ between jets in the leading and subleading Higgs candidates before (left) and after (right) CR derived reweighting for the 2018 4b Control Region.	127
323	<b>8.18 Non-resonant Search (4b):</b> Distributions of the top veto variable, $X_{Wt}$ , before (left) and after (right) CR derived reweighting for the 2018 4b Control Region. Reweighting is done after the cut on this variable is applied.	128
326	<b>8.19 Non-resonant Search (3b1l):</b> Distributions of $\Delta R$ between the closest Higgs Candidate jets, $\Delta R$ between the other two, and average absolute value of HC jet $\eta$ before (left) and after (right) CR derived reweighting for the 2018 3b1l Control Region.	129
330	<b>8.20 Non-resonant Search (3b1l):</b> Distributions of $p_T$ of the 2nd and 4th leading Higgs Candidate jets and the $p_T$ of the di-Higgs system before (left) and after (right) CR derived reweighting for the 2018 3b1l Control Region.	130
333	<b>8.21 Non-resonant Search (3b1l):</b> Distributions of the number of jets before (left) and after (right) CR derived reweighting for the 2018 3b1l Control Region. A minimum of 4 jets is required in each event in order to form Higgs candidates.	131
336	<b>8.22 Non-resonant Search (3b1l):</b> Distributions of $p_T$ of the 1st and 3rd leading Higgs Candidate jets and $\Delta R$ between Higgs candidates before (left) and after (right) CR derived reweighting for the 2018 3b1l Control Region.	132
339	<b>8.23 Non-resonant Search (3b1l):</b> Distributions of $\eta$ of the 1st, 2nd, and 3rd leading Higgs Candidate jets before (left) and after (right) CR derived reweighting for the 2018 3b1l Control Region.	133
342	<b>8.24 Non-resonant Search (3b1l):</b> Distributions of $\eta$ of the 4th leading Higgs Candidate jet and the $p_T$ of the leading and subleading Higgs candidates before (left) and after (right) CR derived reweighting for the 2018 3b1l Control Region.	134
345	<b>8.25 Non-resonant Search (3b1l):</b> Distributions of mass of the leading and subleading Higgs candidates and of the di-Higgs system before (left) and after (right) CR derived reweighting for the 2018 3b1l Control Region.	135

348	8.26 Non-resonant Search (3b1l): Distributions of $\Delta\phi$ between jets in the	
349	leading and subleading Higgs candidates before (left) and after (right) CR	
350	derived reweighting for the 2018 3b1l Control Region. . . . .	136
351	8.27 Non-resonant Search (3b1l): Distributions of the top veto variable, $X_{Wt}$ ,	
352	before (left) and after (right) CR derived reweighting for the 2018 3b1l Control	
353	Region. Reweighting is done after the cut on this variable is applied. . . . .	137
354	9.1 Illustration of the approximate bootstrap band procedure, shown as a ratio to	
355	the nominal estimate for the 2017 non-resonant background estimate. Each	
356	grey line is from the $m_{HH}$ prediction for a single bootstrap training. Figure	
357	9.1(a) shows the variation histograms constructed from median weight $\pm$ the	
358	IQR of the replica weights. It can be seen that this captures the rough shape of	
359	the bootstrap envelope, but is not good estimate for the overall magnitude of	
360	the variation. Figure 9.1(b) demonstrates the applied normalization correction,	
361	and Figure 9.1(c) shows the final band (normalized Figure 9.1(a) + Figure	
362	9.1(b)). Comparing this with the IQR variation for the prediction from each	
363	bootstrap in each bin in Figure 9.1(d), the approximate envelope describes a	
364	very similar variation. . . . .	142
365	9.2 Resonant Search: Example of CR vs VR variation in each $H_T$ region for	
366	2018. The variation nicely factorizes into low and high mass components. . .	144
367	9.3 Non-resonant Search (4b): Example of CR vs VR variation in each signal	
368	region quadrant for 2018. Significantly different behavior is seen between	
369	quadrants, with the largest variation in quadrant 1 and the smallest in quadrant	
370	4. . . . .	145
371	9.4 Resonant Search: Performance of the background estimation method in the	
372	resonant analysis reversed $\Delta\eta_{HH}$ kinematic signal region. A new background	
373	estimate is trained following nominal procedures entirely within the reversed	
374	$\Delta\eta_{HH}$ region, and the resulting model, including uncertainties, is compared	
375	with 4b data in the corresponding signal region. Good agreement is shown.	
376	The the quoted $p$ -value uses the $\chi^2$ test statistic, and demonstrates no evidence	
377	that the data differs from the assessed background. . . . .	149
378	9.5 Non-resonant Search: Performance of the background estimation method	
379	in the 3b + 1 fail validation region. A new background estimate is trained	
380	following nominal procedures but with a reweighting from 2b to 3b + 1 fail	
381	events. Generally good agreement is seen, though there is some deviation at	
382	very low masses in the low $\Delta\eta_{HH}$ low $X_{HH}$ category. . . . .	150

383	10.1 <b>Resonant Search:</b> Demonstration of the performance of the nominal reweighting in the control region on corrected $m_{HH}$ , with Figure 10.1(a) showing 2 <i>b</i> events normalized to the total 4 <i>b</i> yield and Figure 10.1(b) applying the reweighting procedure. Agreement is much improved with the reweighting. Note that overall reweighted 2 <i>b</i> yield agrees with 4 <i>b</i> yield in the control region by construction. . . . .	153
389	10.2 <b>Resonant Search:</b> Demonstration of the performance of the control region derived reweighting in the validation region on corrected $m_{HH}$ . Agreement is generally good for this extrapolated estimate. Note that the uncertainty band includes the extrapolation systematic, which is defined by a reweighting trained in the validation region. . . . .	154
394	10.3 <b>Resonant Search:</b> Signal region agreement of the background estimate and observed data after a background-only profile likelihood fit. The left plot overlays a variety of representative spin-0 signals, while the right does the same for spin-2. The background and data are identical between the two. The closure is generally quite good, though there is an evident deficit in the background estimate relative to the data for higher values of corrected $m_{HH}$ . Note that the spin-2 signals are significantly wider than the spin-0 signals. Near the kinematic threshold of 250 GeV, this leads to, e.g., the double peaked structure of the 280 GeV signal, which is understood to be an effect of the limited kinematic phase space in this region. . . . .	155
404	10.4 <b>Non-resonant Search (4b):</b> Demonstration of the performance of the nominal reweighting in the control region on $m_{HH}$ , split into the two $\Delta\eta_{HH}$ regions. Closure is generally good, with some residual mis-modeling in the low $\Delta\eta_{HH}$ region near 600 GeV. . . . .	157
408	10.5 <b>Non-resonant Search (3b1l):</b> Demonstration of the performance of the nominal reweighting in the control region on $m_{HH}$ , split into the two $\Delta\eta_{HH}$ regions. Closure is generally good, with similar conclusions as for the 4 <i>b</i> region. . . . .	158
411	10.6 <b>Non-resonant Search (4b):</b> Demonstration of the performance of the nominal reweighting in the validation region on $m_{HH}$ , split into the two $\Delta\eta_{HH}$ regions. The low $\Delta\eta_{HH}$ region is consistently overestimated, but, systematic uncertainties are defined via the difference between VR and CR estimates. . . . .	159
415	10.7 <b>Non-resonant Search (3b1l):</b> Demonstration of the performance of the nominal reweighting in the validation region on $m_{HH}$ , split into the two $\Delta\eta_{HH}$ regions. A deficit is present near 600 GeV, but agreement is fairly good otherwise. . . . .	160

418	10.8 Non-resonant Search (4b): Signal region agreement of the background estimate and observed data after a background-only profile likelihood fit for the $4b$ channels, with Standard Model and $\kappa_\lambda = 6$ signal overlaid for reference. Modeling is generally quite good near the Standard Model peak, but disagreements are seen at very low and high masses. A deficit is present in low $\Delta\eta_{HH}$ bins near 600 GeV. . . . .	161
424	10.9 Non-resonant Search (3b1l): Signal region agreement of the background estimate and observed data after a background-only profile likelihood fit for the $3b1l$ channels, with Standard Model and $\kappa_\lambda = 6$ signal overlaid for reference. Conclusions are very similar to the $4b$ channels, with generally good modeling near the Standard Model peak, but disagreements at very low and high masses. A deficit is present near 600 GeV. . . . .	162
430	10.10 Pulls and impacts of the background extrapolation uncertainties for the reso- nant analysis, ranked by magnitude of post-fit impact and shown for a variety of representative scalar signals. Significant pulls of the $H_T$ systematics are present, corresponding to the expectation that the validation region is more similar to the signal region than the control region is. Nuisance parameter pulls are generally consistent across signal mass, but impacts vary, with low $H_T$ having the largest impact for low mass, and high $H_T$ for high mass. 400 GeV is near the split between the two regimes. . . . .	165
438	10.11 Background control/validation region systematic nuisance parameter pulls for the Standard Model non-resonant signal, shown for $4b$ (left) and $3b1l$ (right) separately, though the two channels are fit together. There are four signal region quadrant nuisance parameters for each category in the $2 \times 2$ scheme in $\Delta\eta_{HH}$ and $X_{HH}$ , and each year is treated as a separate channel in the fit. Pulls are generally consistent with zero, though there are some trends: quadrant 1 $4b$ tends to be pulled negatively, 2016 tends to be pulled positively. Note that $4b$ dominates the sensitivity relative to $3b1l$ . . . . .	166

446 10.12 Expected (dashed black) and observed (solid black) 95% CL upper limits  
447 on the cross-section times branching ratio of resonant production for spin-0  
448 ( $X \rightarrow HH$ ) and spin-2 ( $G_{KK}^* \rightarrow HH$ ). The  $\pm 1\sigma$  and  $\pm 2\sigma$  ranges for the  
449 expected limits are shown in the colored bands. The resolved channel expected  
450 limit is shown in dashed pink and covers the range from 251 and 1500 GeV. It  
451 is combined with the boosted channel (dashed blue) between 900 and 1500 GeV.  
452 The theoretical prediction for the bulk RS model with  $k/\bar{M}_{\text{Pl}} = 1$  [25] (solid  
453 red line) is shown, with the decrease below 350 GeV due to a sharp reduction  
454 in the  $G_{KK}^* \rightarrow HH$  branching ratio. The nominal  $H \rightarrow b\bar{b}$  branching ratio is  
455 taken as 0.582. Note that all results use the asymptotic approximation, though  
456 the validity of this approximation for the boosted results above 3 TeV is being  
457 evaluated. . . . .

171

458 10.13 Expected (dashed black) and observed (solid black) 95% CL upper limits  
459 or spin-0 (Scalar  $\rightarrow HH \rightarrow b\bar{b}b\bar{b}$ ) and spin-2 ( $G_{KK} \rightarrow HH \rightarrow b\bar{b}b\bar{b}$ ) from  
460 the early Run 2 4b search [2], to be compared with the results in Figure  
461 10.12. Note that the  $y$ -axis scaling differs from Figure 10.12 by a factor of  
462 the  $HH \rightarrow b\bar{b}b\bar{b}$  branching ratio. An excess is present at 280 GeV, with local  
463 (global) significance  $3.6(2.3)\sigma$ . The spin-2 bulk Randall-Sundrum model with  
464  $k/\bar{M}_{\text{Pl}} = 1$  is excluded for graviton masses between 313 and 1362 GeV. . . .

172

465 10.14 Expected (dashed black) and observed (solid black) 95% CL upper limits on  
466 the cross-section times branching ratio of non-resonant production for a range  
467 of values of the Higgs self-coupling, with the Standard Model value ( $\kappa_\lambda = 1$ )  
468 illustrated with a star. The  $\pm 1\sigma$  and  $\pm 2\sigma$  ranges for the expected limits are  
469 shown in the colored bands. The cross section limit for  $HH$  production is set  
470 at 140 fb (180 fb) observed (expected), corresponding to an observed (expected)  
471 limit of 4.4 (5.9) times the Standard Model prediction.  $\kappa_\lambda$  is constrained to  
472 be within the range  $-4.9 \leq \kappa_\lambda \leq 14.4$  observed ( $-3.9 \leq \kappa_\lambda \leq 10.9$  expected).  
473 The nominal  $H \rightarrow b\bar{b}$  branching ratio is taken as 0.582. The excess present for  
474  $\kappa_\lambda \geq 5$  is thought to be due to a low mass background mis-modeling, present  
475 due to the optimization of this analysis for the Standard Model point, and is not  
476 present in more sensitive channels in this same region (e.g.  $HH \rightarrow bb\gamma\gamma$  [98]).

173

477 10.15 Limits including only events above 381 GeV in  $m_{HH}$ , to be compared with  
478 the limits in Figure 10.14. Such a cut is accomplished by dropping  $m_{HH}$   
479 bins below 381 GeV, with the value of 381 GeV determined by the optimized  
480 variable width binning. All other aspects of the procedure and inputs are kept  
481 the same as in Figure 10.14. The excess at and above  $\kappa_\lambda = 5$  is significantly  
482 reduced, demonstrating that such an excess is driven by low mass. Notably,  
483 there is minimal impact on the expected sensitivity with this  $m_{HH}$  cut. . . .

174

484	11.1 Comparison of full Run 2 ATLAS $HH$ searches for spin-0 resonances. The $b\bar{b}b\bar{b}$ 485 channel (blue) is compared with full Run 2 results from $b\bar{b}\tau^+\tau^-$ (both resolved 486 and boosted) and $b\bar{b}\gamma\gamma$ , as well as the combined early Run 2 results. The 487 $b\bar{b}b\bar{b}$ channel has leading sensitivity above a mass of around 700 GeV, and is 488 competitive with other channels across much of the mass range, demonstrating 489 a strong contribution to the ATLAS $HH$ experimental results. [119] . . . . .	176
490	11.2 Comparison of full Run 2 ATLAS $HH$ searches for Standard Model $HH$ 491 production. The preliminary results presented in this thesis are not yet 492 included in these results. However, the results presented in Table 10.3 are 493 quite competitive with the results from $b\bar{b}\tau^+\tau^-$ and $b\bar{b}\gamma\gamma$ , two of the ATLAS 494 channels with leading sensitivity in the search for $HH$ . Note that these results 495 include signals produced via both gluon-gluon fusion (ggF) and vector boson 496 fusion (VBF), and are normalized as such, while the results of this thesis only 497 include (and are normalized to) ggF production [119] . . . . .	177
498	A.1 Representative Feynman diagrams for the VBF channel. While this channel 499 may be used for both resonant and non-resonant searches [22], this thesis work 500 was developed concurrently with a focused non-resonant search. In addition 501 to variations of the trilinear coupling, $\kappa_\lambda$ , VBF is sensitive to various Higgs 502 couplings to vector bosons, namely $\kappa_V$ and $\kappa_{2V}$ , attached to $VVH$ and $VVHH$ 503 vertices respectively. . . . .	199
504	B.1 Comparison of distributions of $HH p_T$ in the 2018 resonant validation region 505 before reweighting for BDT pairing (left) and pairAGraph (right). $HH p_T$ is 506 a variable with a large difference between $2b$ and $4b$ , but the relative shapes 507 seem to be more similar for pairAGraph than for BDT paring, corresponding 508 to the hypothesis that pairAGraph chooses more “ $4b$ -like” jets. . . . .	205
509	B.2 Comparison of distributions of $HH p_T$ in the 2018 resonant validation region 510 after reweighting for BDT pairing (left) and pairAGraph (right). $HH p_T$ is 511 a variable with a large difference between $2b$ and $4b$ , and the reweighted 512 agreement in the high $p_T$ tail is significantly improved with pairAGraph, with 513 a corresponding reduction in the assigned bootstrap uncertainty in that region.	206
514	B.3 Gaussian process sampling prediction of marginals $m_{H_1}$ and $m_{H_2}$ for $2b$ signal 515 region events compared to real $2b$ signal region events for the 2018 dataset. 516 Good agreement is seen. Only a small fraction (0.01) of the $2b$ dataset is used 517 for both training and this final comparison to mimic $4b$ statistics. . . . .	213

518	B.4 Gaussian process sampling prediction for the mass plane compared to the real 519 $2b$ dataset for 2018. Only a small fraction (0.01) of the $2b$ dataset is used for 520      both training and this final comparison to mimic $4b$ statistics. Good agreement 521      is seen. . . . .	215
522	B.5 Gaussian process sampling prediction of marginals $m_{H1}$ and $m_{H2}$ for $4b$ signal 523      region events compared to both control and validation reweighting predictions. 524      While there are some differences, the estimates are compatible. . . . .	216
525	B.6 Gaussian process sampling prediction for the $4b$ mass plane compared to the 526      reweighted $2b$ estimate in the signal region. Both estimates are compatible. . . . .	217
527	B.7 Comparison of the interpolation background estimate with real $2b$ data in the 528      signal region. Only 1 % of $2b$ data is used in order to mimic $4b$ statistics, and 529      results are presented here summed across years. The “Flow Only” prediction 530      uses samples of actual $2b$ signal region data for the input values of $m_{H1}$ and 531 $m_{H2}$ , whereas the “Flow + GP” prediction uses samples following the Gaussian 532      process procedure above, more closely mimicking a the full background estima- 533      tion procedure. The two predictions are quite comparable, demonstrating the 534      closure of the Gaussian process estimate, and the predicted $m_{HH}$ shape agrees 535      well with $2b$ data. Only $2b$ statistical uncertainty is shown. . . . .	218
536	B.8 Comparison of the interpolation background estimate in the $4b$ signal region 537      with the control region derived reweighted $2b$ estimate, shown for each year 538      individually. Results are generally similar, within around 10 %. . . . .	219
539	C.1 <b>Resonant Search:</b> Distributions of $\Delta R$ between the closest Higgs Candidate 540      jets, $\Delta R$ between the other two, and average absolute value of HC jet $\eta$ before 541      (left) and after (right) CR derived reweighting for the 2018 Validation Region. . . . .	221
542	C.2 <b>Resonant Search:</b> Distributions of $p_T$ of the 2nd and 4th leading Higgs 543      Candidate jets and the $p_T$ of the di-Higgs system before (left) and after (right) 544      CR derived reweighting for the 2018 Validation Region. . . . .	222
545	C.3 <b>Resonant Search:</b> Distributions of the number of jets before (left) and after 546      (right) CR derived reweighting for the 2018 Validation Region. A minimum of 547      4 jets is required in each event in order to form Higgs candidates. . . . .	223
548	C.4 <b>Resonant Search:</b> Distributions of $p_T$ of the 1st and 3rd leading Higgs 549      Candidate jets and $\Delta R$ between Higgs candidates before (left) and after (right) 550      CR derived reweighting for the 2018 Validation Region. . . . .	224
551	C.5 <b>Resonant Search:</b> Distributions of $\eta$ of the 1st, 2nd, and 3rd leading Higgs 552      Candidate jets before (left) and after (right) CR derived reweighting for the 553      2018 Validation Region. . . . .	225

554	<b>C.6 Resonant Search:</b> Distributions of $\eta$ of the 4th leading Higgs Candidate jet 555 and the $p_T$ of the leading and subleading Higgs candidates before (left) and 556 after (right) CR derived reweighting for the 2018 Validation Region. . . . .	226
557	<b>C.7 Resonant Search:</b> Distributions of mass of the leading and subleading Higgs 558 candidates and of the di-Higgs system before (left) and after (right) CR derived 559 reweighting for the 2018 Validation Region. . . . .	227
560	<b>C.8 Resonant Search:</b> Distributions of $\Delta\phi$ between jets in the leading and sub- 561 leading Higgs candidates before (left) and after (right) CR derived reweighting 562 for the 2018 Validation Region. . . . .	228
563	<b>C.9 Resonant Search:</b> Distributions of the top veto variable, $X_{Wt}$ , before (left) 564 and after (right) CR derived reweighting for the 2018 Validation Region. 565 Reweighting is done after the cut on this variable is applied . . . . .	229
566	<b>C.10 Non-resonant Search (4b):</b> Distributions of $\Delta R$ between the closest Higgs 567 Candidate jets, $\Delta R$ between the other two, and average absolute value of HC 568 jet $\eta$ before (left) and after (right) CR derived reweighting for the 2018 4b 569 Validation Region. . . . .	230
570	<b>C.11 Non-resonant Search (4b):</b> Distributions of $p_T$ of the 2nd and 4th leading 571 Higgs Candidate jets and the $p_T$ of the di-Higgs system before (left) and after 572 (right) CR derived reweighting for the 2018 4b Validation Region. . . . .	231
573	<b>C.12 Non-resonant Search (4b):</b> Distributions of the number of jets before (left) 574 and after (right) CR derived reweighting for the 2018 4b Validation Region. A 575 minimum of 4 jets is required in each event in order to form Higgs candidates. . . . .	232
576	<b>C.13 Non-resonant Search (4b):</b> Distributions of $p_T$ of the 1st and 3rd leading 577 Higgs Candidate jets and $\Delta R$ between Higgs candidates before (left) and after 578 (right) CR derived reweighting for the 2018 4b Validation Region. . . . .	233
579	<b>C.14 Non-resonant Search (4b):</b> Distributions of $\eta$ of the 1st, 2nd, and 3rd lead- 580 ing Higgs Candidate jets before (left) and after (right) CR derived reweighting 581 for the 2018 4b Validation Region. . . . .	234
582	<b>C.15 Non-resonant Search (4b):</b> Distributions of $\eta$ of the 4th leading Higgs 583 Candidate jet and the $p_T$ of the leading and subleading Higgs candidates before 584 (left) and after (right) CR derived reweighting for the 2018 4b Validation Region. . . . .	235
585	<b>C.16 Non-resonant Search (4b):</b> Distributions of mass of the leading and sub- 586 leading Higgs candidates and of the di-Higgs system before (left) and after 587 (right) CR derived reweighting for the 2018 4b Validation Region. . . . .	236
588	<b>C.17 Non-resonant Search (4b):</b> Distributions of $\Delta\phi$ between jets in the leading 589 and subleading Higgs candidates before (left) and after (right) CR derived 590 reweighting for the 2018 4b Validation Region. . . . .	237

591	<b>C.18 Non-resonant Search (4b):</b> Distributions of the top veto variable, $X_{Wt}$ , 592 before (left) and after (right) CR derived reweighting for the 2018 4b Validation 593 Region. Reweighting is done after the cut on this variable is applied. . . . .	238
594	<b>C.19 Non-resonant Search (3b1l):</b> Distributions of $\Delta R$ between the closest 595 Higgs Candidate jets, $\Delta R$ between the other two, and average absolute value 596 of HC jet $\eta$ before (left) and after (right) CR derived reweighting for the 2018 597 3b1l Validation Region. . . . .	239
598	<b>C.20 Non-resonant Search (3b1l):</b> Distributions of $p_T$ of the 2nd and 4th leading 599 Higgs Candidate jets and the $p_T$ of the di-Higgs system before (left) and after 600 (right) CR derived reweighting for the 2018 3b1l Validation Region. . . . .	240
601	<b>C.21 Non-resonant Search (3b1l):</b> Distributions of the number of jets before 602 (left) and after (right) CR derived reweighting for the 2018 3b1l Validation 603 Region. A minimum of 4 jets is required in each event in order to form Higgs 604 candidates. . . . .	241
605	<b>C.22 Non-resonant Search (3b1l):</b> Distributions of $p_T$ of the 1st and 3rd leading 606 Higgs Candidate jets and $\Delta R$ between Higgs candidates before (left) and after 607 (right) CR derived reweighting for the 2018 3b1l Validation Region. . . . .	242
608	<b>C.23 Non-resonant Search (3b1l):</b> Distributions of $\eta$ of the 1st, 2nd, and 3rd 609 leading Higgs Candidate jets before (left) and after (right) CR derived reweight- 610 ing for the 2018 3b1l Validation Region. . . . .	243
611	<b>C.24 Non-resonant Search (3b1l):</b> Distributions of $\eta$ of the 4th leading Higgs 612 Candidate jet and the $p_T$ of the leading and subleading Higgs candidates before 613 (left) and after (right) CR derived reweighting for the 2018 3b1l Validation 614 Region. . . . .	244
615	<b>C.25 Non-resonant Search (3b1l):</b> Distributions of mass of the leading and 616 subleading Higgs candidates and of the di-Higgs system before (left) and after 617 (right) CR derived reweighting for the 2018 3b1l Validation Region. . . . .	245
618	<b>C.26 Non-resonant Search (3b1l):</b> Distributions of $\Delta\phi$ between jets in the 619 leading and subleading Higgs candidates before (left) and after (right) CR 620 derived reweighting for the 2018 3b1l Validation Region. . . . .	246
621	<b>C.27 Non-resonant Search (3b1l):</b> Distributions of the top veto variable, $X_{Wt}$ , 622 before (left) and after (right) CR derived reweighting for the 2018 3b1l Vali- 623 dation Region. Reweighting is done after the cut on this variable is applied. 624 . . . . .	247

## ACKNOWLEDGMENTS

626 Five years is both a short time and a long time – many things have happened and many  
627 have stayed the same. I certainly know much more physics than I did at the outset, but also  
628 have learned to ski, discovered a love for hiking, eaten large amounts of cheese, and survived  
629 a pandemic by making sourdough and cinnamon rolls. Of course, the most important part of  
630 any journey is the friends we made along the way – the utmost gratitude and appreciation  
631 goes to the Seattle friends, for the many nights both hard at work and at College Inn, to  
632 the CERN friends, for adventures around Europe and days by the lake, the Chicago friends,  
633 for my position as European correspondent for the Dum Dum Donut Intellectuals, and the  
634 friends from home, for New Years Eve parties and visits in between. Though we’re scattered  
635 across the world, I hope to see you all soon.

636 A thank you, of course, to my family for their continued and constant support, for trying  
637 their best to learn physics along with me, and going along on this Ph.D. adventure every  
638 step of the way.

639 I am only writing this thesis because of the incredible support of my research group, so a  
640 massive thank you to Anna, for your guidance and compassion, for advising me as both a  
641 physicist and a person, and for always being available, and Jana, for shaping who I am as a  
642 physicist and providing feedback on almost literally every talk that I’ve written – I knew I  
643 was getting ready to graduate when you started running out of comments.

644 A special set of thank yous to the SLAC group, namely Nicole, Michael, and Rafael, for  
645 being an excellent set of collaborators with an excellent set of ideas to push the analysis  
646 forward, many of which are in this thesis, and for being my second research family.

647 And last but not least, a thank you to the entire  $HH \rightarrow 4b$  group, of course to Max

648 and Rafael for their guidance and direction, Bejan for being an excellent collaborator and  
649 co-editor for the resonant search, Dale and Alex for excelling on the boosted side of things,  
650 Lucas, for great work on triggers and for diving headfirst into all of my code, the ggF push  
651 squad, for a huge amount of hard work on the non-resonant, and of course the  $HH \rightarrow 4\text{beers}$   
652 team, many of whom have already been mentioned, but who deserve an extra shout out for  
653 keeping things fun even during stressful times.

654 The physics is done, the rest is paperwork. Let us begin.

## PREFACE

656 This thesis focuses primarily on searches for pair production of Higgs bosons in the  $b\bar{b}b\bar{b}$   
657 final state. It begins with an overview of the relevant physics and experimental background  
658 for such work, structured as follows: In Chapter 1, I provide an overview of the Standard  
659 Model of particle physics, with discussion of the theoretical and experimental development of  
660 such a model. Chapter 2 dives more into the details of Higgs boson pair production, as well as  
661 the physics beyond the Standard Model relevant for this thesis. Chapter 3 then provides an  
662 introduction to the experimental apparatus used for the presented searches, with an outline  
663 of the Large Hadron Collider and the ATLAS detector. Chapter 4 details the procedure to  
664 simulate the physics processes discussed in Chapters 1 and 2, including simulation of the  
665 detector discussed Chapter 3. Finally, a review of the procedures to reconstruct objects used  
666 for physics analysis is provided in Chapter 5, with a focus on jets and flavor-tagging.

667 The original contributions of this thesis are discussed in a variety of places. Chapter  
668 4 includes my work on the development of methods to improve the modeling of hadronic  
669 showers within a parametrized simulation of the ATLAS calorimeter. I entirely developed  
670 both the method and the software for the Gaussian method discussed in Chapter 4, including  
671 all of the validations presented there. The development of the Variational Autoencoder  
672 method was done in collaboration with Dalila Salamani. This work has been published in a  
673 set of proceedings [1] and implemented into ATLAS software. At the time of this writing, it  
674 is a candidate for inclusion in the Run 3 simulation infrastructure.

675 Chapters 6 through 10 detail searches for resonant and non-resonant pair production of  
676 Higgs bosons in the  $b\bar{b}b\bar{b}$  final state. I was one of the main analyzers for both of these searches,  
677 responsible for much of the development of the methods, infrastructure, and documentation.

678 My most major contribution was the development of the background estimation procedure  
679 and the associated uncertainties, which I spearheaded both conceptually and practically. This  
680 is quite a significant contribution for both the resonant and non-resonant, as it is the core of  
681 much of the analysis design, with the most direct impact on the final results – to paraphrase  
682 Georges Aad during the resonant review process, “This is the analysis.”

683 This was not my only contribution – for the resonant search, I contributed to the  
684 development of the analysis selection and codebase, performed many of the necessary cross-  
685 checks, and was the co-editor of the ATLAS internal documentation, along with Beojan  
686 Stanislaus, who developed the BDT pairing and much of the analysis software. Credit goes as  
687 well to Lucas Borgna, for much of the work behind the development of the trigger strategy.

688 The resonant search follows many of the procedures of the early Run 2 analysis [2], with  
689 the pairing method and background estimation method constituting the two biggest analysis-  
690 level differences from that work. The non-resonant analysis has several additional changes,  
691 which include a variety of new kinematic variable and region definitions, as well as a different  
692 pairing method than both the early Run 2 search and the resonant search. I was responsible  
693 for a large majority of the studies behind each of these decisions. I am also responsible for  
694 the development of much of the modern  $4b$  software infrastructure, including, of course, the  
695 background estimation framework, a new limit setting framework, and a new centralized  
696 plotting framework, the latter of which greatly facilitates both studies and documentation for  
697 the more complicated non-resonant analysis strategy.

698 At the time of this writing, the preliminary resonant results have been published [3], with  
699 a paper soon to follow, pending some additional studies on the high mass ( $> 3 \text{ TeV}$ ) results  
700 in the boosted analysis channel <sup>1</sup>. The non-resonant results are more preliminary, but the  
701 analysis strategy presented in this thesis is approximately final, and the analysis is beginning

---

<sup>1</sup>This thesis focuses on the resolved analysis channel, so these additional studies do not impact the final results of this thesis work. The boosted channel is included in the limits presented in Figure 10.12, but in no other plots or results. See Appendix A for a description of the boosted analysis selection.

702 internal ATLAS review.

703 While these above results are the main results of this thesis, proof-of-concept studies for  
704 two novel  $4b$  analysis methods are included in Appendix B. This work, done in collaboration  
705 primarily with Nicole Hartman, was not used for the  $4b$  results presented here, but I encourage  
706 the interested reader to consider these for further study in future iterations of the  $4b$  analysis.  
707 I note as well that, while these methods are promising in the context of the  $4b$  analysis, they  
708 are also methodologically interesting, and conceptually related results have been published  
709 concurrently with the development of the work presented in this thesis in [4] and [5].

710

## DEDICATION

711

To family, both given and found

712 Chapter 1

713 **THE STANDARD MODEL OF PARTICLE PHYSICS**

714 The Standard Model of Particle Physics (SM) is a monumental historical achievement,  
715 providing a formalism with which one may describe everything from the physics of everyday  
716 experience to the physics that is studied at very high energies at the Large Hadron Collider  
717 (Chapter 3). In this chapter, we will provide a brief overview of the pieces that go into the  
718 construction of such a model. The primary focus of this thesis is searches for pair production  
719 of Higgs bosons decaying to four  $b$ -quarks. Consequently, we will pay particular attention to  
720 the relevant pieces of the Higgs Mechanism, as well as to the theory behind searches at a  
721 hadronic collider.

722 **1.1 Introduction: Particles and Fields**

723 What is a particle? The Standard Model describes a set of fundamental, point-like, objects  
724 shown in Figure 1.1. These objects have distinguishing characteristics (e.g., mass and spin).  
725 These objects interact in very specific ways. The set of objects and their interactions result  
726 in a set of observable effects, and these effects are the basis of a field of experimental physics.

727 The effects of these objects and their interactions are familiar as fundamental forces:  
728 electromagnetism (photons, electrons), the strong interaction (quarks, gluons), the weak  
729 interaction (neutrinos,  $W$  and  $Z$  bosons). Gravity is not described in this model, as the  
730 weakest, with effects most relevant on much larger distance scales than the rest. However,  
731 the description of these other three is powerful – verifying and searching for cracks in this  
732 description is a large effort, and the topic of this thesis.

733 The formalism for describing these particles and their interactions is that of quantum field  
734 theory. Classical field theory is most familiar in the context of, e.g., electromagnetism – an

735 electric field exists in some region of space, and a charged point-particle experiences a force  
736 characterized by the charge of the point-particle and the magnitude of the field at the location  
737 of the point-particle in spacetime. The same language translates to quantum field theory.  
738 Here, particles are described in terms of quantum fields in some region of spacetime. These  
739 fields have associated charges which describe the forces they experience when interacting  
740 with other quantum fields. Most familiar is electric charge – however this applies to e.g., the  
741 strong interaction as well, where quantum fields have an associated *color charge* describing  
742 behavior under the strong force.

743 Particles are observed to behave in different ways under different forces. These behaviors  
744 respect certain *symmetries*, which are most naturally described in the language of group  
745 theory. The respective fields, charges, and generators of these symmetry groups are the basic  
746 pieces of the SM Lagrangian, which describes the full dynamics of the theory. In the following,  
747 we will build up the basic components of this Lagrangian. The treatment presented here relies  
748 heavily on Jackson's Classical Electrodynamics [7] for the build-up, and Thomson's Modern  
749 Particle Physics [8] for the rest, with reference to Srednicki's Quantum Field Theory [9], and  
750 some personal biases and interjections.

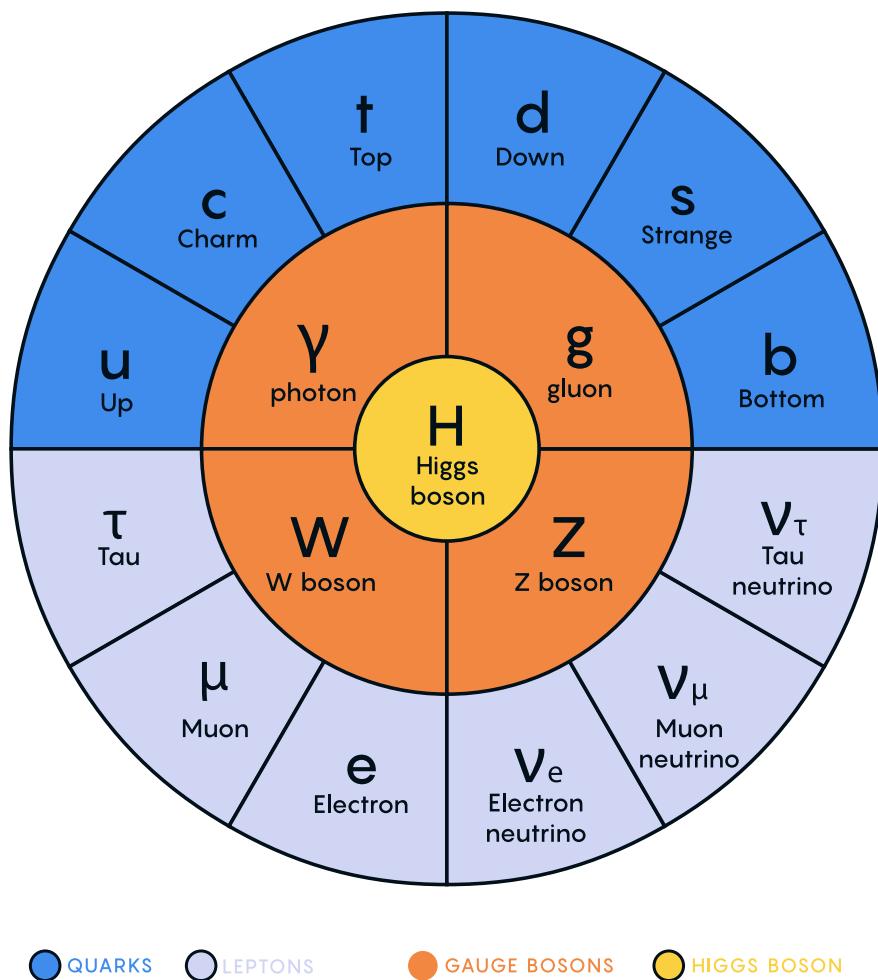


Figure 1.1: Diagram of the elementary particles described by the Standard Model [6].

<sup>751</sup> **1.2 Quantum Electrodynamics**

Classical electrodynamics is familiar to the general physics audience: electric ( $\vec{E}$ ) and magnetic ( $\vec{B}$ ) fields are used to describe behavior of particles with charge  $q$  moving with velocity  $\vec{v}$ , with forces described as  $\vec{F} = q\vec{E} + q\vec{v} \times \vec{B}$ . Hints at some more fundamental properties of electric and magnetic fields come via a simple thought experiment: in a frame of reference moving along with the particle at velocity  $\vec{v}$ , the particle would appear to be standing still, and therefore have no magnetic force exerted. Therefore a *relativistic* formulation of the theory is required. This is most easily accomplished with a repackaging: the fundamental objects are no longer classical fields but the electric and magnetic *potentials*:  $\phi$  and  $\vec{A}$  respectively, with

$$\vec{E} = -\nabla\phi - \frac{\partial\vec{A}}{\partial t} \quad (1.1)$$

$$\vec{B} = \nabla \times \vec{A} \quad (1.2)$$

It is then natural to fully repackage into a relativistic *four-vector*:  $A^\mu = (\phi, \vec{A})$ . Considering  $\partial^\mu = (\frac{\partial}{\partial t}, \nabla)$ , the  $x$  components of these above two equations become:

$$E_x = -\frac{\partial\phi}{\partial x} - \frac{\partial A_x}{\partial t} = -(\partial^0 A^1 - \partial^1 A^0) \quad (1.3)$$

$$B_x = \frac{\partial A_z}{\partial y} - \frac{\partial A_y}{\partial z} = -(\partial^2 A^3 - \partial^3 A^2) \quad (1.4)$$

<sup>752</sup> where we have used the sign convention  $(+, -, -, -)$ , such that  $\partial^\mu = (\frac{\partial}{\partial x_0}, -\nabla)$ .

This is naturally suggestive of a second rank, antisymmetric tensor to describe both the electric and magnetic fields (the *field strength tensor*), defined as:

$$F^{\alpha\beta} = \partial^\alpha A^\beta - \partial^\beta A^\alpha \quad (1.5)$$

Defining a four-current as  $J_\mu = (q, \vec{J})$ , with  $q$  standard electric charge,  $\vec{J}$  standard electric current, conservation of charge may be expressed via the continuity equation

$$\partial_\mu J^\mu = 0 \quad (1.6)$$

and all of classical electromagnetism may be packaged into the Lagrangian density:

$$\mathcal{L} = -\frac{1}{4} F_{\mu\nu} F^{\mu\nu} - J^\mu A_\mu. \quad (1.7)$$

This gets us partway to our goal, but is entirely classical - the description is of classical fields and point charges, not of quantum fields and particles. To reframe this, let us go back to the zoomed out view of the particles of the Standard Model. Two of the most familiar objects associated with electromagnetism are electrons: spin-1/2 particles with charge  $e$ , mass  $m$ , and photons: massless spin-1 particles which are the "pieces" of electromagnetic radiation.

We know that electrons experience electromagnetic interactions with other objects. Given this, and the fact that such interactions must be transmitted *somewhat* between e.g. two electrons, it seems natural that these interactions are facilitated by electromagnetic radiation. More specifically, we may think of photons as *mediators* of the electromagnetic force. It follows, then, that a description of electromagnetism on the level of particles must involve a description of both the "source" particles (e.g. electrons), the mediators (photons), and their interactions. Further, this description must be (1) relativistic and (2) consistent with the classically derived dynamics described above.

The beginnings of a relativistic description of spin-1/2 particles is due to Paul Dirac, with the famous Dirac equation:

$$(i\gamma^\mu \partial_\mu - m)\psi = 0 \quad (1.8)$$

where  $\partial_\mu$  is as defined above,  $\psi$  is a Dirac *spinor*, i.e. a four-component wavefunction,  $m$  is the mass of the particle, and  $\gamma^\mu$  are the Dirac gamma matrices, which define the algebraic structure of the theory. For the following, we also define a conjugate spinor,

$$\bar{\psi} = \psi^\dagger \gamma^0 \quad (1.9)$$

which satisfies the conjugate Dirac equation

$$\bar{\psi}(i\gamma^\mu \partial_\mu - m) = 0 \quad (1.10)$$

where the derivative acts to the left.

The Dirac equation is the dynamical equation for spin-1/2, but we'd like to express these dynamics via a Lagrangian density. Further, to have a relativistic description, we'd like to

have this be density be Lorentz invariant. These constraints lead to a Lagrangian of the form

$$\mathcal{L} = \bar{\psi}(i\gamma^\mu \partial_\mu - m)\psi \quad (1.11)$$

<sup>767</sup> where the Euler-Lagrange equation exactly recovers the Dirac equation.

The question now becomes how to marry the two Lagrangian descriptions that we have developed. Returning for a moment to classical electrodynamics, we know that the Hamiltonian for a charged particle in an electromagnetic field is described by

$$H = \frac{1}{2m}(\vec{p} - q\vec{A})^2 + q\phi. \quad (1.12)$$

Comparing this to the Hamiltonian for a free particle, we see that the modifications required are  $\vec{p} \rightarrow \vec{p} - q\vec{A}$  and  $E \rightarrow E - q\phi$ . Using the canonical quantization trick of identifying  $\vec{p}$  with operator  $-i\nabla$  and  $E$  with operator  $i\frac{\partial}{\partial t}$ , this identification becomes

$$i\partial_\mu \rightarrow i\partial_\mu - qA_\mu \quad (1.13)$$

Allowing for the naive substitution in the Dirac Lagrangian:

$$\mathcal{L} = \bar{\psi}(i\gamma^\mu(\partial_\mu + iqA_\mu) - m)\psi - \frac{1}{4}F_{\mu\nu}F^{\mu\nu}. \quad (1.14)$$

<sup>768</sup> where the source term may be interpreted as coming from the Dirac fields themselves, namely,

<sup>769</sup>  $-q\bar{\psi}\gamma^\mu\psi A_\mu$ .

Setting  $q = e$  here (as appropriate for the case of an electron), and defining  $D_\mu \equiv \partial_\mu + ieA_\mu$ , this may then be written in the form

$$\mathcal{L} = \bar{\psi}(i\gamma^\mu D_\mu - m)\psi - \frac{1}{4}F_{\mu\nu}F^{\mu\nu}. \quad (1.15)$$

<sup>770</sup> which is exactly the quantum electrodynamics Lagrangian.

<sup>771</sup> We have swept a few things under the rug here, however. Recall that the general form  
<sup>772</sup> of a Lagrangian is conventionally  $\mathcal{L} = T - V$ , where  $T$  is the kinetic term, and thus ought  
<sup>773</sup> to contain a derivative with respect to time (c.f. the standard  $\frac{1}{2}m\frac{\partial x}{\partial t}$  familiar from basic  
<sup>774</sup> kinematics). More particularly, given the definition of conjugate momentum as  $\partial\mathcal{L}/\partial\dot{q}$  for

<sup>775</sup>  $\mathcal{L}(q, \dot{q}, t)$  and  $\dot{q} = \frac{\partial q}{\partial t}$ , any field  $q$  which has no time derivative in the Lagrangian has 0  
<sup>776</sup> conjugate momentum, and thus no dynamics.

<sup>777</sup> Looking at this final form, there is an easily identifiable kinetic term for the spinor fields  
<sup>778</sup> (just applying the  $D_\mu$  operator). However trying to identify something similar for the  $A$  fields,  
<sup>779</sup> one comes up short – the antisymmetric nature of  $F^{\mu\nu}$  term means that there is no time  
<sup>780</sup> derivative applied to  $A^0$ .

<sup>781</sup> What does this mean?  $A^\mu$  is a four component object, but it would appear that only three  
<sup>782</sup> of the components have dynamics: we have too many degrees of freedom in the theory. This  
<sup>783</sup> is the principle behind *gauge symmetry* – an extra constraint on  $A^\mu$  (a *gauge condition*) must  
<sup>784</sup> be defined such that a unique  $A^\mu$  defines the theory and satisfies the condition. However,  
<sup>785</sup> we are free to choose this extra condition – the physics content of the theory should be  
<sup>786</sup> independent of this choice (that is, it should be *gauge invariant*).

To ground this a bit, let us return to basic electric and magnetic fields. These are physical quantities that can be measured, and are defined in terms of potentials as

$$\vec{E} = -\nabla\phi - \frac{\partial\vec{A}}{\partial t} \quad (1.16)$$

$$\vec{B} = \nabla \times \vec{A}. \quad (1.17)$$

<sup>787</sup> It is easy to show, for any scalar function  $\lambda$ , that  $\nabla \times \nabla\lambda = 0$ . This implies that the physical  
<sup>788</sup>  $\vec{B}$  field is invariant under the transformation  $\vec{A} \rightarrow \vec{A} + \nabla\lambda$  for any scalar function  $\lambda$ .

<sup>789</sup> Under the same transformation of  $\vec{A}$ , the electric field  $\vec{E}$  becomes  $-\nabla\phi - \frac{\partial\vec{A}}{\partial t} - \frac{\partial\nabla\lambda}{\partial t} =$   
<sup>790</sup>  $-\nabla(\phi + \frac{\partial\lambda}{\partial t}) - \frac{\partial\vec{A}}{\partial t}$ , such that, for the  $\vec{E}$  field to be unchanged, we must additionally apply  
<sup>791</sup> the transformation  $\phi \rightarrow \phi - \frac{\partial\lambda}{\partial t}$ .

This set of transformations to the potentials that leave the physical degrees of freedom invariant is expressed in our four vector notation naturally as

$$A_\mu \rightarrow A_\mu - \partial_\mu \lambda \quad (1.18)$$

<sup>792</sup> where  $A_\mu = (\phi, -\vec{A})$  with our sign convention. It should be noted that this function  $\lambda$  is an  
<sup>793</sup> arbitrary function of *local* spacetime, and thus expresses invariance of the physics content

<sup>794</sup> under a local transformation.

Let us return to the Lagrangian for QED. In particular, focusing on the free Dirac piece

$$\mathcal{L} = \bar{\psi}(i\gamma^\mu \partial_\mu - m)\psi \quad (1.19)$$

we note that if we apply a local transformation of the form  $\psi \rightarrow e^{iq\lambda(x)}\psi$  (and correspondingly  $\bar{\psi} \rightarrow \bar{\psi}e^{-iq\lambda(x)}$ , by definition), the Lagrangian becomes

$$\bar{\psi}e^{-iq\lambda(x)}(i\gamma^\mu \partial_\mu - m)e^{iq\lambda(x)}\psi = \bar{\psi}e^{-iq\lambda(x)}(i\gamma^\mu \partial_\mu)e^{iq\lambda(x)}\psi - m\bar{\psi}\psi. \quad (1.20)$$

As  $\partial_\mu(e^{iq\lambda(x)}\psi) = iq e^{iq\lambda(x)}(\partial_\mu \lambda(x))\psi + e^{iq\lambda(x)}\partial_\mu \psi$ , this becomes

$$\bar{\psi}(i\gamma^\mu(\partial_\mu + iq\partial_\mu \lambda(x)) - m)\psi. \quad (1.21)$$

Thus, the free Dirac Lagrangian on its own is not invariant under this transformation. We may note, however, that on interaction with an electromagnetic field, as described above, this transformed Lagrangian may be packaged as:

$$\bar{\psi}(i\gamma^\mu(\partial_\mu + iq\partial_\mu \lambda(x) + iqA_\mu) - m)\psi = \bar{\psi}(i\gamma^\mu(\partial_\mu + iq(A_\mu + \partial_\mu \lambda(x))) - m)\psi. \quad (1.22)$$

<sup>795</sup> since by the arguments above, the physics content of the Lagrangian is invariant under the  
<sup>796</sup> transformation  $A_\mu \rightarrow A_\mu - \partial_\mu \lambda$ , we may directly make this transformation, and remove this  
<sup>797</sup> extra  $\partial_\mu \lambda(x)$  term. It is straightforward to verify that the  $\frac{1}{4}F_{\mu\nu}F^{\mu\nu}$  term is invariant under  
<sup>798</sup> this same transformation of  $A_\mu$ , so we may say that the QED Lagrangian is invariant under  
<sup>799</sup> local transformations of the form  $\psi \rightarrow e^{iq\lambda(x)}\psi$ .

<sup>800</sup> These arguments illuminate some important concepts which will serve us well going forward.  
<sup>801</sup> First, while we have remained grounded in the “familiar” physics of electromagnetism for the  
<sup>802</sup> above, arguments of the “top down” variety would lead us to the exact same conclusions.  
<sup>803</sup> That is, suppose we wanted to construct a theory of spin-1/2 particles that was invariant  
<sup>804</sup> under local transformations of the form  $\psi \rightarrow e^{iq\lambda(x)}\psi$ . More broadly, we could say that we  
<sup>805</sup> desire this theory to be invariant under local  $U(1)$  transformations, where  $U(1)$  is exactly  
<sup>806</sup> this group, under multiplication, of complex numbers with absolute value 1. By very similar

807 arguments as above, we would see that, to achieve invariance, this theory would necessitate  
808 an additional degree of freedom,  $A_\mu$ , with the exact properties that are familiar to us from  
809 electrodynamics. These arguments based on symmetries are extremely powerful in building  
810 theories with a less familiar grounding, as we will see in the following.

Second, we defined this quantity  $D_\mu \equiv \partial_\mu + ieA_\mu$  above, seemingly as a matter of notational convenience. However, from the latter set of arguments, such a packaging takes on a new power: by explicitly including this gauge field  $A_\mu$  which transforms in such a way as to keep invariance under a given transformation, the invariance is immediately more manifest. That is, to pose the  $U(1)$  invariance in a more zoomed out way, under the transformation  $\psi \rightarrow e^{iq\lambda(x)}\psi$ , while

$$\bar{\psi}\partial_\mu\psi \rightarrow \bar{\psi}(\partial_\mu + iq\partial_\mu\lambda(x))\psi \quad (1.23)$$

with the extra term that gets canceled out by the gauge transformation of  $A_\mu$ ,

$$\bar{\psi}D_\mu\psi \rightarrow \bar{\psi}D_\mu\psi \quad (1.24)$$

811 where this transformation is already folded in. This repackaging, called a *gauge covariant*  
812 *derivative* is much more immediately expressive of the symmetries of the theory.

813 Finally, to emphasize how fundamental these gauge symmetries are to the corresponding  
814 theory, let us examine the additional term needed for  $U(1)$  invariance,  $q\bar{\psi}\gamma^\mu A_\mu\psi$ . While a  
815 first principles examination of Feynman rules is beyond the scope of this thesis, it is powerful  
816 to note that this is expressive of a QED vertex: the  $U(1)$  invariance of the theory and the  
817 interaction between photons and electrons are inextricably tied together.

### 818 1.3 An Aside on Group Theory

819 Quantum electrodynamics is very familiar and well covered, and provides (both historically  
820 and in this thesis) a nice bridge between “standard” physics and the language of symmetries  
821 and quantum field theory. However, now that we are acquainted with the language, we  
822 may set up to dive a bit deeper. To begin, let us look again at the  $U(1)$  group that is so  
823 fundamental to QED. We have expressed this via a set of transformations on our Dirac spinor

824 objects,  $\psi$ , of the form  $e^{iq\lambda(x)}$ . Note that such transformations, though they are local (i.e. a  
825 function of spacetime) are purely *phase* transformations. Relatedly,  $U(1)$  is an Abelian group,  
826 meaning that group elements commute.

827 To set up language to generalize beyond  $U(1)$ , note that we may equivalently write  $U(1)$   
828 elements as  $e^{ig\vec{\alpha}(x)\cdot\vec{T}}$ ,  $\vec{\alpha}(x)$  and  $\vec{T}$  and are vectors in the space of *generators* of the group,  
829 with each  $\alpha^a(x)$  an associated scalar function to generator  $t^a$ , and  $g$  is some scalar strength  
830 parameter. Of course this is a bit silly for  $U(1)$ , which has a single generator, and thus  
831 reduces to the transformation we discussed above. However, this becomes much more useful  
832 for groups of higher degree, with more generators and degrees of freedom.

833 To discuss these groups in a bit more detail, note that  $U(n)$  is the unitary group of degree  
834  $n$ , and corresponds to the group of  $n \times n$  unitary matrices (that is,  $U^\dagger U = UU^\dagger = 1$ ). Given  
835 that group elements are  $n \times n$ , this means that there are  $n^2$  degrees of freedom:  $n^2$  generators  
836 are needed to characterize the group.

837 For  $U(1)$ , this is all consistent with what we have said above – the group of  $1 \times 1$  unitary  
838 matrices have a single generator, and the phases we identify above clearly satisfy unitarity.  
839 Note that these degrees of freedom for the gauge group also characterize the number of gauge  
840 bosons we need to satisfy the local symmetry: for  $U(1)$ , we need one gauge boson, the photon.

841 Of relevance for the Standard Model are also the special unitary groups  $SU(n)$ . These  
842 are defined similarly to the unitary groups, with the additional requirement that group  
843 elements have determinant 1. This extra constraint removes 1 degree of freedom: groups are  
844 characterized by  $n^2 - 1$  generators.

845 In particular, we will examine the groups  $SU(2)$  in the context of the weak interaction,  
846 with an associated  $2^2 - 1 = 3$  gauge bosons (cf. the  $W^\pm$  and  $Z$  bosons), and  $SU(3)$ , with an  
847 associated  $3^2 - 1 = 8$  gauge bosons (cf. gluons of different flavors). Note that these groups  
848 are non-Abelian ( $2 \times 2$  or  $3 \times 3$  matrices do not, in general, commute), leading to a variety of  
849 complications. However, both of these theories feature interactions with spin-1/2 particles,  
850 with transformations of a very similar form:  $\psi \rightarrow e^{ig\vec{\alpha}(x)\cdot\vec{T}}\psi$ , and the general framing of the  
851 arguments for QED will serve us well in the following.

852 **1.4 Quantum Chromodynamics**

853 In some sense, the simplest extension of the development of QED is quantum chromodynamics  
854 (QCD). QCD is a theory in which, once the basic dynamics are framed (a non-trivial task!) the  
855 group structure becomes apparent. The quark model, developed by Murray Gell-Mann [10]  
856 and George Zweig [11], provided the fundamental particles involved in the theory, and had  
857 great success in explaining the expanding zoo of experimentally observed hadronic states.

858 Some puzzles were still apparent – the  $\Delta^{++}$  baryon, e.g., is composed of three up quarks,  
859  $u$ , with aligned spins. As quarks are fermions, such a state should not be allowed by the  
860 Pauli exclusion principle. The existence of such a state in nature implies the existence  
861 of another quantum number, and a triplet of values, called *color charge* was proposed by  
862 Oscar Greenberg [12]. With these pieces in place, the structure becomes more apparent, as  
863 elucidated by Han and Nambu [13].

864 Let us reason our way to the symmetries using color charge. Experimentally, we know  
865 that there is this triplet of color charge values  $r, g, b$  (the “plus” values, cf. electric charge)  
866 and correspondingly anti-color charge  $\bar{r}, \bar{g}, \bar{b}$  (the “minus” values). Supposing that the force  
867 behind QCD (the *strong force*) is, similar to QED, interactions between fermions mediated  
868 by gauge bosons (quarks and gluons respectively), we can start to line up the pieces.

869 What color charge does a gluon have? Similarly to electric charge, we may associate  
870 particles with color charge, anti-particles with anti-color charge. Notably, free particles  
871 observed experimentally are colorless (have no color charge). Thus, in order for charge to  
872 be conserved throughout such processes, this already implies that there are charged gluons.  
873 Further, examining color flow diagrams, it is apparent first that a gluon has not one but  
874 two associated color charges and second that these two must be one color charge and one  
875 anti-color charge.

876 Counting up the available types of gluons, then, we come up with nine. Six of mixed  
877 color type:  $r\bar{b}, r\bar{g}, b\bar{r}, b\bar{g}, g\bar{b}$ , and  $g\bar{r}$ , and three of same color type:  $r\bar{r}, g\bar{g}$ , and  $b\bar{b}$ . In practice,  
878 however, these latter three are a bit redundant: all express a colorless gluon, which, if we

879 could observe this as a free particle, would be indistinguishable from each other. The *color*  
 880 *singlet* state is then a mix of these,  $\frac{1}{\sqrt{3}}(r\bar{r} + g\bar{g} + b\bar{b})$ , leaving two unclaimed degrees of  
 881 freedom, which may be satisfied by the linearly independent combinations  $\frac{1}{\sqrt{2}}(r\bar{r} - g\bar{g})$  and  
 882  $\frac{1}{\sqrt{6}}(r\bar{r} + g\bar{g} - 2b\bar{b})$ .

883 We thus have an octet of color states plus a colorless singlet state. If this colorless singlet  
 884 state existed, however, we would be able to observe it, not only via interactions with quarks,  
 885 but as a free particle. Since do not observe this in nature, this restricts us to 8 gluons. The  
 886 simplest group with a corresponding 8 generators is  $SU(3)$ . Under the assumption that  
 887  $SU(3)$  is the local gauge symmetry of the strong interaction, we may proceed in a similar  
 888 way as we did for QED. The gauge transformation is  $\psi \rightarrow e^{ig_S \vec{\alpha}(x) \cdot \vec{T}} \psi$ , where  $\vec{T}$  is an eight  
 889 component vector of the generators of  $SU(3)$ , often expressed via the Gell-Mann matrices,  
 890  $\lambda^a$ , as  $t^a = \frac{1}{2}\lambda^a$ , and the spinor  $\psi$  represents the fields corresponding to quarks.

891 This  $SU(3)$  symmetry exactly expresses the color structure elucidated above – the Gell-  
 892 Mann matrices are an equivalent presentation of the color combinations described above.  
 893 Proceeding by analogy to QED, gauge invariance is achieved by introducing eight new degrees  
 894 of freedom,  $G_\mu^a$ , which are the gauge fields corresponding to the gluons, with the gauge  
 895 covariant derivative then analogously taking the form  $D_\mu \equiv \partial_\mu + ig_S G_\mu^a t^a$ .

Recall from the QED derivation that the field strength tensor,  $F^{\mu\nu}$  is a rank two antisymmetric tensor which is manifestly gauge invariant and which describes the physical dynamics of the  $A_\mu$  field. We would like to analogously define a term for the gluon fields. Repackaging this QED tensor, it is apparent that

$$[D_\mu, D_\nu] = D_\mu D_\nu - D_\nu D_\mu \quad (1.25)$$

$$= (\partial_\mu + iqA_\mu)(\partial_\nu + iqA_\nu) - (\partial_\nu + iqA_\nu)(\partial_\mu + iqA_\mu) \quad (1.26)$$

$$= \partial_\mu \partial_\nu + iq\partial_\mu A_\nu + iqA_\mu \partial_\nu + (iq)^2 A_\mu A_\nu - (\partial_\nu \partial_\mu + iq\partial_\nu A_\mu + iqA_\nu \partial_\mu + (iq)^2 A_\nu A_\mu) \quad (1.27)$$

$$= iq(\partial_\mu A_\nu - \partial_\nu A_\mu) + (iq)^2 (A_\mu A_\nu - A_\nu A_\mu) \quad (1.28)$$

$$= iq(\partial_\mu A_\nu - \partial_\nu A_\mu) + (iq)^2 [A_\mu, A_\nu]. \quad (1.29)$$

We proceed through this derivation to highlight that, in the specific case of QED, with its Abelian  $U(1)$  gauge symmetry, the field commutator vanishes, leaving exactly the definition of  $F_{\mu\nu}$  as described above, i.e.,

$$F_{\mu\nu} = \frac{1}{iq}[D_\mu, D_\nu]. \quad (1.30)$$

We may proceed to define an analogous field strength term for  $G_\mu^a$  in a similar way:

$$G_{\mu\nu} = \frac{1}{ig_S}[D_\mu, D_\nu] \quad (1.31)$$

This has an extremely nice correspondence, but is complicated by the non-Abelian nature of  $SU(3)$ , with

$$G_{\mu\nu} = \partial_\mu(G_\nu^a t^a) - \partial_\nu(G_\mu^a t^a) + ig_s[G_\mu^a t^a, G_\nu^a t^a]. \quad (1.32)$$

in which the field commutator term is non-zero. In particular (since each term is summing over  $a$ , so we may relabel) as

$$[G_\mu^a t^a, G_\nu^b t^b] = [t^a, t^b]G_\mu^a G_\nu^b \quad (1.33)$$

and as  $[t^a, t^b] = if^{abc}t^c$  for the Gell-Mann matrices, where  $f^{abc}$  are the structure constants of  $SU(3)$ , we have

$$G_{\mu\nu} = \partial_\mu(G_\nu^a t^a) - \partial_\nu(G_\mu^a t^a) - g_s f^{abc} t^c G_\mu^a G_\nu^b \quad (1.34)$$

$$= t^a(\partial_\mu G_\nu^a - \partial_\nu G_\mu^a - f^{bca} G_\mu^b G_\nu^c) \quad (1.35)$$

$$= t^a G_{\mu\nu}^a \quad (1.36)$$

<sup>896</sup> for  $G_{\mu\nu}^a = \partial_\mu G_\nu^a - \partial_\nu G_\mu^a - f^{abc} G_\mu^b G_\nu^c$ .

<sup>897</sup> This gives the component of the field strength corresponding to a particular gauge field  $a$ ,  
<sup>898</sup> where the first two terms have the familiar form of the QED field strength, while the last  
<sup>899</sup> term is new, and explicitly related to the group structure via the  $f^{abc}$  constants. In terms  
<sup>900</sup> of the physics content of the theory, this latter term gives rise to a gluon *self-interaction*, a  
<sup>901</sup> distinguishing feature of QCD.

<sup>902</sup> Similarly as in QED, a Lorentz invariant combination of field strength tensors may be made  
<sup>903</sup> as  $G_{\mu\nu} G^{\mu\nu}$ . However, this is not manifestly gauge invariant. Under a gauge transformation

904  $U$ , the covariant derivative behaves as  $D^\mu \rightarrow UD^\mu U^{-1}$ , corresponding to  $G^{\mu\nu} \rightarrow UG^{\mu\nu}U^{-1}$ .  
905 The cyclic property of the trace thus ensures the gauge invariance of  $\text{tr}(G_{\mu\nu}G^{\mu\nu})$ , which we  
906 will write as  $G_{\mu\nu}^a G_a^{\mu\nu}$  with the implied sum over generators  $a$ .

Packaging up the theory, it is tempting to copy the form of the QED Lagrangian, with the identifications we have made above:

$$\mathcal{L} = \bar{\psi}(i\gamma^\mu D_\mu - m)\psi - \frac{1}{4}G_{\mu\nu}^a G_a^{\mu\nu}. \quad (1.37)$$

However this is not quite correct due to the  $SU(3)$  nature of the theory. In terms of the physics, the Dirac fields  $\psi$  have associated color charge, which must interact appropriately with the  $G_\mu$  fields. Mathematically, the generators  $t^a$  are  $3 \times 3$  matrices, while the  $\psi$  are four component spinors. Adding a color index to the Dirac fields, i.e.,  $\psi_i$  where  $i$  runs over the three color charges, and similarly indexing the generators  $t_{ij}^a$ , we may then express the  $SU(3)$  gauge covariant derivative component-wise as

$$(D_\mu)_{ij} = \partial_\mu \delta_{ij} + ig_S G_\mu^a t_{ij}^a \quad (1.38)$$

907 where  $\delta_{ij}$  is the Kronecker delta, as  $\partial_\mu$  does not participate in the  $SU(3)$  structure.

The Lagrangian then becomes

$$\mathcal{L} = \bar{\psi}_i(i(\gamma^\mu D_\mu)_{ij} - m\delta_{ij})\psi_j - \frac{1}{4}G_{\mu\nu}^a G_a^{\mu\nu}. \quad (1.39)$$

908 and we have constructed QCD.

## 909 1.5 The Weak Interaction

910 One of the first theories of the weak interaction was from Enrico Fermi [14], in an effort to  
911 explain beta decay, a process in which an electron or positron is emitted from an atomic  
912 nucleus, resulting in the conversion of a neutron to a proton or proton to a neutron respectively.  
913 Fermi's hypothesis was of a direct interaction between four fermions. However, in the advent of  
914 QED, it is natural to wonder if a theory based on mediator particles and gauge symmetries  
915 applies to the weak force as well. The modern formulation of such a theory is due to Sheldon

916 Glashow, Steven Weinberg, and Abdus Salam [15], and is what we will describe in the  
917 following.

918 Considering emission of an electron, Fermi's theory involves an initial state neutron that  
919 transitions to a proton with the emission of an electron and a neutrino. This transition  
920 gives a hint that something slightly more complicated is happening than in QED: there is an  
921 apparent mixing between particle types.

922 Now, with the assumption there are mediators for such an interaction, we further know  
923 from beta decay and charge conservation that there must be at least two such degrees of  
924 freedom: e.g. one that decays to an electron and neutrino ( $W^-$ ) and one that decays to a  
925 positron and neutrino ( $W^+$ ). From consideration of the process  $e^+e^- \rightarrow W^+W^-$ , it turns  
926 out that with just these two degrees of freedom, the cross section for this process increases  
927 without limit as a function of center-of-mass energy, ultimately violating unitarity (more  
928  $W^+W^-$  pairs come out than  $e^+e^-$  pairs go in). This is resolved with a third, neutral degree  
929 of freedom, the  $Z$  boson, whose contribution interferes negatively, regulating this process.

930 This leads to three degrees of freedom for the gauge symmetry of the weak interactions, so  
931 we thus need a theory which is locally invariant under transformations of a group with three  
932 generators. The simplest such choice is  $SU(2)$ . We may follow a very similar prescription as  
933 for QED and QCD:  $SU(2)$  has three generators, which implies the existence of three gauge  
934 bosons, call them  $W_\mu^k$ . The gauge transformation may be expressed as  $\psi \rightarrow e^{ig_W \vec{\alpha}(x) \cdot \vec{T}} \psi$ , where  
935 in this case the generators are for  $SU(2)$ , which may be written in terms of the familiar Pauli  
936 matrices:  $\vec{T} = \frac{1}{2}\vec{\sigma}$ . The structure constants for  $SU(2)$  are the antisymmetric Levi-Civita  
937 tensor, so the corresponding gauge covariant derivative is  $D_\mu \equiv \partial_\mu + ig_W W_\mu^k t^k$ , and the field  
938 strength tensor is  $W_{\mu\nu}^k = \partial_\mu W_\nu^k - \partial_\nu W_\mu^k - \epsilon^{ijk} W_\mu^k W_\nu^k$ .

The corresponding Lagrangian would thus be

$$\mathcal{L} = \bar{\psi}_i (i(\gamma^\mu D_\mu)_{ij} - m\delta_{ij}) \psi_j - \frac{1}{4} W_{\mu\nu}^k W_k^{\mu\nu} \quad (1.40)$$

939 where indices  $i$  and  $j$  run over  $SU(2)$  charges.

940 On considering some of the details, the universe unfortunately turns out to be a bit

more complicated. However, this still provides a useful starting place for elucidating the theory of weak interactions. First off, let us consider the particle content, namely, what do the Dirac fields correspond to? This is still a theory of fermionic interactions with gauge bosons. However, we might notice that the fermion content of this theory is both a) broader than QCD, as we know experimentally (cf. beta decay) that both quarks and leptons (e.g. electrons) participate in the weak interaction and b) this fermion content seemingly has a large overlap with QED. In terms of the gauge bosons, we know that at both  $W^+$  and  $W^-$  are electrically charged – this means that we expect some interaction of the weak theory with electromagnetism.

However, before diving deeper into this apparent connection between the weak interaction and QED, let us focus on the gauge symmetry. In QCD, the  $SU(3)$  content of the theory is expressed via a contraction of color indices – the theory allows for transitions between quarks of one color and quarks of another. Thinking similarly in terms of  $SU(2)$  transitions, the beta decay example is already fruitful – there is a transition between an electron and its corresponding neutrino, as well as between two types of quark. In particular, for the case of a neutron (with quark content  $udd$ ) and a proton (with quark content  $udu$ ), the weak interaction provides for a transition from down to up quark.

Such  $SU(2)$  dynamics are described via a quantity called *weak isospin*, denoted  $I_W$  with third component  $I_W^{(3)}$ , and can be thought of in a very similar way as color charge in QCD (i.e. as the charge corresponding to the weak interaction). Since  $SU(2)$  is  $2 \times 2$ , there are two such charge states for the fermions, denoted as  $I_W^{(3)} = \pm\frac{1}{2}$ . This means that the bosons must have  $I_W = 1$  such that, by sign convention corresponding to electric charge, the  $W^+$  boson has  $I_W^{(3)} = +1$ , the  $Z$  boson has  $I_W^{(3)} = 0$ , and the  $W^-$  boson has  $I_W^{(3)} = -1$ .

From conservation of electric charge, this means that transitions involving a  $W^\pm$  are between particles that differ by  $\pm 1$  in both weak isospin  $I_W^{(3)}$  and electric charge. We may thus line up all such doublets as:

$$\begin{pmatrix} \nu_e \\ e^- \end{pmatrix}, \begin{pmatrix} \nu_\mu \\ \mu^- \end{pmatrix}, \begin{pmatrix} \nu_\tau \\ \tau^- \end{pmatrix}, \begin{pmatrix} u \\ d' \end{pmatrix}, \begin{pmatrix} c \\ s' \end{pmatrix}, \begin{pmatrix} t \\ b' \end{pmatrix} \quad (1.41)$$

964 with the top corresponding to the lower weak isospin and electric charge particles, and the  
965 lower quark entries ( $d'$ , etc) corresponding to the weak quark eigenstates (which are related  
966 to the mass eigenstates via the CKM matrix). Similar doublets may be constructed for the  
967 corresponding anti-particles.

The fundamental structuring of these transitions around both electric and weak charge is again indicative of a natural connection. However, nature is again a bit more complicated than we have described. This is because the weak interaction is a *chiral* theory. For massless particles, chirality is the same as the perhaps more intuitive *helicity*. This describes the relationship between a particle's spin and momentum: if the spin vector points in the same direction as the momentum vector, helicity is positive (the particle is “right-handed”), and if the two point in opposite directions, the helicity is negative (the particle is “left-handed”). More concretely:

$$H = \frac{\vec{s} \cdot \vec{p}}{|\vec{s} \cdot \vec{p}|}. \quad (1.42)$$

For massive particles, this generalizes a bit – in the language of Dirac fermions that we have developed, we define projection operators

$$P_R = \frac{1}{2}(1 + \gamma^5) \quad \text{and} \quad P_L = \frac{1}{2}(1 - \gamma^5) \quad (1.43)$$

968 for right and left-handed chiralities respectively – acting on a Dirac field with such operators  
969 projects the field onto the corresponding chiral state.

Experimentally, this pops up via parity violation and the famous  $V - A$  theory. For the scope of this thesis, it is sufficient to say that the weak interaction is only observed to take place for left-handed particles (and correspondingly, right-handed anti-particles). We therefore modify the theory stated above by projecting all fermions participating in the weak interaction onto respective chiral states – in particular, the  $SU(2)$  gauge symmetry only acts on left-handed particles and right-handed anti-particles. We therefore modify the theory appropriately, denoting the chiral projected gauge symmetry as  $SU(2)_L$ , and similarly for the

Dirac fields. In particular, the weak isospin doublets listed above must now be left-handed:

$$\begin{pmatrix} \nu_e \\ e^- \end{pmatrix}_L, \begin{pmatrix} \nu_\mu \\ \mu^- \end{pmatrix}_L, \begin{pmatrix} \nu_\tau \\ \tau^- \end{pmatrix}_L, \begin{pmatrix} u \\ d' \end{pmatrix}_L, \begin{pmatrix} c \\ s' \end{pmatrix}_L, \begin{pmatrix} t \\ b' \end{pmatrix}_L \quad (1.44)$$

and right-handed particle states are placed in singlets and assigned 0 charge under  $SU(2)_L$  ( $I_W = I_W^{(3)} = 0$ ).

With all of these assignments, let us revisit our guess at the form of the weak interaction Lagrangian. First, dwelling on the kinetic term  $\bar{\psi}_i(i(\gamma^\mu D_\mu)_{ij}\psi_j)$ , we note that the assigning of left-handed fermions to isospin doublets and right-handed fermions to isospin singlets allows us to remove explicit  $SU(2)$  indices by treating these as the fundamental objects, that is, for a single *generation* of fermions, we may write:

$$\bar{Q}i\gamma^\mu D_\mu Q + \bar{u}i\gamma^\mu D_\mu u + \bar{d}i\gamma^\mu D_\mu d + \bar{L}i\gamma^\mu D_\mu L + \bar{e}i\gamma^\mu D_\mu e \quad (1.45)$$

for left-handed doublets  $Q$  and  $L$  for quarks and electron fields respectively and right-handed singlets  $u$  and  $d$  for up and down quark fields and  $e$  for electrons.

More concisely, and summing over the three generations of fermions, we may write

$$\sum_f \bar{f}i\gamma^\mu D_\mu f \quad (1.46)$$

where the  $f$  are understood to run over the fermion chiral doublets and singlets as above.

This then leaves our Lagrangian as

$$\mathcal{L} = \sum_f \bar{f}i\gamma^\mu D_\mu f - \frac{1}{4}W_{\mu\nu}^k W_k^{\mu\nu} \quad (1.47)$$

$$= \sum_f \bar{f}\gamma^\mu(i\partial_\mu - \frac{1}{2}g_W W_\mu^k \sigma_k)f - \frac{1}{4}W_{\mu\nu}^k W_k^{\mu\nu}, \quad (1.48)$$

where we have expanded the covariant derivative for clarity. You may note that we have dropped the mass term in the equation above – we will discuss this in detail in just a moment.

First, however, we return to the above comment about fermion content – we neglected to include the sum over fermions in our QED derivation for simplicity. However, all of the

fermions considered in the discussion of the weak interaction have an electric charge (except for the neutrinos). It would be nice to repackage the theory into a coherent *electroweak* theory. This is fairly straightforward when considering the gauge approach – from the discussion above we should expect the electroweak gauge group to be something like  $SU(2) \times U(1)$ , with four corresponding gauge bosons. Consider a gauge theory with group  $SU(2)_L \times U(1)_Y$  – that is, the same weak interaction as discussed previously, but a new  $U(1)_Y$  gauge group for electromagnetism, with transformations defined as

$$\psi \rightarrow e^{ig' \frac{Y}{2} \lambda(x)} \psi \quad (1.49)$$

<sup>977</sup> with *weak hypercharge*  $Y$ .

Similarly to our discussion of QED, we may write the  $U(1)_Y$  gauge field as  $B_\mu$ , and interactions with the Dirac fields take the form  $g' \frac{Y}{2} \gamma^\mu B_\mu \psi$ . The relationship between this hypercharge and new  $B_\mu$  field and classical electrodynamics is not so obvious – however it is convenient to parametrize as

$$\begin{pmatrix} A_\mu \\ Z_\mu \end{pmatrix} = \begin{pmatrix} \cos \theta_W & \sin \theta_W \\ -\sin \theta_W & \cos \theta_W \end{pmatrix} \begin{pmatrix} B_\mu \\ W_\mu^3 \end{pmatrix} \quad (1.50)$$

<sup>978</sup> where  $A_\mu$  and  $Z_\mu$  are the physical fields, and we pick  $W_\mu^3$  as the neutral weak boson.

<sup>979</sup> Note that in the  $SU(2)_L \times U(1)_Y$  theory, the Lagrangian must be invariant under all of  
<sup>980</sup> the local gauge transformations. In particular, this means that the hypercharge must be the  
<sup>981</sup> same for fermion fields in each weak doublet to preserve  $U(1)_Y$  invariance. This gives insight  
<sup>982</sup> into the relation between the charges of  $SU(2)_L \times U(1)_Y$  and electric charge. In particular  
<sup>983</sup> we know that the hypercharge,  $Y$ , of  $e^-$  ( $I_W^{(3)} = -\frac{1}{2}$ ) and  $\nu_e$  ( $I_W^{(3)} = +\frac{1}{2}$ ) is the same.

Supposing that  $Y = \alpha I_W^{(3)} + \beta Q$ , we must have  $-\alpha \frac{1}{2} - \beta = \alpha \frac{1}{2} \implies \beta = -\alpha$ . Therefore, choosing an overall scaling from convention,

$$Y = 2(Q - I_W^{(3)}). \quad (1.51)$$

<sup>984</sup> Some of these particular forms are best understood in the context of the Higgs mechanism  
<sup>985</sup> – we will return to this discussion below.

986 **1.6 The Higgs Potential and the SM**

987 In the above, we have neglected a discussion of masses. However there are several things to  
988 sort out here. In the first place, we know experimentally that the weak interactions occur  
989 over very short ranges at low energies (e.g., why Fermi's effective four fermion interaction was  
990 such a good description). This is consistent with massive  $W^\pm$  and  $Z$  bosons (and indeed, this  
991 is seen experimentally). However, requiring local gauge invariance forbids mass terms in the  
992 Lagrangian. In the simple  $U(1)$  QED example, such a term would have the form  $\frac{1}{2}m_\gamma^2 A_\mu A^\mu$ ,  
993 which is not invariant under the transformation  $A_\mu \rightarrow A_\mu - \partial_\mu \lambda$ , and similar arguments hold  
994 for gauge bosons in the electroweak theory and QCD.

Similar issues are encountered with fermions – in the electroweak theory above, the gauge symmetries are separated into left and right-handed chirality via doublet and singlet states. This means that a mass term would need to be separated as well. Such a term would have the form:

$$m\bar{f}f = m(\bar{f}_L + \bar{f}_R)(f_L + f_R) \quad (1.52)$$

$$= m(\bar{f}_L f_L + \bar{f}_L f_R + \bar{f}_R f_L + \bar{f}_R f_R) \quad (1.53)$$

$$= m(\bar{f}_L f_R + \bar{f}_R f_L) \quad (1.54)$$

995 where we have used that  $f_{L,R} = P_{L,R}f$ ,  $\bar{f}_{L,R} = \bar{f}P_{R,L}$ , and  $P_R P_L = P_L P_R = 0$ . As left  
996 and right-handed particles transform differently under  $SU(2)_L$ , this is manifestly not gauge  
997 invariant.

998 The question then becomes: how do we include particle masses while preserving the  
999 gauge properties of our theory? The answer, due to Robert Brout and François Englert [16],  
1000 Peter Higgs [17], and Gerald Guralnik, Richard Hagen, and Tom Kibble [18] comes via the  
1001 Higgs mechanism, which we will describe in the following. Importantly for this thesis, this  
1002 mechanism predicts the existence of a physical particle, the Higgs boson, and a particle  
1003 consistent with the Higgs boson was seen by both ATLAS [19] and CMS [20] in 2012.

To explain the Higgs, we focus first on generating masses for the electroweak gauge bosons.

Consider adding two complex scalar fields  $\phi^+$  and  $\phi^0$  to the Standard Model embedded in a weak isospin doublet  $\phi$ . We may write the doublet as

$$\phi = \begin{pmatrix} \phi^+ \\ \phi^0 \end{pmatrix} = \frac{1}{\sqrt{2}} \begin{pmatrix} \phi_1 + i\phi_2 \\ \phi_3 + i\phi_4 \end{pmatrix} \quad (1.55)$$

1004 where we explicitly note the four available degrees of freedom.

The Lagrangian for such a doublet takes the form

$$\mathcal{L} = (\partial_\mu \phi)^\dagger (\partial^\mu \phi) - V(\phi) \quad (1.56)$$

where  $V$  is the corresponding potential. Considering the particular form

$$V(\phi) = \mu^2 \phi^\dagger \phi + \lambda (\phi^\dagger \phi)^2 \quad (1.57)$$

1005 we may notice that this has some interesting properties. Considering, as illustration, a similar  
1006 potential for a real scalar field,  $\mu^2 \chi^2 + \lambda \chi^4$ , taking the derivative and setting it equal to 0  
1007 yields extrema when  $\chi = 0$  and  $(\mu^2 + 2\lambda\chi^2) = 0 \implies \chi^2 = -\frac{\mu^2}{2\lambda}$ . For  $\mu^2 > 0$ , there is a  
1008 unique minimum at  $\chi = 0$ , and for  $\mu^2 < 0$  there are degenerate minima at  $\chi = \pm\sqrt{-\frac{\mu^2}{2\lambda}}$ .  
1009 Note that we take  $\lambda > 0$ , otherwise the only minima in the theory are trivial.

The same simple calculus for the complex Higgs doublet above yields degenerate minima for  $\mu^2 < 0$  at

$$\phi^\dagger \phi = \frac{1}{2}(\phi_1^2 + \phi_2^2 + \phi_3^2 + \phi_4^2) = \frac{v}{2} = -\frac{\mu^2}{2\lambda} \quad (1.58)$$

However, though there is this degenerate set of minima, there can only be a single *physical* vacuum state (we say that the symmetry is *spontaneously broken*). Without loss of generality, we may align our axes such that the physical vacuum state is at

$$\langle 0 | \phi | 0 \rangle = \frac{1}{\sqrt{2}} \begin{pmatrix} 0 \\ v \end{pmatrix} \quad (1.59)$$

1010 where we have explicitly chosen a real, non-zero vacuum expectation value for the neutral  
1011 component of the Higgs doublet to maintain a massless photon, as we shall see. Physically,  
1012 however, this makes sense - the vacuum is not electrically charged.

The vacuum is a classical state – we want a quantum one. We may express fluctuations about this nonzero expectation value via an expansion as  $v + \eta(x) + i\xi(x)$ . However, renaming of fields is only meaningful for the non-zero vacuum component - we thus have:

$$\phi = \frac{1}{\sqrt{2}} \begin{pmatrix} \phi_1 + i\phi_2 \\ v + \eta(x) + i\phi_4 \end{pmatrix}. \quad (1.60)$$

where we may expand the Lagrangian listed above:

$$\mathcal{L} = (\partial_\mu \phi)^\dagger (\partial^\mu \phi) - \mu^2 \phi^\dagger \phi - \lambda(\phi^\dagger \phi)^2. \quad (1.61)$$

It is an exercise in algebra to plug in the expansion about  $v$  into this Lagrangian: first expanding the potential

$$V(\phi) = \mu^2 \phi^\dagger \phi + \lambda(\phi^\dagger \phi)^2 \quad (1.62)$$

$$= \mu^2 \left( \sum_i \phi_i(x)^2 + (v + \eta(x))^2 \right) + \lambda \left( \sum_i \phi_i(x)^2 + (v + \eta(x))^2 \right) \quad (1.63)$$

$$= -\frac{1}{4} \lambda v^4 + \lambda v^2 \eta^2 + \lambda v \eta^3 + \frac{1}{4} \lambda \eta^4 \quad (1.64)$$

$$+ \frac{1}{2} \lambda \sum_{i \neq j} \phi_i^2 \phi_j^2 + \lambda v \eta \sum_i \phi_i(x)^2 + \frac{1}{2} \lambda \eta^2 \sum_i \phi_i(x)^2 + \frac{1}{4} \sum_i \phi_i(x)^4 \quad (1.65)$$

where the sums are over the  $i \in 1, 2, 4$ , that is, the fields with 0 vacuum expectation, and we have used the definition  $\mu^2 = -\lambda v^2$ .

Within this potential, we note a quadratic term in  $\eta(x)$  which we may identify with a mass, namely  $m_\eta = \sqrt{2\lambda v^2}$ , whereas the  $\phi_i$  are massless. These  $\phi_i$  are known as *Goldstone bosons*, and correspond to quantum fluctuations along the minimum of the potential. Of particular note for this thesis are the interaction terms  $\lambda v \eta^3$  and  $\frac{1}{4} \lambda \eta^4$ , expressing trilinear and quartic self-interactions of the  $\eta$  field.

Expanding the kinetic term

$$(\partial_\mu \phi)^\dagger (\partial^\mu \phi) = \frac{1}{2} \sum_i (\partial_\mu \phi_i)(\partial^\mu \phi_i) + \frac{1}{2} (\partial_\mu(v + \eta(x)))(\partial^\mu(v + \eta(x))) \quad (1.66)$$

$$= \frac{1}{2} \sum_i (\partial_\mu \phi_i)(\partial^\mu \phi_i) + \frac{1}{2} (\partial_\mu \eta)(\partial^\mu \eta) \quad (1.67)$$

1020 in a similar way completes the story of three massless degrees of freedom (Goldstone bosons)  
1021 and one massive one.

Now, this doublet is embedded in an  $SU(2)_L \times U(1)$  theory, so we would like to preserve that gauge invariance. This is achieved in the same way as for the Dirac fields, with the introduction of the electroweak gauge covariant derivative such that the Lagrangian for the Higgs doublet and the electroweak bosons is just

$$\mathcal{L} = (D_\mu \phi)^\dagger (D^\mu \phi) - \mu^2 \phi^\dagger \phi - \lambda (\phi^\dagger \phi)^2 - \frac{1}{4} W_{\mu\nu}^k W_k^{\mu\nu} - \frac{1}{4} F_{\mu\nu} F^{\mu\nu} \quad (1.68)$$

1022 with  $D_\mu = \partial_\mu + ig_W W_\mu^k t^k + ig' \frac{Y}{2} B_\mu$ .

We note that it is convenient to pick a gauge such that the Goldstone fields do not appear in the Lagrangian, upon which we may identify the field  $\eta(x)$  with the physical Higgs field,  $h(x)$ . The field mass terms then very apparently come via the covariant derivative, namely, as

$$W_\mu^k \sigma^k + B_\mu = \begin{pmatrix} W_\mu^3 + B_\mu & W_\mu^1 - iW_\mu^2 \\ W_\mu^1 + iW_\mu^2 & -W_\mu^3 + B_\mu \end{pmatrix} \quad (1.69)$$

we may then write

$$D_\mu \phi = \frac{1}{2\sqrt{2}} \begin{pmatrix} 2\partial_\mu + ig_W W_\mu^3 + ig' Y B_\mu & ig_W W_\mu^1 + \frac{1}{2} g_W W_\mu^2 \\ ig_W W_\mu^1 - g_W W_\mu^2 & 2\partial_\mu - ig_W W_\mu^3 + ig' Y B_\mu \end{pmatrix} \begin{pmatrix} 0 \\ v + h \end{pmatrix} \quad (1.70)$$

$$= \frac{1}{2\sqrt{2}} \begin{pmatrix} ig_W (W_\mu^1 - iW_\mu^2)(v + h) \\ (2\partial_\mu - ig_W W_\mu^3 + ig' Y B_\mu)(v + h) \end{pmatrix} \quad (1.71)$$

1023 As identified above,  $Y = 2(Q - I_W^{(3)})$ . The Higgs has 0 electric charge, and the lower doublet  
1024 component has  $I_W^{(3)} = -\frac{1}{2}$ , yielding  $Y = 1$ .

Computing  $(D_\mu \phi)^\dagger (D^\mu \phi)$ , then, yields

$$\frac{1}{8} g_W^2 (W_\mu^1 + iW_\mu^2)(W^{\mu 1} - iW^{\mu 2})(v + h)^2 + \frac{1}{8} (2\partial_\mu + ig_W W_\mu^3 - ig' B_\mu)(2\partial^\mu - ig_W W^{\mu 3} + ig' B^\mu)(v + h)^2 \quad (1.72)$$

and extracting terms quadratic in the fields gives

$$\frac{1}{8} g_W^2 v^2 (W_{\mu 1} W^{\mu 1} + W_{\mu 2} W^{\mu 2}) + \frac{1}{8} v^2 (g_W W_\mu^3 - g' B_\mu)(g_W W^{\mu 3} - g' B^\mu) \quad (1.73)$$

meaning that  $W_\mu^1$  and  $W_\mu^2$  have masses  $m_W = \frac{1}{2}g_W v$ . The neutral boson case is a bit more complicated. Writing the corresponding term as

$$\frac{1}{8}v^2 \begin{pmatrix} W_\mu^3 & B_\mu \end{pmatrix} \begin{pmatrix} g_W^2 & -g_W g' \\ -g_W g' & g'^2 \end{pmatrix} \begin{pmatrix} W^{\mu 3} \\ B^\mu \end{pmatrix} \quad (1.74)$$

we note that we must diagonalize this mass matrix to get the physical mass eigenstates. Doing so in the usual way yields eigenvalues  $0$ ,  $g'^2 + g_W^2$ , thus corresponding to  $m_\gamma = 0$  and  $m_Z = \frac{1}{2}v\sqrt{g'^2 + g_W^2}$ , with physical fields as the (normalized) eigenvectors

$$A_\mu = \frac{g' W_\mu^3 + g_W B_\mu}{\sqrt{g_W^2 + g'^2}} \quad (1.75)$$

$$Z_\mu = \frac{g_W W_\mu^3 - g' B_\mu}{\sqrt{g_W^2 + g'^2}} \quad (1.76)$$

From this form, the angular parametrization of the physical fields is very apparent, namely, defining

$$\tan \theta_W = \frac{g'}{g_W}, \quad (1.77)$$

these equations may be written in terms of the single parameter  $\theta_W$  as

$$A_\mu = \cos \theta_W B_\mu + \sin \theta_W W_\mu^3 \quad (1.78)$$

$$Z_\mu = -\sin \theta_W B_\mu + \cos \theta_W W_\mu^3 \quad (1.79)$$

and, notably, from the above equations,

$$\frac{m_W}{m_Z} = \cos \theta_W. \quad (1.80)$$

To get the mass terms from Equation 1.72, we extracted those terms quadratic in fields, i.e., the  $v^2$  terms within  $(v + h)^2$ . However there are also terms of the form  $VVh$  and  $VVhh$  that arise, which describe the Higgs interactions with the corresponding vector bosons  $V = W^\pm, Z$ . Namely, identifying physical  $W$  bosons as

$$W^\pm = \frac{1}{\sqrt{2}}(W^1 \mp iW^2) \quad (1.81)$$

we may express the first term of Equation 1.72 as

$$\frac{1}{4}g_W^2 W_\mu^- W^{+\mu} (v + h)^2 = \frac{1}{4}g_W^2 v^2 W_\mu^- W^{+\mu} + \frac{1}{2}g_W^2 v W_\mu^- W^{+\mu} h + \frac{1}{4}g_W^2 W_\mu^- W^{+\mu} h^2 \quad (1.82)$$

with the first term corresponding to the mass term  $m_W = \frac{1}{2}g_W v$ , and the second two terms corresponding to  $hW^+W^-$  and  $hhW^+W^-$  vertices. Of particular note is the coupling strength

$$g_{HWW} = \frac{1}{2}g_W^2 v = g_W m_W \quad (1.83)$$

1025 which is proportional to the  $W$  mass. A similar analysis with the form of the physical  $Z$   
1026 boson finds that the corresponding coupling,  $g_{HZZ}$ , is proportional to the  $Z$  mass.

The Higgs coupling to fermions (in particular to quarks) is of particular interest for this thesis. We showed above that a naive introduction of a mass term

$$m\bar{f}f = m(\bar{f}_L f_R + \bar{f}_R f_L) \quad (1.84)$$

1027 is manifestly not gauge invariant because right and left handed particles transform differently  
1028 under  $SU(2)_L$ . However, because the Higgs is constructed via an  $SU(2)_L$  doublet,  $\phi$ , writing  
1029 a fermion doublet as  $L$  and conjugate  $\bar{L}$ , it is apparent that  $\bar{L}\phi$  is invariant under  $SU(2)_L$ .

Combining with the right-handed singlet,  $R$ , creates a term invariant under  $SU(2)_L \times U(1)_Y$ ,  $\bar{L}\phi R$  (and correspondingly  $(\bar{L}\phi R)^\dagger$ ), such that we may include Yukawa [21] terms

$$\mathcal{L}_{Yukawa} = -g_f \left[ \begin{pmatrix} \bar{f}_1 & \bar{f}_2 \end{pmatrix}_L \begin{pmatrix} \phi^+ \\ \phi^0 \end{pmatrix} f_R + \bar{f}_R \begin{pmatrix} \phi^{+*} & \phi^{0*} \end{pmatrix} \begin{pmatrix} f_1 \\ f_2 \end{pmatrix}_L \right] \quad (1.85)$$

1030 where  $g_f$  is a corresponding Yukawa coupling,  $f_1$  and  $f_2$  have been used to denote components  
1031 of the left-handed doublet and  $f_R$  the corresponding right-handed singlet.

After spontaneous symmetry breaking, with the gauge as described above to remove the Goldstone fields, the Higgs doublet becomes

$$\phi(x) = \begin{pmatrix} 0 \\ v + h(x) \end{pmatrix} \quad (1.86)$$

giving rise to terms such as

$$-\frac{1}{\sqrt{2}}g_f v(\bar{f}_{2L}\bar{f}_R + \bar{f}_R f_{2L}) - \frac{1}{\sqrt{2}}g_f h(\bar{f}_{2L}\bar{f}_R + \bar{f}_R f_{2L}) \quad (1.87)$$

where we have kept the subscript  $f_{2L}$  to emphasize that these terms *only* impact the lower component of the left-handed doublet because of the 0 in the upper component of the Higgs doublet. Leaving this aside for a second, we note that the first term has the form of the desired mass term above (identifying  $f_{2L}$  to  $f_L$ ) while the second term describes the coupling of the fermion to the physical Higgs field. The corresponding Yukawa coupling may be chosen to be consistent with the observed fermion mass, namely

$$g_f = \sqrt{2} \frac{m_f}{v} \quad (1.88)$$

such that

$$\mathcal{L}_f = -m_f \bar{f}f - \frac{m_f}{v} \bar{f}fh. \quad (1.89)$$

1032 Notably here, the fermion coupling to the Higgs boson scales with the mass of the fermion, a  
1033 fact that is extremely relevant for this thesis analysis.

As we said above, these terms *only* impact the lower component of the left-handed doublet. The inclusion of terms for the upper component is accomplished via the introduction of a Higgs conjugate doublet, defined as

$$\phi_c = -i\sigma_2\phi^* = \begin{pmatrix} -\phi^{0*} \\ \phi^- \end{pmatrix}. \quad (1.90)$$

1034 The argument proceeds similarly to the above, with similar results for couplings and masses  
1035 of upper components.

### 1036 1.7 The Standard Model: A Summary

After all of the above, we may write the Standard Model as a theory with a local  $SU(3) \times SU(2)_L \times U(1)_Y$  gauge symmetry, described by the Lagrangian

$$\mathcal{L} = \sum_f \bar{f}i\gamma^\mu D_\mu f - \frac{1}{4} \sum_{gauges} F_{\mu\nu}F^{\mu\nu} + (D_\mu\phi)^\dagger(D^\mu\phi) - \mu^2\phi^\dagger\phi - \lambda(\phi^\dagger\phi)^2 \quad (1.91)$$

where  $D_\mu = \partial_\mu + ig_W W_\mu^k t^k + ig' \frac{Y}{2} B_\mu + ig_S G_\mu^a t^a$ , in addition to the Yukawa terms, which we write generally as

$$\mathcal{L}_{Yukawa} = - \sum_{f,\phi=\phi,-\phi_c} y_f (\bar{f}\phi f + (\bar{f}\phi f)^\dagger) \quad (1.92)$$

1037 with the sum running over running over appropriate chiral fermion and Higgs doublets.

1038 The  $SU(2)_L \times U(1)_Y$  subgroup is spontaneously broken to a  $U(1)$  symmetry, lending mass  
1039 to the associated gauge bosons and fermions. Of relevance for this thesis is the resulting  
1040 physical Higgs field, with a predicted trilinear self-interaction and associated coupling  $\lambda v$ ,  
1041 related to the experimentally observed Higgs boson mass by  $m_H = \sqrt{2\lambda v^2}$ , as well as the fact  
1042 that the strength of the Higgs coupling to fermions scales proportionally with the fermion  
1043 mass.

1044 **1.8 Experimental Review and Outlook**

1045 The Standard Model has been monumentally successful: as listed in Figure [6], there are 17  
1046 particles in the Standard Model. For each, there is a large body of experimental observations  
1047 and verifications. We here briefly describe the initial observations of these particles, and note  
1048 that, while there is physics that is not explained by the Standard Model, experimental results  
1049 for physics within the Standard Model have so far demonstrated beautiful consistency with  
1050 the theory.

1051 Indicative of the importance and strength of electromagnetism in the everyday world, the  
1052 electron and photon were foundational discoveries that began the theoretical flurry which  
1053 resulted in the Standard Model. While electric charge was observed by even the ancient  
1054 Greeks (and, in fact, the word electric is derived from the Greek word for amber, which picks  
1055 up a charge when rubbed with fur), the connection of this charge to a subatomic particle came  
1056 later, with J.J. Thompson the first (in 1897) to definitively show the existence of electrons,  
1057 using cathode ray tubes to demonstrate a particle with a mass much smaller than hydrogen  
1058 and with a charge to mass ratio independent the of material used in the cathode.

1059 The discovery of the photon is much talked about in any introductory quantum mechanics

1060 course via the dual wave/particle nature of light. The assumption in 1900 of Max Planck that  
1061 electromagnetic radiation could only be emitted or absorbed in discrete quantities (“quanta”)  
1062 resolved the ultraviolet catastrophe, a classical prediction that energy emitted by a black  
1063 body diverges for high frequencies. Soon after, in 1905, Einstein postulated that such quanta  
1064 corresponded to physical particles, explaining, for instance, the photoelectric effect.

1065 These two foundational particles led to the development of both atomic theory and  
1066 quantum mechanics. In 1936, Carl D. Anderson and Seth Neddermeyer, while studying  
1067 cosmic radiation, observed a particle that behaved similarly to an electron but had a shallower  
1068 curvature in a magnetic field (though a sharper curvature than protons). With an assumption  
1069 of the same electric charge, this difference is indicative of a particle with mass in between  
1070 that of an electron and a proton, and this was the first observation of the muon.

1071 The completion of the set of leptons did not come till much later, with SPEAR, an  
1072 electron-positron collider at SLAC, which was used for the discovery of the tau by Martin  
1073 Lewis Perl in experiments between 1974 and 1977. This was done via the detection of  
1074 anomalous events, which required the production and decay of a new particle pair  $\tau^+\tau^-$ .

1075 Though Fermi first proposed a theory of beta decay involving a neutrino in 1934, and hints  
1076 of its existence were present in cloud chamber experiments via nuclear recoil, the electron  
1077 neutrino was first directly observed in 1956, via inverse beta decay in a nuclear reactor by  
1078 Clyde Cowan and Frederick Reines, in which an electron anti-neutrino interacts with a proton  
1079 to produce neutrons and positrons. This confirmed the existence of neutrinos – the fact that  
1080 there are different types of neutrinos was seen soon after, in 1962, by Leon Lederman, Melvin  
1081 Schwartz, and Jack Steinberger, who demonstrated, via pion decay, the existence of the muon  
1082 neutrino. Given these two flavors of neutrino, after the discovery of the  $\tau$ , the existence of a  
1083  $\tau$  neutrino was also expected – this was confirmed in 2000 by the DONUT collaboration at  
1084 Fermilab.

1085 In 1968, deep inelastic scattering experiments at SLAC, in which a beam of electrons is  
1086 fired at atomic nuclei to probe internal structure of protons and neutrons, confirmed the  
1087 existence of internal proton structure. These constituents of the proton would eventually be

1088 identified as quarks, which had been proposed by Gell-Mann and Zweig in 1964. The proton  
 1089 contains two up quarks and a down quark – however the existence of up and down quarks,  
 1090 in conjunction with the observation of kaons and pions and the “eightfold way” particle  
 1091 classification of Gell-Mann, indirectly confirmed the existence of the strange quark.

1092 The charm quark was discovered via the observation of a charm anti-charm meson, called  
 1093  $J/\psi$ , by Burton Richter and Samuel Ting in 1974, with the dual name a consequence of  
 1094 the shared, but independent, discovery. Richter’s group at SLAC made the discovery with  
 1095 SPEAR, whereas Ting’s group utilized fixed target collisions of a proton beam. Both observed  
 1096 a new resonance near 3 GeV.

1097 In 1977, the bottom quark was discovered at Fermilab by Leon Lederman via the obser-  
 1098 vation of a resonance near 9.5 GeV produced by fixed target proton beam collisions. This  
 1099 resonance, the  $\Upsilon$  meson, consists of a bottom quark and an anti-bottom quark, and was  
 1100 observed in the di-muon decay channel.

1101 As the heaviest of the quarks, the top quark was not discovered until 1995. This was done  
 1102 at the Tevatron at Fermilab, a proton anti-proton collider, offering a center of mass energy of  
 1103 1.8 TeV, with observations by the CDF and DØ experiments.

1104 The  $\Upsilon$  meson used for the  $b$ -quark discovery was also important in the discovery of the  
 1105 gluon, observed via electron-positron collisions, first by the PLUTO detector at DORIS  
 1106 (DESY) in 1978 and then by the TASSO, MARK-J, JADE, and PLUTO experiments at  
 1107 PETRA (DESY) in 1979. The 1978 observation demonstrated excellent consistency with a  
 1108 three-gluon decay topology for the  $\Upsilon(9.46\text{ GeV})$  decay, but the mass of the  $\Upsilon(9.46\text{ GeV})$  is  
 1109 not high enough to resolve three distinct jets. Operating at  $\sqrt{s} = 27.4\text{ GeV}$ , the experiments  
 1110 in 1979 demonstrated a three jet topology consistent (at these higher energies) with gluon  
 1111 bremsstrahlung, that is  $e^+e^- \rightarrow q\bar{q}g$ , providing the first evidence for the existence of the  
 1112 gluon.

1113 To complete the picture are the massive bosons, all discovered at CERN. In 1983 the  
 1114  $W$  and  $Z$  bosons were observed, via proton-antiproton collisions and the UA1 and UA2  
 1115 experiments. Carlo Rubbia and Simon van der Meer received the Nobel Prize for this discovery

in 1984. Most recently, in 2012, a particle consistent with the Higgs boson was discovered by ATLAS and CMS at the Large Hadron Collider.

Note the careful phrasing for the Higgs boson – although all tests so far have demonstrated consistency with the particle predicted by the Standard Model, this thesis work probes the trilinear Higgs coupling, which is directly sensitive to the structure of the Higgs potential. Agreement of this coupling with the Standard Model prediction is a crucial part of confirming that this particle is indeed the Standard Model Higgs boson, and therefore is a very important piece of the physics goals of the Large Hadron Collider.

The Standard Model, for all of its power, is notably not a complete theory of the universe – there is no inclusion of gravity, for instance, though a consistent description may be provided with the introduction of a spin-2 particle. Neutrino oscillations demonstrate that neutrinos have mass, but right-handed neutrinos do not participate in the Standard Model and have not been observed, leading to questions about whether there is a different mechanism to provide neutrinos with mass than that described above. Cosmology tells us that dark matter exists, but there is no corresponding particle within the Standard Model. This thesis therefore also participates in searches for physics beyond the Standard Model. We will provide a sketch of the relevant theories in the following chapter, though a detailed theoretical discussion is beyond the scope of this work.

1134

## Chapter 2

1135

# DI-HIGGS PHENOMENOLOGY AND PHYSICS BEYOND THE STANDARD MODEL

1136

1137 This thesis focuses on searches for di-Higgs production in the  $b\bar{b}b\bar{b}$  final state. In this  
 1138 chapter, we will provide a brief overview of the practical theoretical information motivating  
 1139 such searches. Though the searches test for physics beyond the Standard Model, particularly  
 1140 in the search for resonances, the goal of the experimental results is to be somewhat agnostic  
 1141 to particular theoretical frameworks. An in depth treatment of such models is therefore  
 1142 beyond the scope of this thesis, though we will attempt to provide a grounding for the models  
 1143 that we consider.

1144 **2.1 Intro to Di-Higgs**

1145 Di-Higgs searches can be split into two major theoretical categories: *resonant searches*, in  
 1146 which a physical resonance is produced that subsequently decays into two Higgs bosons,  
 1147 and *non-resonant searches* in which no physical resonance is produced, but where the  $HH$   
 1148 production cross section has a contribution from an exchange of a *virtual* or *off-shell* particle.

1149 The focus of this thesis is gluon initiated processes – in the case of di-Higgs this is  
 1150 termed gluon-gluon fusion (ggF).  $HH$  production may also occur via vector boson fusion [22].  
 1151 However the cross section for such production is significantly smaller. Representative Feynman  
 1152 diagrams are shown for gluon-gluon fusion resonant production in Figure 2.1 and for non-  
 1153 resonant production in Figure 2.2.

1154 As shown in Chapter 1, the Higgs coupling to fermions scales with particle mass. As the  
 1155 top quark has a mass of 173 GeV, whereas the  $H$  has a mass of 125 GeV, such that  $H \rightarrow t\bar{t}$  is  
 1156 kinematically disfavored,  $H \rightarrow b\bar{b}$  is the dominant fermionic Higgs decay mode, and, in fact,

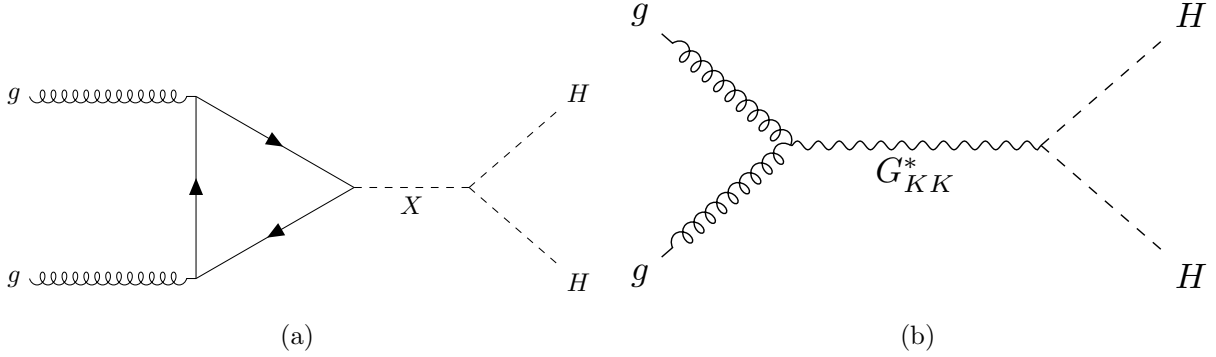


Figure 2.1: Representative diagrams for the gluon-gluon fusion production of spin-0 ( $X$ ) and spin-2 ( $G_{KK}^*$ ) resonances which decay to two Standard Model Higgs bosons. The spin-0 resonance considered for this thesis is a generic narrow width resonance which may be interpreted in the context of two Higgs doublet models [23], whereas the spin-2 resonance is considered as a Kaluza-Klein graviton within the bulk Randall-Sundrum (RS) model [24, 25].

the dominant overall decay mode, with a branching fraction of around 58 %. The dominant top quark Yukawa coupling to the  $H$  does play a role in  $H$  production, however – gluon-gluon fusion is dominated by processes including a top loop.

The single  $H$  properties translate to  $HH$  production, with  $HH \rightarrow b\bar{b}b\bar{b}$  accounting for around 34 % of all  $HH$  decays. The  $H H$  branching fractions are shown in Figure 2.3.

## 2.2 Resonant $HH$ Searches

Resonant di-Higgs production is predicted in a variety of extensions to the Standard Model. In particular, this thesis presents searches for both spin-0 and spin-2 resonances. The decay of spin-1 resonances to two identical spin-0 bosons is prohibited, as the final state must correspondingly be symmetric under particle exchange, but this process would require orbital angular momentum  $\ell = 1$ , and thus an anti-symmetric final state. Each model considered here is implemented in a particular theoretical context, but set up experimental results for generic searches.

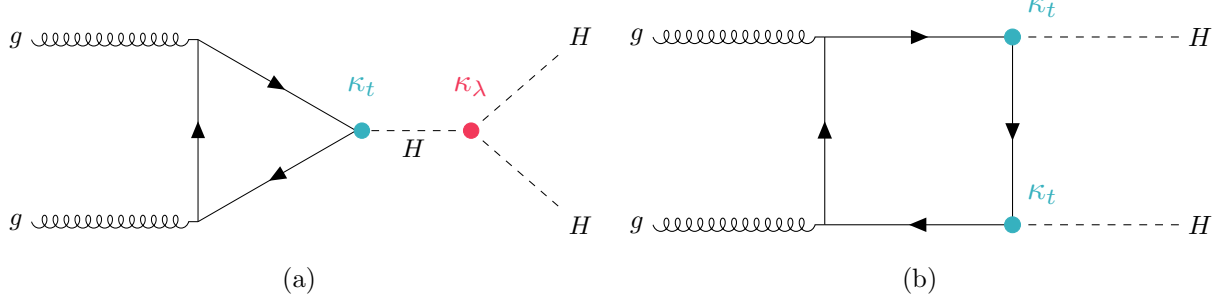


Figure 2.2: Dominant contributing diagrams for non-resonant gluon-gluon fusion production of  $HH$ .  $\kappa_\lambda$  and  $\kappa_t$  represent ratios of the Higgs self-coupling and coupling to top quarks respectively, relative to the values predicted by the Standard Model.

1170        The spin-2 signal considered is implemented within the bulk Randall-Sundrum (RS)  
 1171 model [24, 25], which features spin-2 Kaluza-Klein gravitons,  $G_{KK}^*$ , that are produced via  
 1172 gluon-fusion and which may decay to a pair of Higgs bosons. The model predicts such  
 1173 gravitons as a consequence of warped extra dimensions, and is correspondingly parametrized  
 1174 by a value  $c = k/\overline{M}_{\text{Pl}} = 1$ , where  $k$  describes a curvature scale for the extra dimension and  
 1175  $\overline{M}_{\text{Pl}}$  is the Planck mass. The model considered here has  $c = 1.0$ . However, this model was  
 1176 considered in the early Run 2  $HH$  analyses [26], and was excluded across much of the relevant  
 1177 mass range.

1178        The primary theoretical focus of this work is therefore the spin-0 result, which is imple-  
 1179 mented as a generic resonance with width below detector resolution. Scalar resonances are  
 1180 interesting, for instance, in the context of two Higgs doublet models [23], which posit the  
 1181 existence of a second Higgs doublet. This leads to the existence of five scalar particles in the  
 1182 Higgs sector – roughly, two complex doublets provide eight degrees of freedom, three of which  
 1183 are “eaten” by the electroweak bosons, leaving five degrees of freedom which may correspond  
 1184 to physical fields.

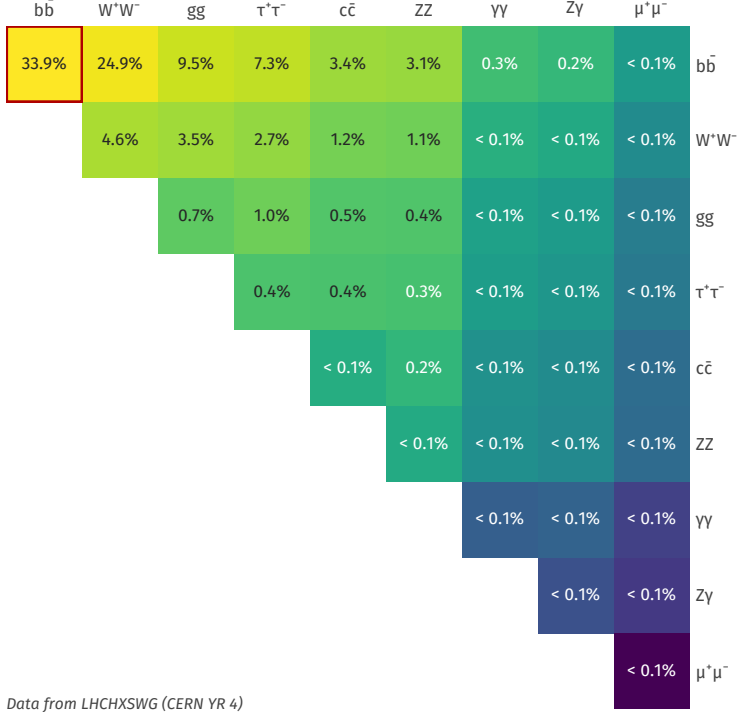


Figure 2.3: Illustration of dominant  $HH$  branching ratios.  $HH \rightarrow b\bar{b}b\bar{b}$  is the most common decay mode, representing 34 % of all  $HH$  events produced at the LHC.

### 1185 2.3 Non-resonant $HH$ Searches

Non-resonant  $HH$  production is predicted by the Standard Model via the trilinear coupling discussed above, as well as via production in a fermion loop. More explicitly, after electroweak symmetry breaking, we have

$$\mathcal{L}_{SM} \supset -\lambda v^2 h^2 - \lambda v h^3 - \frac{1}{4} \lambda h^4 \quad (2.1)$$

$$= -\frac{1}{2} m_H^2 - \lambda_{HHH}^{SM} v h^3 - \lambda_{HHHH}^{SM} h^4 \quad (2.2)$$

where  $m_H = \sqrt{2\lambda v^2}$  so that

$$\lambda_{HHH}^{SM} = \frac{m_H^2}{2v^2}. \quad (2.3)$$

1186 The mass of the SM Higgs boson has been experimentally measured to be 125 GeV [27],  
 1187 and the vacuum expectation value  $v = 246$  GeV has a precise determination from the muon  
 1188 lifetime [28]. This coupling is therefore precisely predicted in the Standard Model, such that  
 1189 an observed deviation from this prediction would be a clear sign of new physics.

1190 The relevant diagrams for non-resonant  $HH$  production are shown in Figure 2.2. Notably,  
 1191 the diagrams *interfere* with each other, which can be easily seen by counting the fermion  
 1192 lines. A detailed theoretical discussion is provided by, e.g. [29].

1193 For the searches presented here, the quark couplings to the Higgs are considered to be  
 1194 consistent with the Standard Model value, with measurements of the dominant top Yukawa  
 1195 coupling left to more sensitive direct measurements, e.g. from  $t\bar{t}$  final states [30]. Variations of  
 1196 the trilinear coupling away from the Standard Model are considered, however. Such variations  
 1197 are parametrized via

$$\kappa_\lambda = \frac{\lambda_{HHH}}{\lambda_{HHH}^{SM}} \quad (2.4)$$

1198 where  $\lambda_{HHH}$  is a varied coupling and  $\lambda_{HHH}^{SM}$  is the Standard Model prediction. As this  
 1199 variation comes as a prefactor only with the *triangle* diagram, significant and interesting  
 1200 effects are observed due to the interference. Examples of the impact of this tradeoff on the  
 1201 di-Higgs invariant mass are shown in Figure 2.4. Generally speaking, the triangle diagram  
 1202 contributes more at low mass, while the box diagram contributes more at high mass.

From a quick analysis of Figure 2.2, one may see that, at leading order, the box diagram,  $B$  has amplitude proportional to  $\kappa_t^2$ , defined as the ratio of the top Yukawa coupling to the value predicted by the Standard Model, whereas the triangle diagram,  $T$  has amplitude proportional to  $\kappa_t \kappa_\lambda$ . Therefore, the cross section is proportional to

$$\sigma(\kappa_t, \kappa_\lambda) = |A(\kappa_t, \kappa_\lambda)|^2 \quad (2.5)$$

$$\sim |\kappa_t^2 B + \kappa_t \kappa_\lambda T|^2 \quad (2.6)$$

$$= \kappa_t^4 |B|^2 + \kappa_t^3 \kappa_\lambda (BT + TB) + \kappa_t^2 \kappa_\lambda^2 |T|^2, \quad (2.7)$$

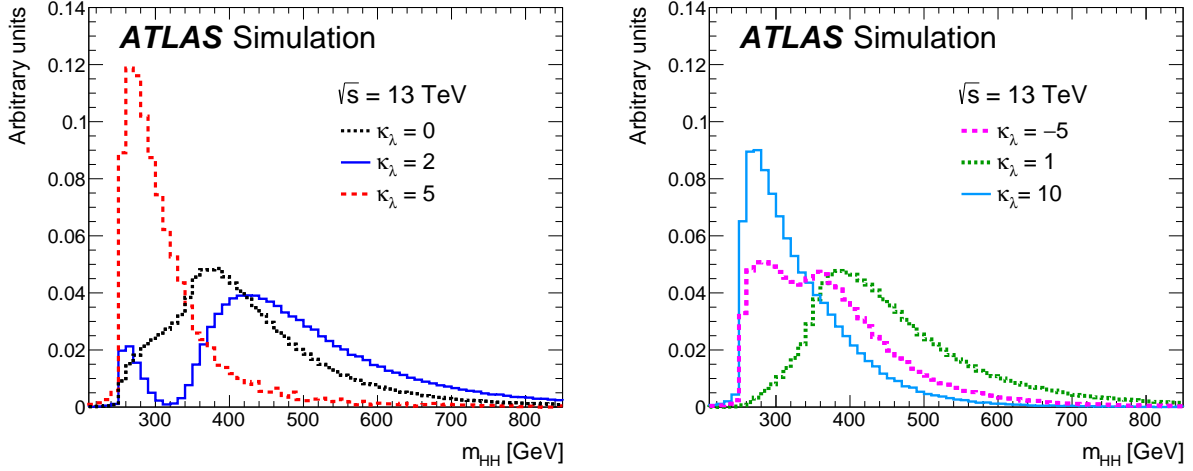


Figure 2.4: Monte Carlo generator level  $m_{HH}$  distributions for various values of  $\kappa_\lambda$ , demonstrating the impact of the interference between the two diagrams of Figure 2.2 on the resulting  $m_{HH}$  distribution. For  $\kappa_\lambda = 0$  there is no triangle diagram contribution, demonstrating the shape of the box diagram contribution, whereas for  $\kappa_\lambda = 10$ , the triangle diagram dominates, with a strong low mass peak. The interplay between the two is quite evident for other values, resulting in, e.g., the double peaked structure present for  $\kappa_\lambda = 2$  (near maximal destructive interference) and  $\kappa_\lambda = -5$ . At  $\kappa_\lambda = 5$ , the interference leads to a deficit at high  $m_{HH}$ , resulting in a narrower distribution (and thus a more pronounced low mass peak) than the  $\kappa_\lambda = 10$  case. [26]

1203 and thus non-resonant  $HH$  production cross section may be parametrized as a second order  
 1204 polynomial in  $\kappa_\lambda$ .

1205 For positive values of  $\kappa_\lambda$ , due to the relative minus sign between the triangle and box  
 1206 diagrams, the interference between the two diagrams is *destructive*, with a maximum in-  
 1207 terference near  $\kappa_\lambda = 2.3$ , corresponding to the minimum cross section prediction. One  
 1208 may note that the Standard Model value of  $\kappa_\lambda = 1$  is not far away from this minimum –  
 1209 correspondingly the Standard Model cross section for  $HH$  production is quite small, namely

1210 31.05 fb at  $\sqrt{s} = 13 \text{ TeV}$  for production via gluon-gluon fusion [31–38] compared to, e.g.  
 1211 single Higgs production, with a gluon-gluon fusion production cross section of 46.86 pb at  
 1212  $\sqrt{s} = 13 \text{ TeV}$  [39] roughly 1500 times larger! For negative values of  $\kappa_\lambda$ , the interference is  
 1213 constructive.

1214 ATLAS projections [40] of  $b\bar{b}b\bar{b}$ ,  $b\bar{b}\gamma\gamma$ , and  $b\bar{b}\tau^+\tau^-$  predict an expected signal strength  
 1215 for Standard Model  $HH$  of  $3.5\sigma$  with no systematic uncertainties and  $3.0\sigma$  with systematic  
 1216 uncertainties using the  $3000 \text{ fb}^{-1}$  of data from the HL-LHC (around  $20\times$  the full Run 2  
 1217 dataset considered in this thesis), constituting an *observation* of  $HH$ . As the cross section  
 1218 for Standard Model  $HHH$  production, corresponding to the quartic Higgs interaction, is  
 1219 much smaller (around 0.1 fb at  $\sqrt{s} = 14 \text{ TeV}$  [41]), observation of triple Higgs production is  
 1220 even farther in the future, and so is not considered here. However this may be interesting for  
 1221 future work in a variety of Beyond the Standard Model scenarios (e.g. [42–44]).

1222

## Chapter 3

1223

### EXPERIMENTAL APPARATUS

1224 What machines must be built to examine the smallest pieces of the universe? The famous  
 1225 equation  $E = m$  provides that to create massive particles, enough energy must be provided.  
 1226 In order to give kinematic phase space to the types of processes that are examined in this  
 1227 thesis (and many others besides), a system must be created in which there is enough energy  
 1228 to (at bare minimum), overcome kinematic thresholds: if you want to search for  $HH$  decays,  
 1229 you should have at least 250 GeV ( $= 2 \times m_H$ ) to work with. It is not enough to simply induce  
 1230 such processes, however. These processes need to be captured in some way, emitted energy  
 1231 and particles must be characterized and identified, and in the end all of this information  
 1232 must be put into a useful and usable form such that selections can be made, statistics can be  
 1233 run, and a meaningful statement can be made about the universe. This chapter describes the  
 1234 machines behind the physics, namely the Large Hadron Collider and the ATLAS experiment.

1235 **3.1 The Large Hadron Collider**

1236 The Large Hadron Collider is a particle accelerator near Geneva, Switzerland. In broad scope,  
 1237 it is a ring with a 27 kilometer circumference. Hadrons (usually protons or heavy ions) move  
 1238 in two counter-circulating beams, which are made to collide at four collision points at various  
 1239 points on the ring. These four collision points correspond to the four detectors placed around  
 1240 the ring: two “general purpose” experiments: ATLAS and CMS; LHCb, focused primarily on  
 1241 flavor physics; and ALICE, focused primarily on heavy ions.

1242 The focus of this thesis is proton-proton collisions at center of mass energy  $\sqrt{s} = 13$  TeV.  
 1243 The process to achieve such collisions proceeds as follows: first, an electric field strips hydrogen  
 1244 of its electrons, creating protons. A linear accelerator, LINAC 2, accelerates protons to

1245 50 MeV. The resulting beam is injected into the Proton Synchrotron Booster (PSB), which  
1246 pushes the protons to 1.4 GeV, and then the Proton Synchrotron, which brings the beam to  
1247 25 GeV.

1248 Protons are then transferred to the Super Proton Synchrotron (SPS), which ramps up  
1249 the energy to 450 GeV. Finally, the protons enter the LHC itself, bringing the beam up to  
1250 6.5 TeV [45].

1251 While there is, of course, much that goes into the Large Hadron Collider development and  
1252 operation, perhaps two of the most fundamental ideas are (1) how are the beams directed  
1253 and manipulated and (2) what is meant by “protons are accelerated”. These questions both  
1254 are directly answered by pieces of hardware, namely (1) magnets and (2) radiofrequency (RF)  
1255 cavities.

1256 One of fundamental components of the LHC is a large set of superconducting niobium-  
1257 titanium magnets. These are cooled by liquid helium to achieve superconducting temperatures,  
1258 and there are several types with very specific purposes. The obvious first question with a  
1259 circular accelerator is how to keep the particle beam moving around in that circle. This job  
1260 is done via a set of dipole magnets placed around the *beam pipes*: the tubes containing the  
1261 beam. These are designed such that the magnetic field in the center of the beam pipe runs  
1262 perpendicular to the velocity of the charged particles, providing the necessary centripetal  
1263 force for the synchrotron motion.

1264 A proton beam is not made of a single proton, however, but of many protons, grouped  
1265 into a series of *bunches*. As all of these are positively charged, if unchecked, these bunches  
1266 would become diffuse and break apart. What is desired is a stable beam with tightly clustered  
1267 protons to maximize the chance of a high energy collision. Such clustering is done via a series  
1268 of quadrupole magnets, with alternating sets of quadrupoles providing the necessary forces for  
1269 a tight, stable beam. While these are the two major components of the LHC magnet system,  
1270 it is not the full story – higher order magnets are used to correct for small imperfections in  
1271 the beam.

1272 Magnetic fields do no work, however, so the magnet system is unable to do the job of the

actual acceleration. This is accomplished via a set of radiofrequency (RF) cavities. Within these cavities, an electric field is made to oscillate (switch direction) at a precise rate. This oscillation creates RF *buckets*, with bunches corresponding to groups of protons that fill a given bucket. The timing is such that protons will always experience an accelerating voltage, corresponding to the 25 ns bunch spacing used at the LHC.

A nice property of this bucket/bunch configuration is that there is some self-correction. There is some finite spread in the grouping of particles. However, if a particle arrives too early, it will experience a decelerating voltage; if too late, it will experience a higher accelerating voltage.

### 3.1.1 The LHC Schedule

The physics program at the Large Hadron Collider is split into a variety of data taking periods called *runs*. These runs correspond to various detector/accelerator configurations, and are interspersed with *long shutdowns* – periods used for detector/accelerator upgrades in preparation for the next run. The LHC timeline is as follows [46, 47]:

1. Run 1 (2010–2013): First run of the LHC, operating at center of mass energy  $\sqrt{s} = 7 \text{ TeV}$ , increased to  $8 \text{ TeV}$  in 2012. ATLAS recorded  $4.57 \text{ fb}^{-1}$  and  $20.3 \text{ fb}^{-1}$  of data usable for physics at  $\sqrt{s} = 7 \text{ TeV}$  and  $8 \text{ TeV}$  respectively.
2. Long Shutdown 1 (LS1; 2013–2015): Upgrades to accelerator complex, magnet system, to allow for increase in energy. Design energy was  $\sqrt{s} = 14 \text{ TeV}$ , delays in “training” of superconducting magnets led to decrease to  $\sqrt{s} = 13 \text{ TeV}$ .
3. Run 2 (2015–2018): Second run of the LHC, operating at center of mass energy  $\sqrt{s} = 13 \text{ TeV}$ . Data from this run is used in this thesis, with  $139 \text{ fb}^{-1}$  of data available for physics from the ATLAS experiment.
4. Long Shutdown 2 (LS2; 2019–2021): Upgrades to ATLAS muon spectrometer (New

1297 Small Wheel), liquid argon calorimeter; upgrades in preparation for the High Luminosity  
1298 LHC (HL-LHC).

1299 5. Run 3 (2021–2023?): Third run of the LHC, target center of mass energy  $\sqrt{s} =$   
1300  $13 - 14 \text{ TeV}$ , total target luminosity  $300 \text{ fb}^{-1}$ .

1301 6. Long Shutdown 3 (LS3; 2024?–2026?): Further upgrades for the HL-LHC.

1302 7. Run 4, 5, … (2026? onward): High Luminosity LHC – goal is to achieve instantaneous  
1303 luminosities by a factor of five, massively enlarging available statistics for physics.  
1304 Projected 3000 to  $4000 \text{ fb}^{-1}$ ,  $> 20$  times the full Run 2 ATLAS dataset.

1305 **3.2 The ATLAS Experiment**

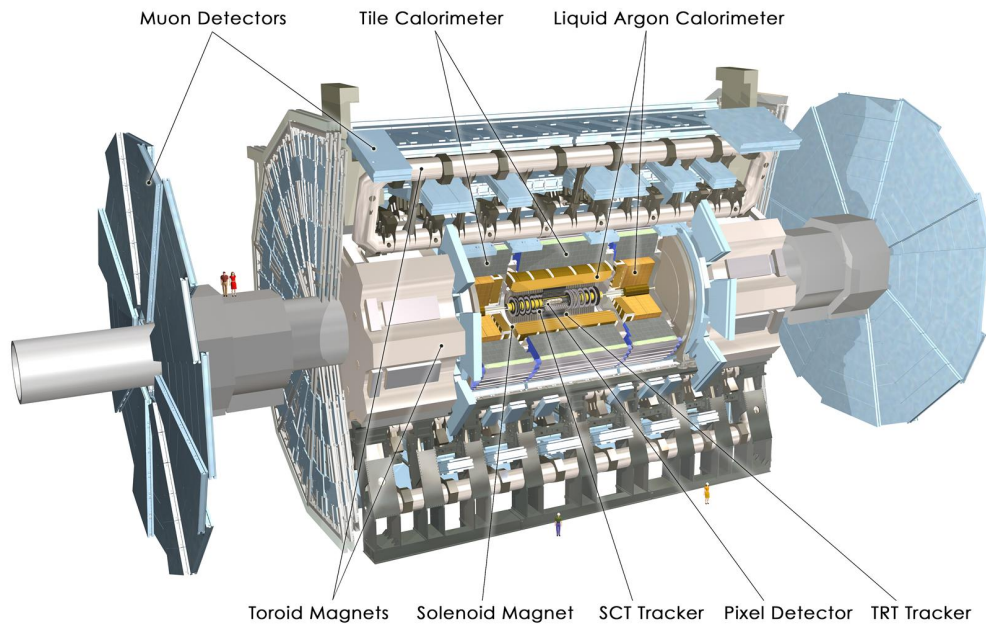


Figure 3.1: Diagram of the ATLAS detector [48]

1306 This thesis focuses on searches done with the ATLAS experiment. As mentioned, this is

one of two “general purpose” experiments at the LHC, meaning that there is a very large and broad variety of physics done within the experimental collaboration. This broad physics focus has a direct relation to the design of the ATLAS detector [49], pictured in Figure 3.1, which is composed of a sophisticated set of subsystems designed to fully characterize the physics of a given high energy particle collision. It consists of an inner tracking detector surrounded by a thin superconducting solenoid, electromagnetic and hadronic calorimeters, and a muon spectrometer incorporating three large superconducting toroidal magnets. The ATLAS detector covers nearly the entire solid angle around the collision point, fully characterizing the “visible” components of a collision and allowing for indirect sensitivity to particles that do not interact with the detector (e.g. neutrinos) via “missing” energy (roughly momentum balance). The design and physics contribution of each of the detector components is described in the following. A schematic of how various particles interact with the detector is shown in Figure 3.2.

### 3.2.1 ATLAS Coordinate System

Of relevance for the following discussion, as well as for the analysis presented in Chapters 6 through 10, is the ATLAS coordinate system. ATLAS uses a right-handed coordinate system with its origin at the nominal interaction point (IP) in the center of the detector and the  $z$ -axis along the beam pipe. The  $x$ -axis points from the IP to the center of the LHC ring, and the  $y$ -axis points upwards. Cylindrical coordinates  $(r, \phi)$  are used in the transverse plane,  $\phi$  being the azimuthal angle around the  $z$ -axis. The pseudorapidity is defined in terms of the polar angle  $\theta$  as  $\eta = -\ln \tan(\theta/2)$ . Angular distance is measured in units of  $\Delta R \equiv \sqrt{(\Delta\eta)^2 + (\Delta\phi)^2}$ . These coordinates are shown in Figure 3.3.

### 3.2.2 Inner Detector

The purpose of the inner detector is the reconstruction of the trajectory of charged particles, called *tracking*. This is accomplished primarily through the collection of electrons displaced when a charged particle passes through a tracking detector. By setting up multiple layers of

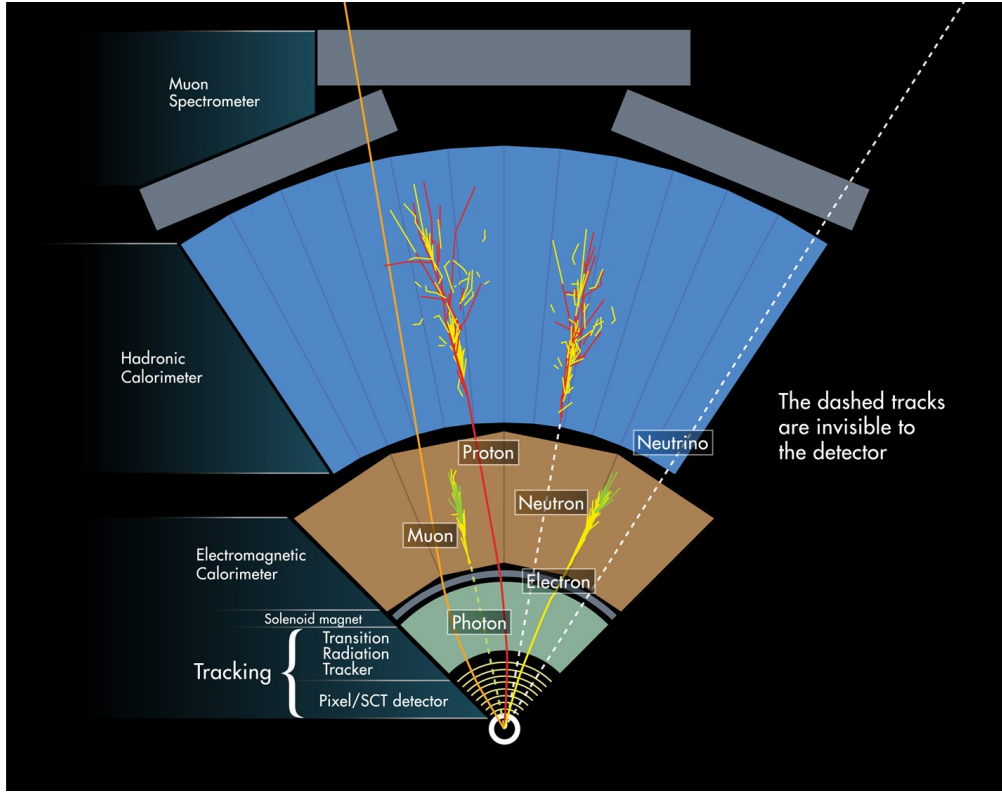


Figure 3.2: Cross section of the ATLAS detector showing how particles interact with various detector components [50]

such detectors, such that a given particle leaves a signature, known as a “hit”, in each layer, the trajectory of the particle may be inferred via “connecting the dots” between these hits.

The raw trajectory of a particle only provides positional information. However, the trajectory of a charged particle in a known magnetic field additionally provides information on particle momentum and charge via the curvature of the corresponding track (cf.  $\vec{F} = q\vec{v} \times \vec{B}$ ). The inner detector system is therefore surrounded by a solenoid magnet, providing a 2 T magnetic field along the  $z$ -axis (yielding curvature in the transverse  $x - y$  plane).

The inner detector provides charged particle tracking in the range  $|\eta| < 2.5$  via a series of detector layers. The innermost of these is the high-granularity silicon pixel detector which typically provides four measurements per track, with the first hit in the insertable B-layer

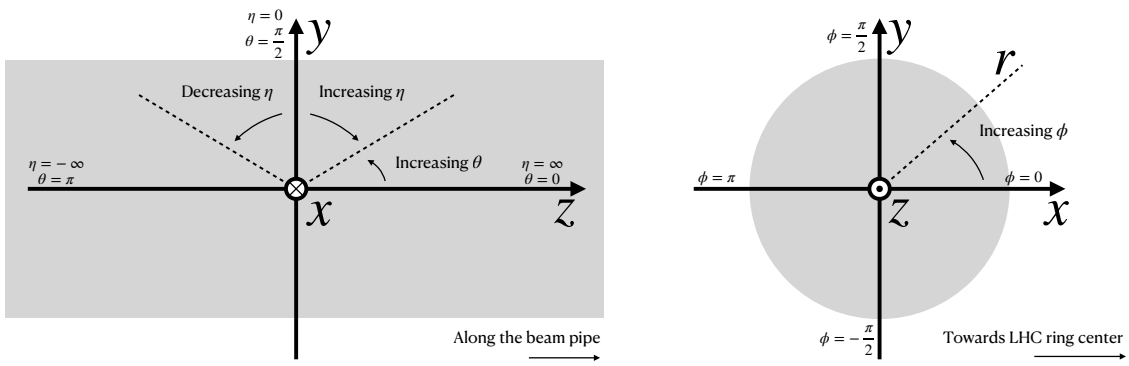


Figure 3.3: 2D projections of the ATLAS coordinate system

1343 (IBL) installed before Run 2 [51, 52]. This is very close to the interaction point with a  
1344 high degree of positional information, and is therefore very important for e.g.  $b$ -tagging (see  
1345 Chapter 5). It is followed by the silicon microstrip tracker (SCT), which usually provides  
1346 eight measurements per track. This is lower granularity, but similar in concept to the pixel  
1347 detector.

1348 Both of these silicon detectors are complemented by the transition radiation tracker  
1349 (TRT), which extends the radial track reconstruction within the range  $|\eta| < 2.0$ . This is  
1350 a different design, composed of *drift tubes*, i.e. straws filled with Xenon gas with a wire  
1351 in the center, but similarly collects electrons displaced by ionizing particles. In addition,  
1352 the TRT includes materials with widely varying indices of refraction, which leads to the  
1353 production of transition radiation, namely radiation produced by a charged particle passing  
1354 through an inhomogeneous medium. The energy loss on such a transition is proportional  
1355 to the Lorentz factor  $\gamma = E/m$  – correspondingly, lighter particles (e.g. electrons) tend to  
1356 lose more energy and emit more photons compared to heavier particles (e.g. pions). In the  
1357 detector, this corresponds to a larger fraction of hits (typically 30 in total) above a given

1358 high energy-deposit threshold for electrons, providing particle identification information.

1359 *3.2.3 Calorimeter*

1360 Surrounding the inner detector in ATLAS is the calorimeter. The principle of the calorimeter  
1361 is to completely absorb the energy of a produced particle in order to measure it. However,  
1362 a pure block of absorber does not provide much information about the particle interaction  
1363 with the material. The ATLAS calorimeter therefore has a *sampling calorimeter* structure,  
1364 namely, layers of absorber interspersed with layers of sensitive material, giving the calorimeter  
1365 “stopping power” while allowing detailed measurement of the resulting particle shower and  
1366 corresponding deposited energy.

1367 The ATLAS calorimeter system covers the pseudorapidity range  $|\eta| < 4.9$ , and is primarily  
1368 composed of two components, an electromagnetic calorimeter, designed to measure particles  
1369 which primarily interact via electromagnetism (e.g. photons and electrons), and a hadronic  
1370 calorimeter, designed to measure particles which interact via the strong force (e.g. pions,  
1371 other hadrons). These differences are further described in Section 3.2.6.

1372 In ATLAS, the electromagnetic calorimeter covers the region of  $|\eta| < 3.2$ , and uses  
1373 lead for the absorbers and liquid-argon for the sensitive material. It is high granularity  
1374 and, geometrically, has two components: the “barrel”, which covers the cylindrical body of  
1375 the detector volume and the “endcap”, covering the ends. An additional thin liquid-argon  
1376 presampler covers  $|\eta| < 1.8$  to correct for energy loss in material upstream of the calorimeters.

1377 The hadronic calorimeter is composed of alternating steel and plastic scintillator tiles,  
1378 segmented into three barrel structures within  $|\eta| < 1.7$ , in addition to two copper/liquid-argon  
1379 endcap calorimeters.

1380 The solid angle coverage is completed with forward copper/liquid-argon and tungsten/liquid-  
1381 argon calorimeter modules optimized for electromagnetic and hadronic energy measurements  
1382 respectively.

1383    *3.2.4 Muon Spectrometer*

1384    While muons interact electromagnetically, they are around 200 times heavier than electrons  
 1385    ( $m_\mu = 106 \text{ MeV}$ , while  $m_e = 0.510 \text{ MeV}$ ). Therefore, electromagnetic interactions with  
 1386    absorbers in the calorimeter are not sufficient to stop them, and, as they do not interact  
 1387    via the strong force, hard scattering with nuclei is rare. A dedicated system for muon  
 1388    measurements is therefore required.

1389    The muon spectrometer (MS) is the outermost layer of ATLAS and is designed for this  
 1390    purpose. It is composed of three parts: a set of triggering chambers, which detect if there is  
 1391    a muon and provide a coordinate measurement, in conjunction with high-precision tracking  
 1392    chambers, which measure the deflection of muons in a magnetic field to measure muon  
 1393    momentum, similar to the inner detector solenoid. The magnetic field is generated by the  
 1394    superconducting air-core toroidal magnets, with a field integral between 2.0 and 6.0 T m  
 1395    across most of the detector. The toroid magnetic field runs roughly in a circle in the  $x - y$   
 1396    plane around the beam line, leading to muon curvature along the z-axis.

1397    The precision tracking system covers the region  $|\eta| < 2.7$  via three layers of monitored  
 1398    drift tubes, and is complemented by cathode-strip chambers in the forward region, where the  
 1399    background is highest. The muon trigger system covers the range  $|\eta| < 2.4$  with resistive-plate  
 1400    chambers in the barrel, and thin-gap chambers in the endcap regions.

1401    *3.2.5 Triggering*

1402    During a typical run of the LHC, there are roughly 1 billion collisions in ATLAS per second  
 1403    (1 GHz), corresponding to a 40 MHz bunch crossing rate [53]. Saving the information from  
 1404    all of them is not only unnecessary, but infeasible. The ATLAS trigger system provides a  
 1405    sophisticated set of selections to filter the collision data and only keep those collision events  
 1406    useful for downstream analysis.

1407    These events are selected by the first-level trigger system, which is implemented in custom  
 1408    hardware, and accepts events at a rate below 100 kHz. Selections are then made by algorithms

1409 implemented in software in the high-level trigger [54], reducing this further, and, in the end,  
1410 events are recorded to disk at much more manageable rate of about 1 kHz.

1411 An extensive set of ATLAS software [55] is open source, including the software used for  
1412 real and simulated data reconstruction and analysis and that used in the trigger and data  
1413 acquisition systems of the experiment.

1414 *3.2.6 Particle Showers and the Calorimeter*

1415 The design of the ATLAS detector is directly tied to the physics it is trying to detect. Of these,  
1416 possibly the most non-trivial distinction is in the calorimeter design. It is therefore useful to  
1417 discuss in more detail the various properties of electromagnetic and hadronic interactions  
1418 with material, and how these correspond to the particle showers measured by the detector  
1419 described above.

1420 Electromagnetic showers in ATLAS predominantly occur via bremsstrahlung, or “braking  
1421 radiation”, and electron-positron pair production. This proceeds roughly as follows: an  
1422 electron entering a material is deflected by the electromagnetic field of a heavy nucleus. This  
1423 results in the radiation of a photon. That photon produces an electron-positron pair, and  
1424 the process repeats, resulting in a shower structure. At each step, characterized by *radiation*  
1425 *length*,  $X_0$ , the number of particles approximately doubles and the average particle energy  
1426 decreases by approximately a factor of two. An illustration of this process is shown in Figure  
1427 3.4.

Note that bremsstrahlung and pair production only dominate in specific energy regimes, with other processes taking over depending on particle energy. For electrons, bremsstrahlung only dominates for higher energies, as low energy electrons will form ions with the atoms of the material. The point where the rates for the two processes are equal is called the *critical energy*, and is roughly

$$E_c \approx \frac{800 \text{ MeV}}{Z} \quad (3.1)$$

1428 where  $Z$  is the nuclear charge. From a similar analysis of rates, it can be seen that the

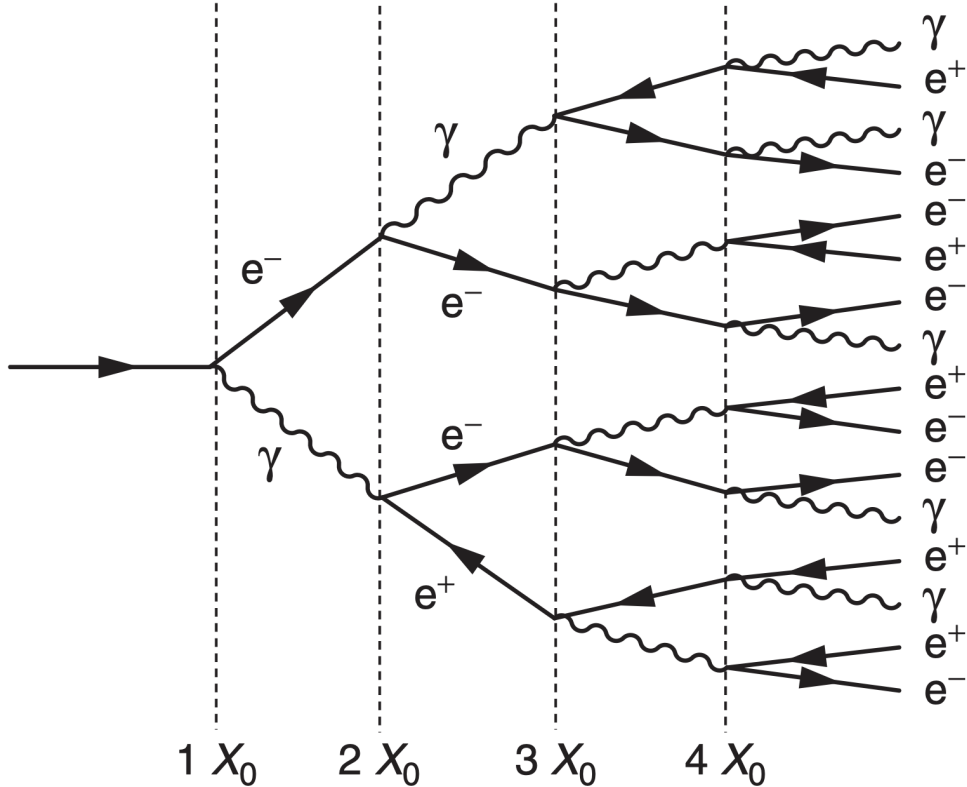


Figure 3.4: Illustration of electromagnetic showering. Repeated bremsstrahlung and electron-positron pair production result in a shower structure in which the number of particles approximately doubles every radiation length,  $X_0$ . Figure taken from [8].

<sup>1429</sup> bremsstrahlung rate is inversely proportional to the square of the mass of the particle. This  
<sup>1430</sup> explains why muons do not shower in a similar way, as the rate of bremsstrahlung is suppressed  
<sup>1431</sup> by  $(m_e/m_\mu)^2$  relative to electrons.

For lead, the absorber used for the ATLAS electromagnetic calorimeter, which has  $Z = 82$ , this critical energy is therefore around 10 MeV. Electrons resulting from LHC collisions are of a  $1.3 \times 10^3$  GeV scale. With the approximation of a reduction in particle energy by a factor of two every radiation length, the number of radiation lengths before the critical energy is

reached is

$$x = \frac{\ln(E/E_c)}{\ln 2} \quad (3.2)$$

such that for a 100 GeV shower in lead,  $x \sim 13$ . The radiation length for lead is around 0.56 cm, such that an electromagnetic shower could be expected to be captured within 10 cm of lead.

Electromagnetic showers are therefore characterized by depositing much of their energy within a small region of space. As shown below (Chapter 4), though electromagnetic showering is not deterministic, the large number of particles and the restricted set of processes involved means that the shower development as a whole is very similar between individual electromagnetic showers of the same energy.

For completeness, note as well that pair production dominates for photons of energy greater than around 10 MeV, whereas for lower energies (below around 1 MeV), the photoelectric effect, namely atomic photon absorption and electron emission, dominates.

Hadronic showers are distinguished by the fact that they interact strongly with atomic nuclei. They are correspondingly more complex because (1) they involve a wider variety of processes than electromagnetic showers, and (2) these processes have a wide variety of associated length scales. Because these are heavier than electrons (e.g. protons and charged pions) bremsstrahlung is suppressed, but ionization interactions with the electrons will cause these particles to lose energy as they pass through the material. Hadronic showering occurs on interaction with atomic nuclei. This may lead to production of, e.g. both charged ( $\pi^\pm$ ) and neutral ( $\pi^0$ ) pions. The  $\pi^0$  lifetime is much much shorter than that of the charged pions (around a factor of  $10^8$ ), and immediately decays to two photons, starting an electromagnetic shower, as described above. The longer lived  $\pi^\pm$  travel further in the detector before experiencing another strong interaction with more particles produced, also with varying lifetimes and decay properties.

It is therefore immediately apparent that hadronic showers are more complex than electromagnetic ones (electromagnetic showers can be a subset of the hadronic!), and therefore much more variable from shower to shower. The length scales involved are also significantly

<sub>1458</sub> larger due to the reliance on nuclear interactions, characterized by length  $\lambda_I$ , which is around  
<sub>1459</sub> 17 cm for iron (used in the ATLAS hadronic calorimeter). This motivates the calorimeter  
<sub>1460</sub> design, and results in the properties demonstrated in Figure 3.2.

1461

## Chapter 4

1462

# SIMULATION

1463     Simulated physics samples are a core piece of the physics output of the Large Hadron  
 1464    Collider, providing a map from a physics theory into what is observed in our detector. This  
 1465    is crucial for searches for new physics, where simulation is necessary to describe what a given  
 1466    signal model looks like, but also extremely valuable for describing the physics of the Standard  
 1467    Model, providing detailed predictions of background processes for use in everything from  
 1468    designing simple cuts to training multivariate discriminators. Broadly, simulation can be split  
 1469    into two stages: *event generation*, in which physics theory is used to generate a description of  
 1470    particles present after a proton-proton collision, and *detector simulation*, which passes this  
 1471    particle description through a simulation of the detector material, providing a view of the  
 1472    physics event as it would be seen in ATLAS data. Such simulation is often called Monte Carlo  
 1473    in reference to the underlying mathematical framework, which relies on random sampling.

1474    **4.1 Event Generation**

1475    A variety of tools are used to simulate various aspects of event generation. One such aspect  
 1476    is generation of the “hard scatter” event, i.e., two protons collide and some desired physics  
 1477    process happens. In practice, this is not quite as simple as two quarks or gluons interacting.  
 1478    Protons are composed of three “valence” quarks with various momenta interacting with each  
 1479    other via exchange of gluons, but also a sea of virtual gluons which may decay into other  
 1480    quarks. A hard scatter event is therefore characterized by the corresponding particle level  
 1481    diagrams, but additionally by a set of *parton distribution functions* (PDFs), which describe  
 1482    the probability to find constituent quarks or gluons at carrying various momenta at a given  
 1483    energy scale (often written  $Q^2$ ). Such PDFs are measured experimentally (see, e.g. [56])

and the selection of a “PDF set” and a given physics process characterizes the hard scatter. Depending on the model being considered and the particular theoretical constraints, processes are often simulated at either leading (LO) or next to leading order (NLO), corresponding to the order of the perturbative expansion (i.e. tree level or 1 loop diagrams). Various additional tools are developed for such NLO calculations, including POWHEG Box v2 [57–59], which is used for this thesis. MADGRAPH [60] is used in this thesis for leading order simulation.

The hard scatter is not the only component of a given collider event, however. Incoming and outgoing particles are themselves very energetic and may radiate particles along their trajectory. In particular, gluons, which have a self-interaction term as described in Chapter 1, may be radiated, which subsequently themselves radiate gluons or decay to quarks which can also radiate gluons, in a whole mess of QCD that both contributes to the particle content of a collider event and is not directly described by the hard scatter. This cascade, called a *parton shower*, has a dedicated set of simulation tools. For this thesis, HERWIG 7 [61][62] and PYTHIA 8 [63] are used, which interface with tools such as MADGRAPH for simulation.

Due to color confinement (Chapter 1), quarks and gluons cannot be observed free particles, but rather undergo a process called hadronization, in which they are grouped into colorless hadrons (e.g. *mesons*, consisting of one quark and one anti-quark). In simulation, this is also handled with tools such as HERWIG 7 or PYTHIA 8.

The physics of  $b$ -quarks is quite important for a variety of searches for new physics and measurements of the Standard Model, including this thesis work. Correspondingly, the decay of “heavy flavor” particles (e.g.  $B$  and  $D$  mesons, containing  $b$  and  $c$  quarks respectively) has been very well studied, and a dedicated simulation tool, EVTGEN [64], is used for such processes.

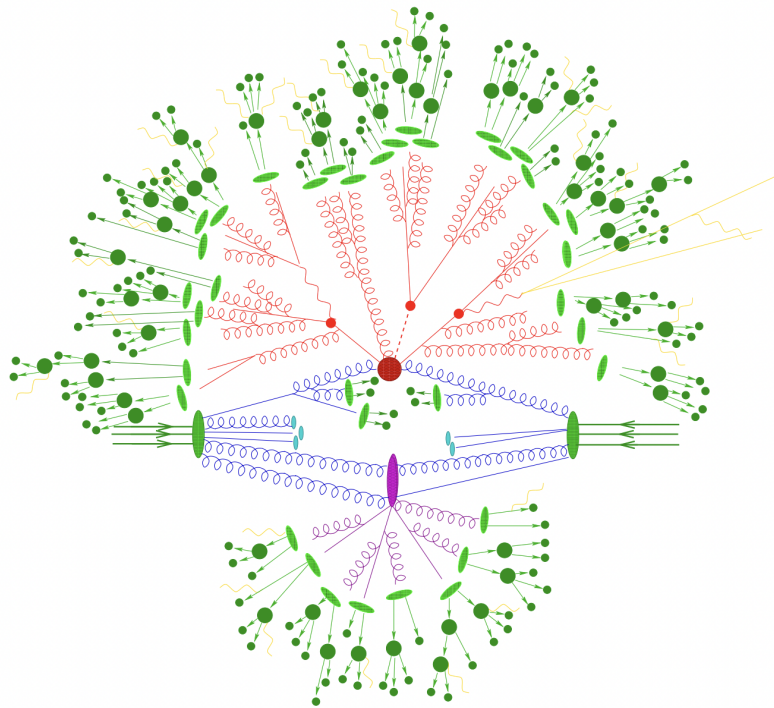


Figure 4.1: Schematic diagram of the Monte Carlo simulation of a hadron-hadron collision. The incoming hadrons are the green blobs with the arrows on the left and right, with the red blob in the center representing the hard scatter event, and the purple representing a secondary hard scatter. Radiation from both incoming and outgoing particles is shown, and the light green blobs represent hadronization, with the outermost dark green circles corresponding to the final state hadrons. Yellow lines are radiated photons. [65]

1507 **4.2 Detector Simulation**

1508 Event generation provides a full and exact description of the particle content of a given  
 1509 collider event. This description is useful, but is an artifact of the simulation – for real physics  
 1510 events, we must rely on the information collected by sophisticated detectors (Chapter 3) to  
 1511 make statements about the physics content of collider events. The simulation of how particles  
 1512 interact with the physical detector and of the corresponding information that is collected is  
 1513 therefore a necessary step of physics simulation at the LHC. The design and components of  
 1514 the ATLAS detector are described in Chapter 3. Simulation of this detector quickly becomes  
 1515 complicated – there are a variety of different materials and sub-detectors, each with particular  
 1516 configurations and resolutions. Interactions of particles with the detector materials can cause  
 1517 showering, and such showers must be simulated and characterized.

1518 In ATLAS, the GEANT4 [66] simulation toolkit is used for detailed simulation of the  
 1519 ATLAS detector, often referred to as *full simulation*. The method can be thought of as  
 1520 proceeding step by step as a particle moves through the detector, simulating the interaction  
 1521 of the material at each stage, and following each branch of each resulting shower with a  
 1522 similarly detailed step by step simulation.

1523 This type of simulation is very computationally intensive, especially in the calorimeter,  
 1524 which has a high density of material, leading to an extremely large set of material interactions  
 1525 to simulate. There is correspondingly a large effort within ATLAS to develop techniques to  
 1526 decrease the computational load – these techniques will be of increasing importance for Run  
 1527 3 and the HL-LHC, which will have increased computational need due to the high complexity  
 1528 and large volume of collected physics events, along with the corresponding set of simulated  
 1529 physics events [67]. The divergence of the baseline computing model from the projected  
 1530 computing budget is shown in Figure 4.2.

1531 The fast simulation used for this thesis, AtlFast-II [70], is one such technique, which uses  
 1532 a parametrized simulation of the calorimeter, called FastCaloSim, in conjunction with full  
 1533 simulation of the inner detector, to achieve an order of magnitude speed up in simulation

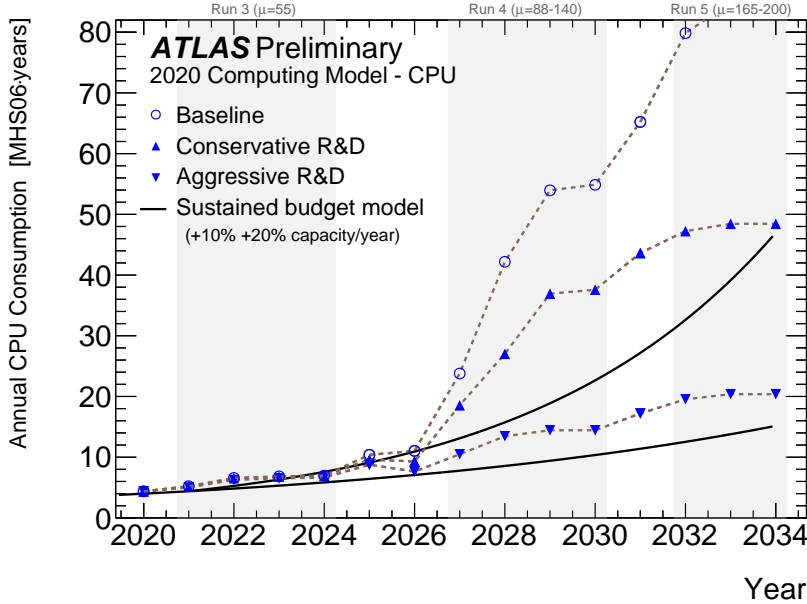


Figure 4.2: The projected ATLAS computational requirements for Run 3 and the HL-LHC relative to the projected computing budget. Aggressive R&D is required to keep resources within budget [68].  $y$ -axis units are in  $MHS06 \cdot \text{years}$ , where HS06 is a high energy physics specific CPU performance benchmark [69].

time. This parametrized simulation uses a simplified detector geometry, in conjunction with a simulation of particle shower development based on statistical sampling of distributions from fully simulated events, to massively speed up simulation time and computational load.

Such a speed up comes at a bit of a cost in performance. In particular, the modeling of jet substructure (see Chapter 5) historically has been an issue for FastCaloSim. The ATLAS authorship qualification work supporting this thesis is an effort to improve such modeling, and is part of a suite of updates being considered for a new fast simulation targeting Run 3. This work is briefly described in the following.

1542 **4.3 Correlated Fluctuations in FastCaloSim**

1543 A variety of developments have been made to FastCaloSim, improving on the version used for  
1544 AtlFast-II. This new fast calorimeter simulation [71] is largely based on two components: one  
1545 which describes the *total energy* deposited in each calorimeter layer as a shower moves from  
1546 the interaction point outward, and one which describes the *shape*, i.e., the pattern of energy  
1547 deposits, of a shower in each respective calorimeter layer. Both methods are parametrizations  
1548 of the full simulation, and therefore are considered to be performing well if they are able  
1549 to reproduce corresponding full simulation distributions. Of course, directly sampling from  
1550 a library of showers would identically reproduce such distributions – however a statistical  
1551 sampling of various shower *properties* provides much more generality in the simulation.

1552 For the simulation of total energy in each given layer, the primary challenge is that such  
1553 energy deposits are highly correlated. The new FastCaloSim thus relies on a technique called  
1554 Principal Component Analysis (PCA) [72] to de-correlate the layers, aiding parametrization.

1555 The PCA chain transforms  $N$  energy inputs into  $N$  Gaussians and projects these Gaussians  
1556 onto the eigenvectors of the corresponding covariance matrix. This results in  $N$  de-correlated  
1557 components, as the eigenvectors are orthogonal. The component of the PCA decomposition  
1558 with the largest corresponding eigenvalue is then used to define bins, in which showers  
1559 demonstrate similar patterns of energy deposition across the calorimeter layers. To further  
1560 de-correlate the inputs, the PCA chain is repeated on the showers within each such bin. This  
1561 full process is reversed for the particle simulation. A full description of the method can be  
1562 found in [71].

1563 Modeling of the lateral shower shape makes use of 2D histograms filled with GEANT4  
1564 hit energies in each layer and PCA bin. Binned in polar  $\alpha - R$  coordinates in a local plane  
1565 tangential to the surface of the calorimeter system, these histograms represent the spatial  
1566 distribution of energy deposits for a given particle shower. Such histograms are constructed  
1567 for a number of GEANT4 events, and the histograms for each event are normalized to total  
1568 energy deposited in the given layer. The average of these histograms is then taken (what is

1569 called here the “average shape”).

1570 In simulation, these average shape histograms are used as probability distributions, from  
1571 which a finite number of equal energy hits are drawn. This finite drawing of hits induces  
1572 a statistical fluctuation about the average shape which is tuned to match the expected  
 calorimeter sampling uncertainty. An example such average shape is shown in Figure 4.3.

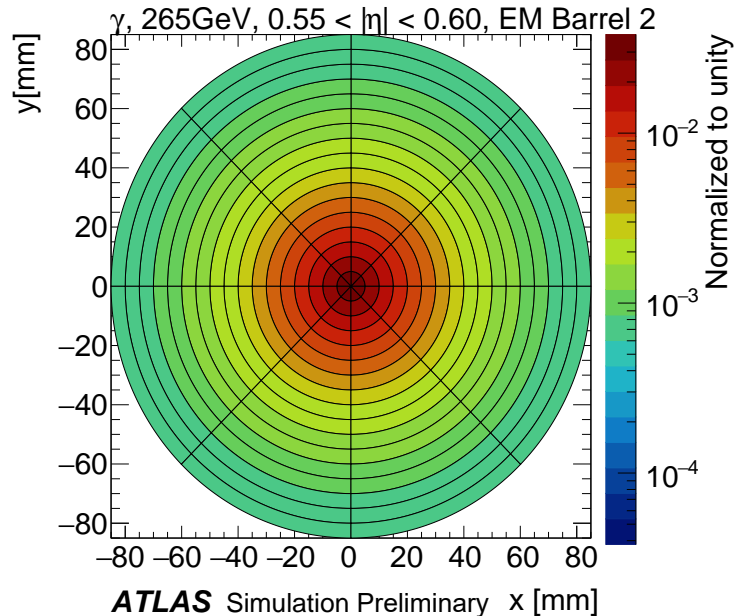


Figure 4.3: Example average lateral shower shape for a 265 GeV photon in the range  $0.55 < |\eta| < 0.60$  in the second layer of the EM barrel. The binning shown here is in polar  $\alpha - R$  coordinates in a local plane tangential to the surface of the calorimeter system. Such a histogram is used as a probability distribution, from which a finite number of “hits” are drawn [71].

1573

1574 As an example, the intrinsic resolution of the ATLAS Liquid Argon calorimeter has a  
1575 sampling term of  $\sigma_{\text{samp}} \approx 10\%/\sqrt{E}$  [73]. The number of hits to be drawn for each layer,  $N_{\text{hits}}^{\text{layer}}$ ,  
1576 is thus taken from a Poisson distribution with mean  $1/\sigma_{\text{samp}}^2$ , where the energy assigned to  
1577 each hit is then just  $E_{\text{hit}} = \frac{E_{\text{layer}}}{N_{\text{hits}}^{\text{layer}}}$ . This induces a fluctuation of the order of  $10\%/\sqrt{E_{\text{bin}}}$  for

1578 each bin in the average shape.

1579 Figure 4.4 shows a comparison of energy and weta2 [74], defined as the energy weighted  
 1580 lateral width of a shower in the second electromagnetic calorimeter layer, for 16 GeV photons  
 1581 simulated with the new FastCaloSim and with full GEANT4 simulation. The agreement is  
 1582 quite good, with FastCaloSim matching the GEANT4 mean to within 0.3 and 0.03 percent  
 respectively. Similar results are seen for other photon energies and  $\eta$  points.

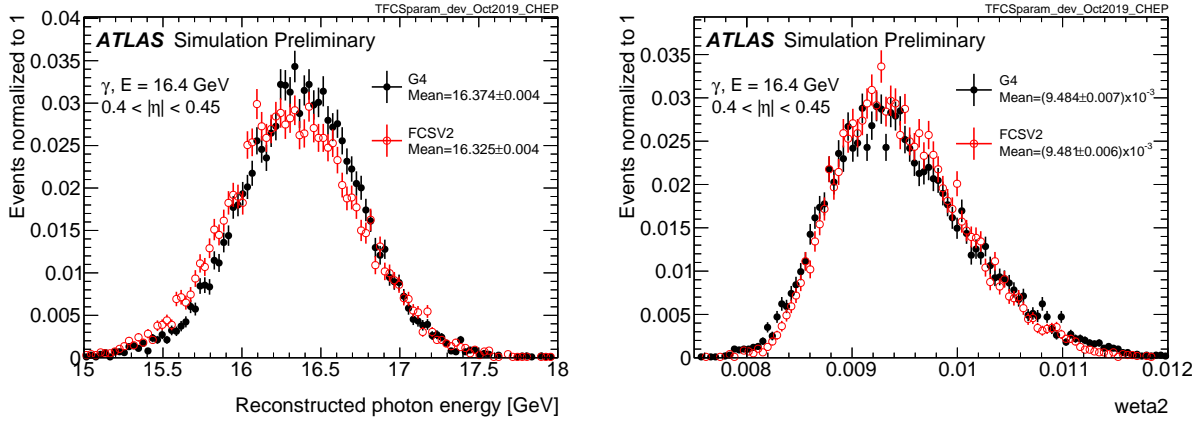


Figure 4.4: Energy and variable weta2, defined as the energy weighted lateral width of a shower in the second electromagnetic calorimeter layer, for 16 GeV photons with full simulation (G4) and FastCaloSimV2 (FCSV2) [71].

1583

#### 1584 4.3.1 Fluctuation Modeling

1585 Figure 4.5 shows the ratio of calorimeter cell energies for single GEANT4 photon and pion  
 1586 events to the corresponding cell energies in their respective average shapes. While the photon  
 1587 event is quite close to the corresponding average, the pion event shows a deviation from the  
 1588 average which is much larger and has a non-trivial structure, reflecting the different natures  
 1589 of electromagnetic and hadronic showering.

1590 While the shape parametrization described above is thus sufficient for describing electro-  
 1591 magnetic showers, we will demonstrate below that it is not sufficient for describing hadronic

1592 showers (Figures 4.8 and 4.9). We therefore present and validate methods to improve this  
 1593 hadronic shower modeling. Such methods have been presented as well in [1].

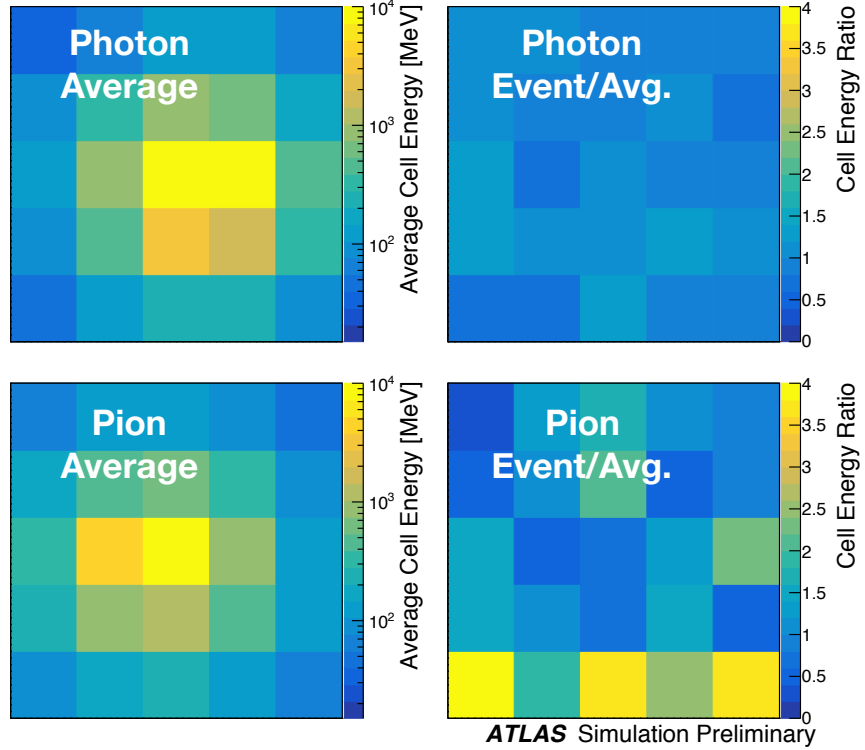


Figure 4.5: Example of photon and pion average shapes in  $5 \times 5$  calorimeter cells. The left column shows the average shape over a sample of 10000 events, while the right column shows the energy ratio, in each cell, of single GEANT4 events with respect to this average. The photon ratios are all close to 1, while the pion ratios show significant deviation from the average.

1594 Two methods for modeling deviations from the average shape have been studied: (1)  
 1595 a neural network based approach using a Variational Autoencoder (VAE) [75] and (2) a  
 1596 map through cumulative distributions to an  $n$ -dimensional Gaussian. With both methods,  
 1597 the shape simulation then proceeds as described in Section 4.3, with the drawing of hits  
 1598 according to the average shape. However, these hits no longer have equal energy, but have

1599 weights applied to increase or decrease their energy depending on their spatial position.  
 1600 This application of weights is designed to mimic a realistic shower structure and to encode  
 1601 correlations between energy deposits.

1602 Both methods are trained on ratios of energy in binned units called voxels. This voxelization  
 1603 is performed in the same polar  $\alpha - R$  coordinates as the average shape, with a 5 mm core in  
 1604  $R$  and 20 mm binning thereafter. There are a total of 8  $\alpha$  bins from 0 to  $2\pi$  and 8 additional  
 1605  $R$  bins from 5 mm to 165 mm. The 5 mm core is filled with the average value of core voxels  
 1606 across the 8  $\alpha$  bins when creating the parametrization. However, during simulation, each of  
 1607 these 8 core bins is treated independently. The outputs of both methods mimic these energy  
 1608 ratios and are used in the shape simulation as the weights described above. In contrast to  
 1609 an approach based on, e.g., calorimeter cells, using voxels allows for flexibility in tuning the  
 1610 binning used in creating the parametrization. Further, due to their relatively large size, using  
 1611 calorimeter cells is subject to “edge effects”, where the splitting of energy between cells has a  
 1612 non-trivial effect on the observed energy ratio. The binning used here is of the order of half  
 1613 of a cell size, mitigating this effect.

1614 The Gaussian method operates by using cumulative distributions to map GEANT4 energy  
 1615 ratios to a multidimensional Gaussian distribution. New events are generated by randomly  
 1616 sampling from this Gaussian distribution.

1617 For the VAE method, a system of two linked neural networks is trained to generate events.  
 1618 The first “encoder” neural network maps input GEANT4 energy ratios to a lower dimensional  
 1619 latent space. A second “decoder” neural network then samples from that latent space and  
 1620 tries to reproduce the inputs. In simulation, events are generated by taking random samples  
 1621 from the latent space and passing them through the trained decoder.

1622 Figure 4.6 shows the distributions of input GEANT4 and Gaussian method generated  
 1623 energy ratios in the grid of voxels. Figure 4.7 shows the correlation coefficient between the  
 1624 center voxel from  $\alpha = 0$  to  $2\pi/8$  for input GEANT4 and the Gaussian and VAE fluctuation  
 1625 methods. Agreement is good throughout.

1626 Validation of the Gaussian and VAE fluctuation methods was performed within FastCaloSimV2.

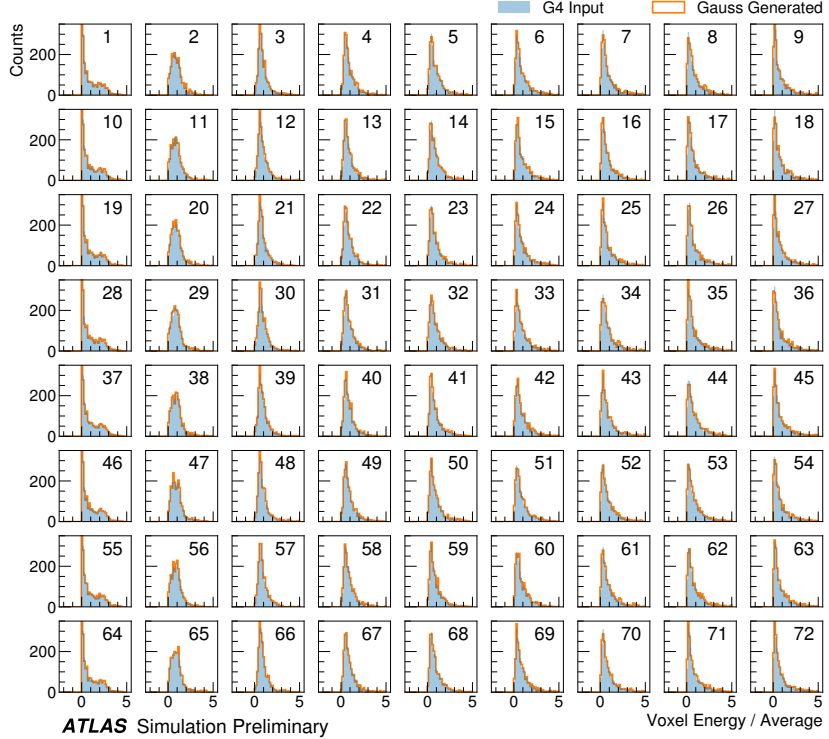


Figure 4.6: Distribution of the ratio of voxel energy in single events to the corresponding voxel energy in the average shape, with GEANT4 events in blue and Gaussian model events in orange, for 65 GeV central pions in EMB2. Moving top to bottom corresponds to increasing  $\alpha$ , left to right corresponds to increasing  $R$ , with core voxels numbered 1, 10, 19, .... Agreement is quite good across all voxels. Results are similar for the VAE method.

1627 Figure 4.8 shows the energy ratio of cells for a given simulation to the corresponding cells in  
 1628 the average shape as a function of the distance from the shower center. The mean for all  
 1629 simulation methods is expected to be around 1, with deviation from the average (the RMS  
 1630 fluctuation) shown by the error bars. The Gaussian method RMS (red) and VAE method  
 1631 RMS (green) both match the GEANT4 RMS (yellow) better than the case without correlated  
 1632 fluctuations (blue) for a variety of energies,  $\eta$  points, and layers, often reproducing 80 – 100 %  
 1633 of the GEANT4 RMS magnitude, compared to the 5 – 30 % observed in the no correlated

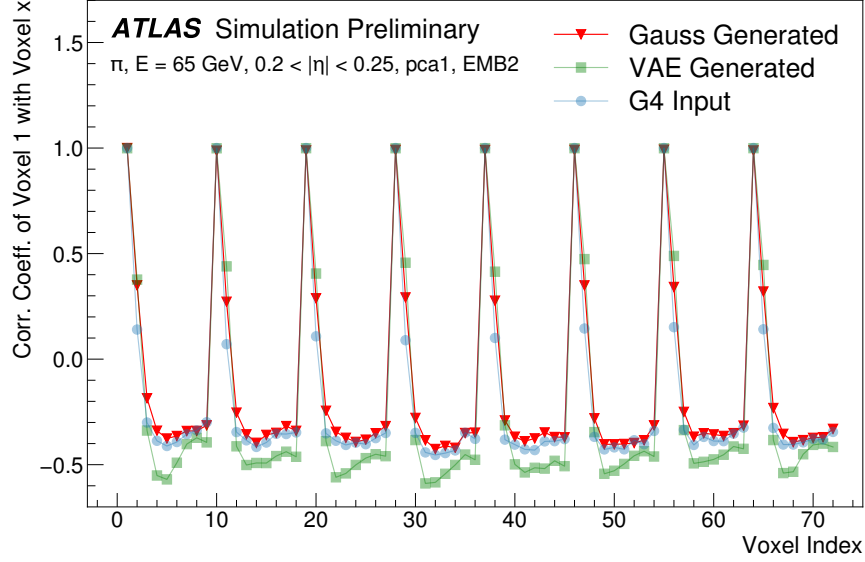


Figure 4.7: Correlation coefficient of ratios of voxel energy in single events to the corresponding voxel energy in the average shape, examined between the core bin from  $\alpha = 0$  to  $2\pi/8$  and each of the other voxels. The periodic structure represents the binning in  $\alpha$ , and the increasing numbers in each of these periods correspond to increasing  $R$ , where the eight points with correlation coefficient 1 are the eight core bins. Both the Gaussian and VAE generated toy events are able to reproduce the major correlation structures for 65 GeV central pions in EMB2.

1634 fluctuations case.

1635 Figure 4.9 shows the result of a simulation with full ATLAS reconstruction for 65 GeV  
 1636 central pions with the Gaussian fluctuation model. Here a *cluster* [76] is defined as a three-  
 1637 dimensional spatial grouping of calorimeter cells which are summed based on the input signals  
 1638 relative to their neighboring cells. The multiplicity, shape, and spatial distribution of such  
 1639 clusters provides a powerful insight on the structure of energy deposits in the calorimeter,  
 1640 and good performance in cluster variables is a promising step towards good performance  
 1641 in the modeling of jet substructure, as these clusters may themselves be summed to form

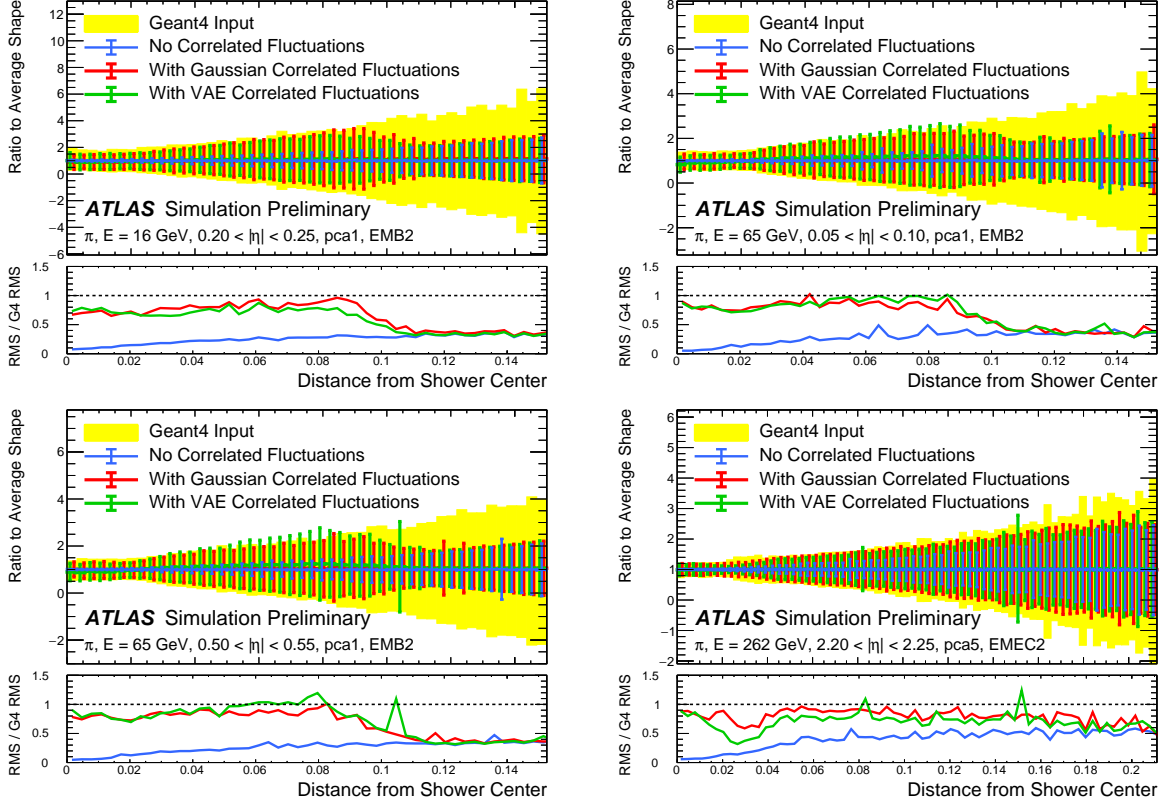


Figure 4.8: Comparison of the RMS fluctuations about the average shape with the Gaussian fluctuation model (red), the VAE fluctuation model (green), and without correlated fluctuations (blue) for a range of pion energies,  $\eta$  points, and layers.

1642 jets (see Chapter 5). The simulation with the Gaussian fluctuation model demonstrates  
 1643 improved modeling of several of these cluster variables relative to baseline FastCaloSimV2,  
 1644 reproducing the distributions of events simulated with GEANT4. These include number and  
 1645 energy of clusters, the 2nd moment in lambda, ( $<\lambda^2>$ ), which describes the square of the  
 1646 longitudinal extension of a cluster, where  $\lambda$  is the distance of a cell from the shower center  
 1647 along the shower axis, and a cluster moment is defined as  $<x^n> = \frac{\sum E_i x_i}{\sum E_i}$ , and the distance  
 1648  $\Delta R$ , between the cluster and the true pion.

1649 The new fast calorimeter simulation is a crucial part of the future of simulation for the

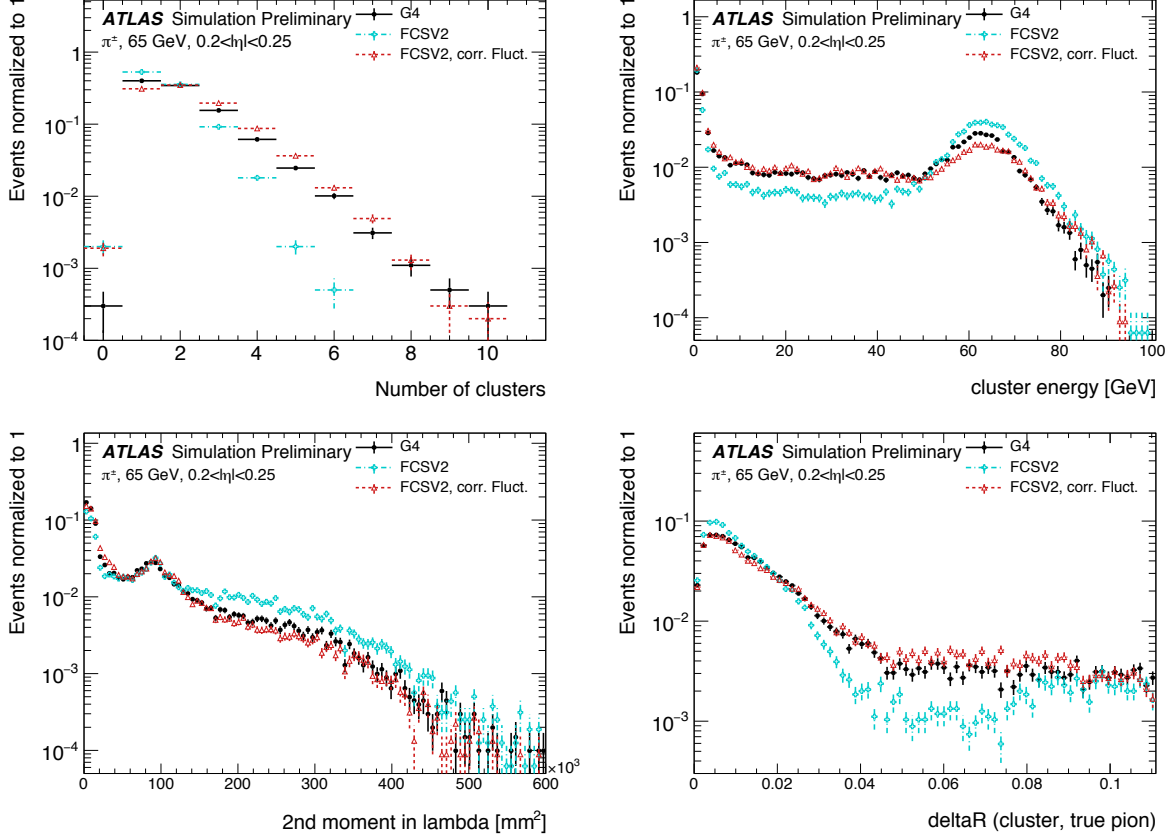


Figure 4.9: Comparison of the Gaussian fluctuation model to the default FCSV2 version and to G4 simulation, using pions of 65 GeV energy and  $0.2 < |\eta| < 0.25$ . Variables shown relate to calorimeter clusters, three-dimensional spatial groupings of cells [76] which provide powerful insight on the structure of energy deposits in the calorimeter. Variables considered include number and energy of clusters, the 2nd moment in lambda, ( $\langle \lambda^2 \rangle$ ), which describes the square of the longitudinal extension of a cluster, where  $\lambda$  is the distance of a cell from the shower center along the shower axis, and a cluster moment is defined as  $\langle x^n \rangle = \frac{\sum E_i x_i}{\sum E_i}$ , and the distance  $\Delta R$ , between the cluster and the true pion. With the correlated fluctuations, variables demonstrate improved modeling relative to default FastCaloSimV2.

1650 ATLAS Experiment at the LHC. The per event simulation time of the full detector with  
 1651 GEANT4, calculated over 100  $t\bar{t}$  events, is 228.9 s. Using FastCaloSim for the calorimeter  
 1652 simulation reduces this to 26.6 s, of which FastCaloSim itself is only 0.015 s, with the majority  
 1653 of the remaining simulation time due to GEANT4. Good physics modeling is achieved, and  
 1654 the correlated fluctuations method shows good proof of concept improvement for the modeling  
 1655 of hadronic showers.

1656 **4.4 Outlook**

1657 There has been significant effort in the community to develop a set of fast simulation tools,  
 1658 with the use of machine learning methods at the forefront of such approaches (e.g. [77], [78]).  
 1659 Most fast simulation approaches generally are based on parametrizations of fully simulated  
 1660 events, but fall into two paradigms - a “by hand” simulation, which focuses on the modeling  
 1661 of individual detector effects, or a fully parametrized simulation, in which a generative model  
 1662 (e.g. a Generative Adversarial Network or Variational Autoencoder) is trained to directly  
 1663 reproduce the input events. Both approaches can be extremely powerful, but each suffer from  
 1664 certain drawbacks. The “by hand” approach offers the advantage of direct encoding of expert  
 1665 knowledge – if an effect needs to be modeled, a new parametrization is introduced. However,  
 1666 by the same token, it requires dedicated parametrizations for each effect. Fully parametrizing  
 1667 the simulation with a generative model offloads this burden onto the network itself. However,  
 1668 by doing so, the ability to use expert knowledge is diminished – the network is required to  
 1669 learn all relevant effects.

1670 The method presented here represents an effort to step towards a hybrid between these two  
 1671 approaches, leveraging the power of machine learning techniques for individual parametriza-  
 1672 tions within the by hand framework. Such hybrid solutions have the potential to be extremely  
 1673 powerful, and further work on the development of these solutions is an interesting direction  
 1674 of future study.

1675

## Chapter 5

1676

# RECONSTRUCTION

1677 Chapter 3 discusses how a proton-proton collision may be captured by a physical detector  
 1678 and turned into data that may be stored and analyzed. Chapter 4 discusses the simulation  
 1679 of this same process. At this most basic level, however, the ATLAS detector is only a  
 1680 machine for turning particles into a set of electrical signals, albeit in a very sophisticated,  
 1681 physics motivated way. This chapter discusses the step of turning these electrical signals into  
 1682 objects which may be identified with the underlying physics processes, and therefore used to  
 1683 make statements about what occurred within a given collision event. This process is termed  
 1684 *reconstruction*, and we will focus particularly on jets and flavor tagging, as the most relevant  
 1685 pieces for this thesis work.

1686 **5.1 Jets**

1687 As discussed in Chapters 3 and 4, the production of particles with color charge from a  
 1688 proton-proton interaction is complicated both by parton showering and by confinement: a  
 1689 quark produced from a hard scatter is not seen as a quark, but rather, as a spray of particles  
 1690 with a variety of hadrons in the final state, which subsequently shower upon interaction with  
 1691 the calorimeter in a complicated way.

1692 For hard scatter electrons, photons, or muons on the other hand, the picture is much  
 1693 clearer: there is no parton showering, and each has a distinct signature in the detector:  
 1694 photons have no tracks and a very localized calorimeter shower, electrons are associated  
 1695 with tracks and are similarly localized in the calorimeter, and muons are associated with  
 1696 tracks, pass through the calorimeter due to their large mass, and leave signatures in the muon  
 1697 spectrometer.

1698     Jets are a tool to deal with the messiness of quarks and gluons. The basic concept is to  
 1699 group the multitude of particles produced by hadronization into a single object. Such an  
 1700 object then has associated properties, including a four-vector, which may be identified with  
 1701 the corresponding initial state particle. In practice a variety of information from the ATLAS  
 1702 detector is used for such a reconstruction. The analysis considered in this thesis uses particle  
 1703 flow jets [79], which combines information from both the tracker and the calorimeter, where  
 1704 the combined objects may be identified with underlying particles. However, jets built from  
 1705 clusters of calorimeter cells [80] as well as from charged particle tracks [81] have also been  
 1706 used very effectively.

1707     A variety of algorithms are used to associate detector level objects to a given jet. The  
 1708 most commonly used in ATLAS is the anti- $k_T$  algorithm [82], which is a successor to the  
 1709  $k_T$  algorithm, among others [83], and develops as follows. Both algorithms are sequential  
 1710 recombination algorithms, which begin with the smallest distance,  $d_{ij}$  between considered  
 1711 objects (e.g. particles or intermediate groupings of particles). If  $d_{ij}$  is less than a parameter  
 1712  $d_{iB}$  ( $B$  for “beam”) object  $i$  is combined with object  $j$ , the distance  $d_{ij}$  is recomputed, and  
 1713 the process repeats. This proceeds until  $d_{ij} \geq d_{iB}$ , at which point the jet is “complete” and  
 1714 removed from the list of considered objects.

The definitional difference between  $k_T$  and anti- $k_T$  is these distance parameters. In general form, these are defined as

$$d_{ij} = \min(p_{Ti}^{2p}, p_{Tj}^{2p}) \frac{\Delta R_{ij}^2}{R^2} \quad (5.1)$$

$$d_{iB} = p_{Ti}^{2p} \quad (5.2)$$

1715 where  $p_{Ti}$  is the transverse momentum of object  $i$ ,  $\Delta R_{ij}$  is the angular distance between  
 1716 objects  $i$  and  $j$ ,  $R$  is a radius parameter, and  $p$  controls the tradeoff between the  $p_T$  and  
 1717 angular distance terms. For the  $k_T$  algorithm  $p = 1$ ; for the anti- $k_T$  algorithm,  $p = -1$ . This  
 1718 is a simple change, but results in significantly different behavior.

The anti- $k_T$  algorithm can be understood as follows: for a single high  $p_T$  particle ( $p_{T1}$ ) surrounded by a bunch of low  $p_T$  particles, the low  $p_T$  particles will be clustered with the

high  $p_T$  one if

$$d_{1j} = \frac{1}{p_{T1}^2} \frac{\Delta R_{1j}^2}{R^2} < \frac{1}{p_{T1}^2} \quad (5.3)$$

$$\implies \Delta R_{1j} < R. \quad (5.4)$$

1719 Therefore, a single high  $p_T$  particle ( $p_{T1}$ ) surrounded by a bunch of low  $p_T$  particles results in  
 1720 a perfectly conical jet. This shape may change with the presence of other high momentum  
 1721 particles, but the key feature of the dynamics is that the jet shape is determined by high  $p_T$   
 1722 objects due to the  $\frac{1}{p_T}$  nature of this definition. In contrast, the  $k_T$  algorithm results in jets  
 1723 influenced by low momentum particles, which results in a less regular shape. This property,  
 1724 of regular jet shapes determined by high momentum objects, as well as demonstrated good  
 1725 practical performance, makes the anti- $k_T$  algorithm the favored jet algorithm in ATLAS.

1726 Because jets are composed of multiple objects, a useful property of jets is jet *substructure*,  
 1727 that is, acknowledging that jets are composite objects, analyzing the structure of a given  
 1728 jet to infer physics information. This leads to the use of *subjets*; that is, after running jet  
 1729 clustering, often to create a “large-R”,  $R = 1.0$  anti- $k_T$  jet, a smaller radius jet clustering  
 1730 algorithm is run within the jet. Subjets are often chosen using the  $k_T$  algorithm, which again  
 1731 is sensitive to lower momentum particles, with  $R = 0.2$  or  $0.3$ . For the boosted version of this  
 1732 thesis analysis, such a strategy is used, in which the subjets are *variable radius* and depend  
 1733 on the momentum of the (proto)jet in question. Beyond this thesis work, substructure is  
 1734 used in a large variety of analyses, with a set of associated variables and tools developed for  
 1735 exploiting this structure (e.g. [84]).

## 1736 5.2 Flavor Tagging

1737 For this this thesis, the physics process being considered is  $HH \rightarrow b\bar{b}b\bar{b}$ . From the previous  
 1738 section, we know that the standard practice is to identify these  $b$  quarks (or, rather, the  
 1739 resulting  $B$  hadrons, due to confinement) with jets – in our case, these  $b$ -*jets* are  $R=0.4$   
 1740 anti- $k_T$  particle flow jets (see Chapters 6 and 7). However, not all jets produced at the LHC  
 1741 are from  $B$  hadrons; rather, there are a variety of different types of jets corresponding to

1742 different flavors of quarks. These are often classified as light jets (from  $u$ ,  $d$ , or  $s$  quarks, or  
1743 gluons) or as other *heavy flavor* jets, e.g.  $c$ -jets, involving  $c$  quarks. Distinguishing between  
1744 these different categories is a very active area of work in ATLAS, termed *flavor tagging*, with  
1745 much focus on *b-tagging* in particular, that is, the identification of jets from  $B$  hadron decays.  
1746 We here briefly describe the techniques used for flavor tagging in ATLAS.

1747 What distinguishes a  $b$ -jet from any other jet? This question is fundamental to the  
1748 design of the various  $b$ -tagging algorithms, and has two major answers: (1)  $B$  hadrons have  
1749 long lifetimes, and (2)  $B$  hadrons have large masses. It is most illustrative to compare  
1750 the  $B$  hadron properties to a common light meson, e.g.  $\pi^0$ , the neutral pion, with quark  
1751 content  $\frac{1}{\sqrt{2}}(u\bar{u} - d\bar{d})$ .  $B$  hadrons have lifetimes around 1.5 ps, corresponding to a decay length  
1752  $c\tau \approx 0.45$  mm. In contrast,  $\pi^0$  has a lifetime of  $8.4 \times 10^{-5}$  ps, which is around 20,000 times  
1753 shorter! Theoretically, this comes from CKM suppression of the  $b$  to  $c$  transition, which  
1754 dominates the  $B$  decay modes. Experimentally, this difference pops up as shown in Figure  
1755 5.1 – light flavor initiated jets decay almost immediately at the proton-proton interaction  
1756 point, whereas  $b$ -jets are distinguished by a displaced secondary vertex, corresponding to  
1757 the 5 mm decay length calculated above. This displaced vertex falls short of the detector  
1758 itself, but may be inferred from larger transverse (perpendicular to beam) and longitudinal  
1759 (parallel to beam) impact parameters of the resulting tracks, termed  $d_0$  and  $z_0$  respectively.

1760 Coming to the mass,  $B$  mesons have masses of around 5.2 GeV, whereas the  $\pi^0$  mass  
1761 is around 0.134 GeV, (around 40 times lighter). This higher mass gives access to a larger  
1762 decay phase space, leading to a high multiplicity for  $b$ -jets (average of 5 charged particles per  
1763 decay).

1764 One final distinguishing feature of  $B$  hadrons is their *fragmentation function*, a function  
1765 describing the production of an observed final state. For  $B$  hadrons, this is particularly  
1766 “hard”, with the  $B$  hadrons themselves contributing to an average of around 75 % of the  $b$ -jet  
1767 energy. Thus, the identification of  $b$ -jets with  $B$  hadrons is, in some sense, descriptive.

1768 We have contrasted  $b$ -jets and light jets, demonstrating that there are several handles  
1769 available for making this distinction.  $c$ -jets are slightly more similar to  $b$ -jets, but the same

1770 handles still apply –  $c$ -hadron lifetimes are between 0.5 and 1 ps, a factor of 2 smaller than  $B$   
1771 hadrons. Their mass is around 1.9 GeV, 2 to 3 times smaller than  $B$  hadrons, and  $c$ -hadrons  
1772 contribute to an average of around 55 % of  $c$ -jet energy. Therefore, while the gap is slightly  
1773 smaller, a distinction may still be made.

1774 The ATLAS flavor tagging framework [86] relies on developing a suite of “low-level”  
1775 taggers, which use a variety of information about tracks and vertices as inputs. The output  
1776 of these lower level taggers are then fed into a higher level tagger, which aggregates these  
1777 results into a high level discriminant. Each of these taggers is described below.

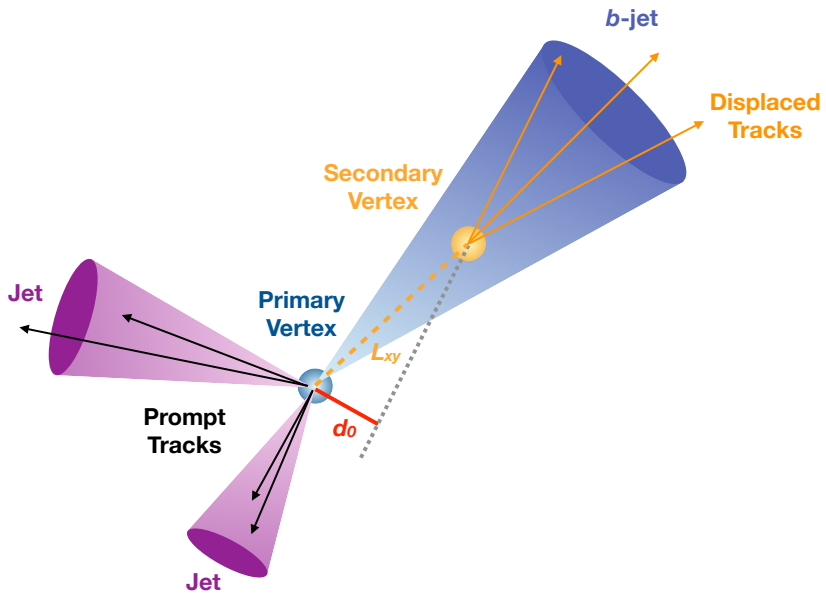


Figure 5.1: Illustration of an interaction producing two light jets and one  $b$ -jet in the transverse plane. While the light jets decay “promptly”, coinciding with the primary vertex of the proton-proton interaction, the longer lifetime of  $B$  hadrons leads to a secondary decay vertex, displaced from the primary vertex by length  $L_{xy}$ . This is typically a few mm, and therefore is not directly visible in the detector, but leads to a large transverse impact parameter,  $d_0$ , for the resulting tracks. [85]

1778 5.2.1 IP2D/3D

1779 IP2D and IP3D are taggers based on the large track impact parameter (IP) nature of  $B$   
 1780 hadron decays. Both are based on histogram templates derived from Monte Carlo simulation,  
 1781 which are used as probability density functions to construct log-likelihood discriminants.  
 1782 IP2D incorporates just the transverse impact parameter information using 1D histogram  
 1783 templates, whereas IP3D uses both transverse and longitudinal impact parameters in a 2D  
 1784 template, which accounts for correlations. Importantly, these are *signed* impact parameters,  
 1785 with sign based on the angle between the impact parameter and the considered jet – positive  
 1786 impact parameters are consistent with a track extrapolation in front of the jet (angle between  
 1787 impact parameter line and jet  $< 90^\circ$ ), and therefore more consistent with tracks originating  
 1788 from a displaced decay.

1789 Rather than using the impact parameters directly, an impact parameter *significance*  
 1790 is used which incorporates an uncertainty on the impact parameter – tracks with a lower  
 1791 uncertainty but the same impact parameter will contribute more in the calculation. This  
 1792 signed significance is what is used to sample from the PDF templates, with the resulting  
 1793 discriminants the sum of probability ratios between given jet hypotheses over tracks associated  
 1794 to a given jet, namely  $\sum_{i=1}^N \log \frac{p_b}{p_{light}}$  between  $b$ -jet and light jet hypotheses, where  $p_b$  and  
 1795  $p_{light}$  are the per-track probabilities. Similar discriminants are defined between  $b$ - and  $c$ -jets  
 1796 and  $c$  and light jets.

1797 5.2.2 SV1

1798 SV1 is an algorithm which aims to find a secondary vertex (SV) in a given jet. Operating  
 1799 on all vertices associated with a considered jet, the algorithm discards tracks based on a  
 1800 variety of cleaning requirements. It then proceeds to first construct all two-track vertices,  
 1801 and then iterates over all the tracks involved in these two track vertices to try to fit a single  
 1802 secondary vertex, which would then be identified with the secondary vertex from the  $b$  or  $c$   
 1803 hadron decay. This fit proceeds by evaluating a  $\chi^2$  for the association of a track and vertex,

removing the track with the largest  $\chi^2$ , and iterating until the  $\chi^2$  is acceptable and the vertex has an invariant mass of less than 6 GeV (for consistency with  $b$  or  $c$  hadron decay).

A variety of discriminating variables may then be constructed, including (1) invariant mass of the secondary vertex, (2) number of tracks associated with the secondary vertex, (3) number of two-track vertices, (4) energy fraction of the tracks associated to the secondary vertex (relative to all of the tracks associated to the jet), and various metrics associated with the secondary vertex position and decay length, including (5) transverse distance between the primary and secondary vertex, (6) distance between the primary and secondary vertex (7) distance between the primary and secondary vertex divided by its uncertainty, and (8)  $\Delta R$  between the jet axis and the direction of the secondary vertex relative to the primary vertex.

While all eight of these variables are used as inputs to the higher level taggers, the number of two-track vertices, the vertex mass, and the vertex energy fraction are additionally used with 3D histogram templates to evaluate flavor tagging performance by constructing log-likelihood discriminants, similar to the procedure for IP2D/3D.

### 5.2.3 JetFitter

Rather than focusing on a particular aspect of the  $B$  hadron or  $D$  hadron decay topology (e.g impact parameter or secondary vertex), the third low level tagger, JETFITTER [87], tries to reconstruct the full decay chain, including all involved vertices. This is structured around a Kalman filter formalism [88], and has the strong underlying assumption that all tracks which stem from  $B$  and  $D$  hadron decay must intersect a common flight path. This assumption provides significant constraints, allowing for the reconstruction of vertices from even a single track, reducing the number of degrees of freedom in the fit, and allowing the use of “downstream” information, e.g., compatibility of tracks with a  $B \rightarrow D$ -like decay. The constructed topology, including primary vertex location and  $B$ -hadron flight path, is iteratively updated over tracks associated to a given jet, and a variety of discriminating variables related to the resulting topology and reconstructed decay are used as inputs to the high level taggers.

1831    5.2.4 *RNNIP*

1832    The IP2D and IP3D algorithms rely on per-track probabilities, and the final discriminating  
 1833    variables (and inputs to the higher level taggers) are sums (products) over these independently  
 1834    considered quantities. In practice, however, the tracks are not independent – this is merely a  
 1835    simplifying assumption to allow for the use of a binned likelihood, as treatment of all of the  
 1836    interdependencies in such a framework quickly becomes intractable. To address this issue, a  
 1837    recurrent neural network-based algorithm, RNNIP [89], is used, which takes as input a variety  
 1838    of per-track variables, including the signed impact parameter significances (as in IP3D) as  
 1839    well as track momentum fraction relative to the jet and  $\Delta R$  between the track and the jet.  
 1840    RNNs are sequence-based, and vectors of input variables corresponding to tracks for a given  
 1841    jet are ordered by magnitude of transverse impact parameter significance and then passed  
 1842    to the network, which outputs class probabilities corresponding to b-jet, c-jet, light-jet, and  
 1843     $\tau$ -jet hypotheses. Such a procedure allows the network to learn interdependencies between  
 1844    tracks, improving performance.

1845    5.2.5 *MV2 and DL1*

1846    Outputs from the above taggers are combined into high level taggers to aggregate all of the  
 1847    information and improve discriminating power relative to the respective individual taggers as,  
 1848    as shown in Figure 5.2. These high level taggers are primarily in two forms: MV2, which  
 1849    uses a Boosted Decision Tree (BDT) for this aggregation, and DL1, which uses a deep neural  
 1850    network. For the baseline versions of these taggers, only inputs from IP2D, IP3D, SV1, and  
 1851    JetFitter are used. The tagger used for this thesis analysis, DL1r, additionally incorporates  
 1852    RNNIP, demonstrating improved performance over the baseline DL1, as shown in Figure 5.3.  
 1853    All high level taggers also include jet  $p_T$  and  $|\eta|$ .

DL1 offers a variety of improvements over MV2. Rather than a single discriminant output, as with MV2, DL1 has a multidimensional output, corresponding to probabilities for a jet to be a *b*-jet, *c*-jet, or light jet. This allows the trained network to be used for both *b*- and *c*-jet

tagging. The final discriminant for  $b$ -tagging with DL1 correspondingly takes the form

$$D_{\text{DL1}} = \ln \left( \frac{p_b}{f_c \cdot p_c + (1 - f_c) \cdot p_{\text{light}}} \right) \quad (5.5)$$

where  $p_b$ ,  $p_c$ , and  $p_{\text{light}}$  are the output  $b$ ,  $c$ , and light jet probabilities, and  $f_c$  corresponds to an effective  $c$ -jet fraction, which may be tuned to optimize performance.

DL1 further includes an additional set of JETFITTER input variables relative to MV2 which correspond to  $c$ -tagging – notably properties of secondary and tertiary vertices, as would be seen in a  $B \rightarrow D$  decay chain.

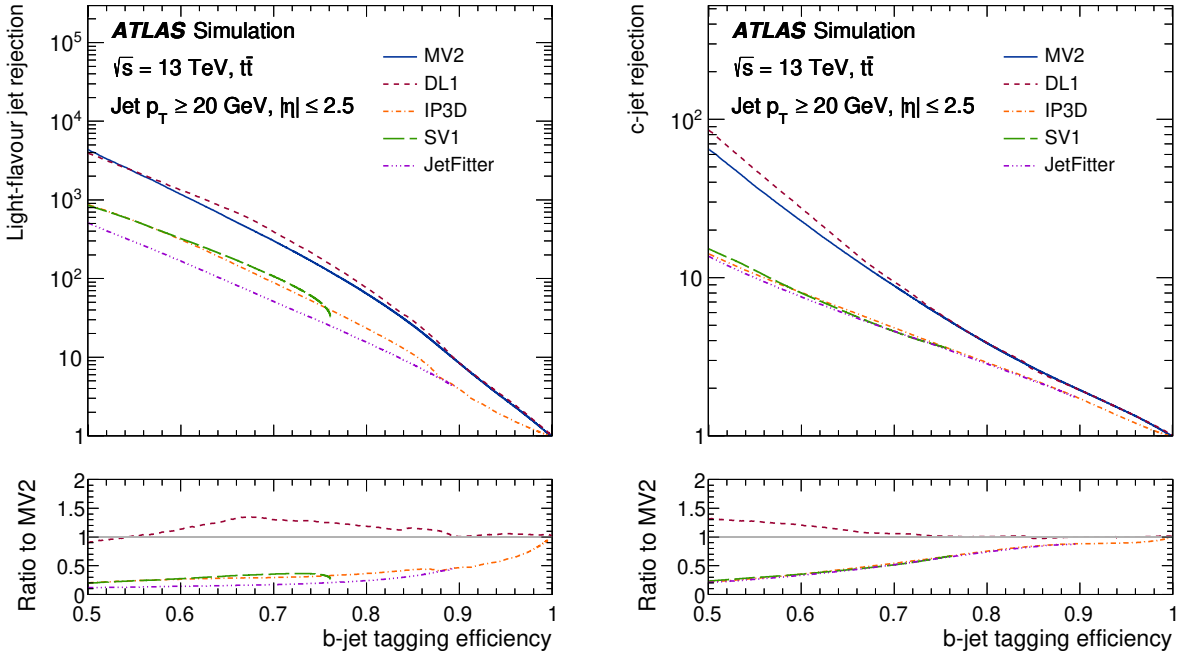


Figure 5.2: Performance of the various low and high level flavor tagging algorithms in  $t\bar{t}$  simulation, demonstrating the tradeoff between  $b$ -jet efficiency and light and  $c$ -jet rejection. The high level taggers demonstrate significantly better performance than any of the individual low level taggers, with DL1 offering slight improvements over MV2 due to the inclusion of additional input variables.

Figure 5.2 shows a comparison of the performance of the various taggers. The  $b$ -tagging performance of DL1 and MV2 is found to be similar, with some improvements in light jet and  $c$ -jet rejection from the additional variables used in DL1. The performance of these high level taggers additionally is seen to be significantly better than any of the individual low level ones, even in regimes where only a single low level tagger is relevant (such as high  $b$ -tagging efficiencies, where SV1 and JETFITTER are limited by selections on tracks entering the respective algorithms).

The inclusion of RNNIP offers a significant improvement on top of baseline DL1, as shown in Figure 5.3, strongly motivating the choice of DL1r for this thesis.

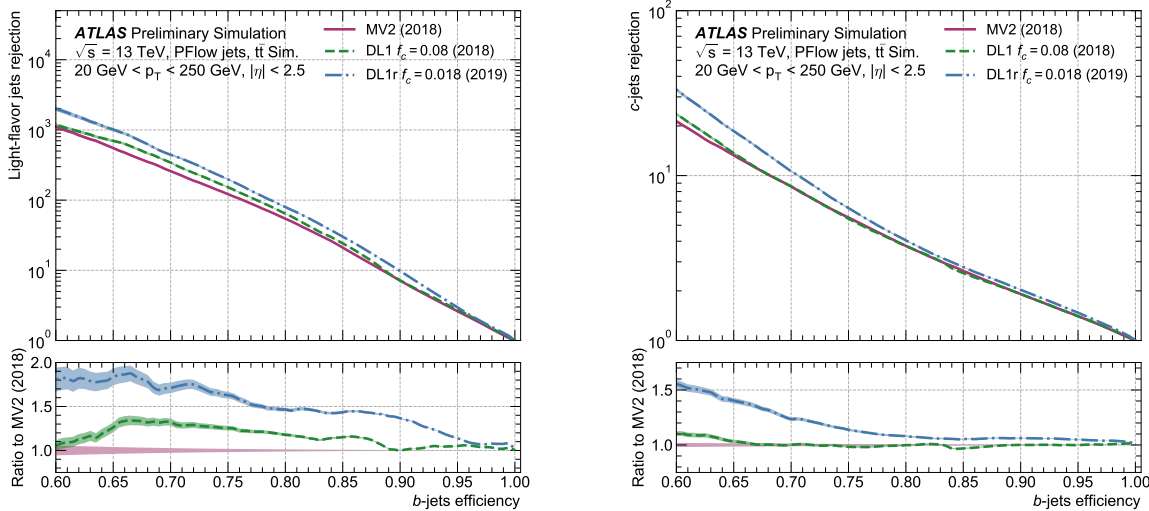


Figure 5.3: Performance of the MV2, DL1, and DL1r algorithms in  $t\bar{t}$  simulation, demonstrating the tradeoff between  $b$ -jet efficiency and light and  $c$ -jet rejection.  $f_c$  controls the importance of  $c$ -jet rejection in the discriminating variable, and values shown have been optimized separately for each DL1 configuration. DL1r demonstrates a significant improvement in both light and  $c$  jet rejection over MV2 and DL1. [90]

1868    5.2.6 *Some Practical Notes*

1869    The  $b$ -tagging metrics presented in Figures 5.2 and 5.3 correspond to evaluating a tradeoff  
1870    between  $b$ -jet efficiency and light jet and  $c$ -jet rejection. In this case,  $b$ -jet efficiency is defined  
1871    such that, e.g. for a 77 % efficiency, 77 % of the real  $b$ -jets will be tagged as such. Somewhat  
1872    counterintuitively, this means that a lower  $b$ -jet efficiency corresponds to a more aggressive  
1873    (“tighter”) selection on the discriminating variable, while a higher  $b$ -jet efficiency corresponds  
1874    to a less aggressive (“looser”) cut (100 % efficiency means no cut). Light and  $c$  jet efficiencies  
1875    are defined similarly, with rejection defined as 1/ the corresponding efficiency.

1876        In ATLAS, the respective  $b$ -tagging efficiencies are used to define various  $b$ -tagging working  
1877    points. The working point used for the nominal  $b$ -jet identification in this thesis is 77 % with  
1878    DL1r. A loosened (less aggressive) selection at the 85 % working point is additionally used.  
1879        See Chapter 7 for further details.

1880

## Chapter 6

1881

### SETTING UP THE $HH \rightarrow b\bar{b}b\bar{b}$ ANALYSIS

1882 The following chapters present two complementary searches for pair production of Higgs  
 1883 bosons in the  $b\bar{b}b\bar{b}$  final state. Such searches are separated based on the signal models being  
 1884 considered: resonant production, in which a new spin-0 or spin-2 particle is produced and  
 1885 decays to two Standard Model Higgs bosons, and non-resonant production, which is sensitive  
 1886 to the value of the Higgs self-coupling  $\lambda_{HHH}$ . Further information on the theory behind both  
 1887 channels can be found in Chapter 2.

1888 ATLAS has performed a variety of searches for both resonant and non-resonant  $HH$  in  
 1889 complementary decay channels, notably for early Run 2 in the  $b\bar{b} W^+ W^-$  [91],  $b\bar{b}\tau^+\tau^-$  [92],  
 1890  $W^+ W^- W^+ W^-$  [93],  $b\bar{b}\gamma\gamma$  [94], and  $W^+ W^- \gamma\gamma$  [95] final states, which were combined along  
 1891 with  $b\bar{b}b\bar{b}$  in [26]. ATLAS has also released a variety of full Run 2 results, including boosted  
 1892  $b\bar{b}\tau^+\tau^-$  [96], VBF  $b\bar{b}b\bar{b}$  [22],  $b\bar{b}\ell\nu\ell\nu$  [97], and  $b\bar{b}\gamma\gamma$  [98].

1893 CMS has also performed searches for production of Higgs boson pairs in the  $b\bar{b}b\bar{b}$  final  
 1894 state (among others) for early Run 2 [99] and full Run 2 [100]. A combination of CMS  
 1895 searches in the  $b\bar{b}b\bar{b}$ ,  $b\bar{b}\tau^+\tau^-$ ,  $b\bar{b}\gamma\gamma$ , and  $b\bar{b}VV$  channels was performed for early Run 2  
 1896 in [101].

1897 While the resonant and non-resonant searches presented here face many similar challenges  
 1898 and proceed (in broad strokes) in a very similar manner, separate optimizations are performed  
 1899 to maximize the respective sensitivities for these two very different sets of signal hypotheses.  
 1900 More particularly, resonant signal hypotheses are (1) very peaked in values of the mass of the  
 1901  $HH$  candidate system near the value of the resonance mass considered and (2) considered  
 1902 across a very broad range of signal mass hypotheses. The resonant searches are therefore split  
 1903 into resolved and boosted topologies based on Lorentz boost of the decay products, with the

resolved channel as one of the primary focuses of this thesis. Further, several analysis design decisions are made to allow for sensitivity to a broad range of masses – in particular, though sensitivity is limited at lower values of  $m_{HH}$  relative to other channels (see, e.g. Chapter 11) due to the challenging background, retaining and properly reconstructing these low mass events allows the  $b\bar{b}b\bar{b}$  channel to retain sensitivity as low as the kinematic threshold at 250 GeV.

In contrast, non-resonant signal hypotheses are quite broad in  $m_{HH}$ , and have a much more limited mass range, with Standard Model production peaking near 400 GeV, and the majority of the analysis sensitivity able to be captured with a resolved topology. Even for Beyond the Standard Model signal hypotheses, which may have more events at low  $m_{HH}$ , the non-resonant nature of the production allows the  $b\bar{b}b\bar{b}$  channel to retain sensitivity while discarding much of the challenging low mass background. Such freedom allows for decisions which focus on improved background modeling for the middle to upper  $HH$  mass regime, resulting in improved modeling and smaller uncertainties than would be obtained with a more generic approach.

Both searches are presented in the following, with emphasis on particular motivations for, and consequences of, the various design decisions involved for each respective set of signal hypotheses. A comparison of representative signals for both the resonant and non-resonant analyses is shown in Figure 6.1.

The analyses improve upon previous work [2] in several notable ways. The resonant search leverages a Boosted Decision Tree (BDT) based algorithm for the reconstruction of the  $HH$  system from the jets considered for the analysis, offering an improved efficiency of that reconstruction over a broad mass spectrum. The non-resonant adopts a different approach, with a simplified algorithm based on the minimum angular distance ( $\Delta R$ ) between jets in a reconstructed Higgs candidate. Such an approach very efficiently discards low mass background events, resulting in an easier to estimate background with reduced systematic uncertainties.

A particular contribution of this thesis is the background estimation, which uses a novel,

1932 neural network based approach to perform a data-driven estimation of the background, which  
 1933 is dominated by QCD processes, for which a sufficient simulation is not available. This new  
 1934 approach offers improved modeling over previous methods, as well as the ability to model  
 1935 correlations between observables. While all aspects of the analysis of course contribute to  
 1936 the final result, the author of this thesis wishes to emphasize that the background estimate,  
 1937 with the corresponding uncertainties and all other associated decisions, really is the core of  
 1938 the  $HH \rightarrow b\bar{b}b\bar{b}$  analysis – the development of this procedure, and all associated decisions, is  
 1939 similarly the core of this thesis work.

1940 This analysis also benefits from improvements to ATLAS jet reconstruction and calibration,  
 1941 and flavor tagging [86]. In particular, this analysis benefits from the introduction of particle  
 1942 flow jets [79]. These make use of tracking information to supplement calorimeter energy  
 1943 deposits, improving the angular and transverse momentum resolution of jets by better  
 1944 measuring these quantities for charged particles in those jets.

1945 The analysis also benefits from the new DL1r ATLAS flavor tagging algorithm. Whereas  
 1946 the flavor tagging algorithm used in the previous analysis (MV2) used a boosted decision tree  
 1947 (BDT) to combine the output of various low level algorithms, DL1r (and the baseline DL1  
 1948 algorithm) uses a deep neural network to do this combination. In addition to the low level  
 1949 algorithms used as inputs to MV2, DL1 includes a variety of additional variables used for  
 1950  $c$ -tagging. DL1r further incorporates RNNIP, a recurrent neural network designed to identify  
 1951  $b$ -jets using the impact parameters, kinematics, and quality information of the tracks in the  
 1952 jets, while also taking into account the correlations between the track features.

1953 The overall analysis sensitivity further benefits from a factor of 4.6 increase in integrated  
 1954 luminosity.

## 1955 **6.1 Data and Monte Carlo Simulation**

1956 Both the resonant and non-resonant searches are performed on the full ATLAS Run 2 dataset,  
 1957 consisting of  $\sqrt{s} = 13$  TeV proton-proton collision data taken from 2016 to 2018 inclusive.  
 1958 Data taken in 2015 is not used due to a lack of trigger jet matching information and  $b$ -jet

<sup>1959</sup> trigger scale factors<sup>1</sup>. The integrated luminosity collected and usable in this analysis<sup>2</sup> was:

<sup>1960</sup> •  $24.6 \text{ fb}^{-1}$  in 2016

<sup>1961</sup> •  $43.65 \text{ fb}^{-1}$  in 2017

<sup>1962</sup> •  $57.7 \text{ fb}^{-1}$  in 2018

<sup>1963</sup> This gives a total integrated luminosity of  $126 \text{ fb}^{-1}$ . This is lower than the  $139 \text{ fb}^{-1}$  ATLAS  
<sup>1964</sup> collected during Run 2 [103] due to the inefficiency described in footnote 2 as well as the  
<sup>1965</sup>  $3.2 \text{ fb}^{-1}$  of 2015 data which is unused due to the trigger scale factor issue mentioned above.

<sup>1966</sup> In this analysis, Monte Carlo samples are used purely for modelling signal processes. The  
<sup>1967</sup> background is strongly dominated by events produced by QCD multijet processes, which are  
<sup>1968</sup> difficult to correctly model in simulation due to the complexity of the interactions involved  
<sup>1969</sup> (including, e.g. non-perturbative effects), as well as the harsh requirement of four  $b$ -tagged  
<sup>1970</sup> jets, which makes it difficult to collect sufficient Monte Carlo statistics. This necessitates the  
<sup>1971</sup> use of a data-driven background modeling technique, which is described in Chapter 8.

<sup>1972</sup> The scalar resonance signal model is simulated at leading order in  $\alpha_s$  using MADGRAPH  
<sup>1973</sup> [60]. Hadronization and parton showering are done using HERWIG 7 [61][62] with EVTGEN [64],  
<sup>1974</sup> and the nominal PDF is NNPDF 2.3 LO. In practice this is implemented as a two Higgs  
<sup>1975</sup> doublet model where the new neutral scalar is produced through gluon fusion and required  
<sup>1976</sup> to decay to a pair of SM Higgs bosons. The heavy scalar is assigned a width much smaller  
<sup>1977</sup> than detector resolution, and the other 2HDM particles do not enter the calculation.

<sup>1978</sup> Scalar samples are produced at resonance masses between 251 and 900 GeV and the  
<sup>1979</sup> detector simulation is done using AtlFast-II [70]. In addition the samples at 400 GeV and  
<sup>1980</sup> 900 GeV are also fully simulated to verify that the use of AtlFast-II is acceptable. For higher

<sup>1</sup>These trigger scale factors account for differences in the performance of the  $b$ -tagging algorithms between simulation and data, with the jet matching providing a correspondence between the jets in the trigger decision and the jets in the offline analysis

<sup>2</sup>approximately  $9 \text{ fb}^{-1}$  of data was collected but could not be used in this analysis due to an inefficiency in the  $b$ -jet triggers at the start of 2016 [102]

1981 masses, as well as for the boosted analysis, samples are produced between 1000 and 5000 GeV,  
 1982 and the detector is fully simulated. As discussed in Chapter 4, an outstanding issue with  
 1983 AtlFast-II is the modeling of jet substructure. While such variables are not used for the  
 1984 resolved analysis, the boosted analysis begins at 900 GeV, motivating the different detector  
 1985 simulation in these two regimes.

1986 The spin-2 resonance signal model is also simulated at LO in  $\alpha_s$  using MADGRAPH.  
 1987 Hadronization and parton showering are done using PYTHIA 8 [63] with EVTGEN, and the  
 1988 nominal PDF is NNPDF 2.3 LO. In practice this is implemented as a Randall-Sundrum  
 1989 graviton with  $c = 1.0$ .

1990 Spin-2 resonance samples are produced at masses between 251 and 5000 GeV, and these  
 1991 samples are all produced with full detector simulation.

1992 For the non-resonant search, samples are produced at values of  $\kappa_\lambda = 1.0$  and 10.0, and are  
 1993 simulated using POWHEG Box v2 generator [57–59] at next-to-leading order (NLO), with full  
 1994 NLO corrections with finite top mass, using the PDF4LHC [104] parton distribution function  
 1995 (PDF) set. Parton showers and hadronization are simulated with PYTHIA 8.

## 1996 6.2 Triggers

1997 To maximize analysis sensitivity, a combination of multi- $b$ -jet triggers is used. Due to the use  
 1998 of events with two  $b$ -tagged jets in the background estimate, such triggers have a maximum  
 1999 requirement of two  $b$ -tagged jets. For the resonant analysis, a combination of triggers of  
 2000 various topologies is used, namely

- 2001 • 2 $b$  + HT, which requires two  $b$ -tagged jets and a minimum value of  $H_T$ , defined to  
 2002 be the scalar sum of  $p_T$  across all jets in the event.
- 2003 • 2 $b$  + 2j, which requires two  $b$ -tagged jets and two other jets matching some kinematic  
 2004 requirements
- 2005 • 2 $b$  + 1j, which requires two  $b$ -tagged jets and one other jet matching some kinematic

2006 requirements

- 2007 • 1b, which requires one  $b$ -tagged jet

2008 Due to minimal contributions from some of these triggers for the Standard Model non-resonant  
2009 signal, a simplified strategy relying entirely on  $2b + 1j$  and  $2b + 2j$  triggers is used for the  
2010 non-resonant search.

2011 While the use of multiple triggers is beneficial for analysis sensitivity, it comes with some  
2012 complications. Namely, a set of scale factors must be assigned to simulated events to account  
2013 for differences in trigger efficiency between real and simulated events. Because these scale  
2014 factors may differ between triggers, the use of multiple triggers becomes complicated: an event  
2015 may pass more than one trigger, while trigger scale factors are only provided for individual  
2016 triggers.

2017 To simplify this calculation, a set of hierarchical offline selections is applied, closely  
2018 mimicking the trigger selection. Based on these selections, events are sorted into categories  
2019 (*trigger buckets*), after which the decision of a *single trigger* is checked. Note that the set  
2020 of events which enter the analysis via this trigger category selection must pass both the  
2021 offline selection as well as the corresponding online trigger selection. Particularly for the  
2022  $2b$  categories, this means that the explicit requirement of two  $b$ -tagged jets is left to the  
2023 trigger decision itself, with the categorization designed around the other considered objects  
2024 (non-tagged jets or  $H_T$ ).

2025 The resonant search applies such categorization in the following way, with selections  
2026 considered in order:

- 2027 1. If the leading jet is  $b$ -tagged with  $p_T > 325\text{ GeV}$ , the event is in the  $1b$  trigger category.
- 2028 2. Otherwise, if the leading jet is not  $b$ -tagged, but has  $p_T > 168.75\text{ GeV}$ , the event is in  
2029 the  $2b + 1j$  trigger category.

2030     3. If neither of the first two selections pass, if the scalar sum of jet  $p_T$ s,  $H_T > 900 \text{ GeV}$ ,  
 2031       the event falls into the  $2b + HT$  trigger category.

2032     4. Events that do not pass any of the above offline selections are in the  $2b + 2j$  trigger  
 2033       category.

2034   Corresponding triggers are then checked in each category, and the final set of events consists  
 2035   of those events that pass the trigger decision in their respective categories.

2036   For the resonant search, the  $2b + 1j$  and  $2b + 2j$  triggers are the dominant categories,  
 2037   containing roughly 26 % and 49 % of spin-2 events, evaluated on MC16d samples with  
 2038   resonance masses between 300 and 1200 GeV. Notably, the  $1b$  trigger efficiency is largest at  
 2039   high ( $> 1 \text{ TeV}$ ) resonance masses.

2040   For the non-resonant search, it was noted that the  $1b$  trigger has minimal contribution,  
 2041   while the  $2b + HT$  events are largely captured by the  $2b + 2j$  trigger. Therefore, a simplified  
 2042   scheme is considered, with selections:

2043     1. If the 1st leading jet has  $p_T > 170 \text{ GeV}$  and the 3rd leading jet has  $p_T > 70 \text{ GeV}$ , the  
 2044       event is in the  $2b + 1j$  trigger category.

2045     2. Otherwise, the event is in the  $2b + 2j$  trigger category.

2046   The additional cut (on the 3rd leading jet) added here for the  $2b + 1j$  category was found  
 2047   to enhance the overall signal yield in the two bucket strategy relative to the single cut on  
 2048   leading jet  $p_T$  used for the same category in the resonant strategy.

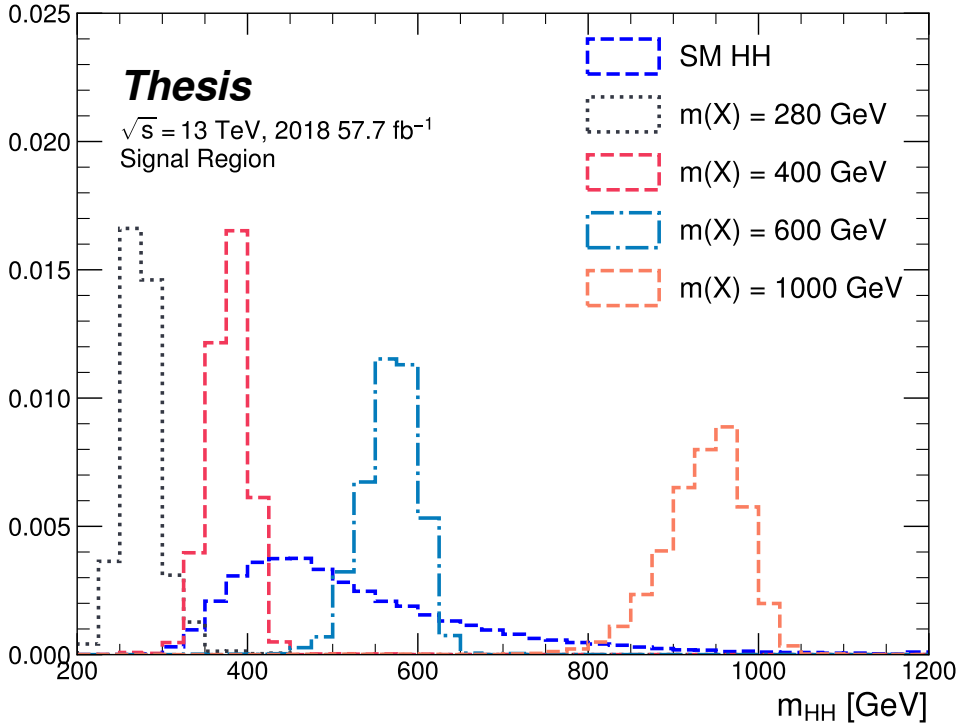


Figure 6.1: Example distributions in invariant mass of the reconstructed di-Higgs system for a variety of spin-0 resonances ( $m(X)$ ) compared to the Standard Model non-resonant signal (SM HH). Both are presented in their respective signal regions, after all corresponding analysis selections. The resonant signals are sharply peaked at values near their respective resonance masses, whereas the non-resonant signal is much more broad. The different character of these different signals informs the analysis design.

2049

## Chapter 7

2050

# ANALYSIS SELECTION

## 2051 7.1 Analysis Selection

2052 After the trigger selections of Section 6.2, a variety of selections on the analysis objects are  
 2053 made, with the goal of (1) reconstructing a  $HH$ -like topology and (2) suppressing contributions  
 2054 from background processes.

2055 Both analyses begin with a common pre-selection, requiring at least four  $R = 0.4$  anti- $k_T$   
 2056 jets with  $|\eta| < 2.5$  and  $p_T > 40 \text{ GeV}$ . The  $|\eta| < 2.5$  requirement is necessary for  $b$ -tagging  
 2057 due to the coverage of the ATLAS tracking detector (see Chapter 3), while the  $p_T > 40 \text{ GeV}$   
 2058 requirement is motivated by the trigger thresholds. A low  $p_T$  category, which would include  
 2059 events failing the analysis selection due to this  $p_T$  cut, was considered for the non-resonant  
 2060 search, but was found to contribute minimal sensitivity. At least two of the jets passing this  
 2061 pre-selection are required to be  $b$ -tagged, and additional  $b$ -tagging requirements are made to  
 2062 define the following regions:

- 2063 • “2 $b$  Region”: require exactly two  $b$ -tagged jets, used for background estimation
- 2064 • “4 $b$  Region”: require at least (but possibly more) four  $b$ -tagged jets, used as a signal  
 2065 region for both resonant and non-resonant searches

2066 The non-resonant analysis additionally defines two 3 $b$  regions:

- 2067 • “3 $b$ +1 loose Region”: require exactly three  $b$ -tagged jets which pass the 77 % b-tagging  
 2068 working point (nominal) and one additional jet that fails the 77 % b-tagging working  
 2069 point but passes the *looser* 85 % b-tagging working point. Used as a signal region for  
 2070 the non-resonant search.

- 2071     • “3 $b$ +1 fail Region”: complement of 3 $b$ +1 loose. Require exactly three  $b$ -tagged jets  
 2072       which pass the 77 % b-tagging working point, but require that none of the remaining jets  
 2073       pass the 85 % b-tagging working point. Used as a validation region for the non-resonant  
 2074       search.

2075   After these requirements, four jets are chosen, ranked first by  $b$ -tagging requirement and then  
 2076   by  $p_T$  (e.g. for the 2 $b$  region, the jets chosen are the two  $b$ -tagged jets and the two highest  $p_T$   
 2077   non-tagged jets; for the 4 $b$  region, the jets are the four highest  $p_T$   $b$ -tagged jets). To match  
 2078   the topology of a  $HH \rightarrow b\bar{b}b\bar{b}$  event, these four jets are then *paired* into *Higgs candidates*: the  
 2079   four jets are split into two sets of two, and each of these pairs is used to define a reconstructed  
 2080   object that is a proxy for a Higgs in a  $HH$  event. The four-vectors of these reconstructed  
 2081   objects may then be used for a variety of selections which check the consistency of the  
 2082   reconstructed  $HH$  system with the expected  $HH$  signal kinematics. Kinematic quantities  
 2083   corresponding to each Higgs candidate are denoted with subscripts  $H1$  and  $H2$  for leading  
 2084   and subleading Higgs candidates respectively (e.g.  $m_{H1}$  and  $m_{H2}$  for the Higgs candidate  
 2085   masses).

2086   For four jets there are three possible pairings of jets into Higgs candidates. For signal  
 2087   events, a correct pairing can be identified (provided all necessary jets pass pre-selection) using  
 2088   the truth information of the Monte Carlo simulation, and such information may be used to  
 2089   design/select an appropriate pairing algorithm. This is only part of the story, however. The  
 2090   vast majority of the events in data do *not* include a real  $HH$  decay (this is a search for a  
 2091   reason!), either because the event originates from a background process (e.g. for 4 $b$  events), or  
 2092   because the selection is not designed to maximize the signal (e.g. 2 $b$  events). As the pairing  
 2093   is part of the selection, it must still be run on such events, such that various algorithms which  
 2094   achieve similar performance in terms of pairing efficiency may have vastly different impacts in  
 2095   terms of the shape of the background and the biases inherent in the background estimation  
 2096   procedure. The interplay between these two facets of the pairing is an important part of the  
 2097   choices made for this analysis.

A comparison of different shapes due to three different paring strategies is shown in Figure 7.1. The Boosted Decision Tree (BDT) pairing and min  $\Delta R$  pairing are used for the analyses presented here, and are described in more detail below. The  $D_{HH}$  pairing was used for the early Run 2 searches [2], and is based on minimizing the quantity

$$D_{HH} = \frac{|m_{H1} - \frac{120}{110}m_{H2}|}{\sqrt{1 + \left(\frac{120}{110}\right)^2}}, \quad (7.1)$$

corresponding to the the distance of the reconstructed Higgs candidate masses from a line running from  $(0, 0)$  to the center of the signal region,  $(120 \text{ GeV}, 110 \text{ GeV})$  in leading and subleading Higgs candidate masses,  $(m_{H1}, m_{H2})$ . Note that while this achieves good pairing efficiency with respect to truth across a broad  $HH$  mass range, it significantly sculpts the mass plane (as seen in Figure 7.1), motivating the new approaches considered here.

### 7.1.1 Resonant Pairing Strategy

For the resonant analysis, a Boosted Decision Tree (BDT) is used for the pairing. The boosted decision tree is given the total separation between the two jets in each of the two pairs ( $\Delta R_1$  and  $\Delta R_2$ ), the pseudo-rapidity separation between the two jets in each pair ( $\Delta\eta_1$  and  $\Delta\eta_2$ ), and the angular separation between the two jets in each pair in the  $x - y$  plane ( $\Delta\phi_1$  and  $\Delta\phi_2$ ). The total separations ( $\Delta R_s$ ) are provided in addition to the components in order to avoid requiring the boosted decision tree to reconstruct these variables in order to use them. For these variables, pair 1 is the pair with the highest scalar sum of jet  $p_{\text{TS}}$ , and pair 2 the other pair.

The boosted decision tree is also parameterized on the di-Higgs mass ( $m_{HH}$ ) by providing this as an additional feature. Since the boosted decision tree is trained on correct and incorrect pairings in signal events, there will be exactly one correct pairing and two incorrect pairings in the training set for each  $m_{HH}$  value present in that set. As a result, this variable cannot, in itself, distinguish a correct pairing from an incorrect pairing, and therefore the

2117 inclusion of this variable simply serves to parameterize the BDT on  $m_{HH}$ <sup>1</sup>.

2118 The boosted decision tree was trained on one quarter of the total AFII simulated scalar  
 2119 MC statistics, using the Gradient-based One Side Sampling (GOSS) algorithm which allows  
 2120 rapid training with very large datasets. A preselection was applied requiring events to have  
 2121 four jets with a  $p_T$  of at least 35 GeV. Note that this is a looser requirement than the 40 GeV  
 2122 used in the analysis selection, and is meant to increase the available statistics for events with  
 2123 low  $m_{HH}$  and to ensure a better performance as a function of that variable. Events were also  
 2124 required to have four distinct jets that could be geometrically matched (to within  $\Delta R \leq 0.4$ )  
 2125 to the  $b$ -quarks. The events used to train the BDT were not included when the analysis was  
 2126 run on these signal simulations. The boosted decision tree was constructed with the following  
 2127 hyperparameters:

```
2128 min_data_in_leaf=50,  

2129 num_leaves=180,  

2130 learning_rate=0.01
```

2131 These hyperparameters were optimized using a Bayesian optimization procedure [105].  
 2132 Three fold cross-validation was used to perform this optimization without the need for an  
 2133 additional sample, while avoiding over-training on signal events.

### 2134 7.1.2 Non-resonant Pairing Strategy

2135 For the non-resonant analysis, a simpler pairing algorithm is used, which proceeds as follows:  
 2136 in a given event, Higgs candidates for each possible pairing are sorted by the  $p_T$  of the vector  
 2137 sum of constituent jets. The angular separation,  $\Delta R$  is computed between jets in the each of  
 2138 the leading Higgs candidates, and the pairing with the smallest separation ( $\Delta R_{jj}$ ) is selected.  
 2139 This method will be referred to as  $\min \Delta R$  in the following.

2140 The primary motivation for the use of this pairing in the non-resonant search is a *smooth*  
 2141 *mass plane*: by efficiently discarding low mass events,  $\min \Delta R$  removes the background peak

---

<sup>1</sup>That is, the conditions placed on the other variables by the BDT vary with  $m_{HH}$ .

2142 present in the resonant search while maintaining good pairing efficiency for the Standard  
2143 Model non-resonant signal. This facilitates a background estimate with small kinematic bias  
2144 – the region in which the background estimate is derived is more similar to the signal region.

2145 Along with discarding low mass background, there is a corresponding loss of low mass  
2146 signal. This predominantly impacts points away from the Standard Model (see Figure 7.2),  
2147 but, because the  $4b$  channel has the strongest contribution near the Standard Model and  
2148 because of the large low mass background present with other pairing methods, the impact on  
2149 analysis sensitivity is mitigated. The min  $\Delta R$  pairing is thus adopted for the non-resonant  
2150 search.

### 2151 7.1.3 Pairing Efficiencies

2152 Though this is implicit in the above descriptions, an explicit examination of the pairing  
2153 efficiencies with respect to truth for the respective signal samples has been performed for both  
2154 min  $\Delta R$  and the BDT pairing. Conceptually, for high invariant mass of the  $HH$  system, each  
2155 Higgs has a high  $p_T$  and the the  $b$ -jets corresponding to a given Higgs are more collimated.  
2156 In this case, angular information such as that exploited both directly by min  $\Delta R$  and as  
2157 inputs in the BDT pairing may be expected to be a good discriminant for determining the  
2158  $HH$  system. Indeed for resonance masses above 500 GeV, the pairing efficiency for both  
2159 algorithms is close to 100 %.

2160 For lower  $HH$  masses, the jets corresponding to a given Higgs are no longer as collimated,  
2161 such that min  $\Delta R$  is no longer guaranteed to pick up the correct pairing (e.g. in a case when  
2162 the four jets involved are isotropic), and the pairing efficiency steadily gets worse as the  $HH$   
2163 mass decreases. On resonant samples, e.g., the min  $\Delta R$  efficiency drops below 80 % near  
2164 400 GeV. The additional information exploited by the BDT mitigates this somewhat, though  
2165 there is still a drop in efficiency at lower  $m_{HH}$ . Interestingly, the BDT pairing demonstrates  
2166 a rise in pairing efficiency near the threshold of 250 GeV, likely due to the limited kinematic  
2167 phase space for the  $HH$  system in this region.

2168 The examination of the pairing efficiency as a function of  $m_{HH}$  has a more direct cor-

2169   respondecne for resonant samples, but it of course applies to non-resonant samples as well,  
2170   resulting in the behavior shown in Figure 7.2. Note that the above statement that  $\min \Delta R$   
2171   discards low mass events is a consequence of the reduced pairing efficiency at low mass – the  
2172   pairing algorithm itself does not make any cuts, but the mis-reconstruction of low mass signal  
2173   results in the reconstruction of Higgs candidates with masses away from 125 GeV, placing  
2174   such events outside of the kinematic signal regions defined in Section 7.3.

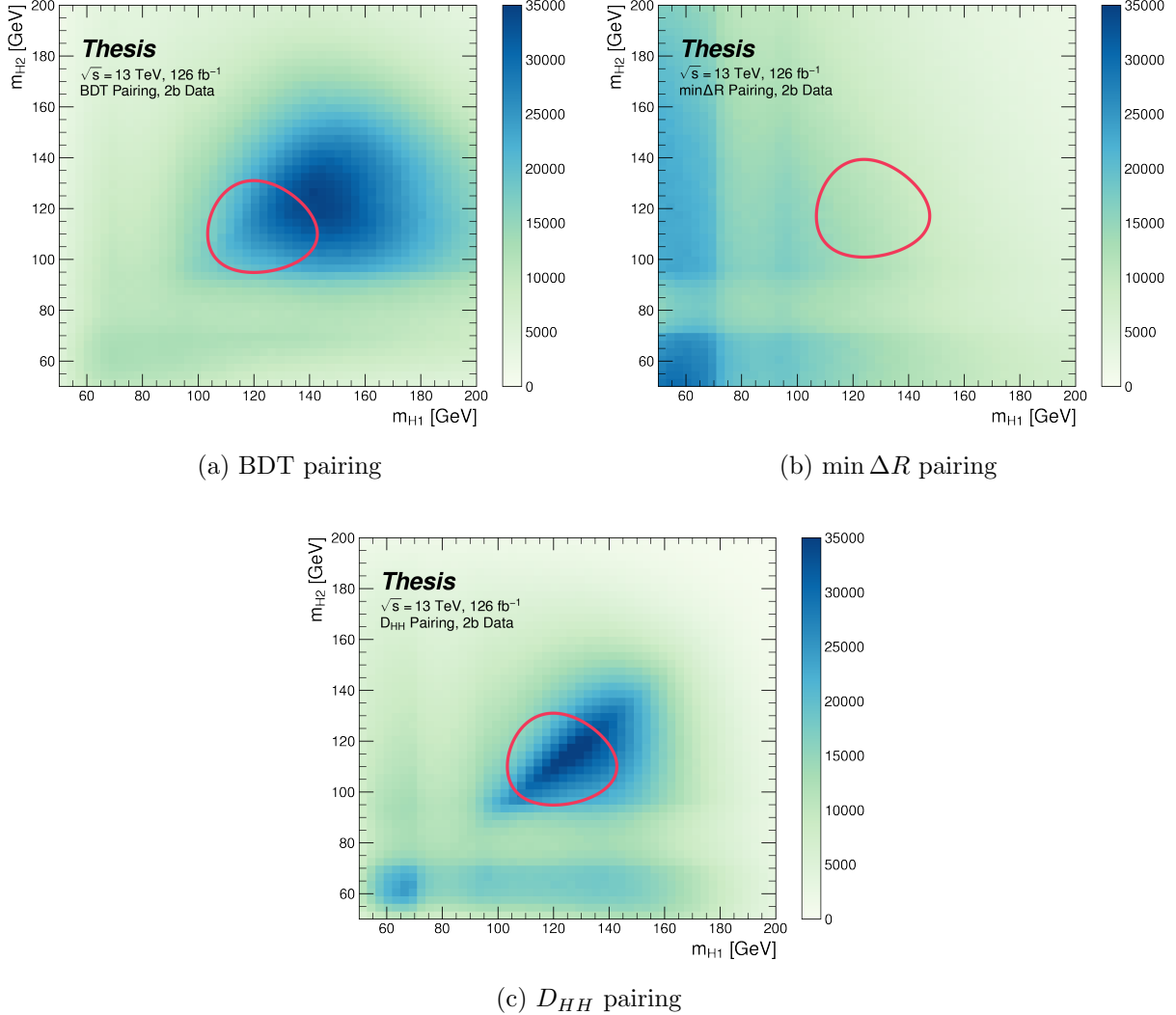


Figure 7.1: Comparison of  $m_{H1}$  vs  $m_{H2}$  planes for the full Run 2 2b dataset with different pairings, where  $m_{H1}$  and  $m_{H2}$  are the invariant masses of the leading and subleading Higgs candidates. As evidenced, this choice significantly impacts where events fall in this plane, and therefore which events fall into the various kinematic regions defined in this plane (see Section 7.3). The signal regions for the resonant/early Run 2 analysis are shown for reference for the BDT and  $D_{HH}$  pairings, while the the  $\min \Delta R$  signal region shifted is shifted slightly up and to the right to match the non-resonant selection. Note that the band structure around 80 GeV in both  $m_{H1}$  and  $m_{H2}$  is introduced by the top veto described in Section 7.2.

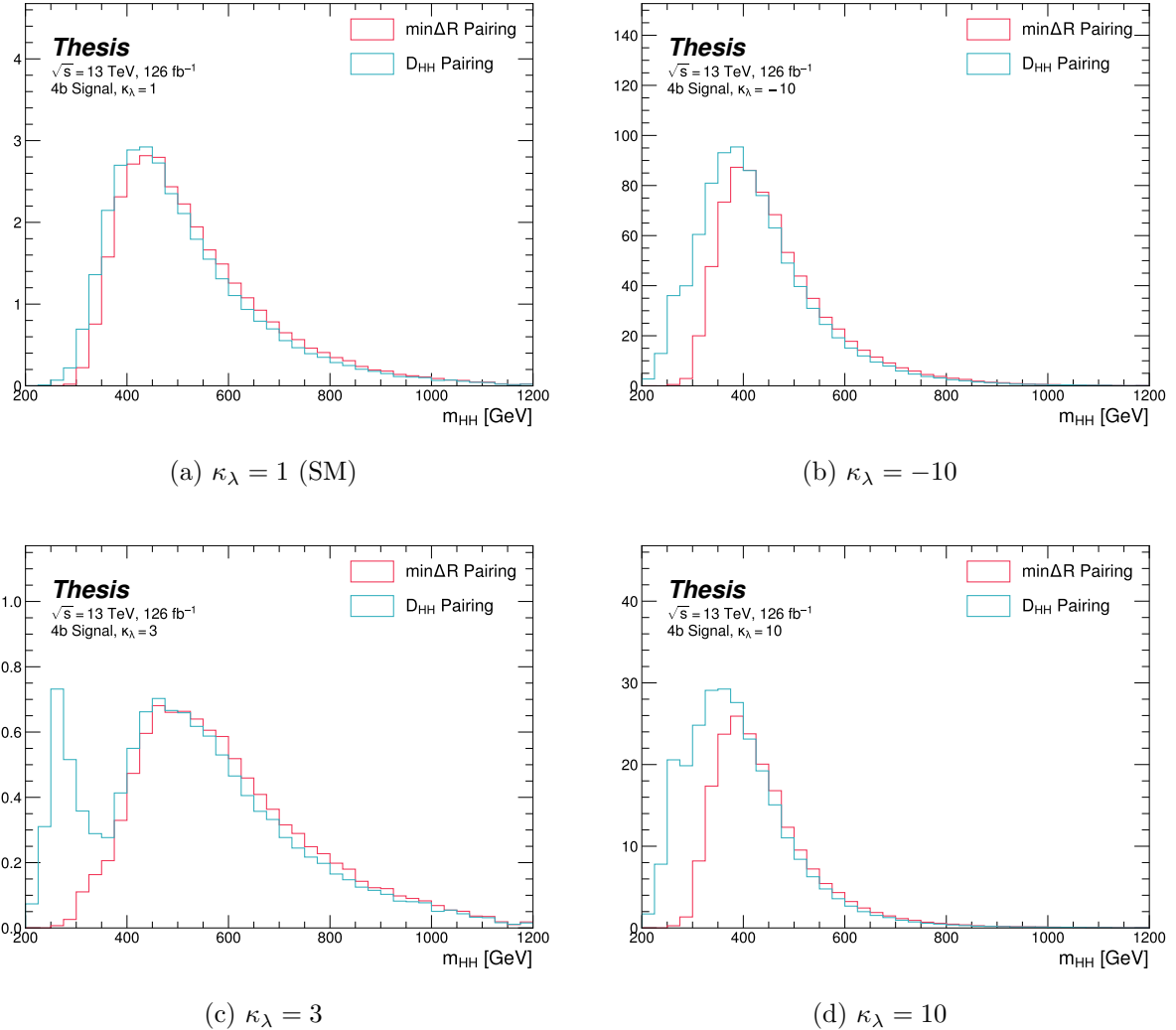


Figure 7.2: Comparison of signal distributions in the respective signal regions for the  $\text{min } \Delta R$  and  $D_{HH}$  pairing for various values of the Higgs trilinear coupling. The distributions are quite similar at the Standard Model point, but for other variations,  $\text{min } \Delta R$  does not pick up the low mass features.

2175 **7.2 Background Reduction and Top Veto**

2176 Choosing a pairing of the four b-tagged jets fully defines the di-Higgs candidate system used  
2177 for each event in the remainder of the analysis chain. A requirement of  $|\Delta\eta_{HH}| < 1.5$  on this  
2178 di-Higgs candidate system mitigates QCD multijet background.

2179 In order to mitigate the hadronic  $t\bar{t}$  background, a top veto is then applied, removing  
2180 events consistent with a  $t \rightarrow b(W \rightarrow q_1\bar{q}_2)$  decay.

2181 The jets in the event are separated into *HC jets* which are the four jets used to build the  
2182 Higgs candidates, and *non-*HC jets**, the other jets (passing the  $p_T$  and  $|\eta|$  requirements) in  
2183 the event.

2184  $W$  candidates are built by forming all possible pairs of all jets in each event. With  $n$  jets,  
2185 there are  $\binom{n}{2}$  such pairs.  $t$  candidates are then built by pairing each  $W$  candidate with each  
2186 HC jet (for  $4\binom{n}{2}$  combinations). Note that all jets in a  $t$  candidate must be distinct (i.e. a  
2187 HC jet may not be used both on its own and in a  $W$  candidate).

With  $m_t$  denoting the invariant mass of the  $t$  candidate, and  $m_W$  the invariant mass of the  $W$  candidate, the quantity

$$X_{Wt} = \sqrt{\left(\frac{m_W - 80.4 \text{ GeV}}{0.1 \cdot m_W}\right)^2 + \left(\frac{m_t - 172.5 \text{ GeV}}{0.1 \cdot m_t}\right)^2} \quad (7.2)$$

2188 is constructed for each combination.

2189 Events are then vetoed if the minimum  $X_{Wt}$  over all combinations is less than 1.5.

2190 The same definitions and procedures are used for both the resonant and non-resonant  
2191 analyses. However, for the non-resonant search, the top candidates considered for  $X_{Wt}$  have  
2192 the additional requirement that the jet used for the  $b$  is  $b$ -tagged. While this is identical to  
2193 the resonant analysis by definition for  $4b$  events, it does change the set of events considered in  
2194 lower tag regions, in particular for the  $2b$  events considered in the derivation of the background  
2195 estimate. Such a change is found to reduce the impact of background systematics, an effect  
2196 that is thought to be due to the shifting of  $2b$  events to higher values of  $X_{Wt}$  (due to this  
2197 more stringent requirement), where, e.g, the Standard Model signal peaks.

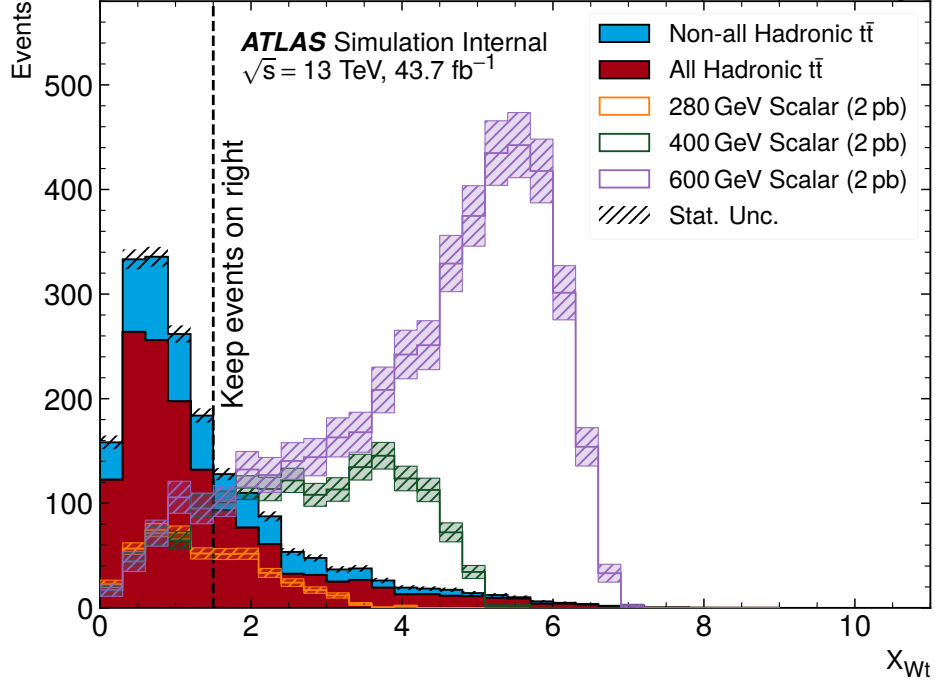


Figure 7.3: **Resonant search:** Illustration of the impact of the top veto on  $t\bar{t}$  Monte Carlo for the resonant analysis, with representative scalar signals shown for reference. The cut value used is 1.5, shown in the dashed black, and events below this value are discarded. This top veto clearly removes the bulk of  $t\bar{t}$  events, and the value of the cut is chosen to retain analysis sensitivity, particularly for low mass.

2198     The distribution of this variable is shown for  $t\bar{t}$  Monte Carlo and representative signal  
 2199   samples for the resonant and non-resonant 4 $b$  signal regions in Figures 7.3 and 7.4 respectively,  
 2200   with a line at the cut value of 1.5. Individual years are shown, but results are representative  
 2201   across years. For the resonant analysis, the value of the cut is constrained by low mass  
 2202   resonances, with the value of 1.5 chosen as a compromise between  $t\bar{t}$  rejection and retaining  
 2203   sensitivity for these signals. For the non-resonant, though e.g., the SM signal peaks at higher  
 2204   values, a more aggressive cut on  $X_{Wt}$  was found to decrease analysis sensitivity, so the value  
 2205   of 1.5 is kept.

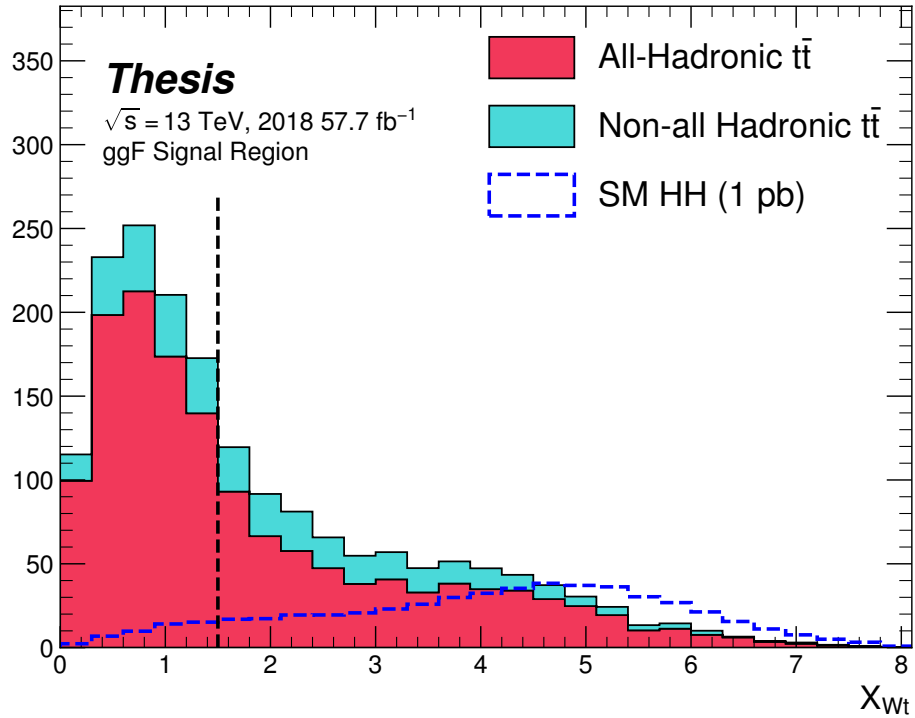


Figure 7.4: **Non-resonant search:** Illustration of the impact of the top veto on  $t\bar{t}$  Monte Carlo for the non-resonant analysis, with the Standard Model signal shown for reference. The cut value used is 1.5, shown in the dashed black, and events below this value are discarded. This top veto clearly removes the bulk of  $t\bar{t}$  events. While this plot may seem to motivate a more aggressive cut on  $X_{Wt}$ , increasing the value of the cut was found to reduce analysis sensitivity.

2206 **7.3 Kinematic Region Definition**

As has been mentioned, an important piece of the analysis is the plane defined by the two Higgs candidate masses (the *Higgs candidate mass plane*). After the selection described above, a signal region is defined by requiring  $X_{HH} < 1.6$ , where:

$$X_{HH} = \sqrt{\left(\frac{m(H_1) - c_1}{0.1 \cdot m(H_1)}\right)^2 + \left(\frac{m(H_2) - c_2}{0.1 \cdot m(H_2)}\right)^2} \quad (7.3)$$

2207 with  $m(H_1)$ ,  $m(H_2)$  the leading and subleading Higgs candidate masses,  $c_1$  and  $c_2$  correspond  
2208 to the center of the signal region, and the denominator provides a Higgs candidate mass  
2209 dependent resolution of 10 %. For consistency with the  $HH$  decay hypothesis,  $c_1$  and  $c_2$   
2210 are nominally (125 GeV, 125 GeV). However, these are allowed to vary due to energy loss,  
2211 with specific values chosen described below. The selection of these values is one of several  
2212 significant differences between the regions defined for the resonant and non-resonant search.  
2213 Both are described below.

2214 **7.3.1 Resonant Kinematic Regions**

2215 For the resonant analysis, the signal region is centered at (120 GeV, 110 GeV) to account for  
2216 energy loss leading to the Higgs masses being under-reconstructed. Note that leading and  
2217 subleading Higgs candidates are defined according to the *scalar sum* of constituent jet  $p_T$ .

For the background estimation, two regions are defined which are roughly concentric around the signal region: a *validation region* which consists of those events not in the signal region, but which do pass

$$\sqrt{(m(H_1) - 1.03 \times 120 \text{ GeV})^2 + (m(H_2) - 1.03 \times 110 \text{ GeV})^2} < 30 \text{ GeV} \quad (7.4)$$

and a *control region* which consists of those events not in the signal or validation regions, but which do pass

$$\sqrt{(m(H_1) - 1.05 \times 120 \text{ GeV})^2 + (m(H_2) - 1.05 \times 110 \text{ GeV})^2} < 45 \text{ GeV} \quad (7.5)$$

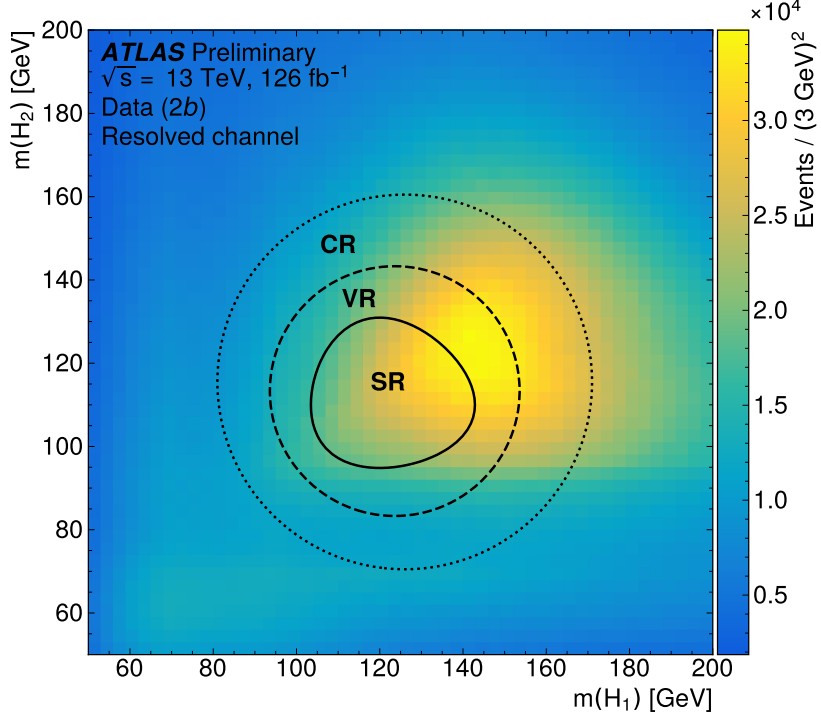


Figure 7.5: Regions used for the resonant search, shown on the  $2b$  data mass plane. The outermost region (the “control region”) is used for derivation of the nominal background estimate. The innermost region is the signal region, where the signal extraction fit is performed. The region in between (the “validation region”) is used for the assessment of an uncertainty.

<sup>2218</sup> For simplicity, the SR/VR/CR definitions from the early Run 2 paper [2] were chosen for  
<sup>2219</sup> the resonant analysis, and were found to be close to optimal. These regions are shown in  
<sup>2220</sup> Figure 7.5.

### <sup>2221</sup> 7.3.2 Non-resonant Kinematic Regions

<sup>2222</sup> For the non-resonant analysis the signal region is centered at (124 GeV, 117 GeV), corre-  
<sup>2223</sup> sponding to the means of *correctly paired* Standard Model signal events. The shape of the  
<sup>2224</sup> signal region (other than this change of center) was found to remain optimal.

2225 For the non-resonant search, leading and subleading Higgs candidates are defined according  
 2226 to the *vector sum* of constituent jet  $p_T$ , more closely corresponding to the  $1 \rightarrow 2$  decay  
 2227 assumption behind the min  $\Delta R$  pairing algorithm.

2228 Two areas for improvement were identified in the resonant analysis, which will be discussed  
 2229 in more detail below: *signal contamination* of the validation region (which impacts the  
 2230 uncertainty assessed due to extrapolation) and *large nuisance parameter pulls* for this  
 2231 uncertainty, corresponding to a rough assumption that the validation region is closer to the  
 2232 signal region in the mass plane, and so offers a better estimate of the signal region. Extensive  
 2233 cross-checks were performed for the resonant search, which demonstrated minimal bias due  
 2234 to the signal contamination and healthy behavior of the signal extraction fit, despite the  
 2235 large pulls. However, these large pulls imply that the nominal estimate may be improved by  
 2236 incorporating some of the information entering the definition of the extrapolation uncertainty.  
 2237 Further, the resonant search benefits from a set of highly peaked signals, such that the  
 2238 smooth nature of the background helps to mitigate signal contamination bias. With the  
 2239 broad non-resonant signals, a bias due to signal contamination becomes more of a concern,  
 2240 such that addressing this is highly motivated.

A redesign of the control and validation regions is therefore performed for the non-resonant analysis. The outer boundary defined by the shifted resonant control region:

$$\sqrt{(m(H_1) - 1.05 \times 124 \text{ GeV})^2 + (m(H_2) - 1.05 \times 117 \text{ GeV})^2} < 45 \text{ GeV} \quad (7.6)$$

2241 is kept, roughly corresponding to combining the regions used for the resonant analysis. In  
 2242 order to assess the variation of the background estimate, two sets of regions are desired, so  
 2243 this combined region is split into *quadrants*, that is, divided into four pieces along axes that  
 2244 intersect with the signal region center. To avoid kinematic bias, quadrants on opposite sides  
 2245 of the signal region are paired, with these pairs corresponding to the non-resonant control  
 2246 and validation regions.

2247 The particular orientation of the regions is chosen such that region centers align with the  
 2248 leading and subleading Higgs candidate masses, corresponding to a set of axes rotated at

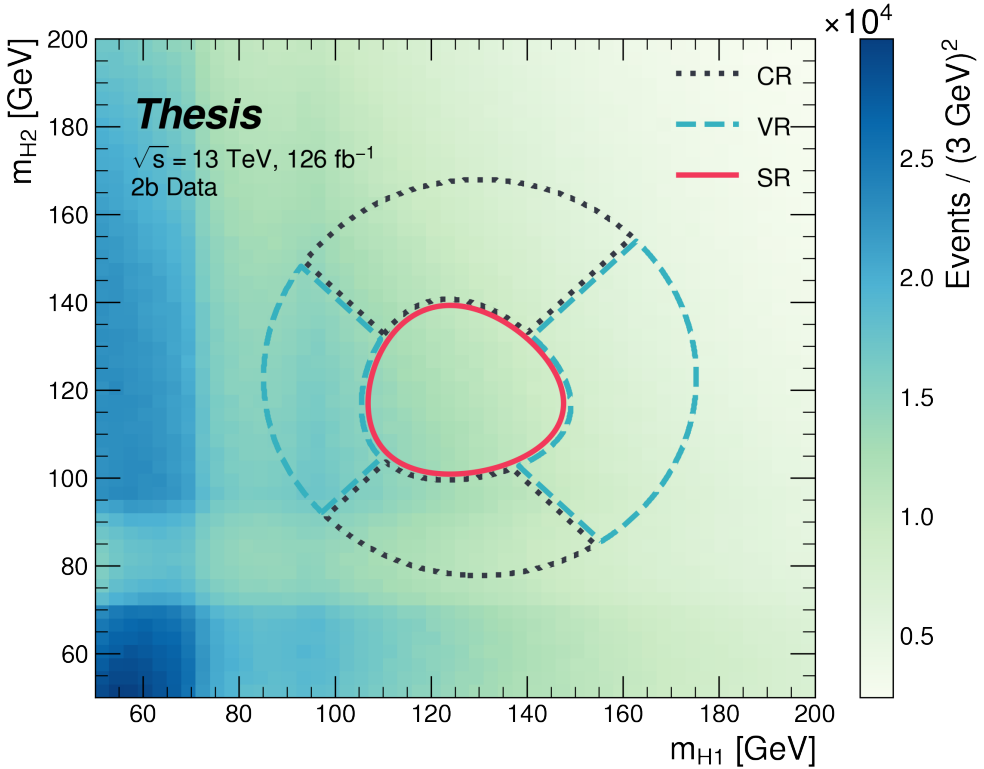


Figure 7.6: Regions used for the non-resonant search. The “top” and “bottom” quadrants together comprise the control region, in which the nominal background estimate is derived. The “left” and “right” quadrants together comprise the validation region, which is used to assess an uncertainty. The signal region, in the center, is where the signal extraction fit is performed.

2249    45°, with the “top” and “bottom” quadrants together comprising the control region, and the  
 2250    other set (“left” and “right”) the validation region. These regions are shown in Figure 7.6

2251    This design of regions includes a set of events closer to the signal region in the mass plane,  
 2252    leveraging the assumption that these events are more similar to signal region events, while  
 2253    also including events further away from the signal region, mitigating signal contamination.  
 2254    This region selection is found to have good performance in alternate validation regions (see  
 2255    Section 9.4).

2256      Figure 7.7 shows the signal acceptance times efficiency for the respective analysis selections  
2257 described above for spin-0, spin-2, and 4b Standard Model signals.

2258 **7.4 Discriminating Variable**

2259 The discriminant used for the resonant analysis is *corrected*  $m_{HH}$ . This variable is calculated  
2260 by re-scaling the Higgs candidate four vectors such that each  $m_H = 125$  GeV. These re-scaled  
2261 four-vectors are then summed, and their invariant mass is the corrected  $m_{HH}$ . These re-scaled  
2262 four-vectors are not used for any other purpose. The effect of this correction, which sharpens  
2263 the  $m_{HH}$  peak and correctly centers it, is shown in Figure 7.8.

2264      For the non-resonant analysis, due to the broad nature of the signal in  $m_{HH}$ , such a  
2265 correction is not as motivated, and, indeed, is found to have very minimal impact. The  
2266 uncorrected  $m_{HH}$  (just referred to as  $m_{HH}$ ) is therefore used as a discriminant. To maximize  
2267 sensitivity, the non-resonant analysis additionally uses two variables for categorization:  $\Delta\eta_{HH}$ ,  
2268 an angular variable which, along with  $m_{HH}$ , fully characterizes the  $HH$  system [106], and  
2269  $X_{HH}$ , the variable used for the signal region definition, which leverages the peaked structure  
2270 of the signal in the  $(m(H_1), m(H_2))$  plane to split the signal extraction fit into lower  
2271 and higher purity regions (highest purity near  $X_{HH} = 0$ , the center of the signal region).  
2272 The categorization used for this thesis has been optimized to be  $2 \times 2$  in these variables,  
2273 with corresponding selections  $0 \leq \Delta\eta_{HH} \leq 0.75$  and  $0.75 \leq \Delta\eta_{HH} \leq 1.5$  for  $\Delta\eta_{HH}$ , and  
2274  $0 \leq X_{HH} \leq 0.95$  and  $0.95 \leq X_{HH} \leq 1.6$  for  $X_{HH}$ .

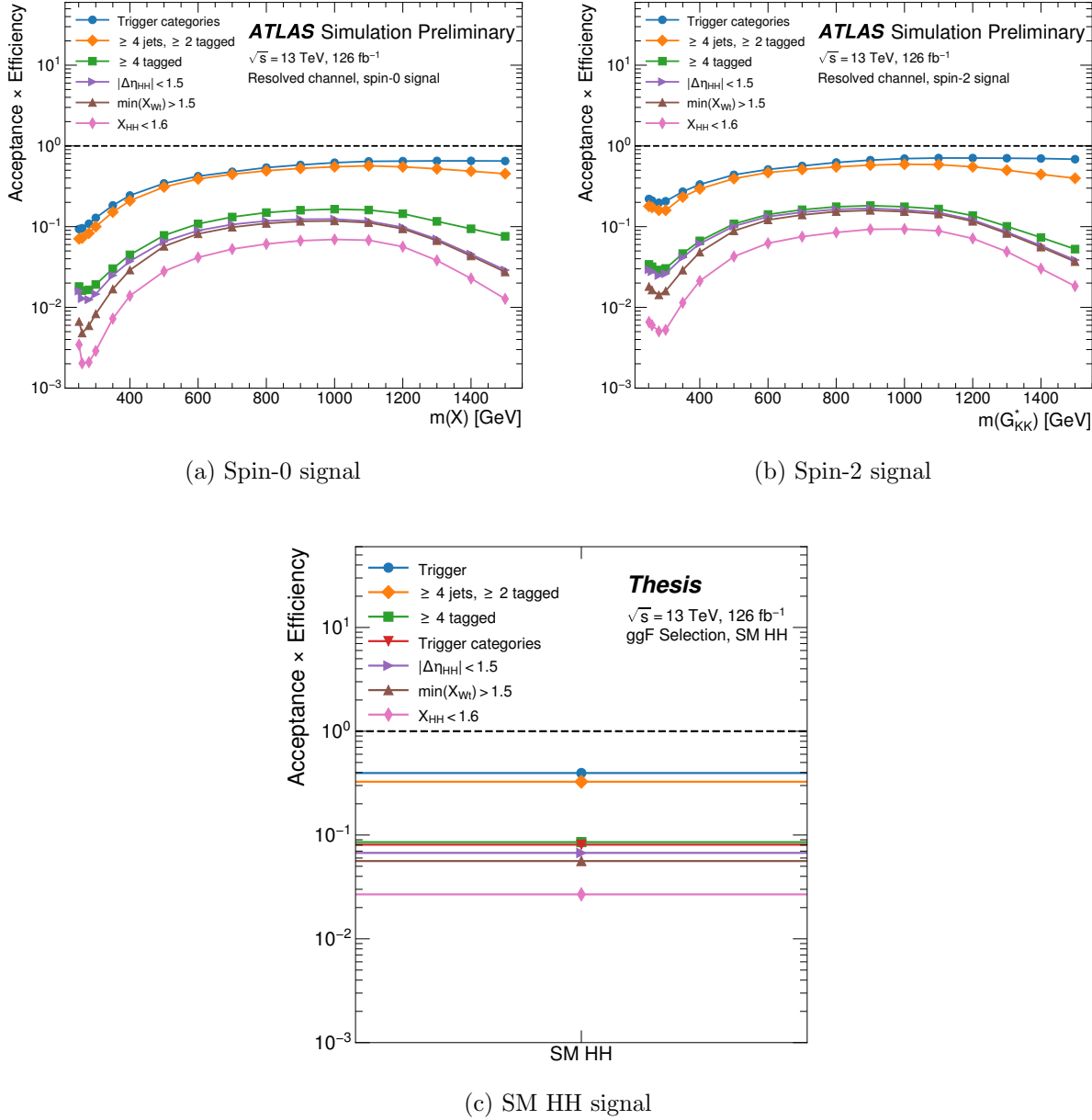


Figure 7.7: Acceptance times efficiency for the respective analysis selections for spin-0, spin-2, and 4*b* Standard Model signals. The Standard Model acceptance times efficiency is roughly consistent with the resonant signals in the mass range near the Standard Model peak (near 400 to 600 GeV). Acceptance times efficiency at low mass is mostly limited by the trigger, whereas for higher masses, the jets start to merge together, and the efficiency for reconstructing four *b*-tagged jets decreases. The spin-2 signal has a higher low mass acceptance times efficiency than spin-0 due to the broader signal distributions of this variable, which leads to a distortion of this distribution towards higher mass values. The increase in acceptance times efficiency at very low mass reflects the impact of the kinematic threshold of 250 GeV.

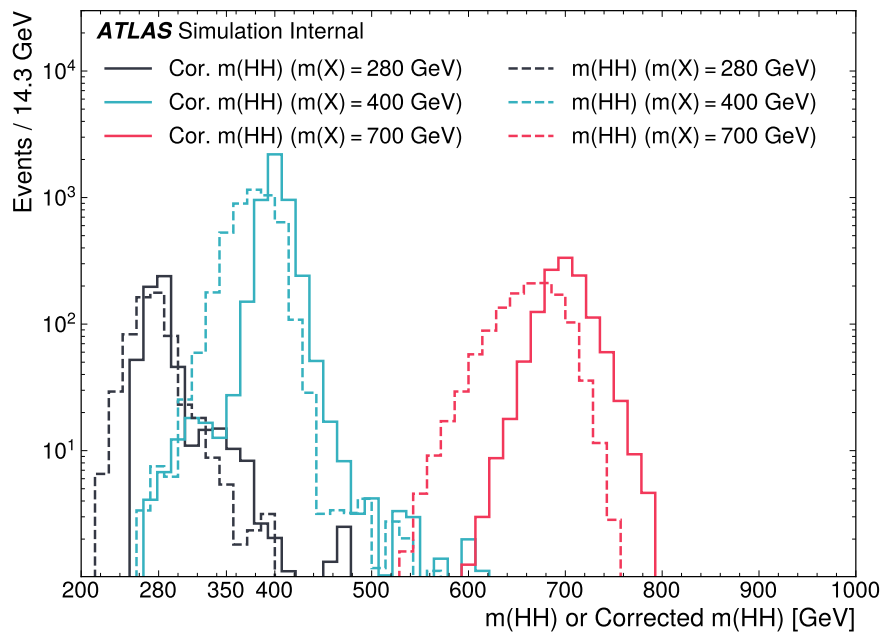


Figure 7.8: Impact of the  $m_{HH}$  correction on a range of spin-0 resonant signals. The corrected  $m_{HH}$  distributions (solid lines) are much sharper and more centered on the corresponding resonance masses than the uncorrected  $m_{HH}$  distributions (dashed).

2275

## Chapter 8

2276

### BACKGROUND ESTIMATION

2277 After the event selection described above, there are two major backgrounds, QCD and  $t\bar{t}$ .  
 2278 A very similar approach is used for both the resonant and the non-resonant analyses, with  
 2279 some small modifications. This approach is notably fully data-driven, which is warranted due  
 2280 to the flexibility of the estimation method, as well as the high relative proportion of QCD  
 2281 background ( $> 90\%$ ), and allows for the use of machine learning methods in the construction  
 2282 of the background estimate. However, it sacrifices an explicit treatment of the  $t\bar{t}$  component.  
 2283 Performance of the background estimate on the  $t\bar{t}$  component is checked explicitly, and  
 2284 minimal impact due to  $t\bar{t}$  mis-modeling is seen.

2285 Contributions of single Higgs processes and  $ZZ$  are found to be negligible, and the  
 2286 Standard Model  $HH$  background is found to have no impact on the resonant search.

2287 The foundation of the background estimate lies in the derivation of a reweighting function  
 2288 which matches the kinematics of events with exactly two  $b$ -tagged jets to those of events in  
 2289 the higher tagged regions (events with three or four  $b$ -tagged jets). The reweighting function  
 2290 and overall normalization are derived in the control region. Systematic bias of this estimate  
 2291 is assessed in the validation region.

2292 For the resonant analysis, the systematic bias is a bias due to extrapolation: the validation  
 2293 region lies between the control and signal regions. For the non-resonant analysis, the bias  
 2294 instead comes from different possible interpolations of the signal region kinematics – given the  
 2295 choice of nominal estimate, the validation region is a conceptually equivalent, but maximally  
 2296 different, signal region estimate.

2297 **8.1 The Two Tag Region**

2298 Events in data with exactly two b-tagged jets are used for the data driven background estimate.  
2299 The hypothesis here is that, due to the presence of multiple  $b$ -tagged jets, the kinematics of  
2300 such events are similar to the kinematics of events in higher b-tagged regions (i.e. events  
2301 with three and four  $b$ -tagged jets, respectively), and any differences can be corrected by a  
2302 reweighting procedure. The region with three  $b$ -tagged jets is split into two  $b$ -tagging regions,  
2303 as described in Section 7.1, with the  $3b + 1$  loose region used as an additional signal region.  
2304 The lower tagged  $3b$  component ( $3b + 1$  fail) is reserved for validation of the background  
2305 modelling procedure. Events with fewer than two  $b$ -tagged jets are not used for this analysis,  
2306 as they are relatively more different from the higher tag regions.

2307 The nominal event selection requires at least four jets in order to form Higgs candidates.  
2308 For the four tag region, these are the four highest  $p_T$   $b$ -tagged jets. For the three tag regions,  
2309 these jets are the three  $b$ -tagged jets, plus the highest  $p_T$  jet satisfying a loosened  $b$ -tagging  
2310 requirement. Similarly, and following the approach of the resonant analysis, the two tag region  
2311 uses the two  $b$ -tagged jets and the two highest  $p_T$  non-tagged jets to form Higgs candidates.  
2312 Combinatoric bias from selection of different numbers of  $b$ -tagged jets is corrected as a part  
2313 of the kinematic reweighting procedure through the reweighting of the total number of jets in  
2314 the event. In this way, the full event selection may be run on two tagged events.

2315 **8.2 Kinematic Reweighting**

2316 The set of two tagged data events is the fundamental piece of the data driven background  
2317 estimate. However, kinematic differences from the four tag region exist and must be corrected  
2318 in order for this estimate to be useful. Binned approaches based on ratios of histograms  
2319 have been previously considered [2], [22], but are limited in their handling of correlations  
2320 between variables and by the ‘‘curse of dimensionality’’, i.e. the dataset becomes sparser and  
2321 sparser in ‘‘reweighting space’’ as the number of dimensions in which to reweight increases,  
2322 limiting the number of variables used for reweighting. This leads either to an unstable fit

2323 result (overfitting with finely grained bins) or a lower quality fit result (underfitting with  
2324 coarse bins).

2325 Note that even some machine learning methods such as Boosted Decision Trees (BDTs) [107],  
2326 may suffer from this curse of dimensionality, as the depth of each decision tree used is limited  
2327 by the available statistics after each set of corresponding selections (cf. binning in a more  
2328 sophisticated way), limiting the expressivity of the learned reweighting function.

2329 To solve these issues, a neural network based reweighting procedure is used here. This  
2330 is a truly multivariate approach, allowing for proper treatment of variable correlations. It  
2331 further overcomes the issues associated with binned approaches by learning the reweighting  
2332 function directly, allowing for greater sensitivity to local differences and helping to avoid the  
2333 curse of dimensionality.

### 2334 8.2.1 Neural Network Reweighting

Let  $p_{4b}(x)$  and  $p_{2b}(x)$  be the probability density functions for four and two tag data respectively across some input variables  $x$ . The problem of learning the reweighting function between two and four tag data is then the problem of learning a function  $w(x)$  such that

$$p_{2b}(x) \cdot w(x) = p_{4b}(x) \quad (8.1)$$

from which it follows that

$$w(x) = \frac{p_{4b}(x)}{p_{2b}(x)}. \quad (8.2)$$

This falls into the domain of density ratio estimation, for which there are a variety of approaches. The method considered here is modified from [108, 109], and depends on a loss function of the form

$$\mathcal{L}(R(x)) = \mathbb{E}_{x \sim p_{2b}}[\sqrt{R(x)}] + \mathbb{E}_{x \sim p_{4b}}\left[\frac{1}{\sqrt{R(x)}}\right]. \quad (8.3)$$

where  $R(x)$  is some estimator dependent on  $x$  and  $\mathbb{E}_{x \sim p_{2b}}$  and  $\mathbb{E}_{x \sim p_{4b}}$  are the expectation values with respect to the 2b and 4b probability densities. A neural network trained with

such a loss function has the objective of finding the estimator,  $R(x)$ , that minimizes this loss. It is straightforward to show that

$$\arg \min_R \mathcal{L}(R(x)) = \frac{p_{4b}(x)}{p_{2b}(x)} \quad (8.4)$$

2335 which is exactly the form of the desired reweighting function.

In practice, to avoid imposing explicit positivity constraints, the substitution  $Q(x) \equiv \log R(x)$  is made. The loss function then takes the equivalent form

$$\mathcal{L}(Q(x)) = \mathbb{E}_{x \sim p_{2b}} [\sqrt{e^{Q(x)}}] + \mathbb{E}_{x \sim p_{4b}} \left[ \frac{1}{\sqrt{e^{Q(x)}}} \right], \quad (8.5)$$

with solution

$$\arg \min_Q \mathcal{L}(Q(x)) = \log \frac{p_{4b}(x)}{p_{2b}(x)}. \quad (8.6)$$

2336 Taking the exponent then results in the desired reweighting function.

2337 Note that similar methods for density ratio estimation are available [110], e.g. from a  
2338 more standard binary cross-entropy loss. However, these were found to perform no better  
2339 than the formulation presented here.

### 2340 8.2.2 Variables and Results

2341 The neural network is trained on a variety of variables sensitive to two vs. four tag differences.  
2342 To help bring out these differences, the natural logarithm of some of the variables with a  
2343 large, local change is taken. The set of training variables used for the resonant analysis is

2344 1.  $\log(p_T)$  of the 4th leading Higgs candidate jet

2345 2.  $\log(p_T)$  of the 2nd leading Higgs candidate jet

2346 3.  $\log(\Delta R)$  between the closest two Higgs candidate jets

2347 4.  $\log(\Delta R)$  between the other two Higgs candidate jets

2348 5. Average absolute value of  $\eta$  across the four Higgs candidate jets

- 2349     6.  $\log(p_T)$  of the di-Higgs system.
- 2350     7.  $\Delta R$  between the two Higgs candidates
- 2351     8.  $\Delta\phi$  between the jets in the leading Higgs candidate
- 2352     9.  $\Delta\phi$  between the jets in the subleading Higgs candidate
- 2353     10.  $\log(X_{Wt})$ , where  $X_{Wt}$  is the variable used for the top veto
- 2354     11. Number of jets in the event.
- 2355     The non-resonant analysis uses an identical set of variables with two notable changes
- 2356       1. The definition of  $X_{Wt}$  differs from the resonant definition (as described in Section 7.2).
- 2357       2. An integer encoding of the two trigger categories is used as an input (variable which  
2358           takes on the value 0 or 1 corresponding to each of the two categories). This was found  
2359           to improve a mis-modeling near the tradeoff in  $m_{HH}$  of the two buckets.
- 2360     The neural network used for both resonant and non-resonant reweighting has three densely  
2361     connected hidden layers of 50 nodes each with ReLU activation functions and a single node  
2362     linear output. This configuration demonstrates good performance in the modelling of a variety  
2363     of relevant variables, including  $m_{HH}$ , when compared to a range of networks of similar size.
- 2364     In practice, a given training of the reweighting neural network is subject to variation  
2365     due to training statistics and initial conditions. An uncertainty is assigned to account for  
2366     this (Chapter 9), which relies on training an ensemble of reweighting networks [111]. To  
2367     increase the stability of the background estimate, the median of the predicted weight for each  
2368     event is calculated across the ensemble. This median is then used as the nominal background  
2369     estimate. This approach is indeed seen to be much more stable and to demonstrate a better  
2370     overall performance than a single arbitrary training. Each ensemble used for this analysis  
2371     consists of 100 neural networks, trained as described in Chapter 9.

2372 The training of the ensemble used for the nominal estimate is done in the kinematic  
 2373 Control Region. The prediction of these networks in the Signal Region is then used for the  
 2374 nominal background estimate. In addition, a separate ensemble of networks is trained in the  
 2375 Validation Region. The difference between the prediction of the nominal estimate and the  
 2376 estimate from the VR derived networks in the Signal Region is used to assign a systematic  
 2377 uncertainty. Further details on this systematic uncertainty are discussed in Chapter 9. Note  
 2378 that although the same procedure is used for both Control and Validation Region trained  
 2379 networks, only the median estimate from the VR derived reweighting is used for assessing a  
 2380 systematic – no additional “uncertainty on the uncertainty” from VR ensemble variation is  
 2381 applied.

2382 Each reweighted estimate is normalized such that the reweighted  $2b$  yield matches the  $4b$   
 2383 yield in the corresponding training region. Note that this applies to each of the networks used  
 2384 in each ensemble, where the normalization factor is also subject to the procedure described  
 2385 in Chapter 9. As the median over these normalized weights is not guaranteed to preserve this  
 2386 normalization, a further correction is applied such that the  $2b$  yield, after the median weights  
 2387 are applied, matches the  $4b$  yield in the corresponding training region. As no pre-processing  
 2388 is applied to correct for the class imbalance between  $2b$  and  $4b$  events entering the training,  
 2389 this ratio of number of  $4b$  events ( $n(4b)$ ) over number of  $2b$  events ( $n(2b)$ ) is folded into the  
 2390 learned weights. Correspondingly, the set of normalization factors described above is near 1  
 2391 and the learned weights are centered around  $n(4b)/n(2b)$  (roughly 0.01 over the full dataset).  
 2392 This normalization procedure applies for all instances of the reweighting (e.g. those used for  
 2393 validations in Section 9.4), with appropriate substitutions of reweighting origin (here  $2b$ ) and  
 2394 reweighting target (here  $4b$ ).

2395 Note that, due to different trigger and pileup selections during each year, the reweighting  
 2396 is trained on each year separately. An approach of training all of the years together with  
 2397 a one-hot encoding was explored, but was found to have minimal benefit over the split  
 2398 years approach, and in fact to increase the systematic bias of the corresponding background  
 2399 estimate. Because of this, and because trigger selections for each year significantly impact

2400 the kinematics of each year, such that categorizing by year is expected to reflect groupings  
 2401 of kinematically similar events and to provide a meaningful degree of freedom in the signal  
 2402 extraction fit, the split-year approach is kept.

2403 The control region closure for the 2018 dataset is shown for a large variety of variables for  
 2404 the resonant search in Figures 8.1 through 8.9 and for the non-resonant search in Figures  
 2405 8.10 through 8.18 for 4b and Figures 8.19 through 8.27 for 3b1l. The impact of this control  
 2406 region derived reweighting in the validation region for the same set of variables is included in  
 2407 Appendix C. Demonstration of the performance of the reweighting on the final discriminant  
 2408 distributions is included in Chapter 10. 2018 is chosen because it is the largest subset of  
 2409 the data on which the year-by-year reweighting is trained. The other years are omitted here  
 2410 for brevity, but demonstrate very similar results. Generally good performance is seen, with  
 2411 some occasional mis-modeling. For the resonant search, this is most notable in the case of  
 2412 individual jet  $p_T$ . Such mis-modeling may be corrected by including the variables in the input  
 2413 set, but this was found to not improve the modeling of  $m_{HH}$ , and so is not done here. This  
 2414 mis-modeling is notable for the non-resonant search in the leading Higgs candidate jet  $p_T$ ,  
 2415 and is a direct consequence of the trigger category input, which improves modeling of  $m_{HH}$ .  
 2416 Results are similar for other years, but are not included here for brevity.

2417 One other salient feature of the non-resonant plots is the distributions of  $m_{H1}$  and  $m_{H2}$ ,  
 2418 which emphasize the quadrant region definitions – the control region has a peak around  
 2419 125 GeV in  $m_{H1}$ , which may be thought of as “signal region-like”, motivating this alignment,  
 2420 though consequently the distribution of  $m_{H2}$  is quite bimodal. The reverse is true for the  
 2421 validation region.

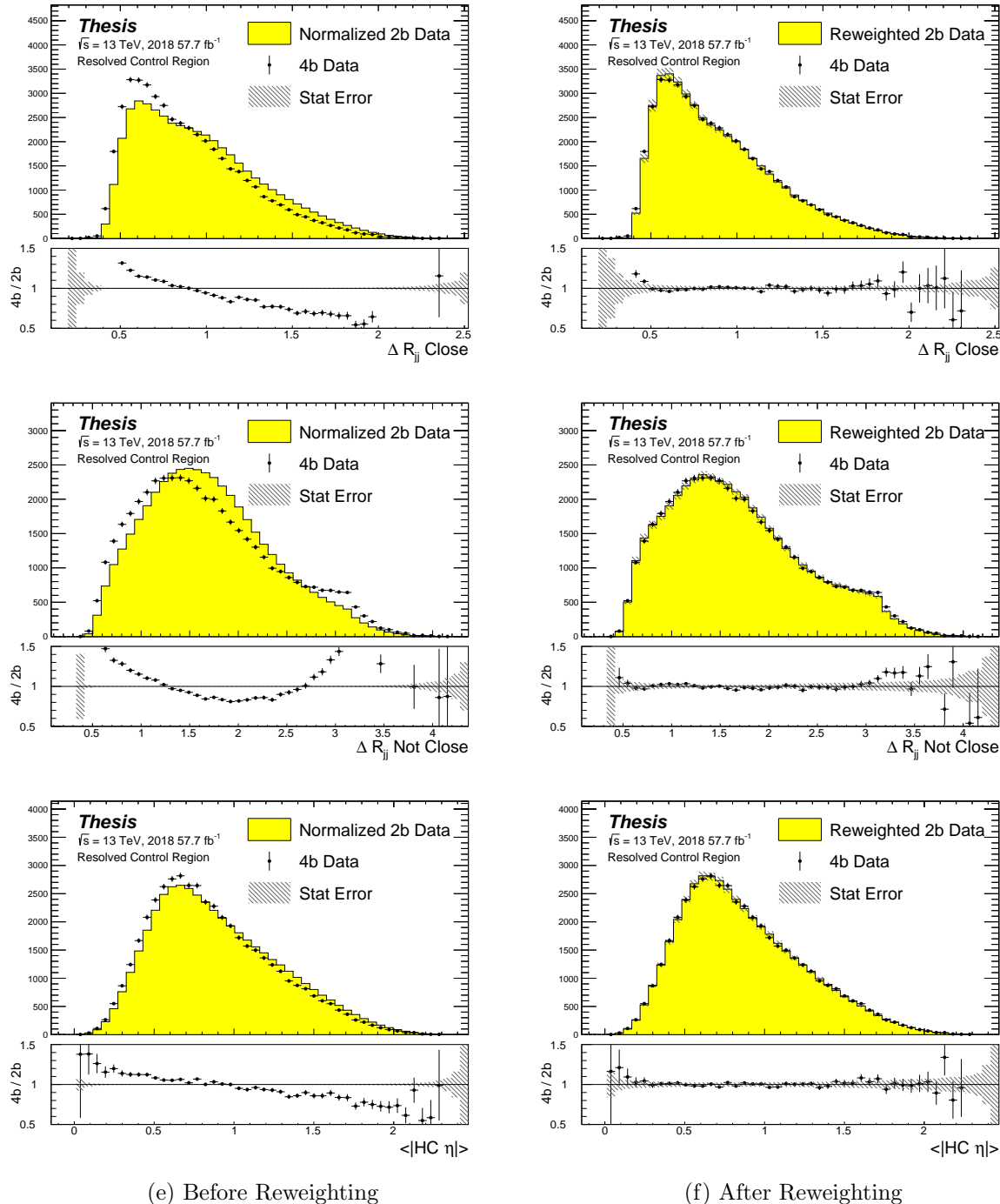


Figure 8.1: **Resonant Search:** Distributions of  $\Delta R$  between the closest Higgs Candidate jets,  $\Delta R$  between the other two, and average absolute value of HC jet  $\eta$  before (left) and after (right) CR derived reweighting for the 2018 Control Region.

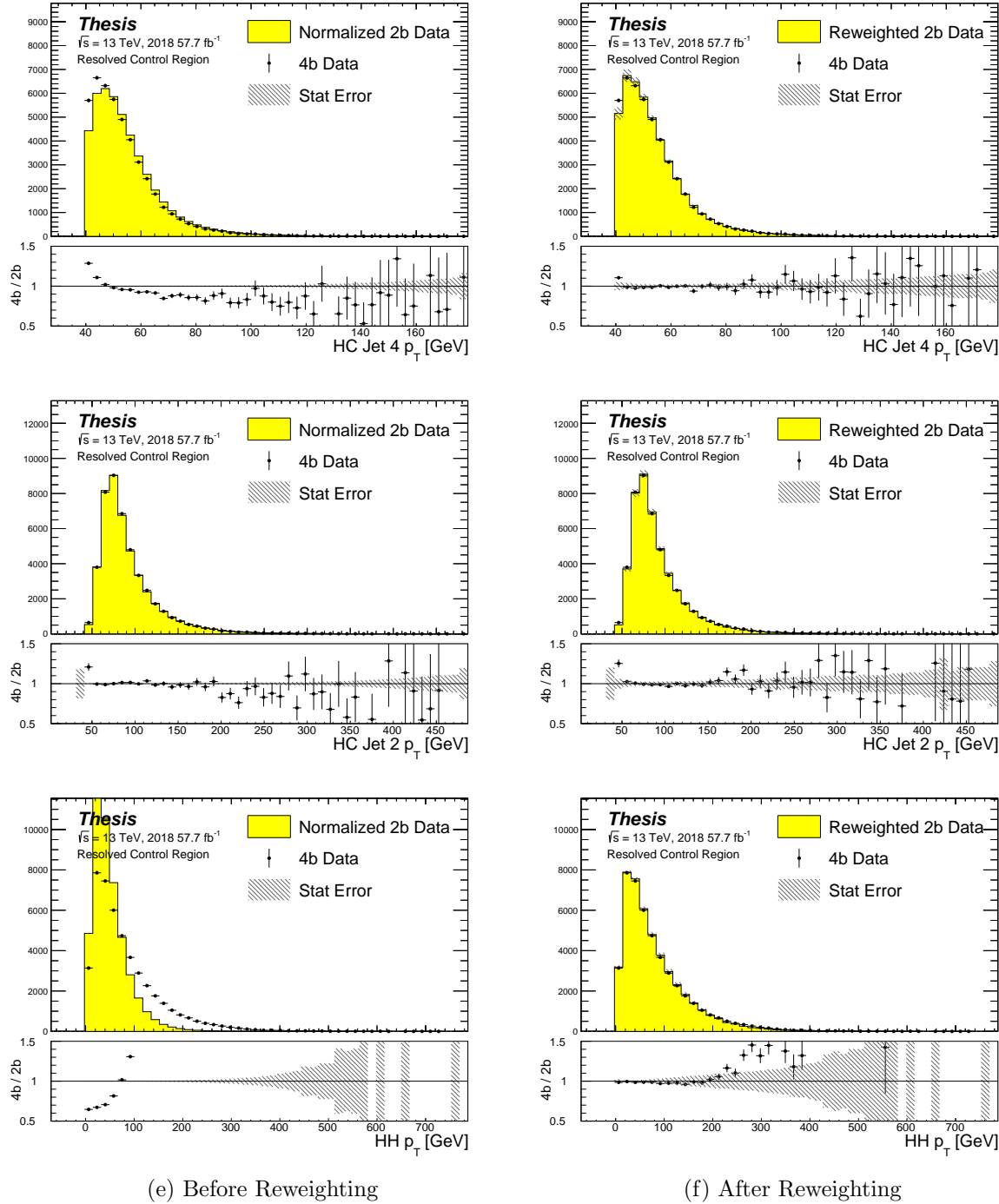


Figure 8.2: **Resonant Search:** Distributions of  $p_T$  of the 2nd and 4th leading Higgs Candidate jets and the  $p_T$  of the di-Higgs system before (left) and after (right) CR derived reweighting for the 2018 Control Region.

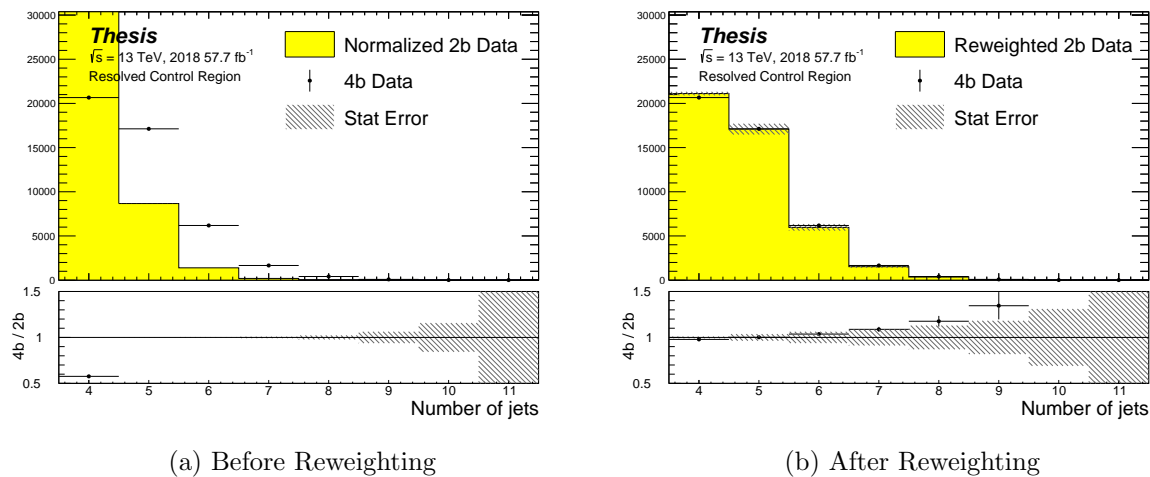


Figure 8.3: **Resonant Search:** Distributions of the number of jets before (left) and after (right) CR derived reweighting for the 2018 Control Region. A minimum of 4 jets is required in each event in order to form Higgs candidates.

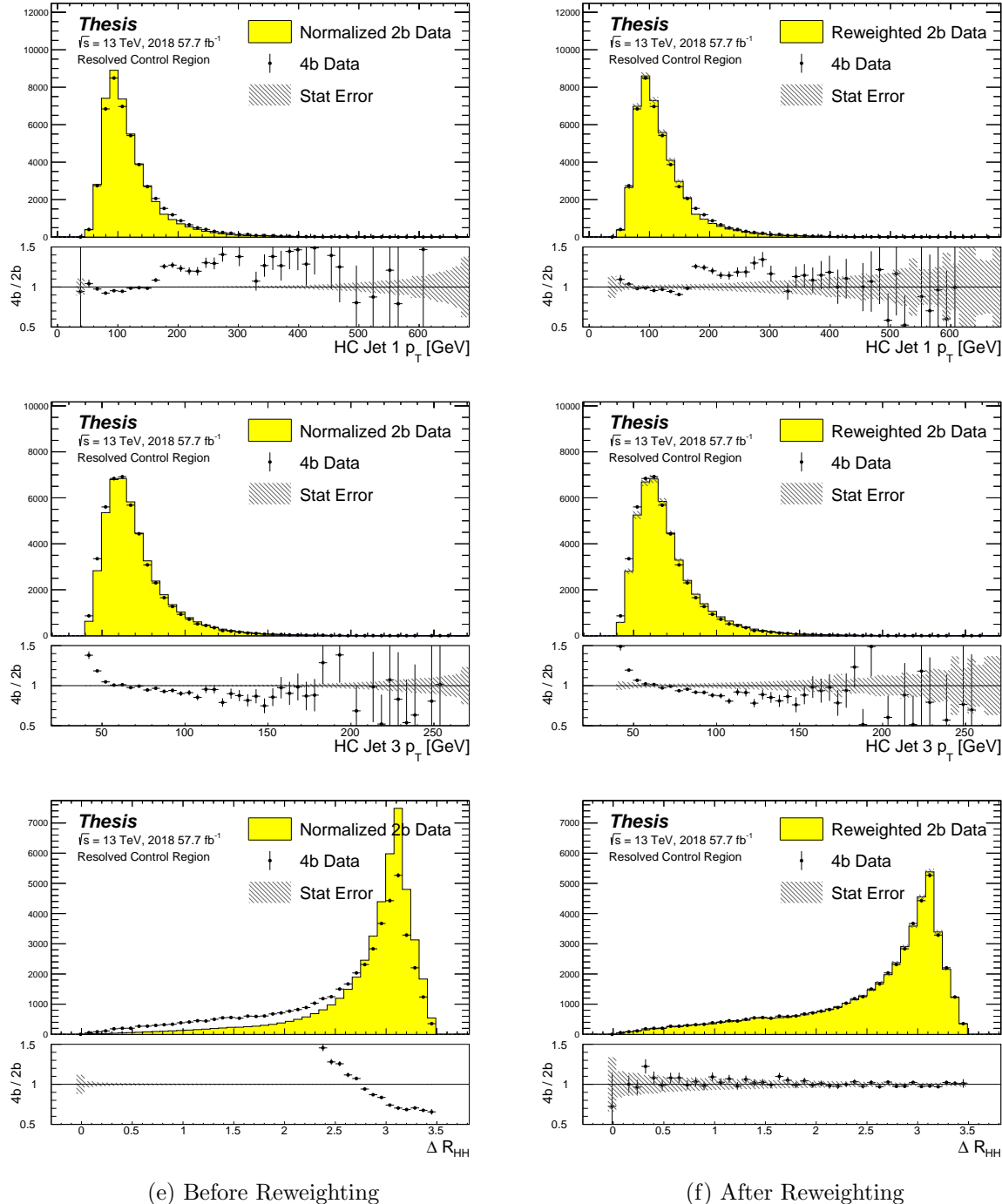


Figure 8.4: **Resonant Search:** Distributions of  $p_T$  of the 1st and 3rd leading Higgs Candidate jets and  $\Delta R$  between Higgs candidates before (left) and after (right) CR derived reweighting for the 2018 Control Region.

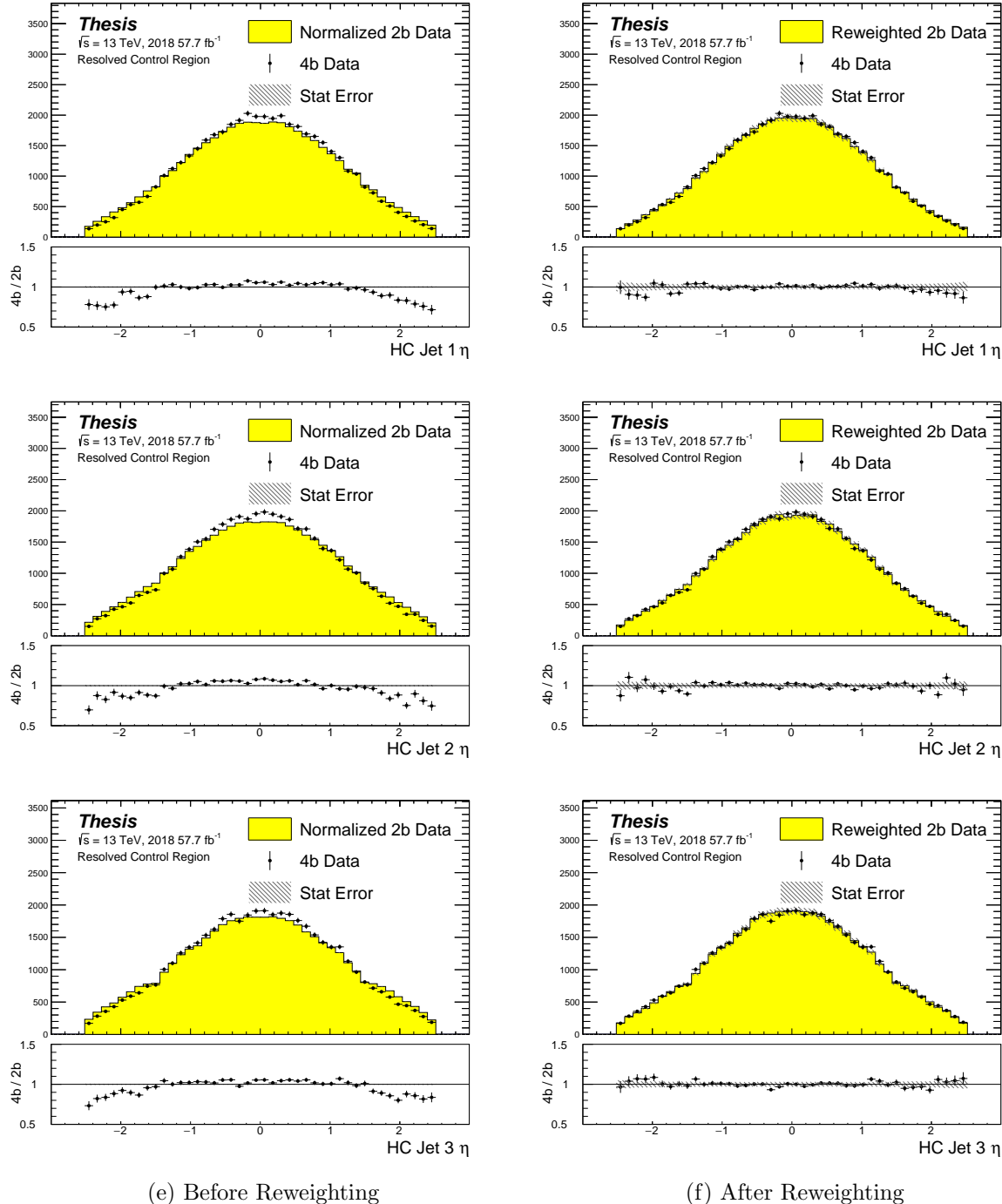


Figure 8.5: **Resonant Search:** Distributions of  $\eta$  of the 1st, 2nd, and 3rd leading Higgs Candidate jets before (left) and after (right) CR derived reweighting for the 2018 Control Region.

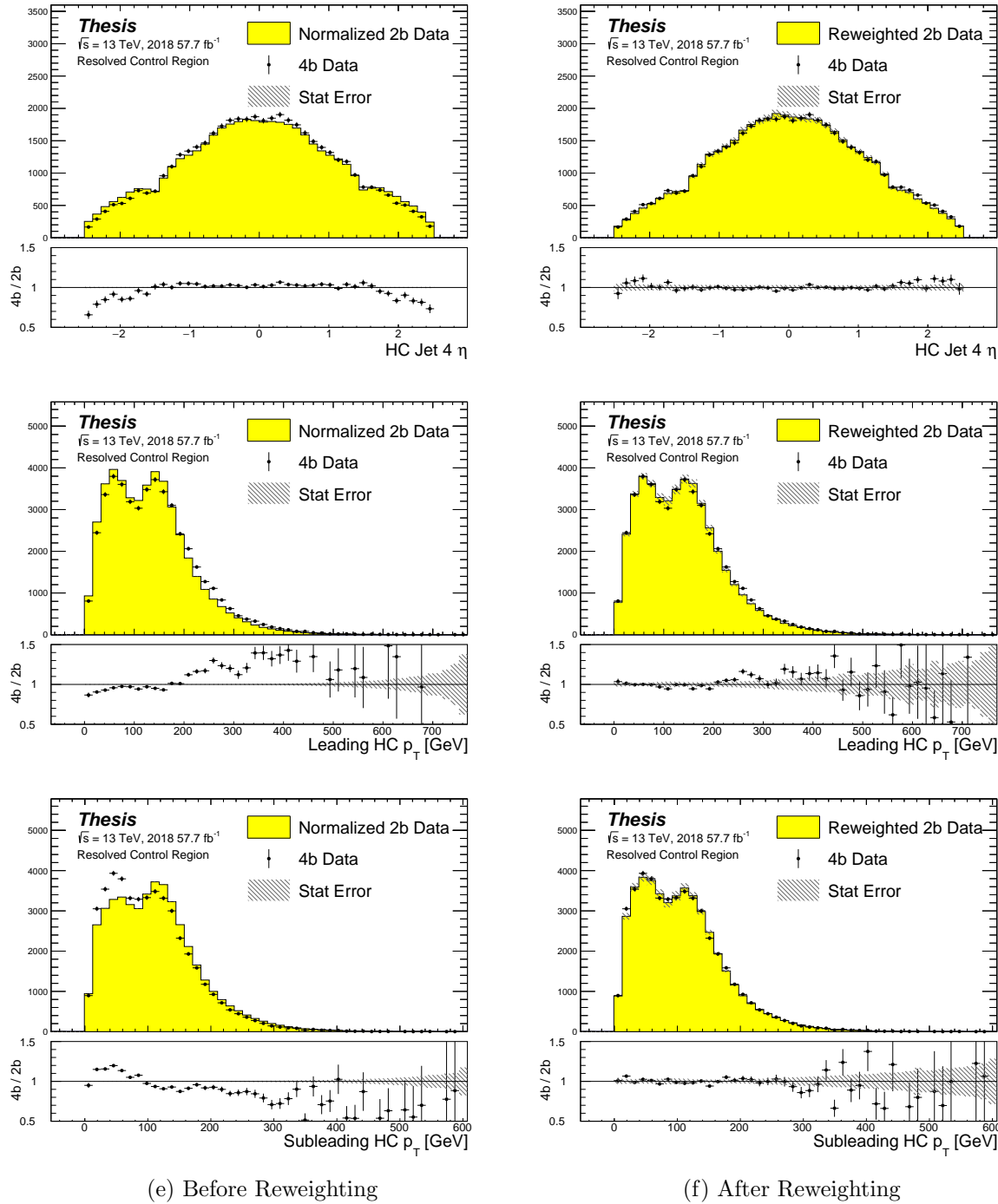


Figure 8.6: **Resonant Search:** Distributions of  $\eta$  of the 4th leading Higgs Candidate jet and the  $p_T$  of the leading and subleading Higgs candidates before (left) and after (right) CR derived reweighting for the 2018 Control Region.

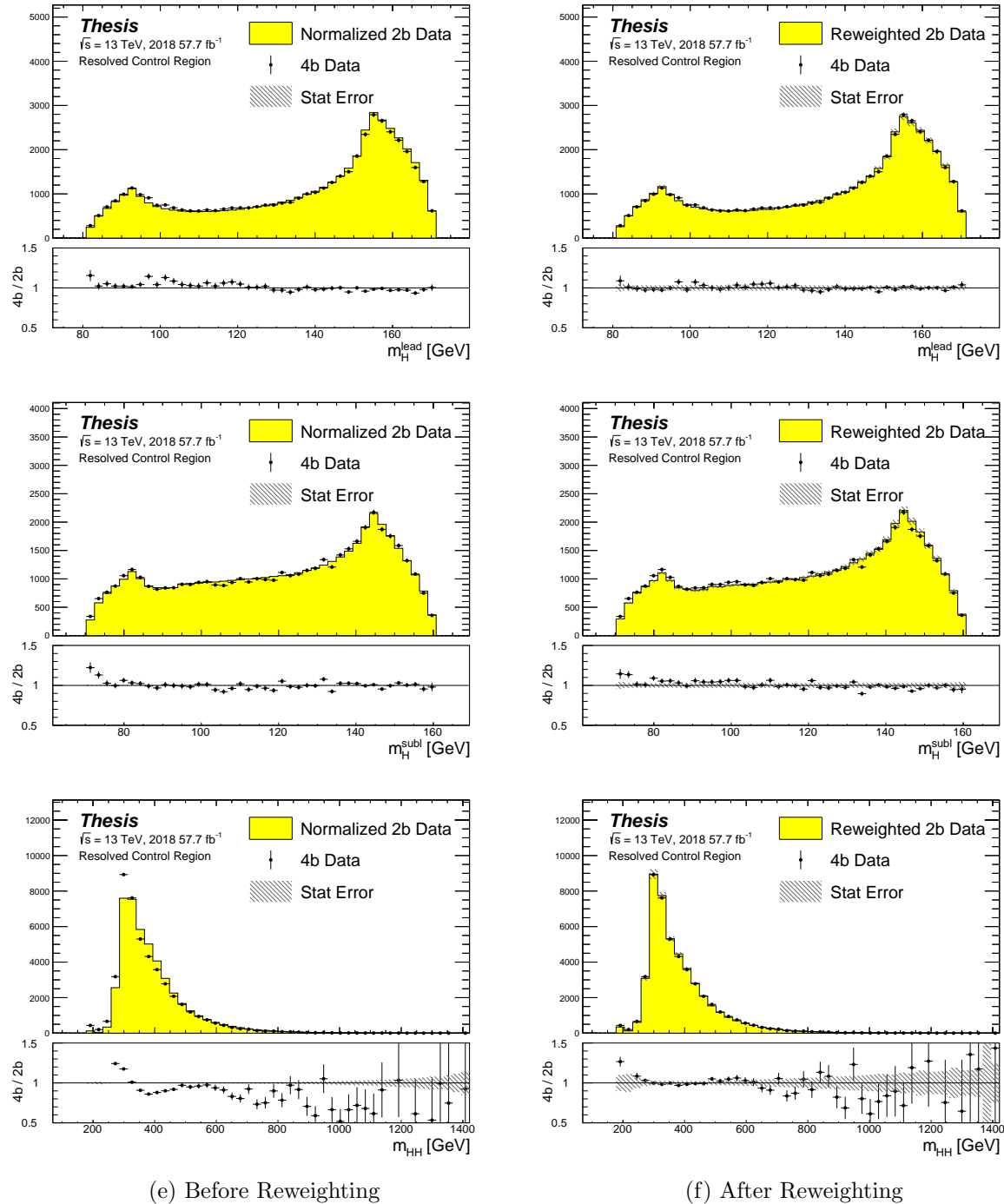


Figure 8.7: **Resonant Search:** Distributions of mass of the leading and subleading Higgs candidates and of the di-Higgs system before (left) and after (right) CR derived reweighting for the 2018 Control Region.

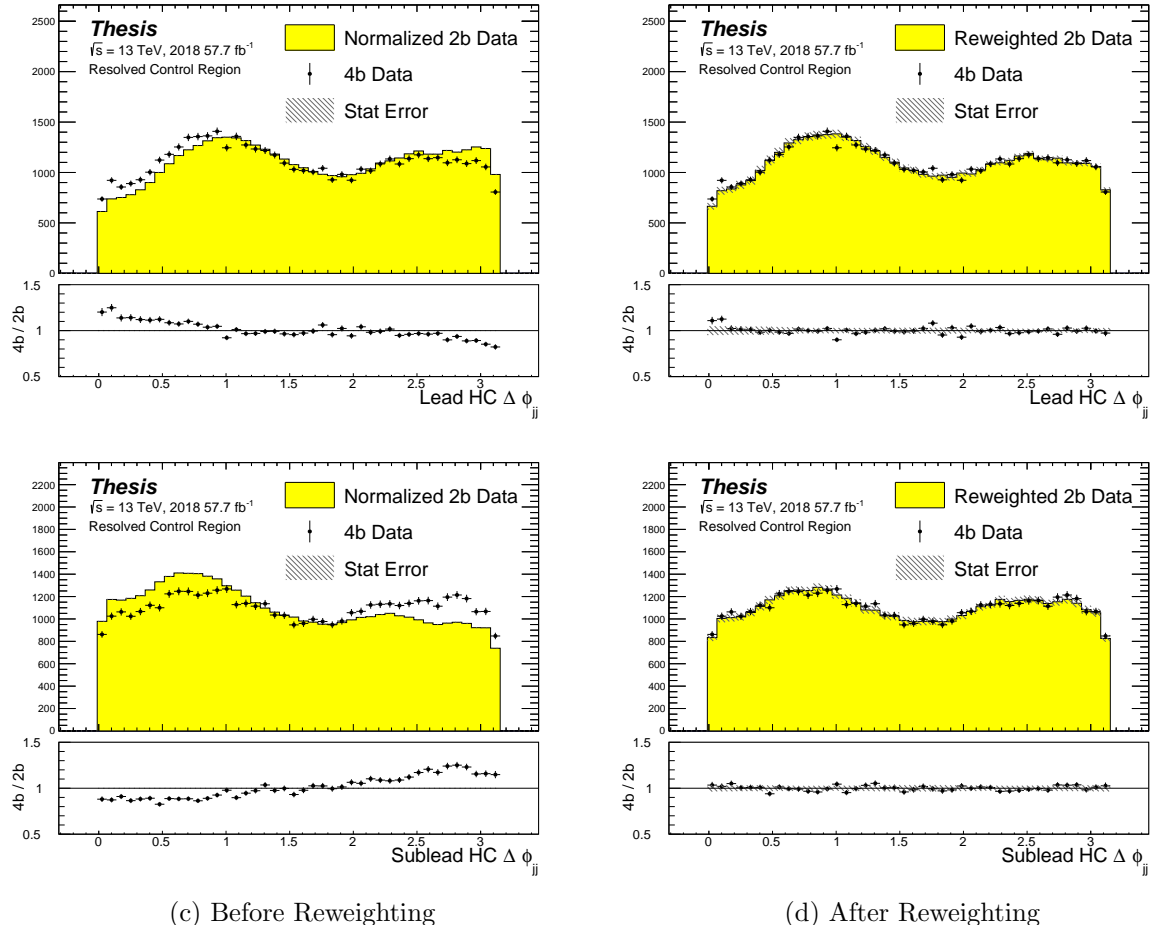


Figure 8.8: **Resonant Search:** Distributions of  $\Delta\phi$  between jets in the leading and subleading Higgs candidates before (left) and after (right) CR derived reweighting for the 2018 Control Region.

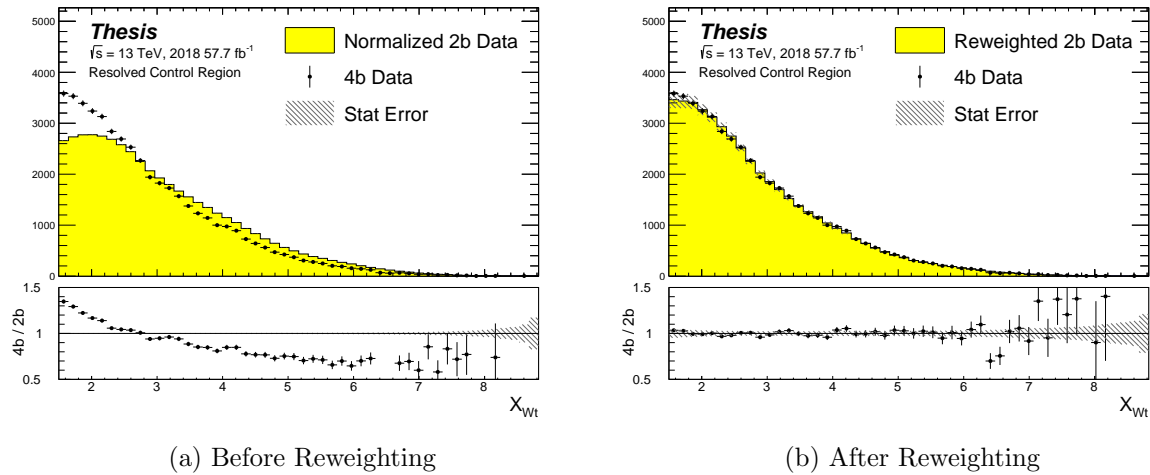


Figure 8.9: **Resonant Search:** Distributions of the top veto variable,  $X_{Wt}$ , before (left) and after (right) CR derived reweighting for the 2018 Control Region. Reweighting is done after the cut on this variable is applied

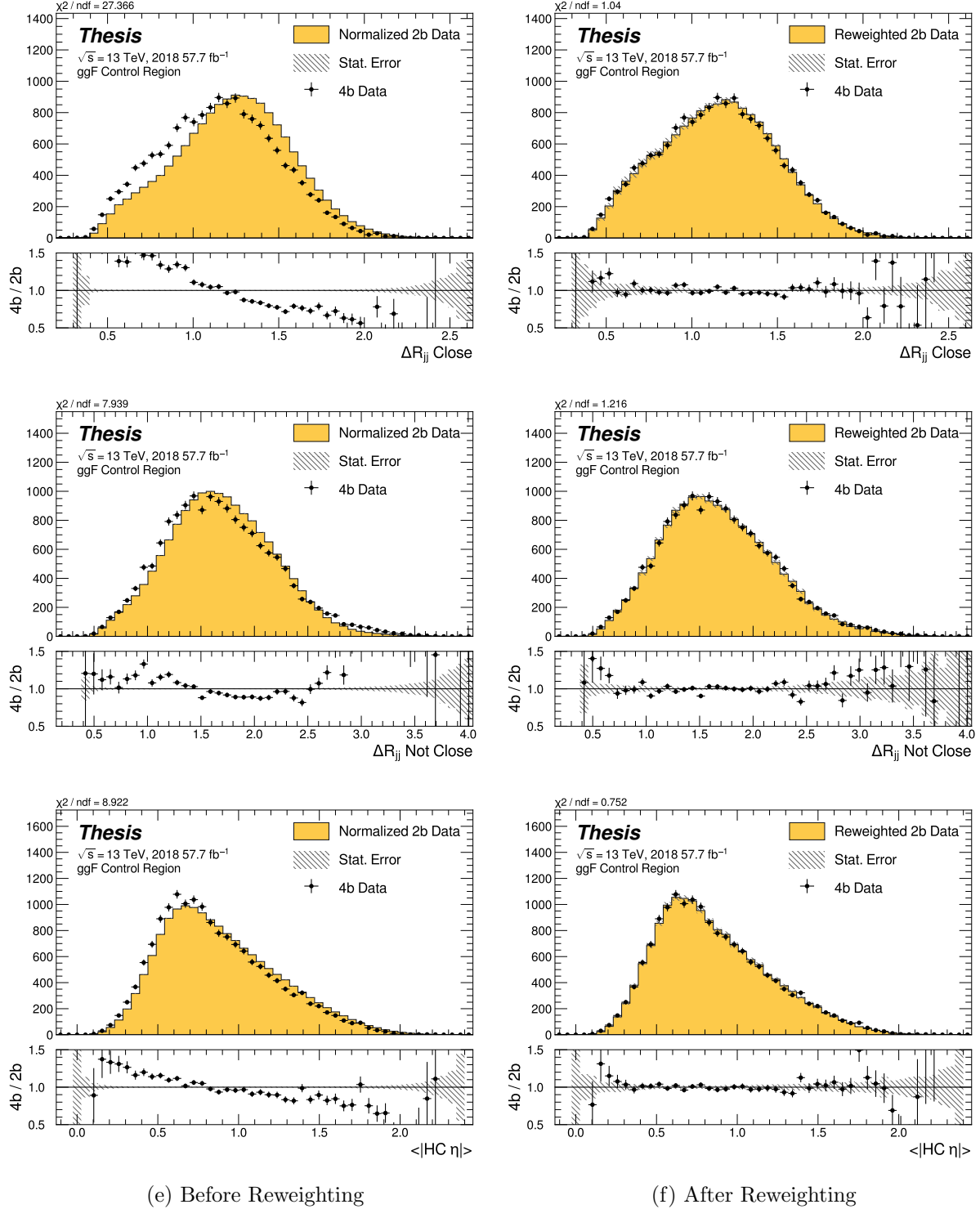


Figure 8.10: **Non-resonant Search (4b):** Distributions of  $\Delta R$  between the closest Higgs Candidate jets,  $\Delta R$  between the other two, and average absolute value of HC jet  $\eta$  before (left) and after (right) CR derived reweighting for the 2018 4b Control Region.

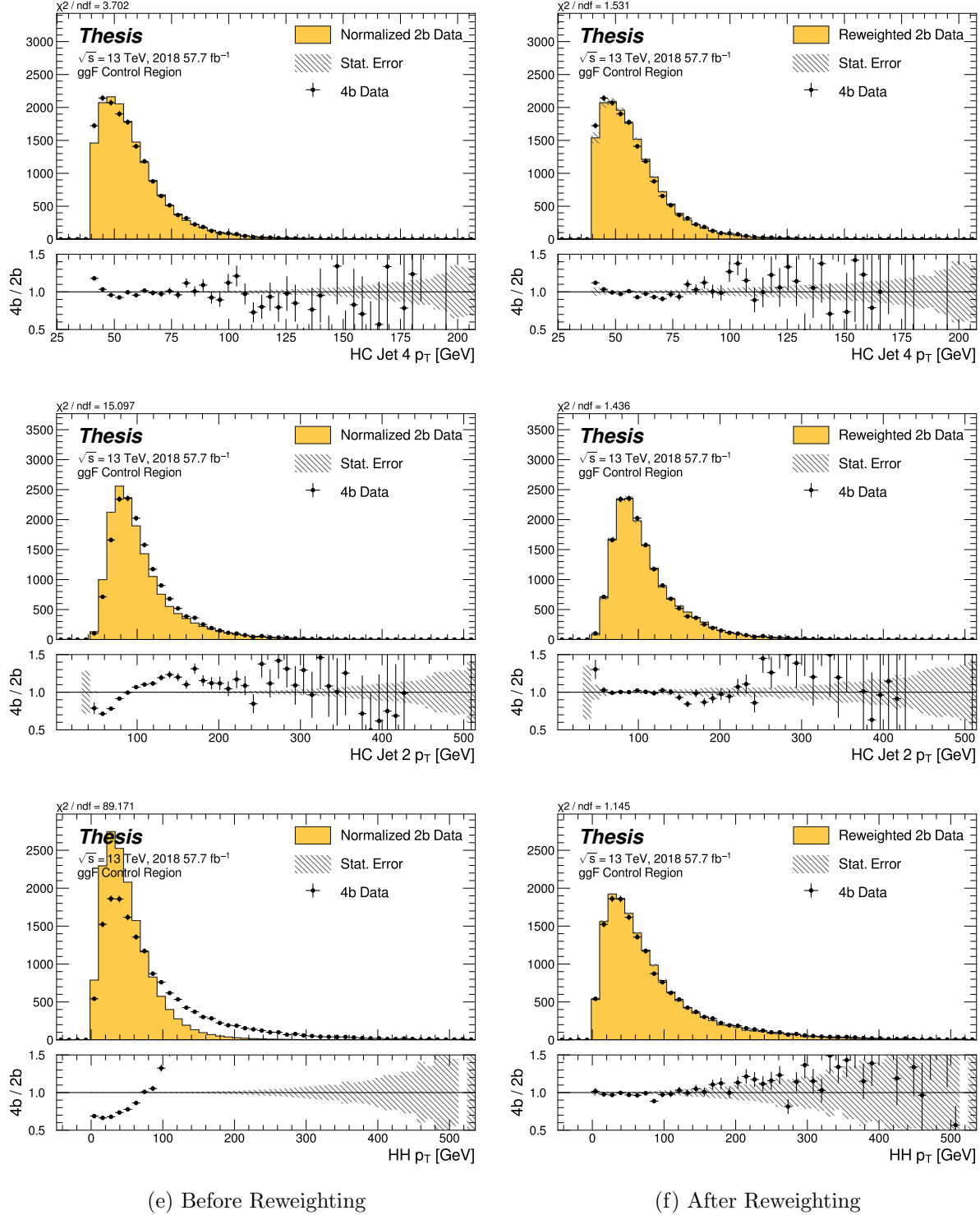


Figure 8.11: **Non-resonant Search (4b):** Distributions of  $p_T$  of the 2nd and 4th leading Higgs Candidate jets and the  $p_T$  of the di-Higgs system before (left) and after (right) CR derived reweighting for the 2018 4b Control Region.

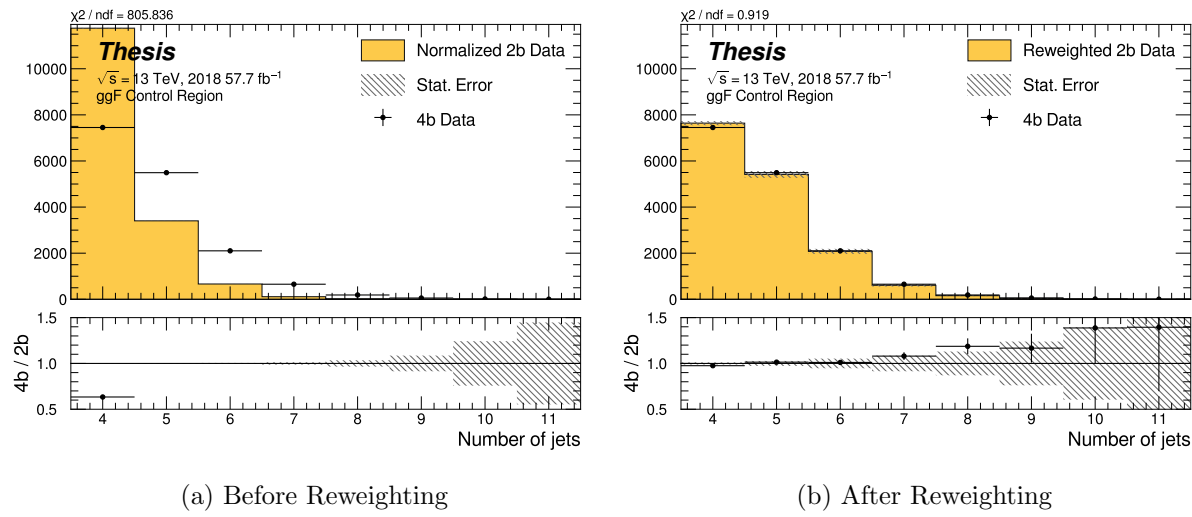


Figure 8.12: **Non-resonant Search (4b):** Distributions of the number of jets before (left) and after (right) CR derived reweighting for the 2018 4b Control Region. A minimum of 4 jets is required in each event in order to form Higgs candidates.

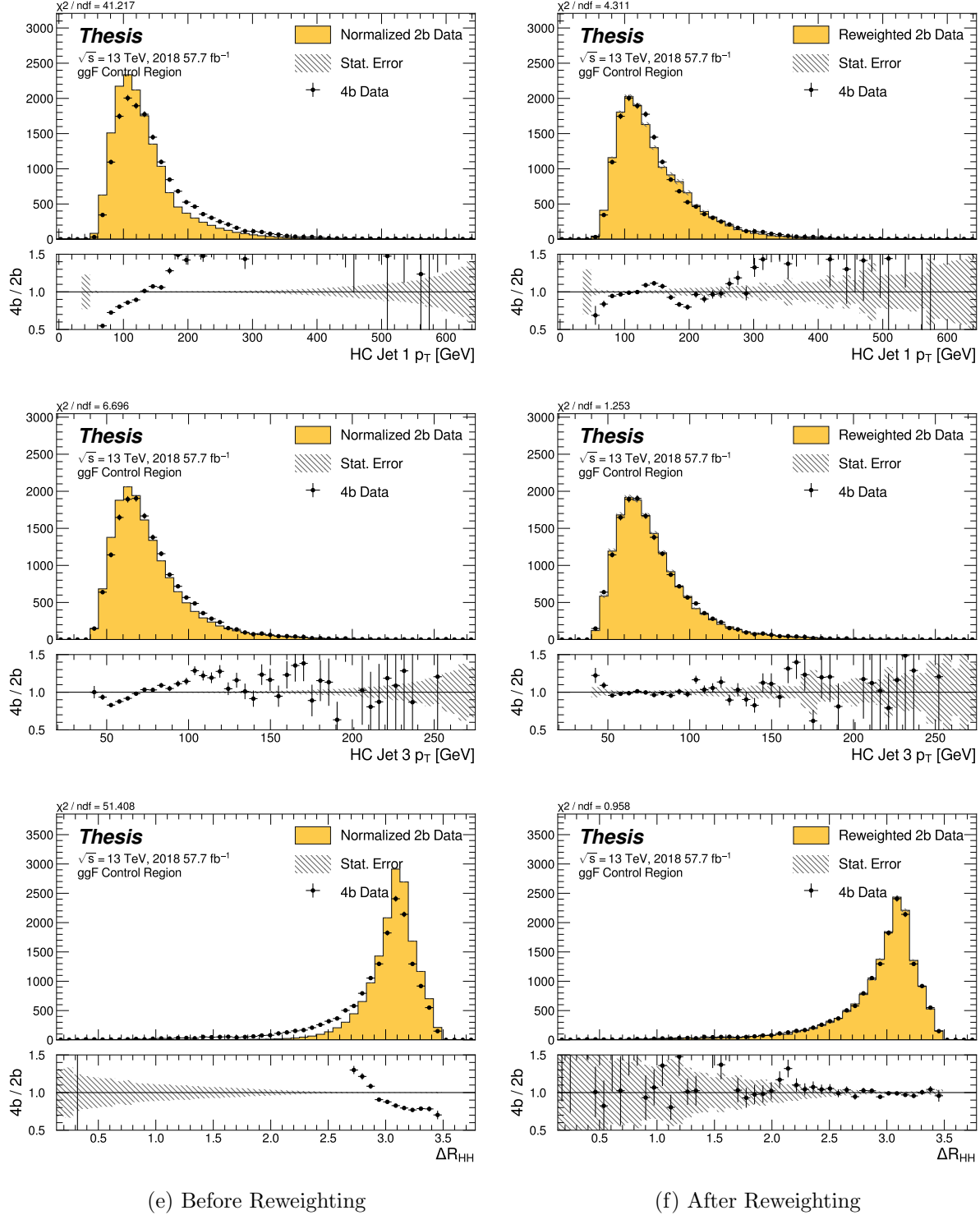


Figure 8.13: **Non-resonant Search (4b):** Distributions of  $p_T$  of the 1st and 3rd leading Higgs Candidate jets and  $\Delta R$  between Higgs candidates before (left) and after (right) CR derived reweighting for the 2018 4b Control Region.

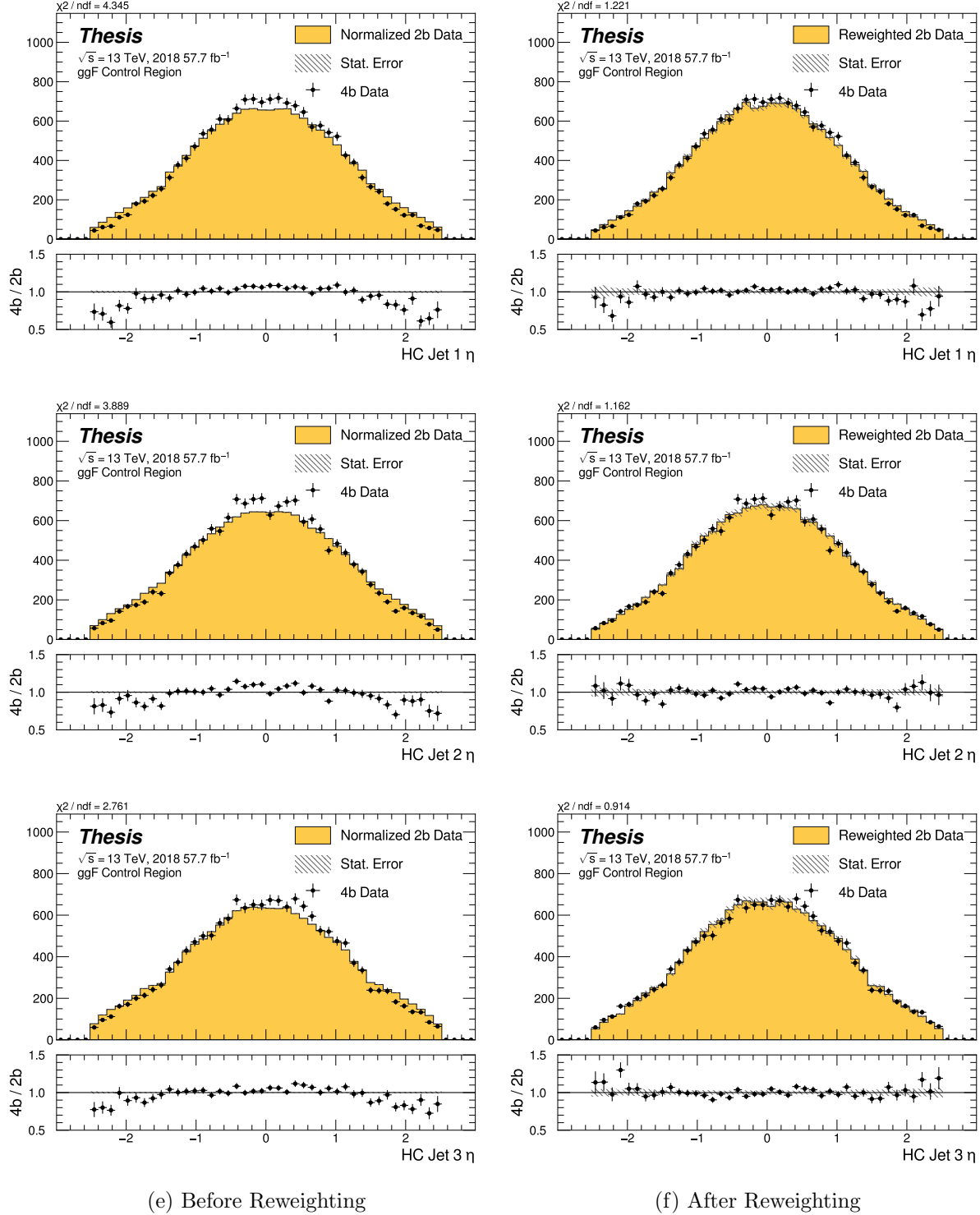


Figure 8.14: **Non-resonant Search (4b):** Distributions of  $\eta$  of the 1st, 2nd, and 3rd leading Higgs Candidate jets before (left) and after (right) CR derived reweighting for the 2018 4b Control Region.

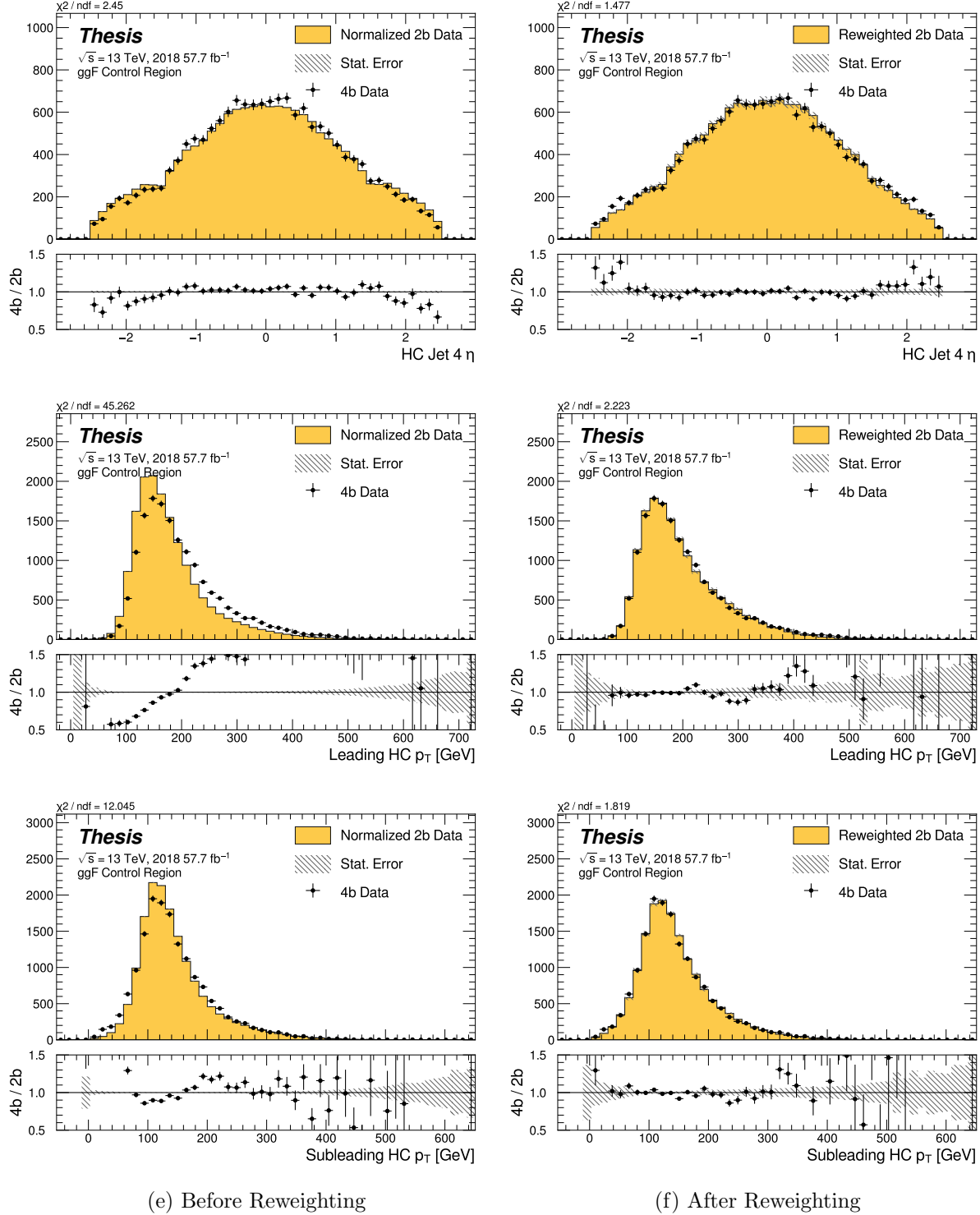


Figure 8.15: **Non-resonant Search (4b):** Distributions of  $\eta$  of the 4th leading Higgs Candidate jet and the  $p_T$  of the leading and subleading Higgs candidates before (left) and after (right) CR derived reweighting for the 2018 4b Control Region.

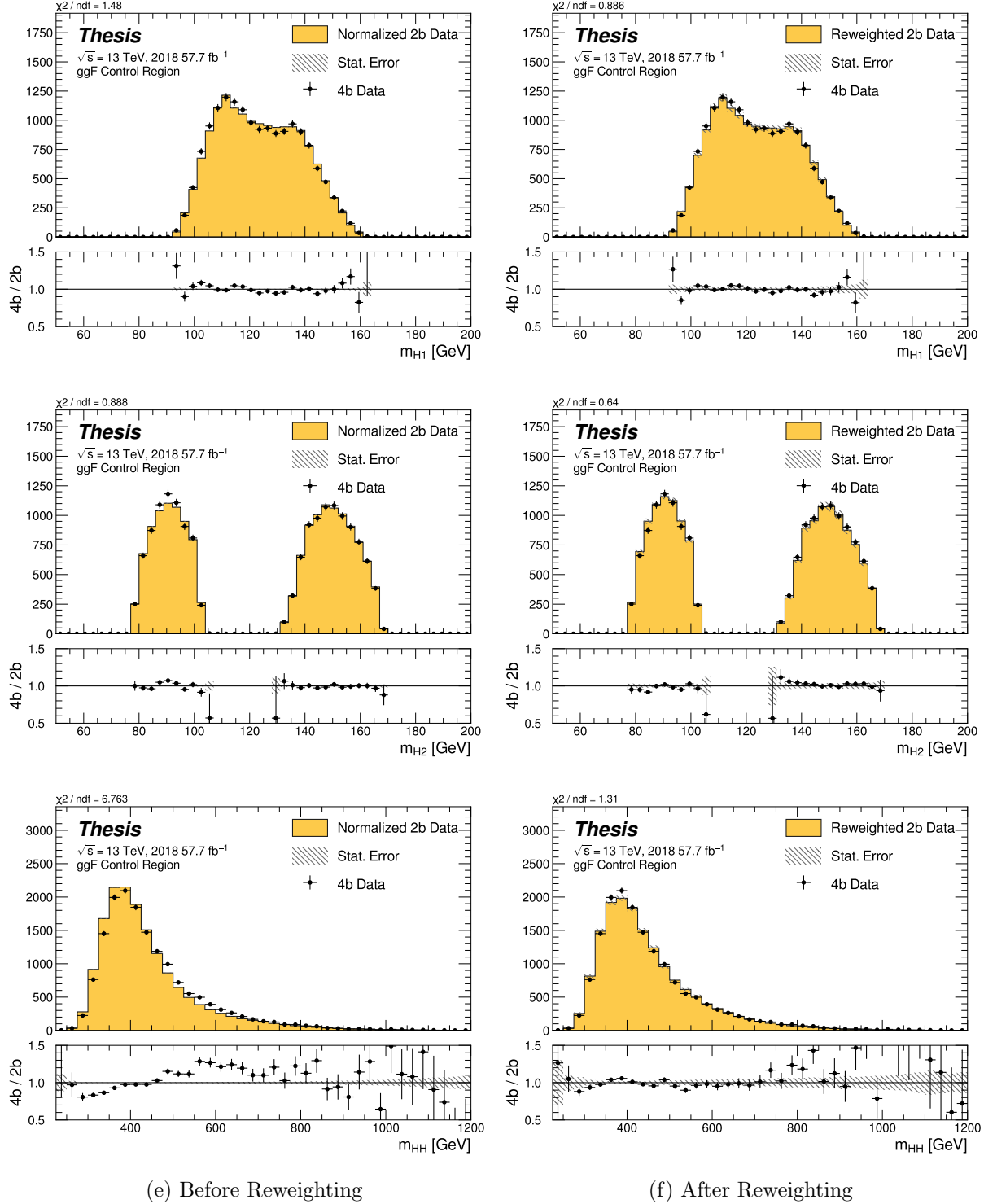


Figure 8.16: **Non-resonant Search (4b):** Distributions of mass of the leading and subleading Higgs candidates and of the di-Higgs system before (left) and after (right) CR derived reweighting for the 2018 4b Control Region.

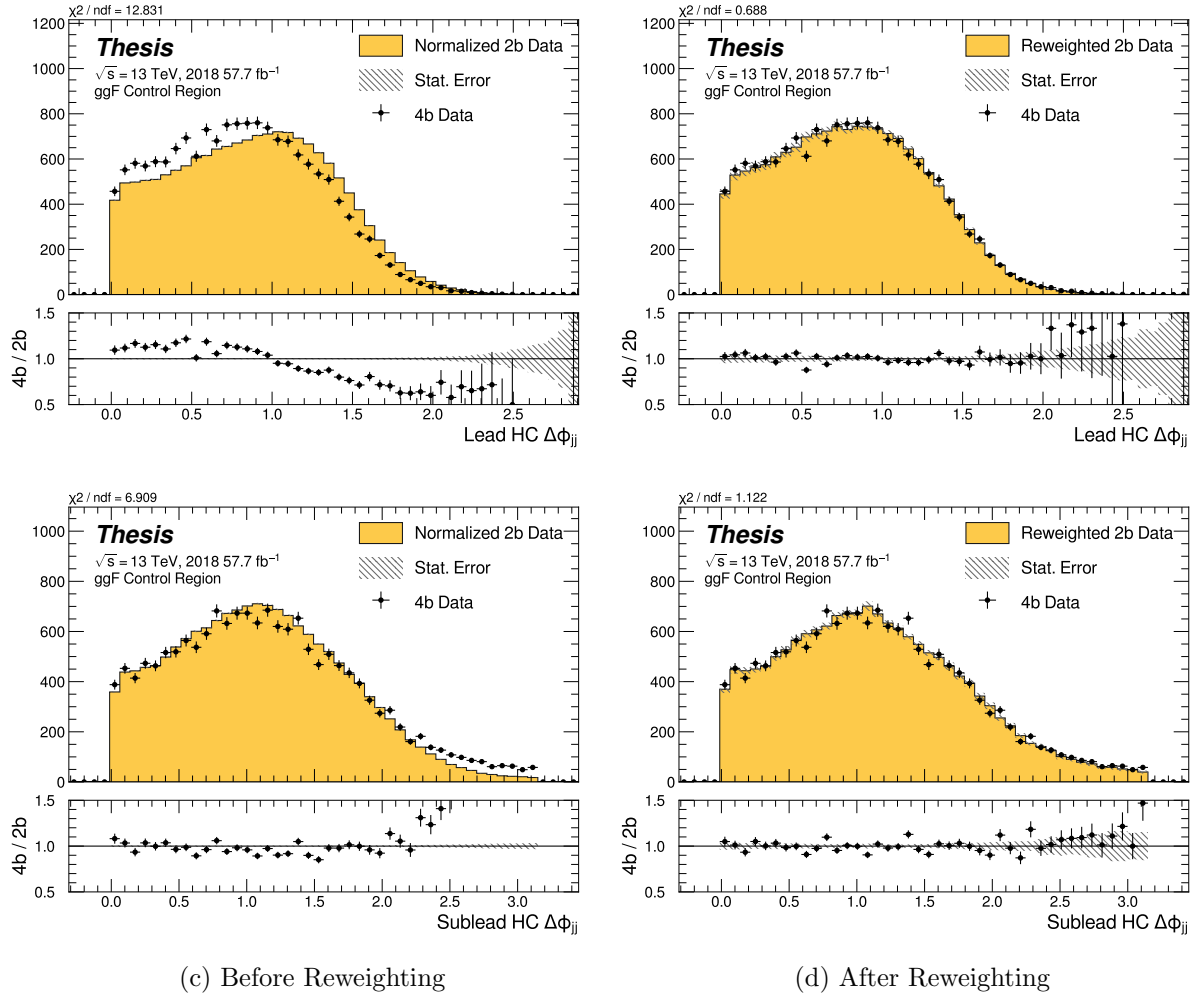


Figure 8.17: **Non-resonant Search (4b):** Distributions of  $\Delta\phi$  between jets in the leading and subleading Higgs candidates before (left) and after (right) CR derived reweighting for the 2018 4b Control Region.

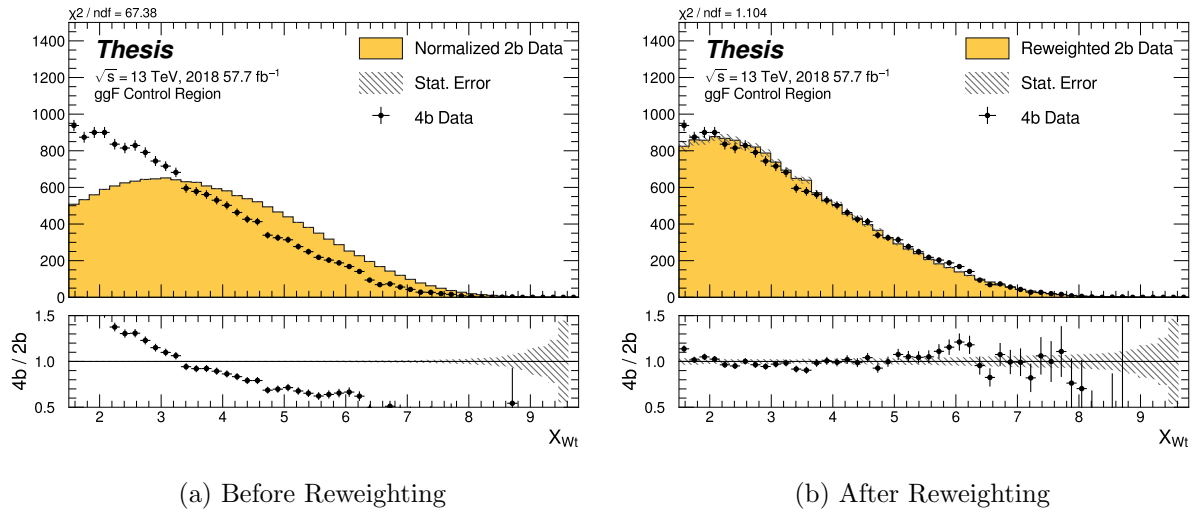


Figure 8.18: **Non-resonant Search (4b)**: Distributions of the top veto variable,  $X_{Wt}$ , before (left) and after (right) CR derived reweighting for the 2018 4b Control Region. Reweighting is done after the cut on this variable is applied.

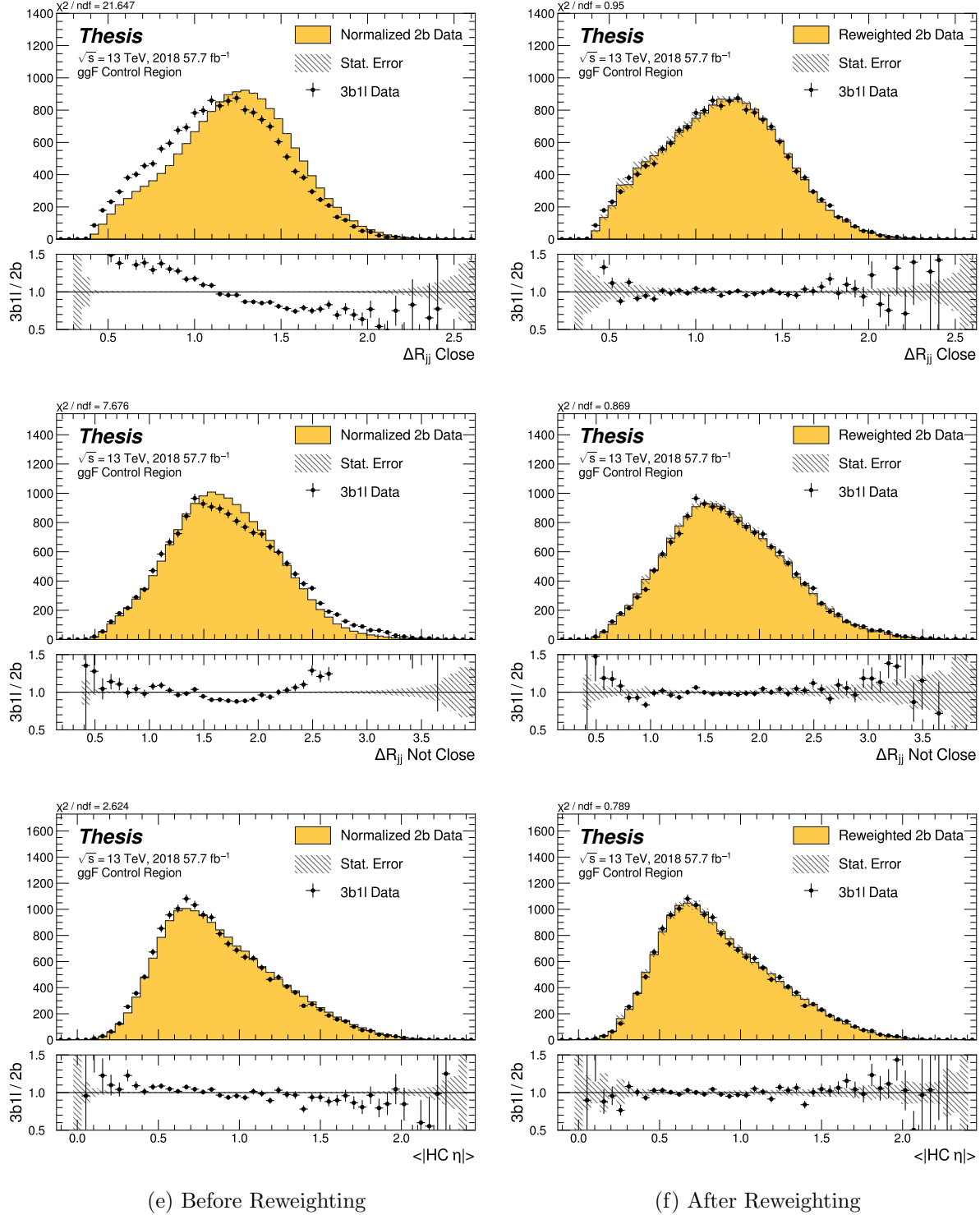


Figure 8.19: **Non-resonant Search (3b1l):** Distributions of  $\Delta R$  between the closest Higgs Candidate jets,  $\Delta R$  between the other two, and average absolute value of HC jet  $\eta$  before (left) and after (right) CR derived reweighting for the 2018 3b1l Control Region.

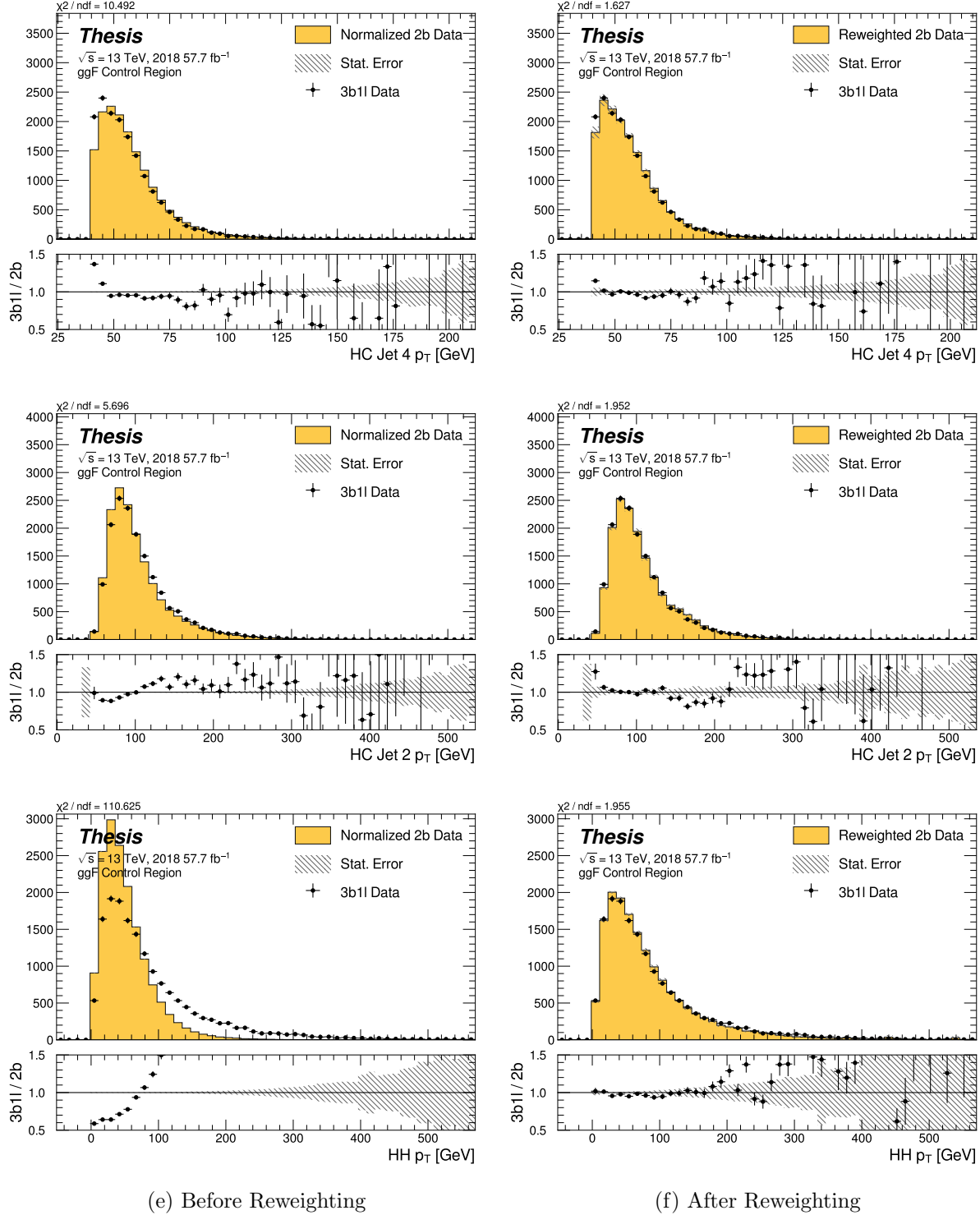


Figure 8.20: **Non-resonant Search (3b1l):** Distributions of  $p_T$  of the 2nd and 4th leading Higgs Candidate jets and the  $p_T$  of the di-Higgs system before (left) and after (right) CR derived reweighting for the 2018 3b1l Control Region.

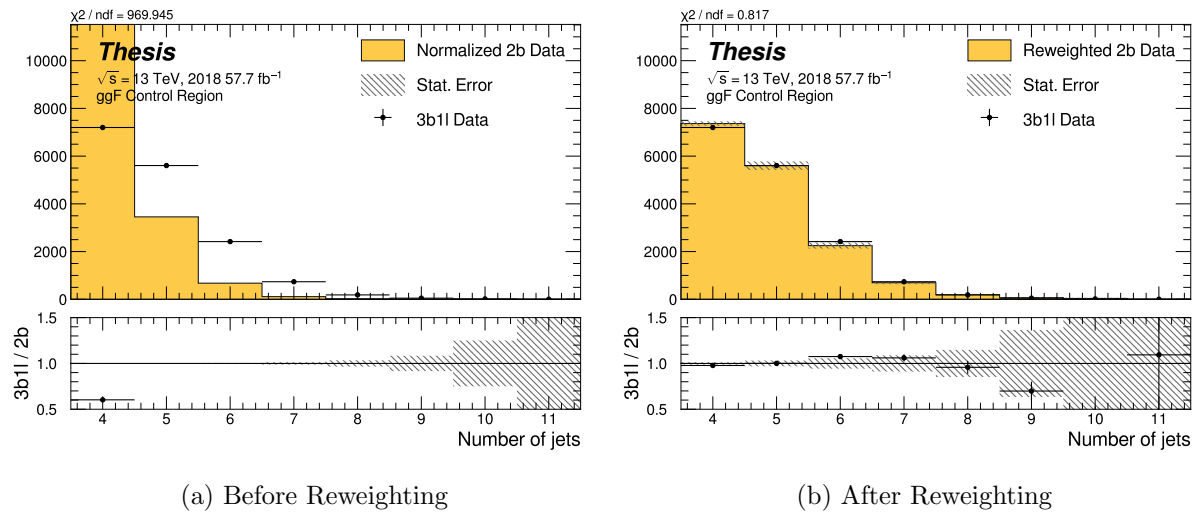


Figure 8.21: **Non-resonant Search (3b1l)**: Distributions of the number of jets before (left) and after (right) CR derived reweighting for the 2018 3b1l Control Region. A minimum of 4 jets is required in each event in order to form Higgs candidates.

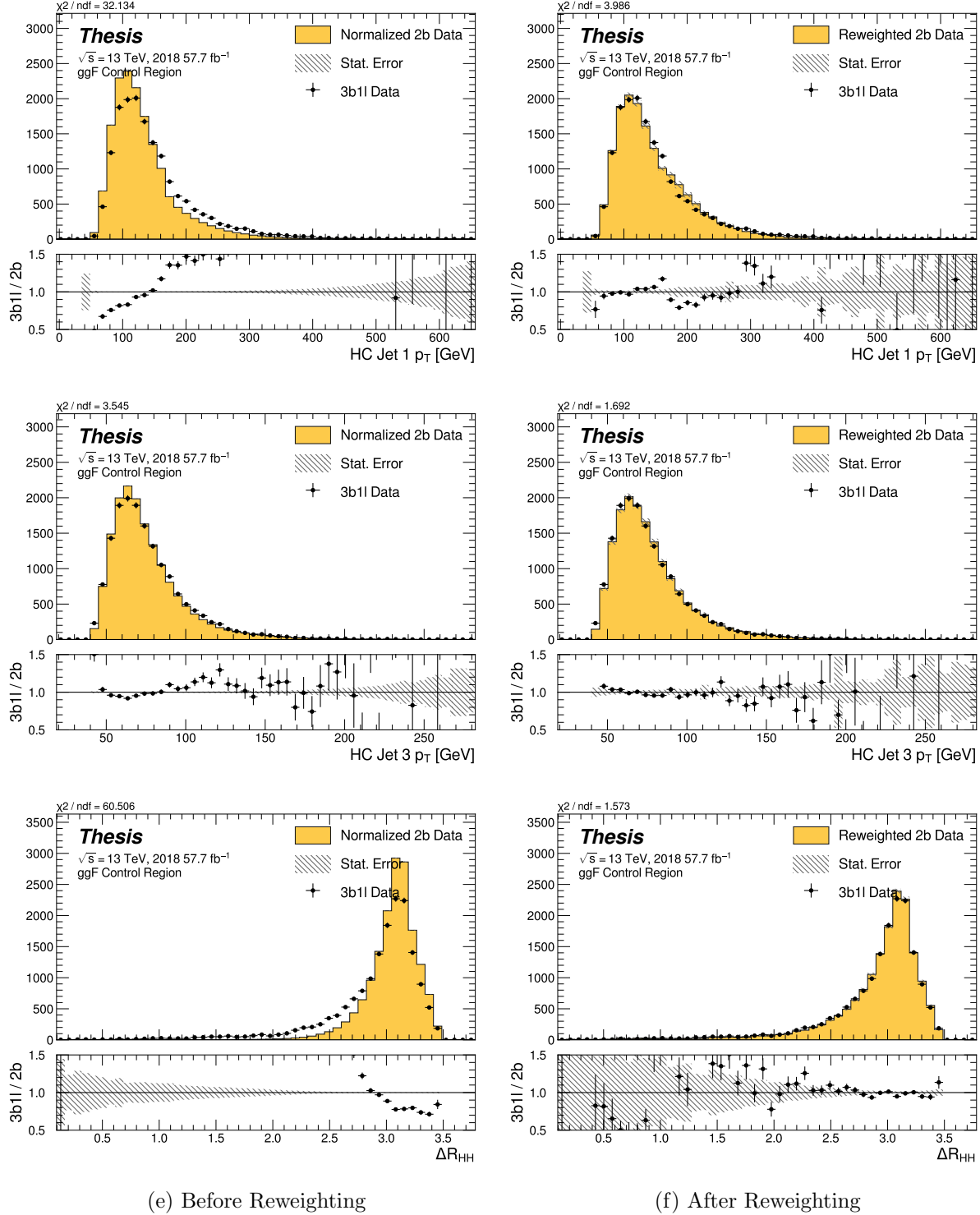


Figure 8.22: **Non-resonant Search (3b1l):** Distributions of  $p_T$  of the 1st and 3rd leading Higgs Candidate jets and  $\Delta R$  between Higgs candidates before (left) and after (right) CR derived reweighting for the 2018 3b1l Control Region.

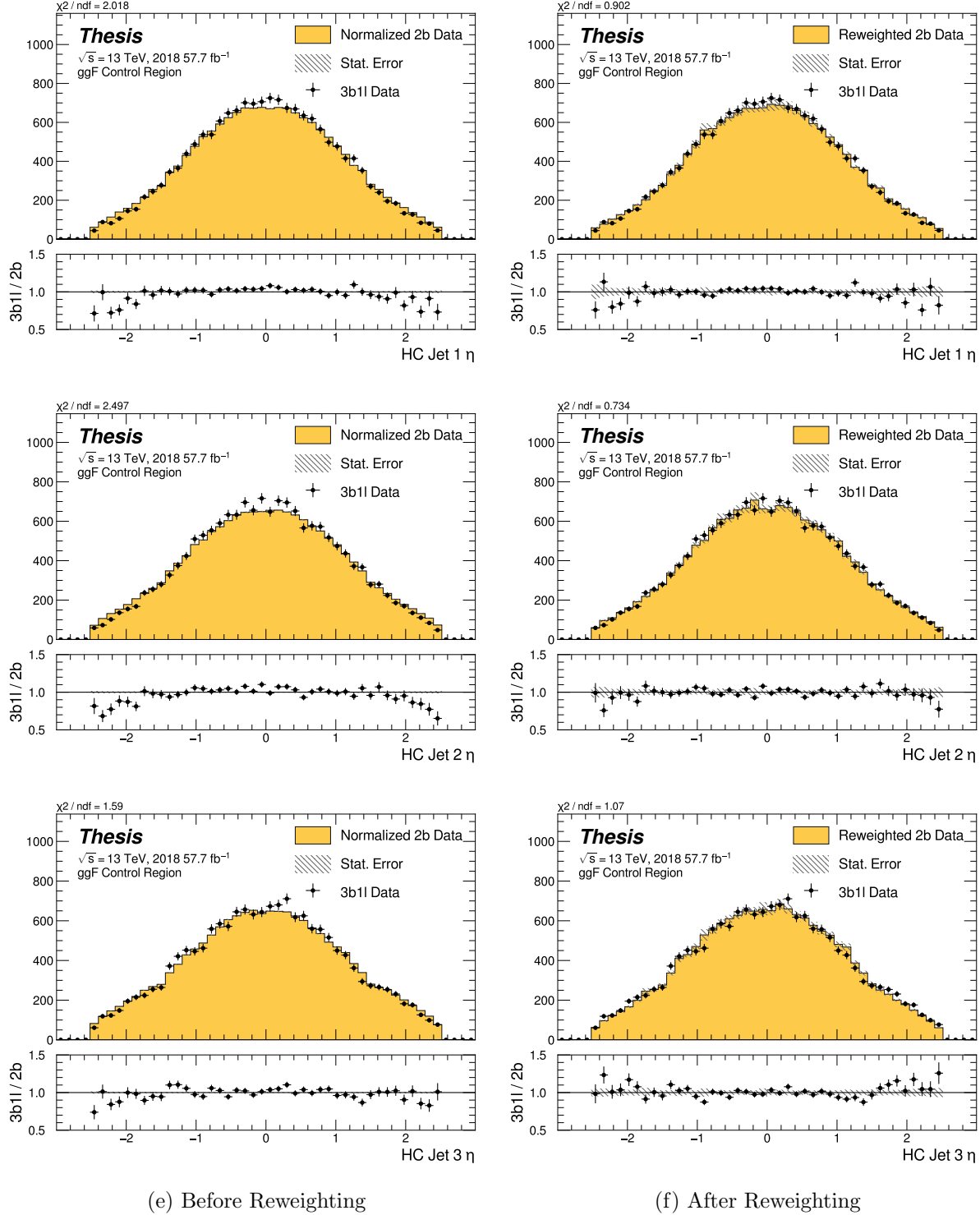


Figure 8.23: **Non-resonant Search (3b1l):** Distributions of  $\eta$  of the 1st, 2nd, and 3rd leading Higgs Candidate jets before (left) and after (right) CR derived reweighting for the 2018 3b1l Control Region.

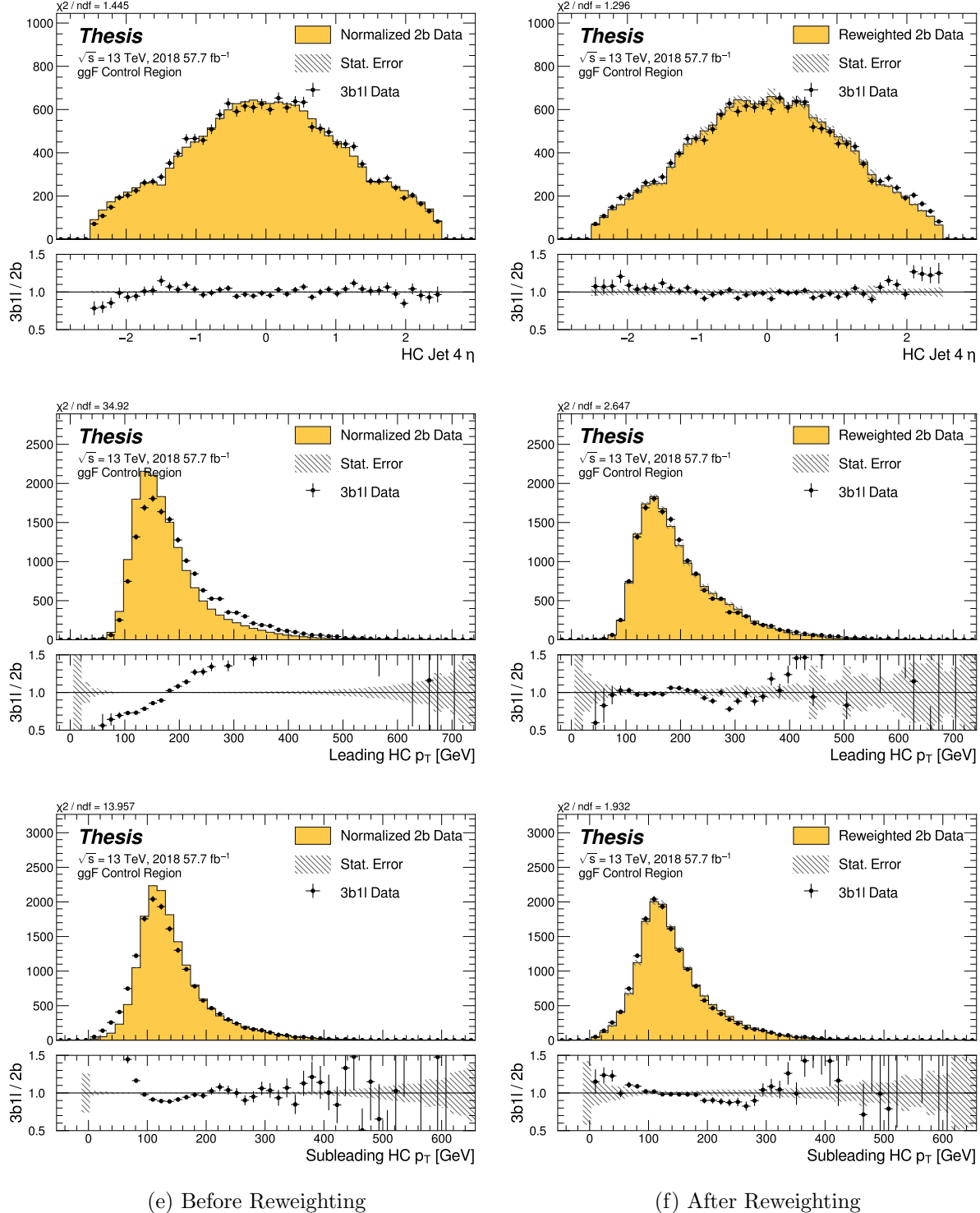


Figure 8.24: **Non-resonant Search (3b1l):** Distributions of  $\eta$  of the 4th leading Higgs Candidate jet and the  $p_T$  of the leading and subleading Higgs candidates before (left) and after (right) CR derived reweighting for the 2018 3b1l Control Region.

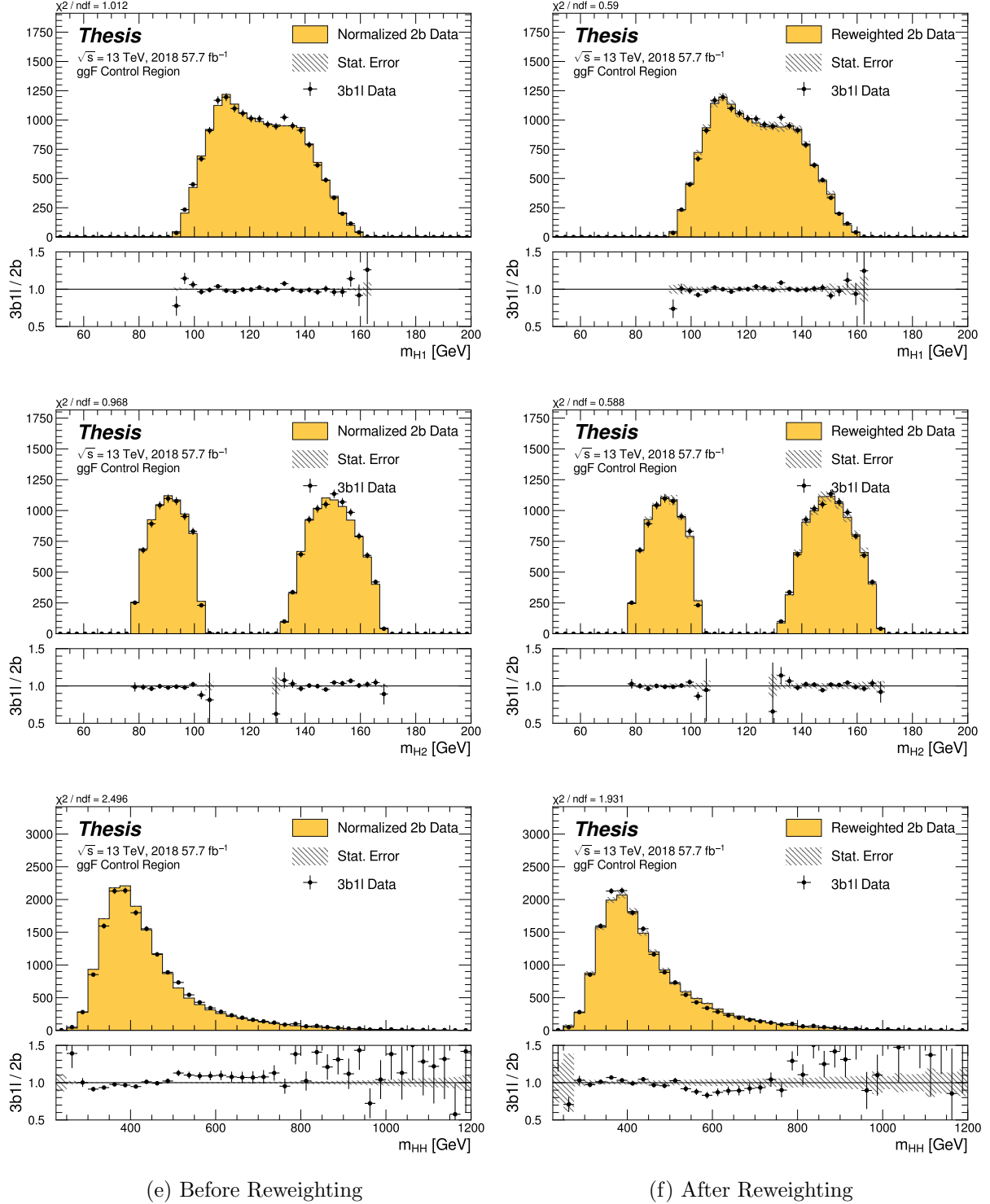


Figure 8.25: **Non-resonant Search (3b1l):** Distributions of mass of the leading and subleading Higgs candidates and of the di-Higgs system before (left) and after (right) CR derived reweighting for the 2018 3b1l Control Region.

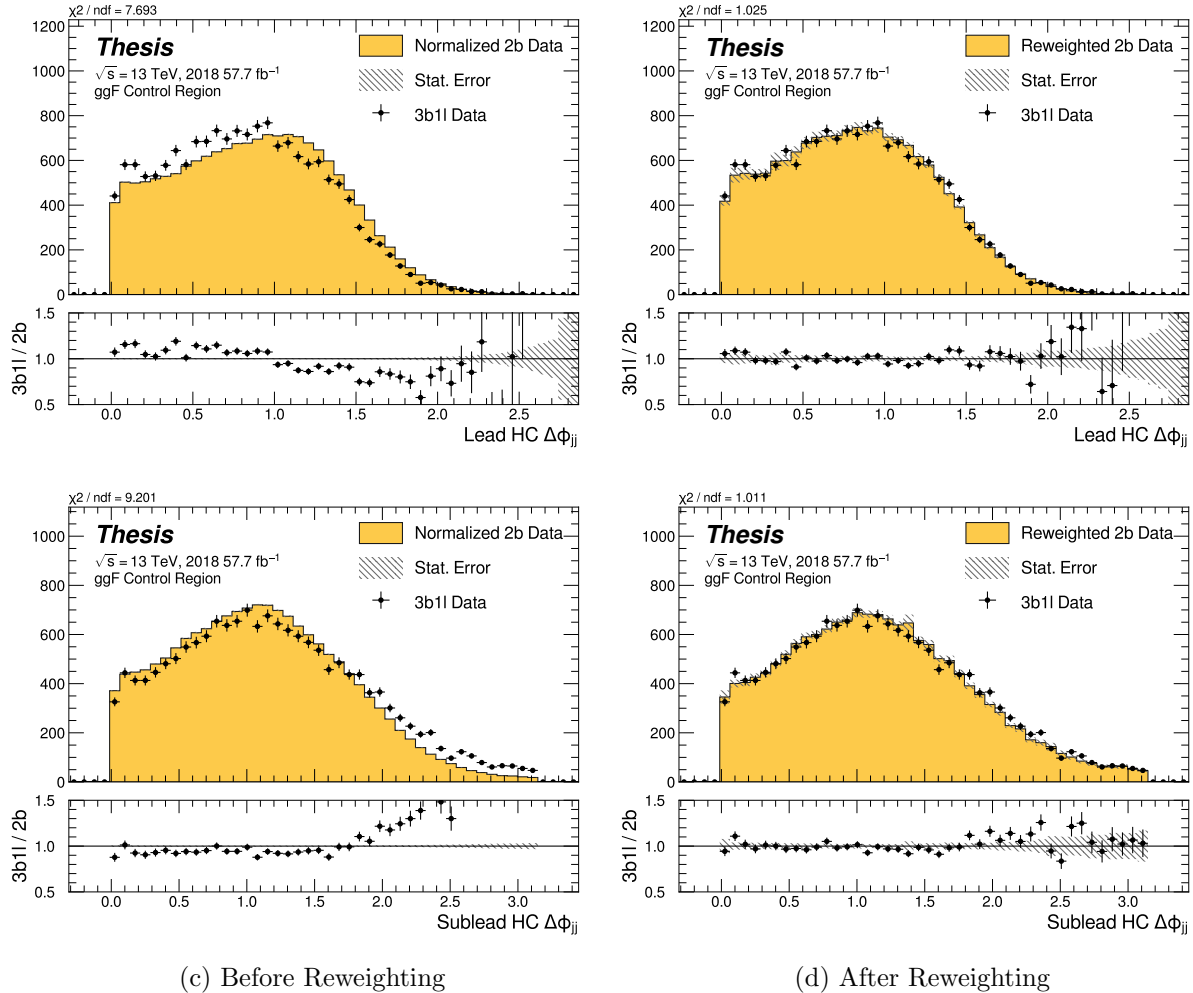


Figure 8.26: **Non-resonant Search (3b1l):** Distributions of  $\Delta\phi$  between jets in the leading and subleading Higgs candidates before (left) and after (right) CR derived reweighting for the 2018 3b1l Control Region.

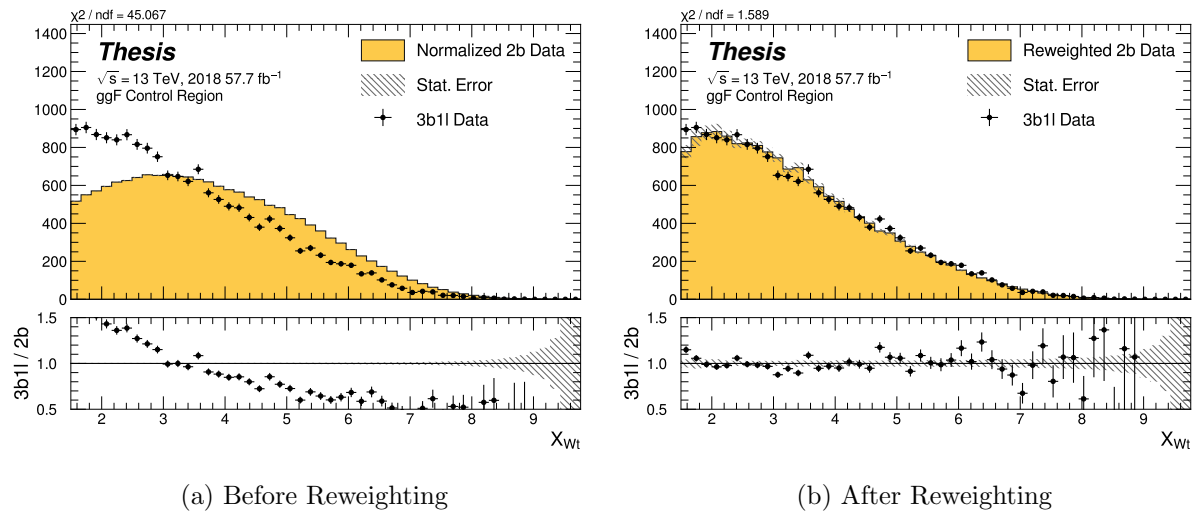


Figure 8.27: **Non-resonant Search (3b1l):** Distributions of the top veto variable,  $X_{Wt}$ , before (left) and after (right) CR derived reweighting for the 2018 3b1l Control Region. Reweighting is done after the cut on this variable is applied.

2422

## Chapter 9

2423

### UNCERTAINTIES AND VALIDATION

2424 A variety of uncertainties are assigned to account for known biases in the underlying  
 2425 methods, calibrations, and objects used for this analysis. The largest such uncertainty is  
 2426 associated with the kinematic bias inherent in deriving the background estimate outside of  
 2427 the signal region. However, a statistical biasing of this same estimate also has a significant  
 2428 impact. Additionally, due to the use of Monte Carlo for signal modelling and  $b$ -tagging  
 2429 calibration, uncertainties related to mis-modelings in simulation must also be accounted for.  
 2430 Note that the results for the non-resonant analysis presented here are preliminary and only  
 2431 include background systematic, such that the discussion of the signal systematics *only* applies  
 2432 for the resonant search. However, these background systematics are expected to be by far  
 2433 the dominant uncertainties.

2434 **9.1 Statistical Uncertainties and Bootstrapping**

2435 There are two components to the statistical error for the neural network background estimate.  
 2436 The first is standard Poisson error, i.e., a given bin,  $i$ , in the background histogram has value  
 2437  $n_i = \sum_{j \in i} w_j$ , where  $w_j$  is the weight for an event  $j$  which falls in bin  $i$ . Standard techniques  
 2438 then result in statistical error  $\delta n_i = \sqrt{\sum_{j \in i} w_j^2}$ , which reduces to the familiar  $\sqrt{N}$  Poisson error  
 2439 when all  $w_j$  are equal to 1.

2440 However, this procedure does not take into account the statistical uncertainty on the  
 2441  $w_j$  due to the finite training dataset. Due to the large size difference between the two tag  
 2442 and four tag datasets, it is the statistical uncertainty due to the four tag training data that  
 2443 dominates that on the background. A standard method for estimating this uncertainty is the  
 2444 bootstrap resampling technique [112]. Conceptually, a set of statistically equivalent sets is

2445 constructed by sampling with replacement from the original training set. The reweighting  
 2446 network is then trained on each of these separately, resulting in a set of statistically equivalent  
 2447 background estimates. Each of these sets is below referred to as a replica.

2448 In practice, as the original training set is large, the resampling procedure is able to  
 2449 be simplified through the relation  $\lim_{n \rightarrow \infty} \text{Binomial}(n, 1/n) = \text{Poisson}(1)$ , which dictates that  
 2450 sampling with replacement is approximately equivalent to applying a randomly distributed  
 2451 integer weight to each event, drawn from a Poisson distribution with a mean of 1.

2452 Though the network configuration itself is the same for each bootstrap training, the  
 2453 network initialization is allowed to vary. It should therefore be noted that the bootstrap  
 2454 uncertainties implicitly capture the uncertainty due to this variation in addition to the  
 2455 previously mentioned training set variation.

2456 The variation from this bootstrapping procedure is used to assign a bin-by-bin uncertainty  
 2457 which is treated as a statistical uncertainty in the fit. Due to practical constraints, a  
 2458 procedure for approximating the full bootstrap error band is developed which demonstrates  
 2459 good agreement with the full bootstrap uncertainty. This procedure is described below.

#### 2460 *9.1.1 Calculating the Bootstrap Error Band*

2461 The standard procedure to calculate the bootstrap uncertainty would proceed as follows: first,  
 2462 each network trained on each bootstrap replica dataset would be used to produce a histogram  
 2463 in the variable of interest. This would result in a set of replica histograms (e.g. for 100  
 2464 bootstrap replicas, 100 histograms would be created). The nominal estimate would then be  
 2465 the mean of bin values across these replica histograms, with errors set by the corresponding  
 2466 standard deviation.

2467 In practice, such an approach is inflexible and demanding both in computation and in  
 2468 storage, in so far as we would like to produce histograms in many variables, with a variety  
 2469 of different cuts and binnings. This motivates a derivation based on event-level quantities.  
 2470 However, due to non-trivial correlations between replica weights, simple linear propagation of  
 2471 event weight variation is not correct.

2472 We therefore adopt an approach which has been empirically found to produce results  
 2473 (for this analysis) in line with those produced by generating all of the histograms, as in the  
 2474 standard procedure. This approach is described below. Note that, for robustness to outliers  
 2475 and weight distribution asymmetry, the median and interquartile range (IQR) are used for  
 2476 the central value and width respectively (as opposed to the mean and standard deviation).

2477 The components involved in the calculation have been mentioned in Chapter 8 and are as  
 2478 follows:

- 2479 1. Replica weight ( $w_i$ ): weight predicted for a given event by a network trained on replica  
   dataset  $i$ .
- 2481 2. Replica norm ( $\alpha_i$ ): normalization factor for replica  $i$ . This normalizes the reweighting  
   prediction of the network trained on replica dataset  $i$  to match the corresponding target  
   yield.
- 2483 3. Median weight ( $w_{med}$ ): median weight for a given event across replica datasets, used  
   for the nominal estimate. Defined (for 100 bootstrap replicas) as

$$w_{med} \equiv \text{median}(\alpha_1 w_1, \dots, \alpha_{100} w_{100}) \quad (9.1)$$

- 2484 4. Normalization correction ( $\alpha_{med}$ ): normalization factor to match the predicted yield of  
 2485 the median weights ( $w_{med}$ ) to the target yield in the training region.

2486 As mentioned in Chapter 8, the *nominal estimate* is constructed from the set of median  
 2487 weights and the normalization correction, i.e.  $\alpha_{med} \cdot w_{med}$ .

2488 For the bootstrap error band, a “varied” histogram is then generated by applying, for  
 2489 each event, a weight equal to the median weight (with no normalization correction) plus half  
 2490 the interquartile range of the replica weights:  $w_{varied} = w_{med} + \frac{1}{2} \text{IQR}(w_1, \dots, w_{100})$ .

2491 This varied histogram is scaled to match the yield of the nominal estimate. To account  
 2492 for variation of the nominal estimate yield, a normalization variation is calculated from the

2493 interquartile range of the replica norms:  $\frac{1}{2} \text{IQR}(\alpha_1, \dots, \alpha_{100})$ . This variation, multiplied into  
2494 the nominal estimate, is used to set a baseline for the varied histogram described above.

Denoting  $H(\text{weights})$  as a histogram constructed from a given set of weights,  $Y(\text{weights})$  as the predicted yield for a given set of weights, the final varied histogram is thus:

$$H(w_{med} + \frac{1}{2} \text{IQR}(w_1, \dots, w_{100})) \cdot \frac{Y(\alpha_{med} w_{med})}{Y(w_{med} + \frac{1}{2} \text{IQR}(w_1, \dots, w_{100}))} + \frac{1}{2} \text{IQR}(\alpha_1, \dots, \alpha_{100}) \cdot H(\alpha_{med} w_{med}) \quad (9.2)$$

2495 where the first term roughly describes the behavior of the bootstrap variation across the  
2496 distribution of the variable of interest while the second term describes the normalization  
2497 variation of the bootstrap replicas.

2498 The difference between the varied histogram and the nominal histogram is then taken to  
2499 be the bootstrap statistical uncertainty on the nominal histogram.

2500 Figure 9.1 demonstrates how each of the components described above contribute to the  
2501 uncertainty envelope for the non-resonant 2017 Control Region and compares this approximate  
2502 band to the variation of histograms from individual bootstrap estimates. The error band  
2503 constructed from the above procedure is seen to provide a good description of the bootstrap  
2504 variation.

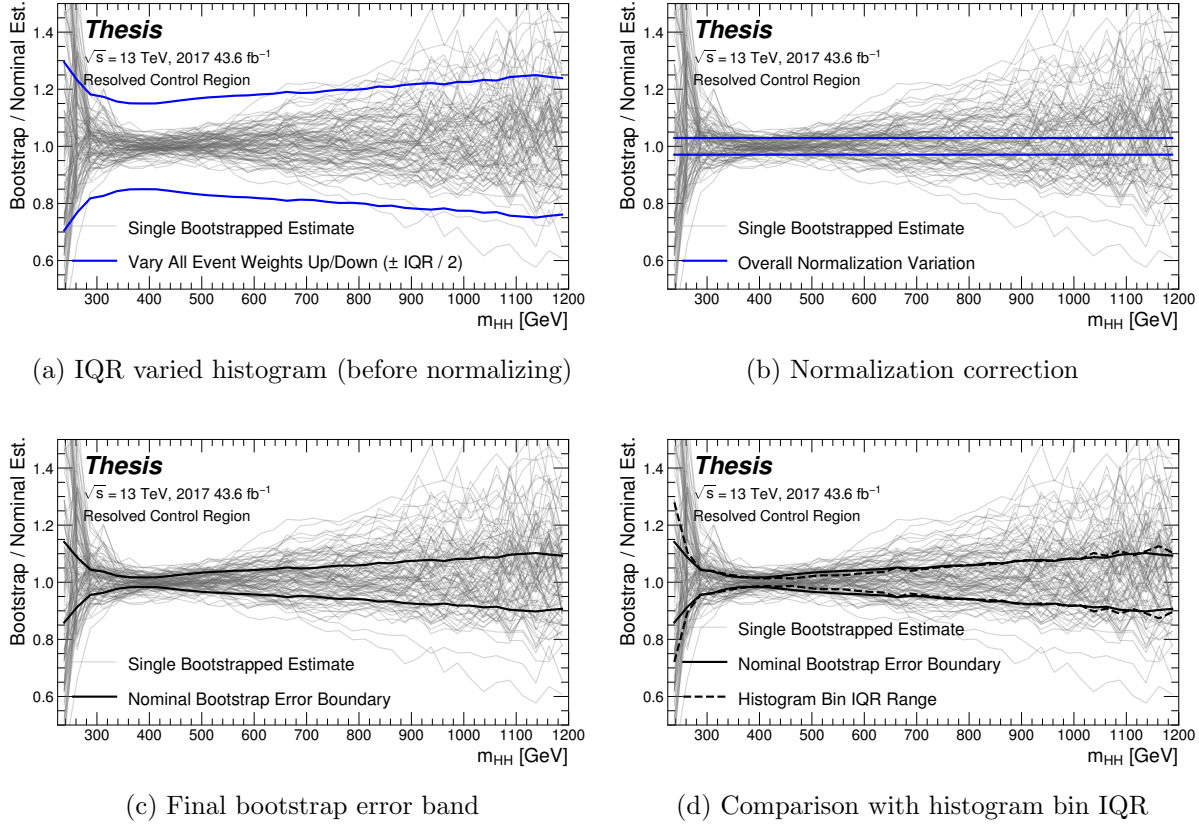


Figure 9.1: Illustration of the approximate bootstrap band procedure, shown as a ratio to the nominal estimate for the 2017 non-resonant background estimate. Each grey line is from the  $m_{HH}$  prediction for a single bootstrap training. Figure 9.1(a) shows the variation histograms constructed from median weight  $\pm$  the IQR of the replica weights. It can be seen that this captures the rough shape of the bootstrap envelope, but is not good estimate for the overall magnitude of the variation. Figure 9.1(b) demonstrates the applied normalization correction, and Figure 9.1(c) shows the final band (normalized Figure 9.1(a) + Figure 9.1(b)). Comparing this with the IQR variation for the prediction from each bootstrap in each bin in Figure 9.1(d), the approximate envelope describes a very similar variation.

2505 **9.2 Background Shape Uncertainties**

2506 To account for the systematic bias associated with deriving the reweighting function in the  
 2507 control region and extrapolating to the signal region, an alternative background model is  
 2508 derived in the validation region. Because of the fully data-driven nature of the background  
 2509 model, this is an uncertainty assessed on the full background. The alternative model and  
 2510 the baseline are consistent with the observed data in their training regions, and differences  
 2511 between the alternative and baseline models are used to define a shape uncertainty on the  
 2512  $m_{HH}$  spectrum, with a two-sided uncertainty defined by symmetrizing the difference about  
 2513 the baseline.

2514 For the resonant analysis, this uncertainty is split into two components to allow for two  
 2515 independent variations of the  $m_{HH}$  spectrum: a low- $H_T$  and a high- $H_T$  component, where  
 2516  $H_T$  is the scalar sum of the  $p_T$  of the four jets constituting the Higgs boson candidates, and  
 2517 serves as a proxy for  $m_{HH}$ , while avoiding introducing a sharp discontinuity. The boundary  
 2518 value is 300 GeV. The low- $H_T$  shape uncertainty primarily affects the  $m_{HH}$  spectrum below  
 2519 400 GeV (close to the kinematic threshold) by up to around 5%, and the high- $H_T$  uncertainty  
 2520 mainly  $m_{HH}$  above this by up to around 20% relative to nominal. These separate  $m_{HH}$   
 2521 regimes are by design – the  $H_T$  split is introduced to prevent low mass bins from constraining  
 2522 the high mass uncertainty and vice-versa.

2523 This was the *status quo* shape uncertainty decomposition from the Early Run 2 analysis.  
 2524 A decomposition in terms of orthogonal polynomials, which would provide increased flexibility,  
 2525 was also evaluated. This study revealed that both decompositions are able to account for the  
 2526 systematic deviations between four tag data and the background estimate (evaluated in the  
 2527 kinematic validation region), and produce almost identical limits. The simpler *status quo*  
 2528 decomposition is therefore kept.

2529 For the non-resonant analysis, the quadrant nature of the background estimation leads to  
 2530 a natural breakdown of the nuisance parameters: quadrants are defined in the signal region  
 2531 along the same axes as those used for the control and validation region definitions. Variations

2532 are then assessed in each of these signal region quadrants, corresponding to regions that  
 2533 are “closer to” and “further away from” the nominal and alternate estimate regions, fully  
 2534 leveraging the power of the two equivalent but systematically different estimates.

2535 Figure 9.2 shows an example of the variation in each  $H_T$  region for the 2018 resonant  
 2536 analysis. Figure 9.3 shows the example quadrant variation for the 2018 4 $b$  non-resonant  
 analysis.

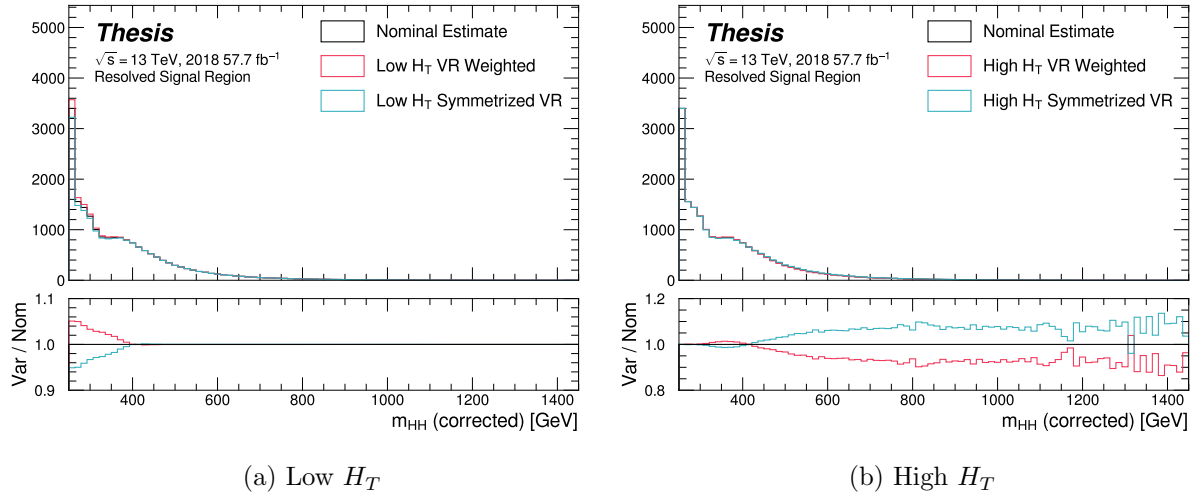
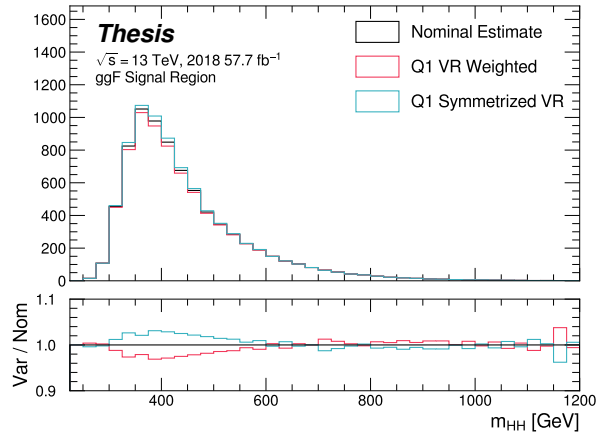
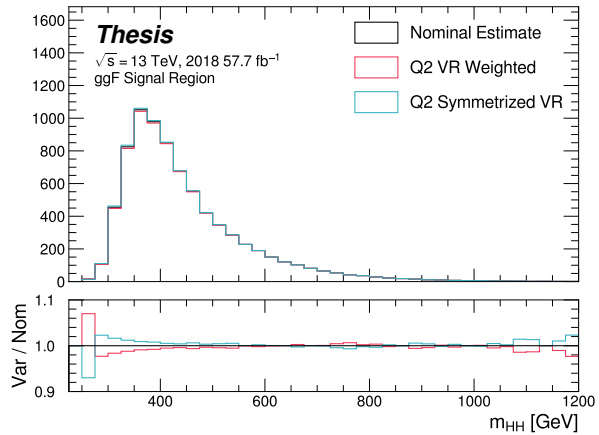


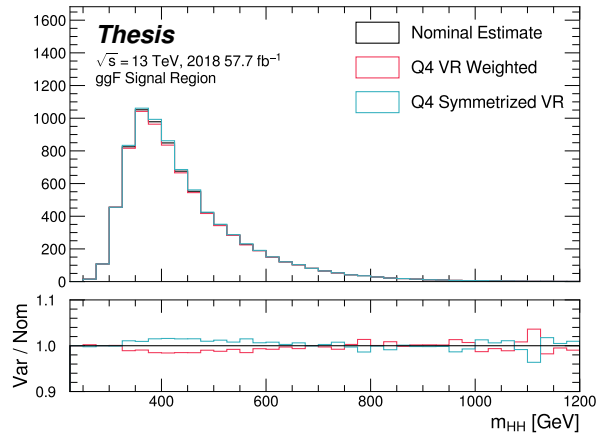
Figure 9.2: **Resonant Search:** Example of CR vs VR variation in each  $H_T$  region for 2018.  
 The variation nicely factorizes into low and high mass components.



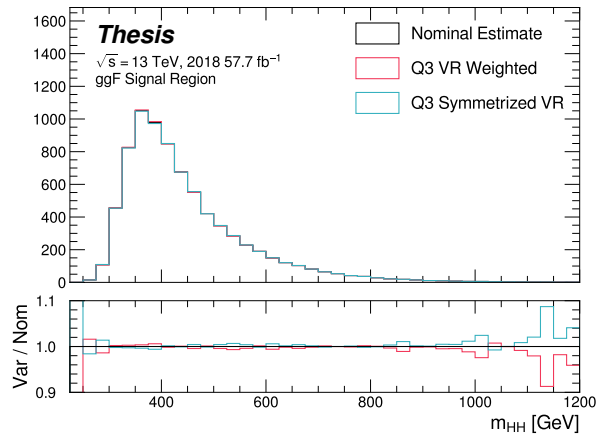
(a) Q1 (top)



(b) Q2 (left)



(c) Q4 (right)



(d) Q3 (bottom)

Figure 9.3: **Non-resonant Search (4b):** Example of CR vs VR variation in each signal region quadrant for 2018. Significantly different behavior is seen between quadrants, with the largest variation in quadrant 1 and the smallest in quadrant 4.

2538    **9.3 Signal Uncertainties**

2539    A variety of uncertainties are assessed on the signal Monte Carlo simulation. As the  
 2540    background estimate is fully data driven, such uncertainties are not needed for the background  
 2541    estimate. Note again that the results presented for the non-resonant search only include the  
 2542    background systematics described above.

2543    Detector modeling and reconstruction uncertainties account for differences between Monte  
 2544    Carlo simulation and real data due to mis-modeling of the detector as well as due to the  
 2545    different performance of algorithms on simulation compared to data. In this analysis they  
 2546    consist of uncertainties related to jet properties and uncertainties stemming from the flavor  
 2547    tagging procedure. The jet uncertainties are treated according to the prescription in [113] and  
 2548    are implemented as variations of the jet properties. These cover uncertainty in jet energy scale  
 2549    and resolution. Uncertainties in  $b$ -tagging efficiency are treated according to the prescription  
 2550    in Ref. [86] and implemented as scale factors applied to the Monte Carlo event weights.

2551    Trigger uncertainties stem from imperfect knowledge of the ratio between the efficiency of  
 2552    a given trigger in data to its efficiency in Monte Carlo simulation. This ratio is applied as a  
 2553    scale factor to all simulated events, with the systematic variations produced by varying the  
 2554    scale factor up or down by one sigma. Such variations are evaluated based on measurements  
 2555    of per-jet online efficiencies for both jet reconstruction and  $b$ -tagging, and these are used to  
 2556    compute event-level uncertainties. These are then applied as overall weight variations on the  
 2557    simulated events.

2558    An uncertainty on the total integrated luminosity used in this analysis is also applied,  
 2559    and is measured to be 1.7% [103], obtained using the LUCID-2 detector for the primary  
 2560    luminosity measurements [114].

2561    A variety of theoretical uncertainties are also assessed on the signal. Such uncertainties  
 2562    are assessed by generating samples following the configuration of the baseline samples, but  
 2563    with modifications to probe various aspects of the simulation. These include uncertainties in  
 2564    the parton density functions (PDFs); uncertainties due to missing higher order terms in the

2565 matrix elements; and uncertainties in the modelling of the underlying event, which includes  
 2566 multi-parton interactions, of hadronic showers and of initial and final state radiation.

2567 Uncertainties due to modelling of the parton shower and the underlying event are eval-  
 2568 uated by comparing results from using two different generators, namely HERWIG 7.1.3 and  
 2569 PYTHIA 8.235. No significant dependence on the variable of interest,  $m_{HH}$ , is observed.  
 2570 Therefore, a 5% flat systematic uncertainty is assigned to all signal samples, extracted from  
 2571 the acceptance comparison for the full 4-tag selection.

2572 Uncertainties in the matrix element calculation are evaluated by varying the factorization  
 2573 and renormalization scales used in the generator up and down by a factor of two, both  
 2574 independently and simultaneously. This results in an effect smaller than 1% for all variations  
 2575 and all masses; the impact of such uncertainties is therefore neglected.

2576 PDF uncertainties are evaluated using the PDF4LHC\_NLO\_MC set [104] by calculating  
 2577 the signal acceptance for each PDF replica and taking the standard deviation. In all cases,  
 2578 these uncertainties result in an effect smaller than 1% on the signal acceptance; therefore  
 2579 these are also neglected.

2580 Theoretical uncertainties on the  $H \rightarrow b\bar{b}$  branching ratio [115] are also included.

2581 **9.4 Background Validation**

2582 In addition to checking the performance of the background estimate in the control and  
2583 validation regions, a variety of alternative selections are defined to allow for a full “dress  
2584 rehearsal” of the background estimation procedure.

2585 Both the resonant and non-resonant analyses make use of a *reversed*  $\Delta\eta$  region, in which  
2586 the kinematic cut on  $\Delta\eta_{HH}$  is reversed, so that events are required to have  $\Delta\eta_{HH} > 1.5$ .  
2587 This is orthogonal to the nominal signal region and has minimal sensitivity, allowing for the  
2588 comparison of the background estimate  $4b$  data in the corresponding “signal region”. For  
2589 this validation, a new reweighting is trained following nominal procedures, but entirely in  
2590 the  $\Delta\eta_{HH} > 1.5$  region. An example of such a validation is shown for the resonant search in  
2591 Figure 9.4.

2592 The non-resonant analysis additionally makes use of the  $3b + 1$  fail region mentioned  
2593 above, which again is orthogonal to the nominal signal regions and has minimal sensitivity.  
2594 The reweighting in this case is between  $2b$  and  $3b + 1$  fail events rather than between  $2b$   
2595 and  $3b + 1$  loose or  $2b$  and  $4b$ . However, the kinematic selections of signal region events are  
2596 otherwise identical, allowing for a complementary test of the background estimate. This  
2597 validation is shown in Figure 9.5.

2598 Additional validation regions are also being explored, including those based on shifting  
2599 the position of the set of analysis regions in the Higgs candidate mass plane and rederiving  
2600 the background estimate in these shifted regions. Though each of these validations is different  
2601 in some way from the set of regions in which the analysis is performed, evaluation of the  
2602 performance of the background estimate in these regions is useful for developing and gaining  
2603 confidence in the background estimation method and the corresponding uncertainties. Non-  
2604 closure of the method in such regions may additionally be used for assessing uncertainties,  
2605 but this is not considered here.

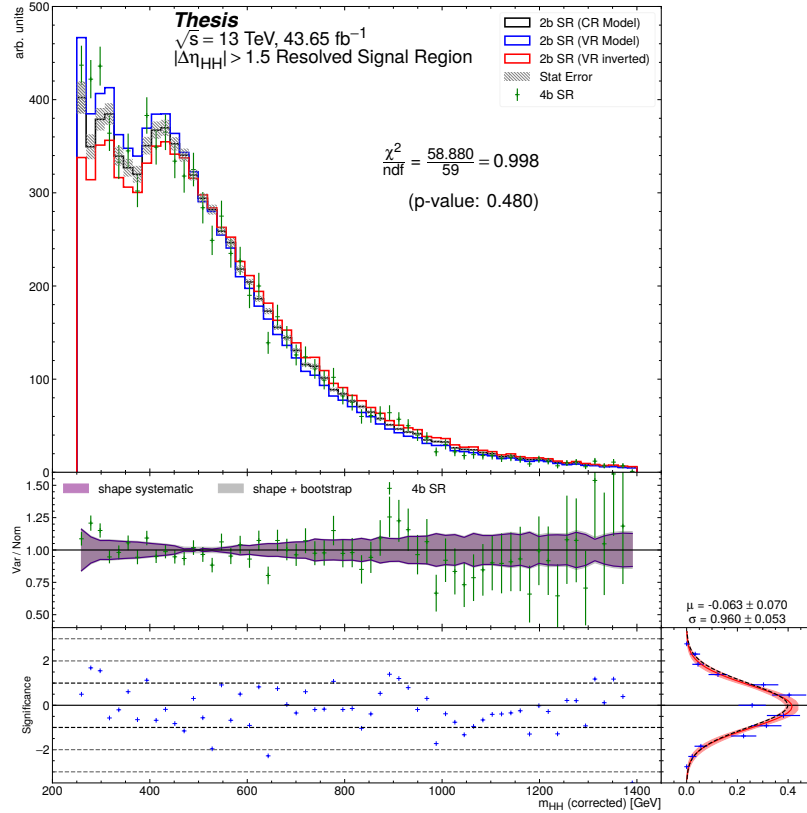


Figure 9.4: **Resonant Search:** Performance of the background estimation method in the resonant analysis reversed  $\Delta\eta_{HH}$  kinematic signal region. A new background estimate is trained following nominal procedures entirely within the reversed  $\Delta\eta_{HH}$  region, and the resulting model, including uncertainties, is compared with  $4b$  data in the corresponding signal region. Good agreement is shown. The quoted  $p$ -value uses the  $\chi^2$  test statistic, and demonstrates no evidence that the data differs from the assessed background.

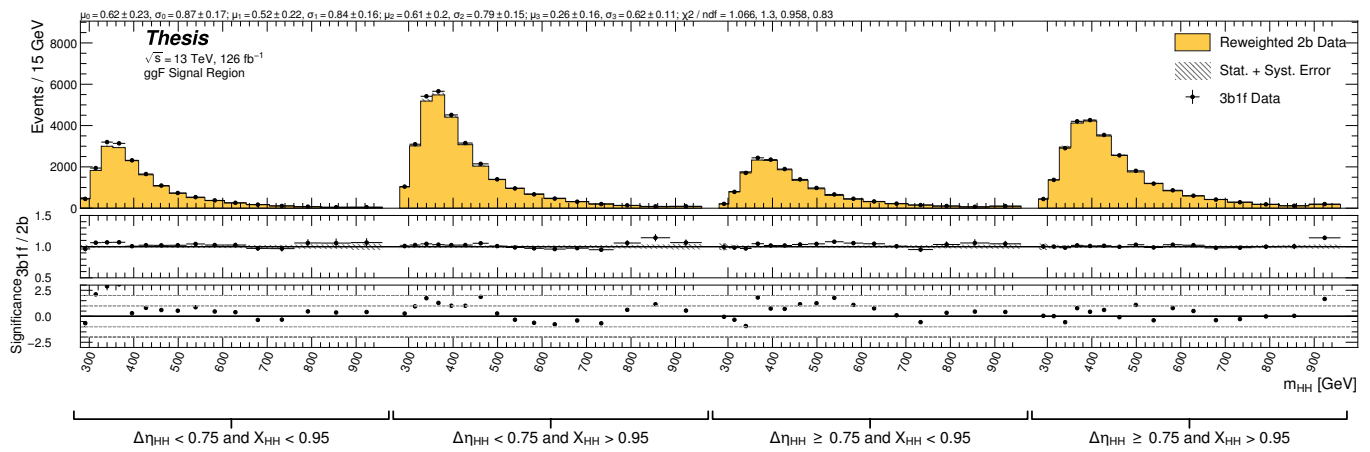


Figure 9.5: **Non-resonant Search:** Performance of the background estimation method in the  $3b + 1$  fail validation region. A new background estimate is trained following nominal procedures but with a reweighting from  $2b$  to  $3b + 1$  fail events. Generally good agreement is seen, though there is some deviation at very low masses in the low  $\Delta\eta_{HH}$  low  $X_{HH}$  category.

2606

## Chapter 10

2607

# RESULTS

## 2608 **10.1 $m_{HH}$ Distributions**

### 2609 *10.1.1 Resonant Search*

2610 The final discriminant used for the resonant search is corrected  $m_{HH}$ . Histogram binning  
2611 was optimized for the resonant search to be 84 equal width bins from 250 GeV to 1450 GeV,  
2612 corresponding to a bin width of 14.3 GeV, and overflow events (events above 1450 GeV) are  
2613 included in the last bin. A demonstration of the performance of the reweighting on this  
2614 distribution is shown in Figure 10.1 for the control region and Figure 10.2 for the validation  
2615 region. A background-only profile likelihood fit is run for the distribution in the  
2616 signal region, and results with representative signals overlaid are shown in Figure 10.3. 4b  
2617 data yields, estimated background, and signal event yields are extracted for representative  
2618 mass hypotheses in a corrected  $m_{HH}$  window containing roughly 90 % of the corresponding  
2619 signal after this same background-only fit in the signal region. These results are shown in  
2620 Tables 10.1 and 10.2 for spin-0 and spin-2 respectively. Note that the plots and tables show  
2621 the sum across all years, but the signal extraction fit and background estimate are run with  
2622 the years separately. Agreement is generally good throughout.

Table 10.1: Resolved 4*b* signal region data, estimated background, and signal event yields in corrected  $m_{HH}$  windows containing roughly 90% of each signal, for representative spin-0 mass hypotheses. The signal is normalized to the overall expected limit on its cross-section; its uncertainties are evaluated by adding all individual components in quadrature. The background yields and uncertainties are evaluated after a background-only fit to the data. [3].

$m(X)$ [GeV]	Corrected $m_{HH}$ range [GeV]	Data	Background model	Spin-0 signal model
260	[250, 321]	18 554	18 300 $\pm$ 110	503 $\pm$ 43
500	[464, 536]	2 827	2 866 $\pm$ 22	105.40 $\pm$ 5.70
800	[750, 850]	358	366.2 $\pm$ 7.3	37.70 $\pm$ 1.70
1200	[1079, 1250]	68	52.6 $\pm$ 1.7	11.71 $\pm$ 0.62

Table 10.2: Resolved 4*b* signal region data, estimated background, and signal event yields in corrected  $m_{HH}$  windows containing roughly 90% of each signal, for representative spin-2 mass hypotheses. The signal is normalized to the overall expected limit on its cross-section; its uncertainties are evaluated by adding all individual components in quadrature. The background yields and uncertainties are evaluated after a background-only fit to the data. [3].

$m(G_{KK}^*)$ [GeV]	Corrected $m_{HH}$ range [GeV]	Data	Background model	Spin-2 signal model
260	[250, 393]	26 775	26 650 $\pm$ 130	368 $\pm$ 25
500	[464, 636]	4 655	4 719 $\pm$ 37	138.60 $\pm$ 5.70
800	[707, 950]	795	811 $\pm$ 13	52.10 $\pm$ 1.90
1200	[993, 1279]	146	120.6 $\pm$ 2.8	14.45 $\pm$ 0.67

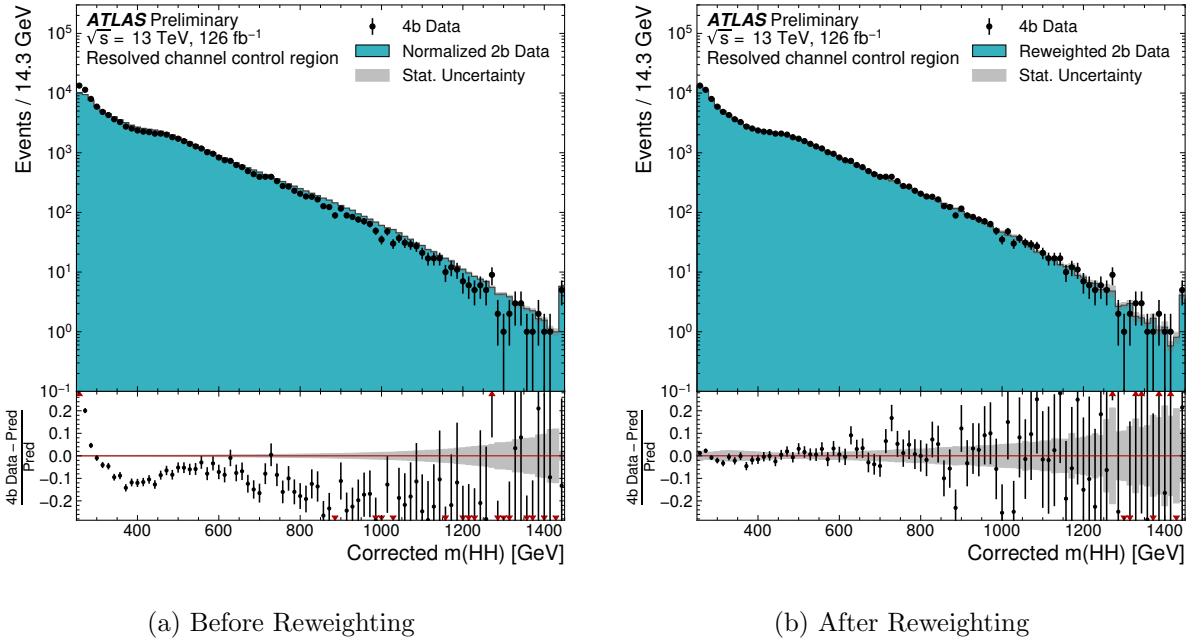


Figure 10.1: **Resonant Search:** Demonstration of the performance of the nominal reweighting in the control region on corrected  $m_{HH}$ , with Figure 10.1(a) showing  $2b$  events normalized to the total  $4b$  yield and Figure 10.1(b) applying the reweighting procedure. Agreement is much improved with the reweighting. Note that overall reweighted  $2b$  yield agrees with  $4b$  yield in the control region by construction.

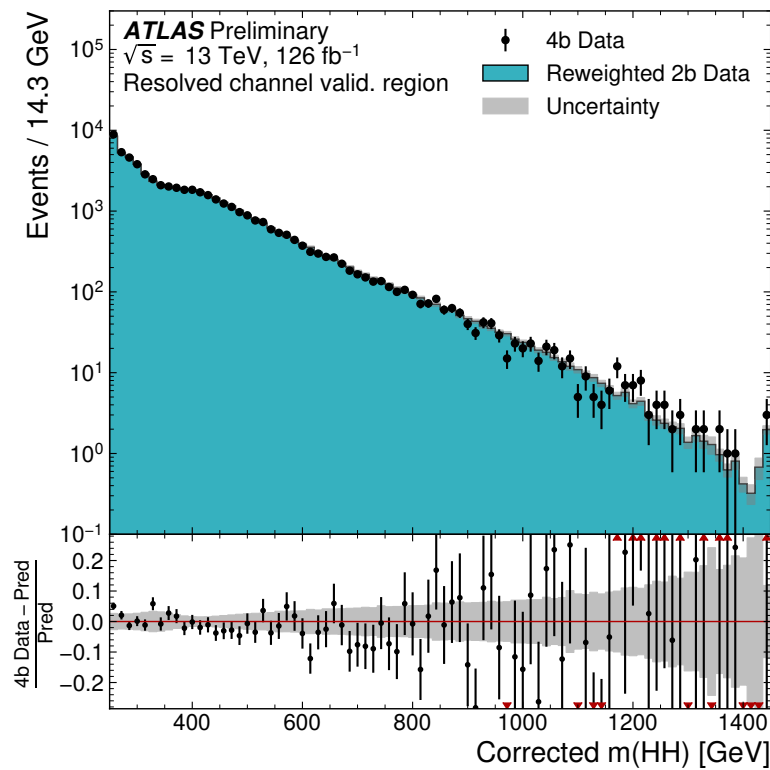


Figure 10.2: **Resonant Search:** Demonstration of the performance of the control region derived reweighting in the validation region on corrected  $m_{HH}$ . Agreement is generally good for this extrapolated estimate. Note that the uncertainty band includes the extrapolation systematic, which is defined by a reweighting trained in the validation region.

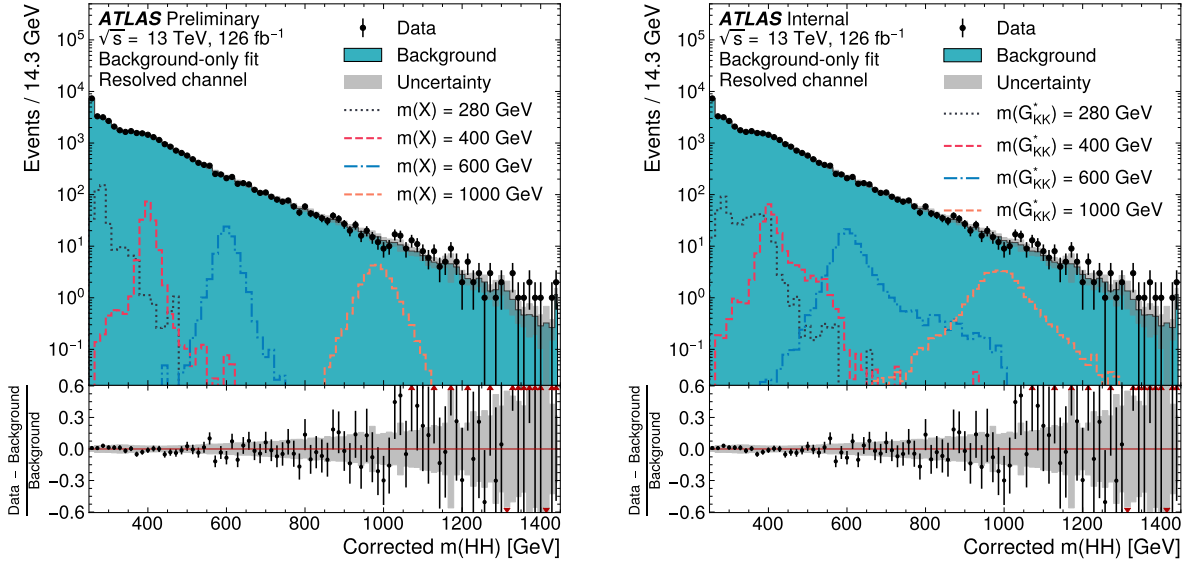


Figure 10.3: **Resonant Search:** Signal region agreement of the background estimate and observed data after a background-only profile likelihood fit. The left plot overlays a variety of representative spin-0 signals, while the right does the same for spin-2. The background and data are identical between the two. The closure is generally quite good, though there is an evident deficit in the background estimate relative to the data for higher values of corrected  $m_{HH}$ . Note that the spin-2 signals are significantly wider than the spin-0 signals. Near the kinematic threshold of 250 GeV, this leads to, e.g., the double peaked structure of the 280 GeV signal, which is understood to be an effect of the limited kinematic phase space in this region.

2623 10.1.2 Non-resonant Search

As discussed above, the non-resonant search splits the signal extraction into two categories of  $\Delta\eta_{HH}$  ( $0 \leq \Delta\eta_{HH} < 0.75$  and  $0.75 \leq \Delta\eta_{HH} < 1.5$ ), and two categories of  $X_{HH}$  ( $0 \leq X_{HH} < 0.95$  and  $0.95 \leq X_{HH} < 1.6$ ). To maintain reasonable statistics in each bin entering the signal extraction fit, a variable width binning is considered defined by a resolution parameter,  $r$ , and a set range in  $m_{HH}$ , where bin edges are determined iteratively as

$$b_{low}^{i+1} = b_{low}^i + r \cdot b_{low}^i, \quad (10.1)$$

2624 where  $b_{low}^i$  is the low edge of bin  $i$ . The parameters used here are  $r = 0.08$  over a range  
2625 from 280 GeV to 975 GeV, and underflow and overflow are included in the initial and final  
2626 bin contents respectively.  $m_{HH}$  with no correction is used as the final discriminant in each  
2627 category.

2628 A demonstration of the performance of the reweighting on distributions unrolled across  
2629 categories is shown in Figures 10.4 and 10.5 for the control region and Figures 10.6 and 10.7  
2630 for the validation region. A background-only profile likelihood fit is run for the distribution in  
2631 the signal region, and results with the Standard Model  $HH$  signal and  $\kappa_\lambda = 6$  signal overlaid  
2632 are shown for  $4b$  in Figure 10.8 and  $3b1l$  in Figure 10.9. Note that the plots show the sum  
2633 across all years, but the signal extraction fit and background estimate are run with the years  
2634 separately. All bins are normalized to represent a density of Events / 15 GeV.

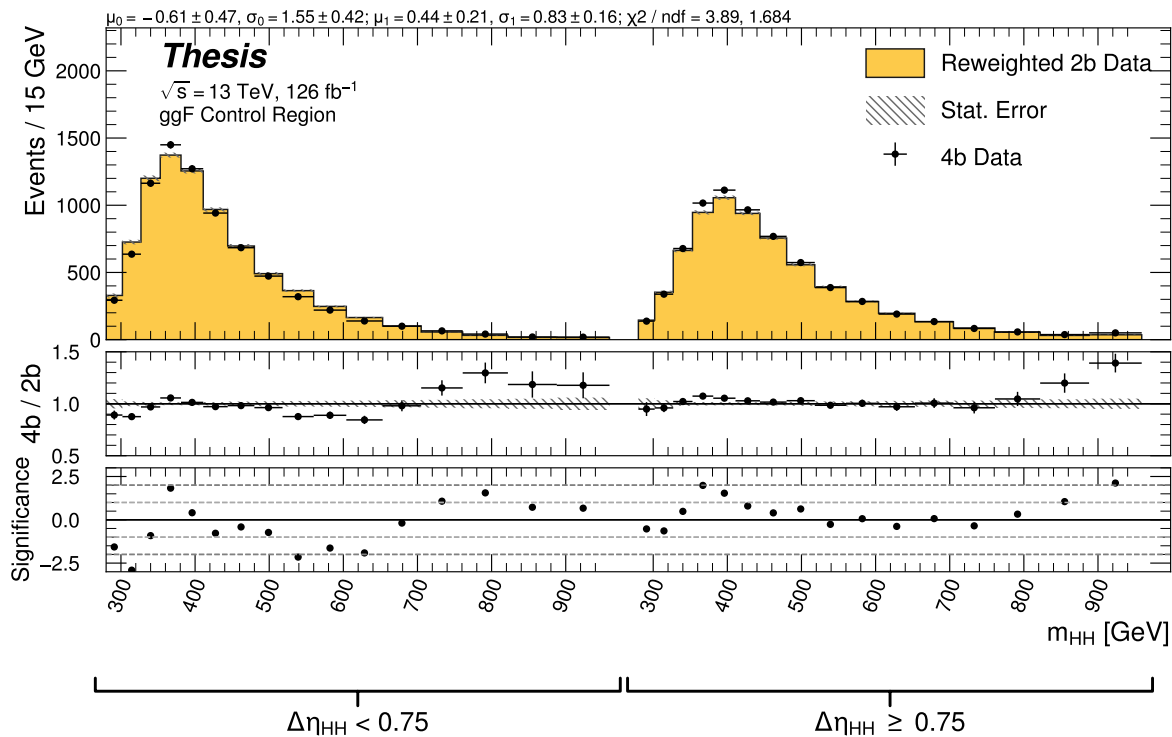


Figure 10.4: **Non-resonant Search (4b)**: Demonstration of the performance of the nominal reweighting in the control region on  $m_{HH}$ , split into the two  $\Delta\eta_{HH}$  regions. Closure is generally good, with some residual mis-modeling in the low  $\Delta\eta_{HH}$  region near 600 GeV.

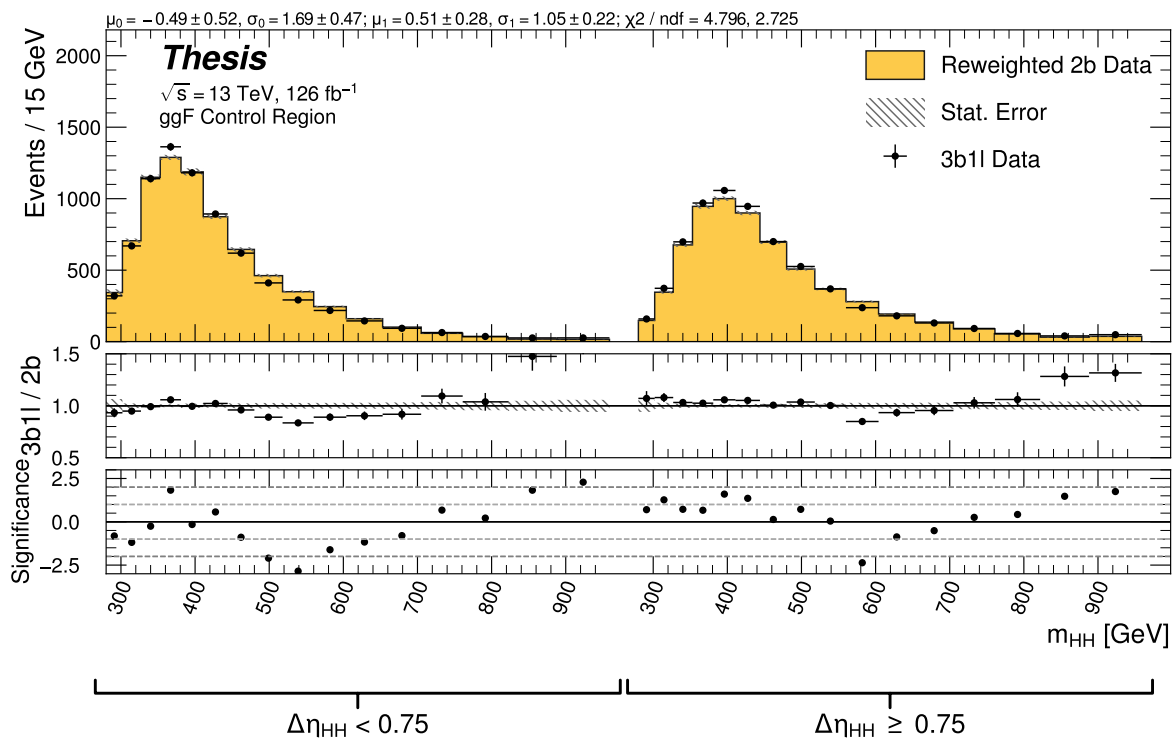


Figure 10.5: **Non-resonant Search (3b1l):** Demonstration of the performance of the nominal reweighting in the control region on  $m_{HH}$ , split into the two  $\Delta\eta_{HH}$  regions. Closure is generally good, with similar conclusions as for the  $4b$  region.

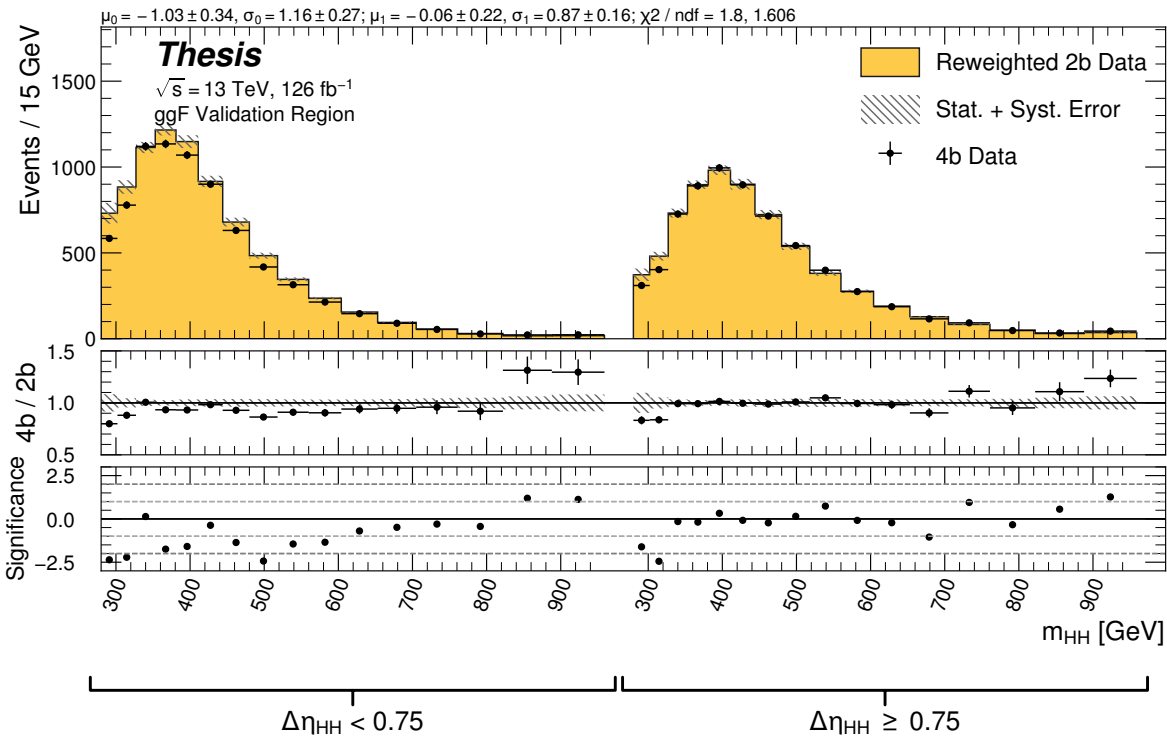


Figure 10.6: **Non-resonant Search (4b)**: Demonstration of the performance of the nominal reweighting in the validation region on  $m_{HH}$ , split into the two  $\Delta\eta_{HH}$  regions. The low  $\Delta\eta_{HH}$  region is consistently overestimated, but, systematic uncertainties are defined via the difference between VR and CR estimates.

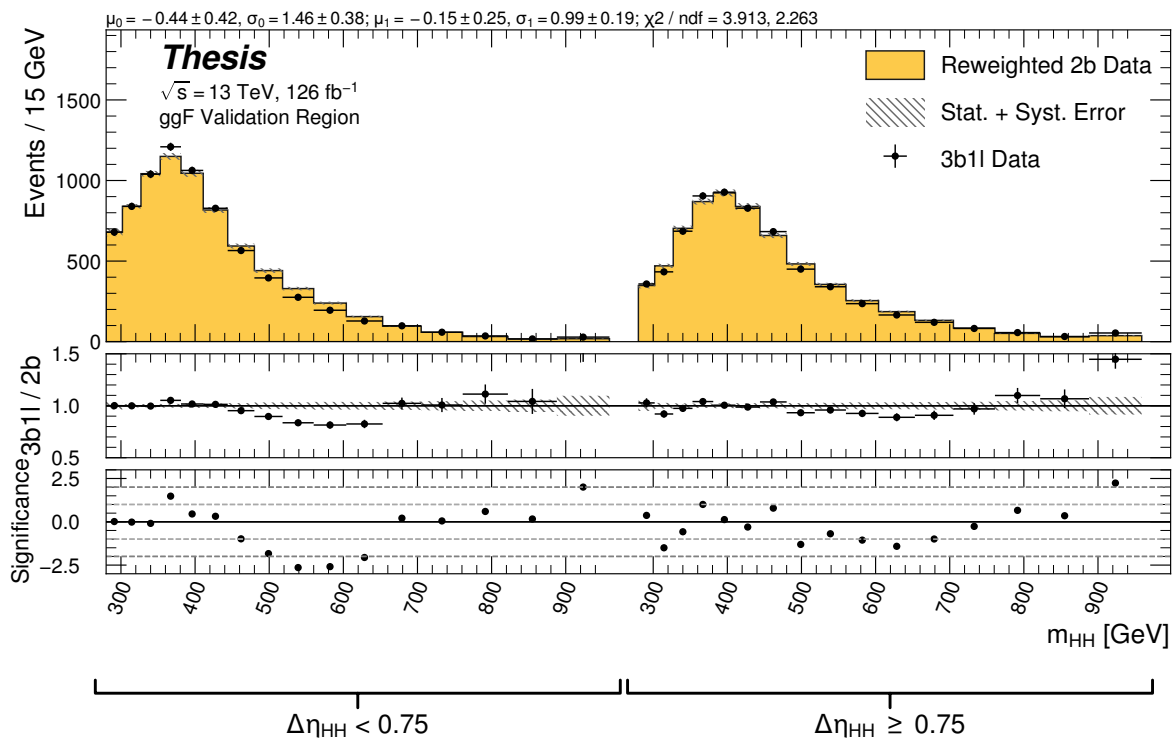


Figure 10.7: **Non-resonant Search (3b1l):** Demonstration of the performance of the nominal reweighting in the validation region on  $m_{HH}$ , split into the two  $\Delta\eta_{HH}$  regions. A deficit is present near 600 GeV, but agreement is fairly good otherwise.

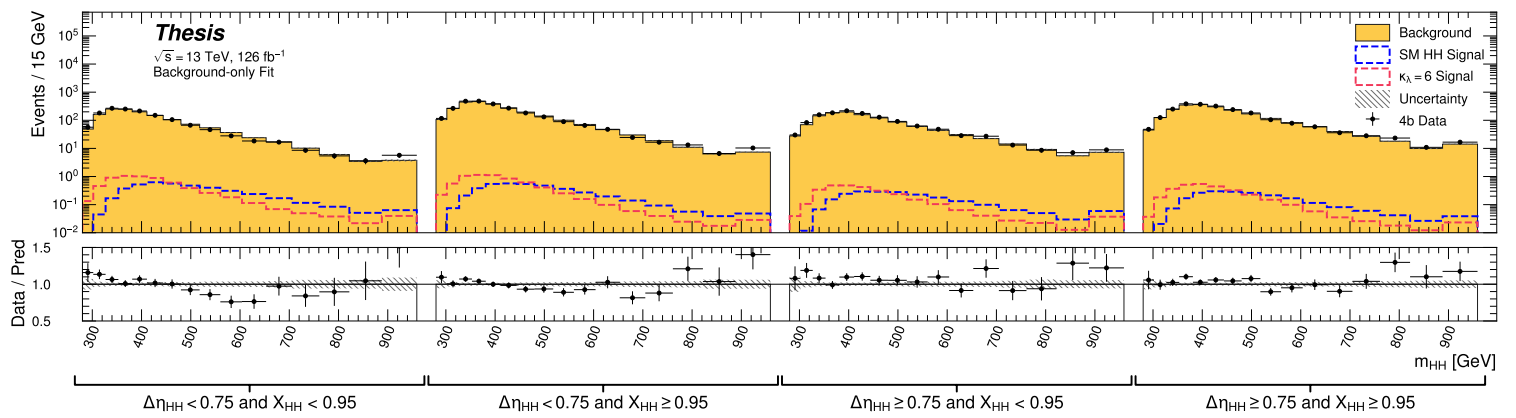


Figure 10.8: **Non-resonant Search (4b):** Signal region agreement of the background estimate and observed data after a background-only profile likelihood fit for the 4b channels, with Standard Model and  $\kappa_\lambda = 6$  signal overlaid for reference. Modeling is generally quite good near the Standard Model peak, but disagreements are seen at very low and high masses. A deficit is present in low  $\Delta\eta_{HH}$  bins near 600 GeV.

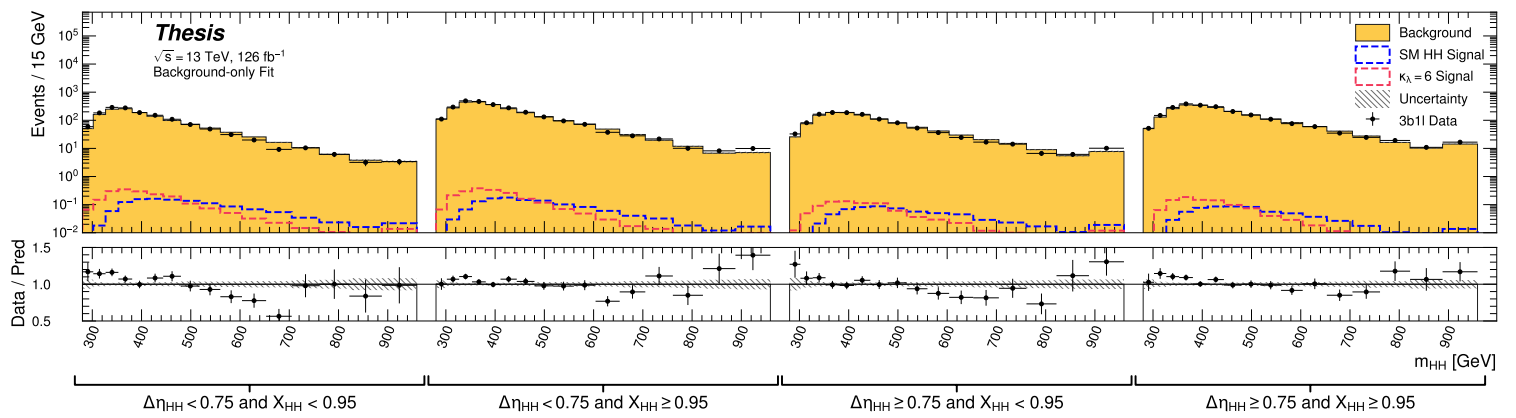


Figure 10.9: **Non-resonant Search (3b1l):** Signal region agreement of the background estimate and observed data after a background-only profile likelihood fit for the 3b1l channels, with Standard Model and  $\kappa_\lambda = 6$  signal overlaid for reference. Conclusions are very similar to the 4b channels, with generally good modeling near the Standard Model peak, but disagreements at very low and high masses. A deficit is present near 600 GeV.

2635 **10.2 Statistical Analysis**

2636 The resonant analysis is used to set a 95% confidence level upper limit on the  $pp \rightarrow X \rightarrow$   
2637  $HH \rightarrow b\bar{b}b\bar{b}$  and  $pp \rightarrow G_{KK}^* \rightarrow HH \rightarrow b\bar{b}b\bar{b}$  cross-sections, while the non-resonant analysis  
2638 is used to set a 95% confidence level upper limit on the  $pp \rightarrow HH \rightarrow b\bar{b}b\bar{b}$  cross sections for  
2639 a variety of values of the trilinear Higgs coupling.

2640 The upper limit is extracted using the  $CL_s$  method [116]. The test statistic used is  $q_\mu$   
2641 [117], where  $\mu$  is the signal strength, and  $\theta$  represents the nuisance parameters. A single  
2642 hat represents the maximum likelihood estimate of a parameter, while  $\hat{\theta}(x)$  represents the  
2643 conditional maximum likelihood estimate of the nuisance parameters if the signal cross-section  
2644 is fixed at  $x$ .

$$q_\mu = \begin{cases} -2 \ln \left( \frac{\mathcal{L}(\mu, \hat{\theta}(\mu))}{\mathcal{L}(\hat{\mu}, \hat{\theta})} \right) & \hat{\mu} \leq \mu \\ 0 & \hat{\mu} > \mu \end{cases} \quad (10.2)$$

2645  $CL_s$  for some test value of  $\mu$  is then defined by

$$CL_s = \frac{CL_{s+b}}{CL_b} = \frac{p(q_\mu \geq q_{\mu, \text{obs}} | s+b)}{p(q_\mu \geq q_{\mu, \text{obs}} | b)}, \quad (10.3)$$

2646 where the  $p$ -values are calculated in the asymptotic approximation [117], which is valid in  
2647 the large sample limit.

2648 The signal cross-section  $\mu$  fb is excluded at the 95% confidence level if  $CL_s < 0.05$ .

2649 Nuisance parameter pulls and impacts for the background extrapolation uncertainties  
2650 are shown for representative scalar resonances in Figure 10.10. Note that the fit includes all  
2651 uncertainties. The  $H_T$  nuisance parameters are significantly pulled, corresponding to the  
2652 expectation that the resonant validation region is more similar to the signal region than  
2653 the resonant control region is, though the control region is where the nominal estimate is  
2654 derived. A variety of cross-checks have been done to confirm the healthy behavior of the  
2655 signal extraction fit, despite these large pulls.

2656 Corresponding nuisance parameter pulls for the Standard Model non-resonant search are  
2657 shown in Figure 10.11. There are significantly more parameters than the resonant search  
2658 due to the category scheme, as well as due to the splitting of the control/validation region  
2659 comparison systematic into four signal region quadrants. In general, however, the pulls  
2660 are well behaved, and are generally consistent with 0. The largest deviating pulls are less  
2661 constrained than in the resonant search, such that these deviations are still within  $2\sigma$  of 0.

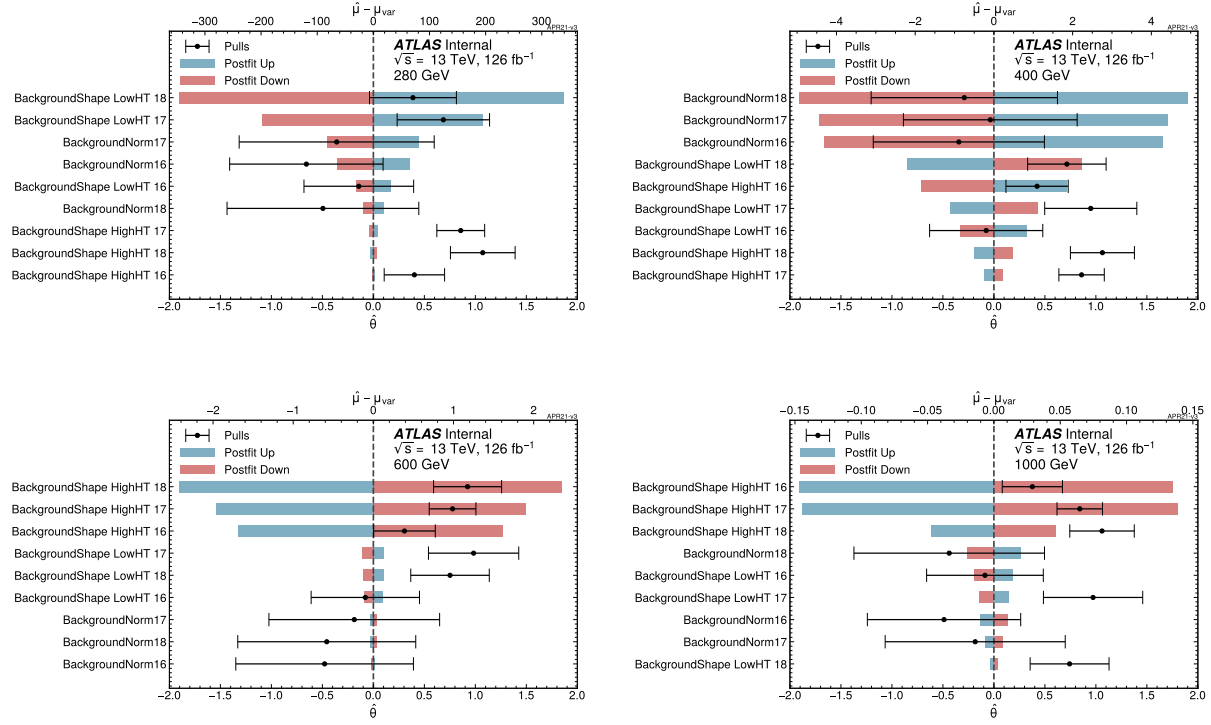


Figure 10.10: Pulls and impacts of the background extrapolation uncertainties for the resonant analysis, ranked by magnitude of post-fit impact and shown for a variety of representative scalar signals. Significant pulls of the  $H_T$  systematics are present, corresponding to the expectation that the validation region is more similar to the signal region than the control region is. Nuisance parameter pulls are generally consistent across signal mass, but impacts vary, with low  $H_T$  having the largest impact for low mass, and high  $H_T$  for high mass. 400 GeV is near the split between the two regimes.

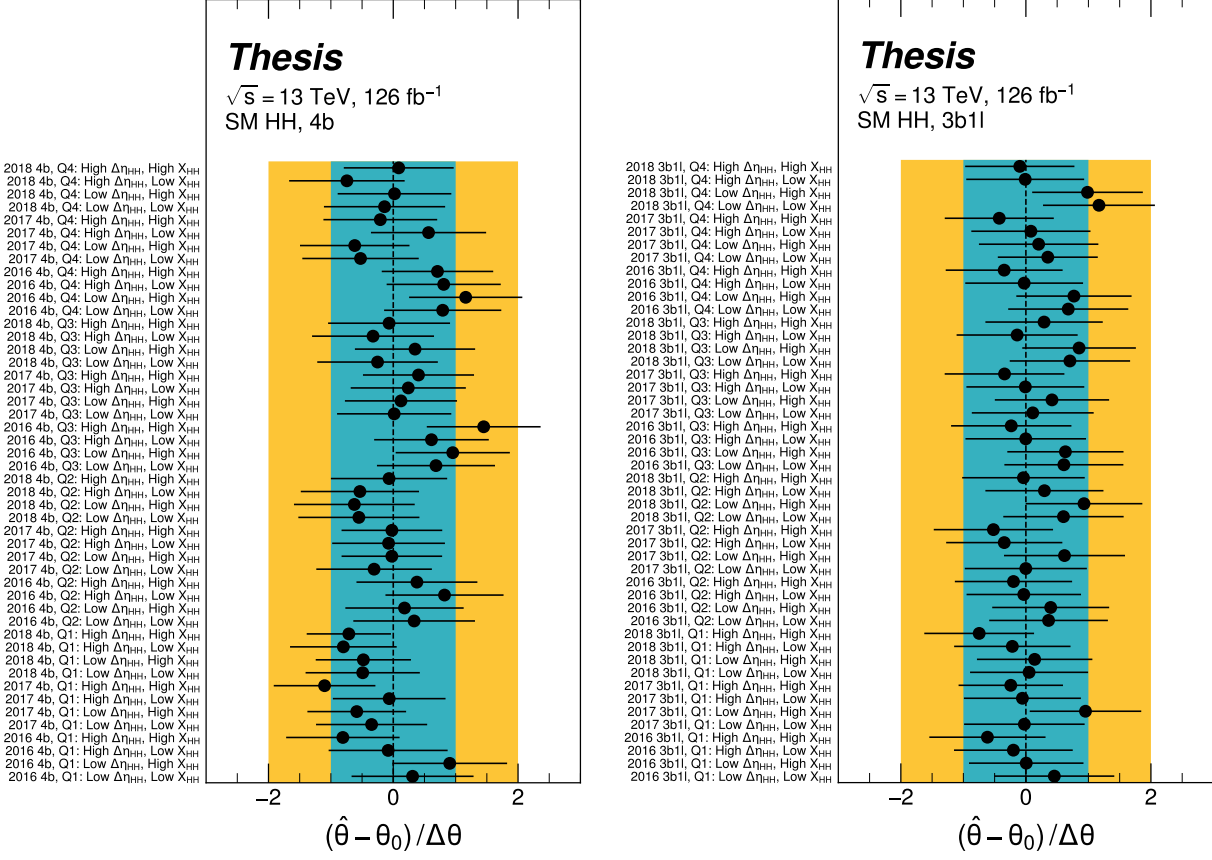


Figure 10.11: Background control/validation region systematic nuisance parameter pulls for the Standard Model non-resonant signal, shown for 4b (left) and 3b1l (right) separately, though the two channels are fit together. There are four signal region quadrant nuisance parameters for each category in the  $2 \times 2$  scheme in  $\Delta\eta_{HH}$  and  $X_{HH}$ , and each year is treated as a separate channel in the fit. Pulls are generally consistent with zero, though there are some trends: quadrant 1 4b tends to be pulled negatively, 2016 tends to be pulled positively. Note that 4b dominates the sensitivity relative to 3b1l.

2662 **10.3 Results**

2663 Figure 10.12 shows the expected limit for the spin-0 and spin-2 resonant search. The resolved  
2664 channel covers the range between 251 and 1500 GeV and is combined with the boosted channel  
2665 (see Appendix A) between 900 and 1500 GeV. The boosted channel then extends to 5 TeV.  
2666 All results use the asymptotic approximation, though the validity of such an approximation  
2667 for the boosted results above 3 TeV is being studied. The most significant excess is seen for a  
2668 signal mass of 1100 GeV, with local significance of  $2.6\sigma$  for the spin-0 signal and  $2.7\sigma$  for the  
2669 spin-2 signal. To account for the look-elsewhere effect, namely, the fact that the search is  
2670 performed over many mass points rather than just one, a global significance is calculated  
2671 following the procedure in [118]. Pseudo-experiments are generated from a background-only  
2672 model which has been fit to data. These are used to construct a distribution of local  $p$ -values  
2673 as a function of resonance mass. The number of level crossings below a reference level of  
2674  $p = 0.5$  is used together with the local  $p$ -value to compute a global  $p$ -value. After this  
2675 procedure, the local significance of the 1100 GeV excess is reduced to a global significance of  
2676  $1.0\sigma$  and  $1.2\sigma$  for spin-0 and spin-2 respectively.

2677 The spin-2 bulk Randall-Sundrum model with  $k/\overline{M}_{\text{Pl}} = 1$  is excluded for graviton masses  
2678 between 298 and 1440 GeV.

2679 Results from the early Run 2  $4b$  resonant search [2] are included in Figure 10.13 for  
2680 comparison. The full Run 2 results of this thesis represent an improvement in sensitivity, with  
2681 an expanded exclusion for the spin-2 search of graviton masses between 298 and 1440 GeV,  
2682 relative to the early Run 2 result, with exclusion between 313 and 1362 GeV. An excess is  
2683 present in the early Run 2 results at 280 GeV, with local (global) significance  $3.6(2.3)\sigma$ . This  
2684 is no longer present in the full Run 2 results, indicative of improved background modeling in  
2685 this low mass region.

2686 Preliminary results are presented here for the gluon-gluon fusion non-resonant search,  
2687 combining results from the  $4b$  and  $3b + 1l$  signal regions in the  $2 \times 2$  category scheme in  
2688  $\Delta\eta_{HH}$  and  $X_{HH}$ . These results will be further combined with a VBF channel (discussed in

Observed	$-2\sigma$	$-1\sigma$	Expected	$+1\sigma$	$+2\sigma$
<b>4.4</b>	3.1	4.2	<b>5.9</b>	8.2	11.0

Table 10.3: Limits on Standard Model  $HH \rightarrow b\bar{b}b\bar{b}$  production, presented in units of the predicted Standard Model cross section. Results do not include signal systematics.

2689 Appendix A), but this is left for future work. Results shown here include background all  
 2690 background uncertainties, but do not include signal systematics. Limits are set for  $\kappa_\lambda$  values  
 2691 from  $-20$  to  $20$ . The cross section limit for  $HH$  production is set at  $140\text{ fb}$  ( $180\text{ fb}$ ) observed  
 2692 (expected), corresponding to an observed (expected) limit of  $4.4$  ( $5.9$ ) times the Standard  
 2693 Model prediction (see Table 10.3).  $\kappa_\lambda$  is constrained to be within the range  $-4.9 \leq \kappa_\lambda \leq 14.4$   
 2694 observed ( $-3.9 \leq \kappa_\lambda \leq 10.9$  expected). These results are shown in Figure 10.14.

2695 This is a significant improvement over the early Run 2 result, which achieved an observed  
 2696 (expected) limit of  $12.9$  ( $20.7$ ) times the Standard Model prediction. The dataset is  $4.6$  times  
 2697 larger, and a naive scaling of the early Run 2 result (Poisson statistics  $\implies$  a factor of  
 2698  $1/\sqrt{4.6}$ ) would predict an observed (expected) limit of  $6.0$  ( $9.7$ ) times the Standard Model.  
 2699 The result of  $4.4$  ( $5.9$ ) observed (expected) presented here is therefore both an improvement  
 2700 by a factor of  $3$  ( $3.5$ ) over the previous result and also beats the statistical scaling by around  
 2701  $30$  ( $40$ ) %, demonstrating the impact of the various analysis improvements presented here.  
 2702 Note again that these results do not include the complete set of uncertainties – however,  
 2703 the addition of the remaining uncertainties is expected to have no more than a few percent  
 2704 impact.

2705 Further comparisons of both the resonant and non-resonant results are presented in  
 2706 Chapter 11.

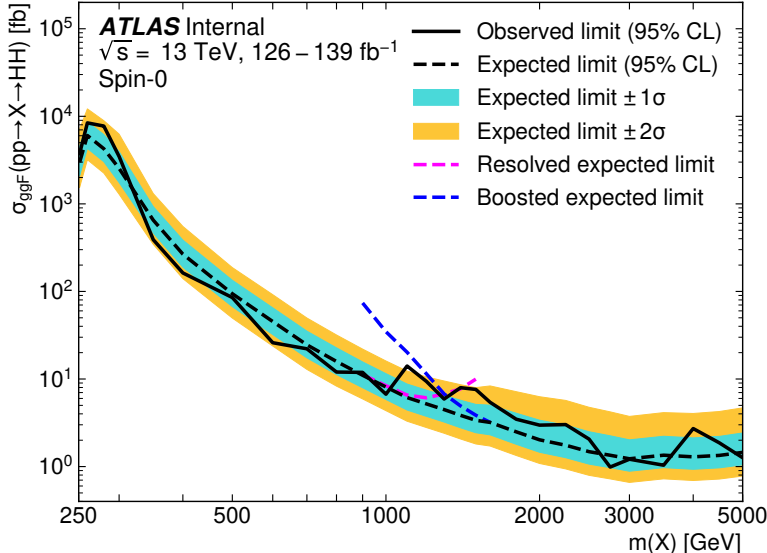
2707 The observed limits presented in Figure 10.14 are consistently above the  $2\sigma$  band for  
 2708 values of  $\kappa_\lambda \geq 5$ , peaking at a local significance of  $3.8\sigma$  for  $\kappa_\lambda = 6$ . As this analysis is  
 2709 optimized for points near the Standard Model, and as there is no excess present in more

sensitive channels in this same region (e.g.  $HH \rightarrow bb\gamma\gamma$  [98]), it is not believed this is a real effect, but is rather due to a mis-modeling of the background at low mass, where the min  $\Delta R$  pairing has poor signal efficiency and the assumption of well behaved background in the mass plane breaks down. This is consistent with the location of the  $\kappa_\lambda = 6$  signal in  $m_{HH}$ , as shown in Figures 10.8 and 10.9. It was considered, but not implemented, for this analysis to impose a cut on  $m_{HH}$  near 350 or 400 GeV to avoid such a low mass modeling issue.

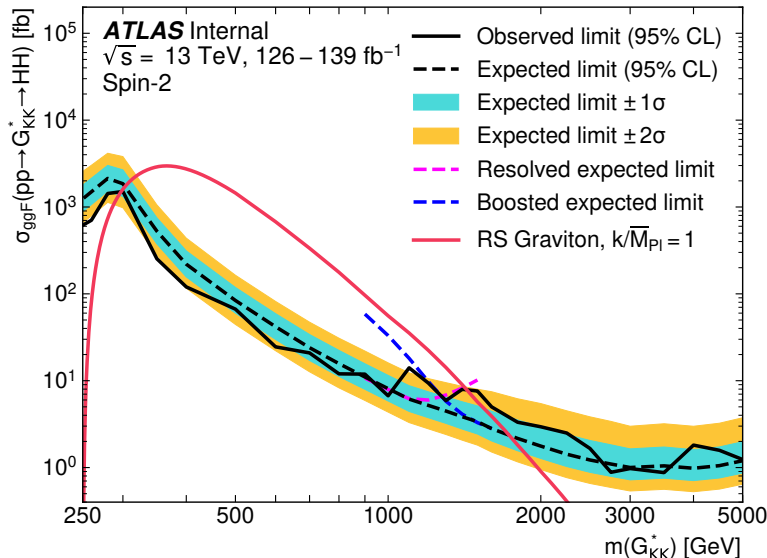
To check the impact of if such a cut would have been imposed, and to verify that the excess is due to the low mass regime, the same set of limits is run without the low mass bins. In this case, the first few bins in  $m_{HH}$  are simply dropped, such that everything else, including the higher mass bin edges, is kept the same. Due to the variable width binning, this corresponds to an  $m_{HH}$  cut of 381 GeV. The results of this check are shown in Figure 10.15, and the corresponding limits for Standard Model  $HH$  are quoted in Table 10.4. With the  $m_{HH}$  cut imposed, there is a slight degradation in the expected limits for larger positive and negative values of  $\kappa_\lambda$ , but the points near the Standard Model are nearly identical. Further, the observed excess is significantly reduced, with observed limits for  $\kappa_\lambda \geq 5$  now falling entirely within the expected  $1\sigma$  band. Due to the preliminary nature of these results, further study is left for future work. However, in conjunction with the  $HH \rightarrow bb\gamma\gamma$  results and expectations about the difficulty of the background estimation at low mass, it is believed that this is demonstrative of a mis-modeling rather than a real excess.

<b>Observed</b>	$-2\sigma$	$-1\sigma$	<b>Expected</b>	$+1\sigma$	$+2\sigma$
<b>3.7</b>	3.2	4.3	<b>5.9</b>	8.3	11.2

Table 10.4: Limits on Standard Model  $HH \rightarrow b\bar{b}b\bar{b}$  production, presented in units of the predicted Standard Model cross section, corresponding to the  $m_{HH} > 381$  GeV selection of Figure 10.15. Results do not include signal systematics. The deficit in the observed limit is larger than that of Table 10.3, but still within the  $2\sigma$  band. There are only very minor differences in the expected limit band.

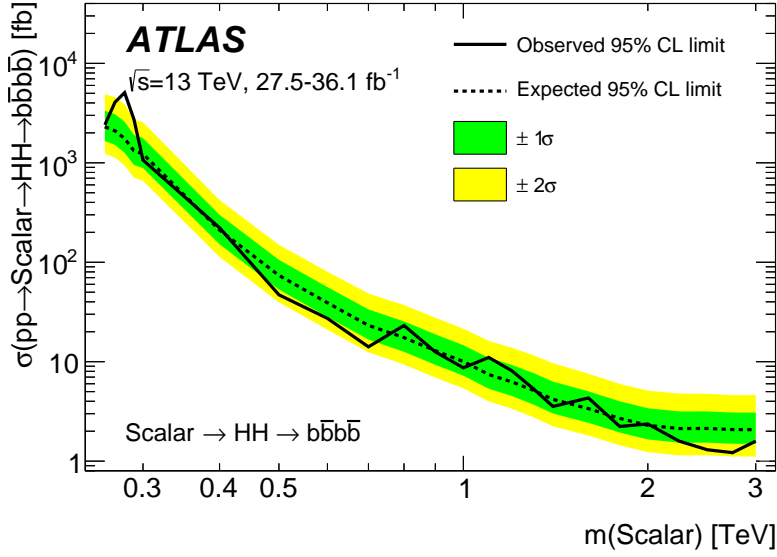


(a)

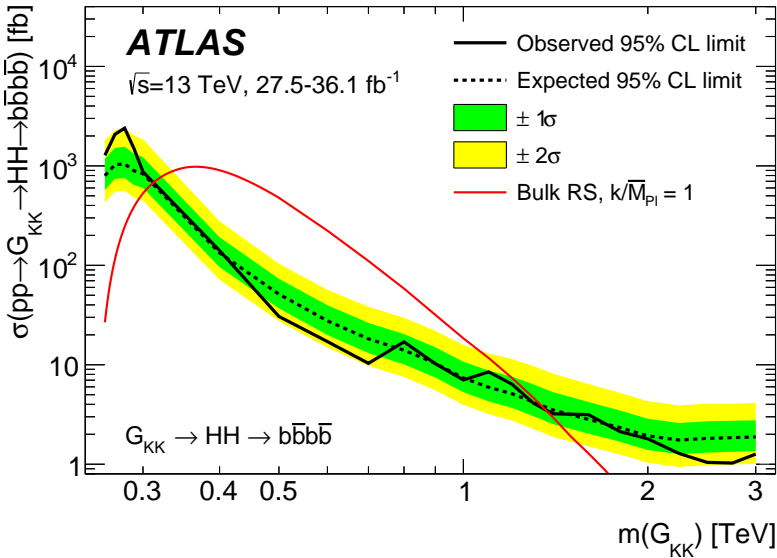


(b)

Figure 10.12: Expected (dashed black) and observed (solid black) 95% CL upper limits on the cross-section times branching ratio of resonant production for spin-0 ( $X \rightarrow HH$ ) and spin-2 ( $G_{KK}^* \rightarrow HH$ ). The  $\pm 1\sigma$  and  $\pm 2\sigma$  ranges for the expected limits are shown in the colored bands. The resolved channel expected limit is shown in dashed pink and covers the range from 251 and 1500 GeV. It is combined with the boosted channel (dashed blue) between 900 and 1500 GeV. The theoretical prediction for the bulk RS model with  $k/\bar{M}_{Pl} = 1$  [25] (solid red line) is shown, with the decrease below 350 GeV due to a sharp reduction in the  $G_{KK}^* \rightarrow HH$  branching ratio. The nominal  $H \rightarrow b\bar{b}$  branching ratio is taken as 0.582. Note that all results use the asymptotic approximation, though the validity of this approximation for the boosted results above 3 TeV is being evaluated.



(a)



(b)

Figure 10.13: Expected (dashed black) and observed (solid black) 95% CL upper limits or spin-0 ( $\text{Scalar} \rightarrow HH \rightarrow b\bar{b}b\bar{b}$ ) and spin-2 ( $G_{KK} \rightarrow HH \rightarrow b\bar{b}b\bar{b}$ ) from the early Run 2 4b search [2], to be compared with the results in Figure 10.12. Note that the  $y$ -axis scaling differs from Figure 10.12 by a factor of the  $HH \rightarrow b\bar{b}b\bar{b}$  branching ratio. An excess is present at 280 GeV, with local (global) significance  $3.6(2.3)\sigma$ . The spin-2 bulk Randall-Sundrum model with  $k/\bar{M}_{\text{Pl}} = 1$  is excluded for graviton masses between 313 and 1362 GeV.

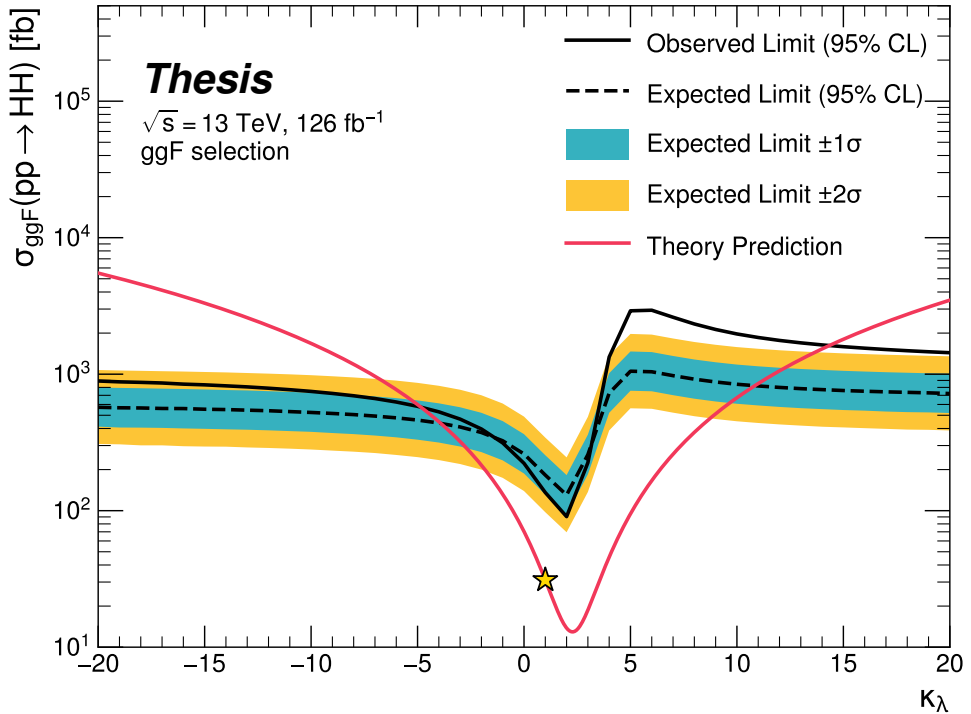


Figure 10.14: Expected (dashed black) and observed (solid black) 95% CL upper limits on the cross-section times branching ratio of non-resonant production for a range of values of the Higgs self-coupling, with the Standard Model value ( $\kappa_\lambda = 1$ ) illustrated with a star. The  $\pm 1\sigma$  and  $\pm 2\sigma$  ranges for the expected limits are shown in the colored bands. The cross section limit for  $HH$  production is set at 140 fb (180 fb) observed (expected), corresponding to an observed (expected) limit of 4.4 (5.9) times the Standard Model prediction.  $\kappa_\lambda$  is constrained to be within the range  $-4.9 \leq \kappa_\lambda \leq 14.4$  observed ( $-3.9 \leq \kappa_\lambda \leq 10.9$  expected). The nominal  $H \rightarrow b\bar{b}$  branching ratio is taken as 0.582. The excess present for  $\kappa_\lambda \geq 5$  is thought to be due to a low mass background mis-modeling, present due to the optimization of this analysis for the Standard Model point, and is not present in more sensitive channels in this same region (e.g.  $HH \rightarrow bb\gamma\gamma$  [98]).

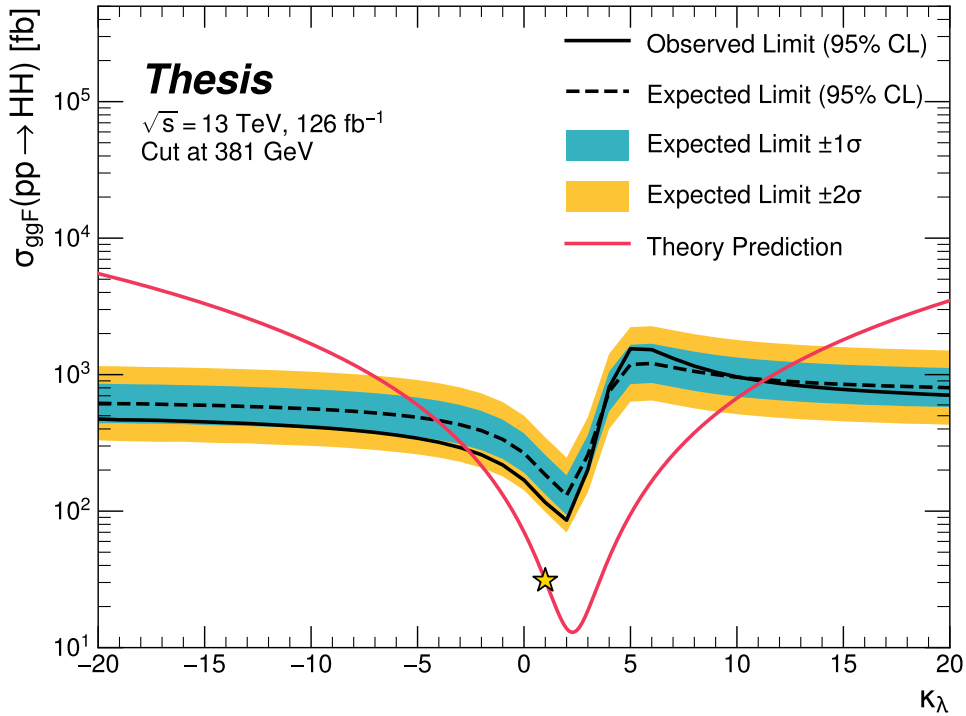


Figure 10.15: Limits including only events above 381 GeV in  $m_{HH}$ , to be compared with the limits in Figure 10.14. Such a cut is accomplished by dropping  $m_{HH}$  bins below 381 GeV, with the value of 381 GeV determined by the optimized variable width binning. All other aspects of the procedure and inputs are kept the same as in Figure 10.14. The excess at and above  $\kappa_\lambda = 5$  is significantly reduced, demonstrating that such an excess is driven by low mass. Notably, there is minimal impact on the expected sensitivity with this  $m_{HH}$  cut.

2729

## Chapter 11

2730

### COMPARISONS WITH OTHER CHANNELS

2731 ATLAS has published comparisons of the released Full Run 2 results [119], shown for  
 2732 the spin-0 resonant results in Figure 11.1 and the non-resonant results in Figure 11.2. The  
 2733 results of this thesis for the  $b\bar{b}b\bar{b}$  channel are included in the resonant plot up to 3 TeV. The  
 2734 preliminary non-resonant results presented here are not yet included. Both figures include a  
 2735 comparison with the combined early Run 2 result [26].

2736 For the resonant, the  $b\bar{b}b\bar{b}$  channel has the leading sensitivity above a mass of around  
 2737 700 GeV, and is competitive across much of the considered range, though it has limited sensi-  
 2738 tivity at very low masses. The individual channels shown in general represent improvements  
 2739 over the early Run 2 combined result, a promising indicator for a large increase in sensitivity  
 2740 with the full Run 2 combination across channels, for which the  $b\bar{b}b\bar{b}$  channel will be a strong  
 2741 contributor.

2742 The Standard Model non-resonant limits presented in this thesis are 4.4(5.9) times the  
 2743 Standard Model observed (expected) for the gluon-gluon fusion channel only. This is a  
 2744 significant gain on its own above the early Run 2 combined result. Though the leading  
 2745 channels presented in Figure 11.2 include both VBF and ggF production modes, and are  
 2746 normalized as such, the  $b\bar{b}b\bar{b}$  results of this thesis can still be seen to be quite competitive,  
 2747 again demonstrating a strong contribution to the ATLAS experimental results for  $HH$ .  
 2748 Roughly estimating the combined result for full Run 2  $b\bar{b}b\bar{b}$ ,  $b\bar{b}\tau^+\tau^-$ , and  $b\bar{b}\gamma\gamma$  yields a limit  
 2749 of around 2 to 3 times the Standard Model. Such a result sets the stage for a very exciting  
 2750 Run 3 – with a projected factor of around 2× increase in luminosity, plus any additional  
 2751 analysis improvements, sensitivity to  $HH$  may be just on the horizon.

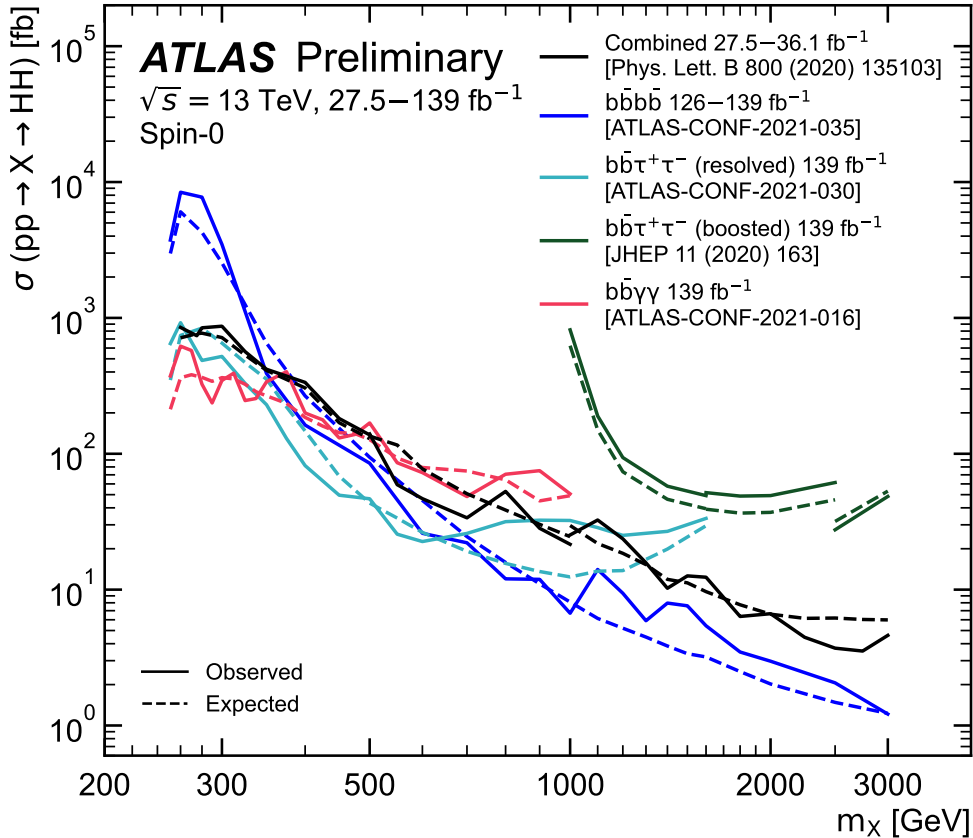


Figure 11.1: Comparison of full Run 2 ATLAS  $HH$  searches for spin-0 resonances. The  $b\bar{b}b\bar{b}$  channel (blue) is compared with full Run 2 results from  $b\bar{b}\tau^+\tau^-$  (both resolved and boosted) and  $b\bar{b}\gamma\gamma$ , as well as the combined early Run 2 results. The  $b\bar{b}b\bar{b}$  channel has leading sensitivity above a mass of around 700 GeV, and is competitive with other channels across much of the mass range, demonstrating a strong contribution to the ATLAS  $HH$  experimental results. [119]

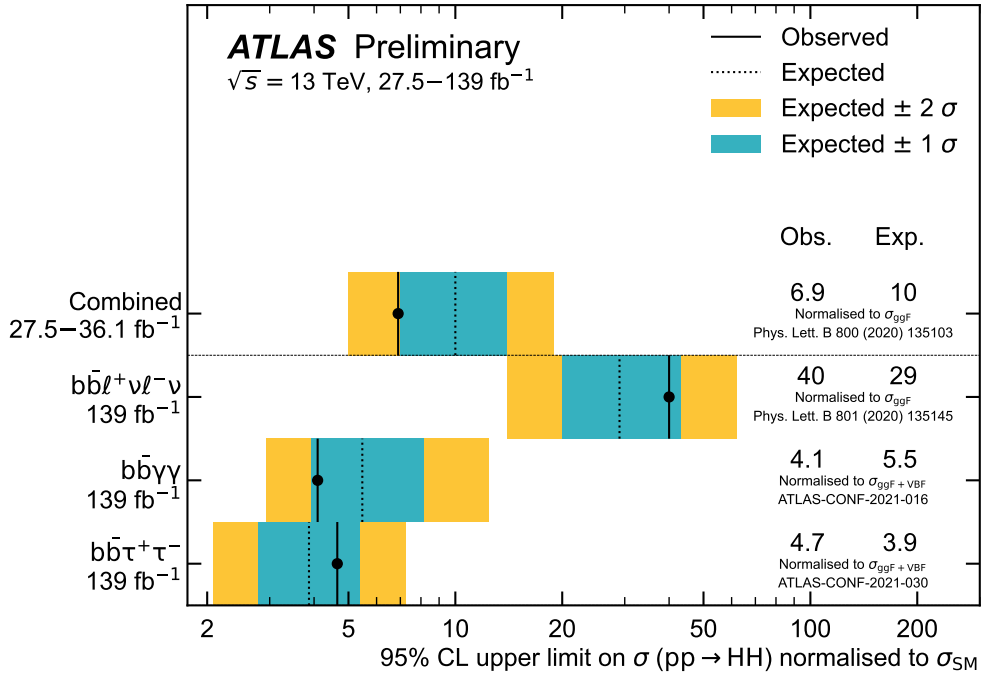


Figure 11.2: Comparison of full Run 2 ATLAS  $HH$  searches for Standard Model  $HH$  production. The preliminary results presented in this thesis are not yet included in these results. However, the results presented in Table 10.3 are quite competitive with the results from  $b\bar{b}\tau^+\tau^-$  and  $b\bar{b}\gamma\gamma$ , two of the ATLAS channels with leading sensitivity in the search for  $HH$ . Note that these results include signals produced via both gluon-gluon fusion (ggF) and vector boson fusion (VBF), and are normalized as such, while the results of this thesis only include (and are normalized to) ggF production [119]

2752

## Chapter 12

2753

### CONCLUSIONS

2754 This thesis has provided an overview of the Standard Model, with an emphasis on pair  
 2755 production of Higgs bosons and how this process may be used to both verify the Standard  
 2756 Model and to search for new physics. An overview of the Large Hadron Collider and the  
 2757 ATLAS detector has been provided, and the design and use of simulation infrastructure  
 2758 has been explained, including work to improve hadronic shower modeling in fast detector  
 2759 simulation. The translation of detector level information to analysis level information has  
 2760 been explained, with an emphasis on jets and the identification of  $B$  hadron decay. Finally,  
 2761 two searches for Higgs boson pair production have been presented, with a complete set of  
 2762 results for resonant production included, focusing on searches beyond the Standard Model,  
 2763 and a preliminary set of results for non-resonant production, targeting Standard Model  
 2764 production, with variations of the Higgs self-coupling.

2765 This thesis represents a powerful contribution in multiple areas. My simulation work  
 2766 provides two powerful options for the improvement of hadronic showering in fast calorimeter  
 2767 simulation, and is emblematic of a hybrid approach to fast simulation which may leverage both  
 2768 expert knowledge and the power of machine learning methods. The  $HH$  results presented in  
 2769 this thesis are leading contributions to the full Run 2 statement from ATLAS about Higgs  
 2770 boson pair production, and improve on previous results in a variety of ways.

2771 Within these  $HH$  searches, I was responsible for the development of the background  
 2772 estimation and corresponding uncertainties, one of the most important aspects of the  $4b$   
 2773 channel. For the resonant search, I contributed strongly to the development of the selection,  
 2774 the documentation, and final development of the result. No significant excesses are observed,  
 2775 but a low mass mis-modeling has been reduced relative to the early Run 2 searches, and the

2776 limits set by the  $b\bar{b}b\bar{b}$  channel are very competitive with the other full Run 2 ATLAS results.

2777 For the non-resonant search, in addition to the background estimation, I was behind many  
2778 of the changes that were made relative to the resonant search. These changes result in a very  
2779 competitive limit of 4.4(5.9) times the Standard Model observed (expected), a result which is  
2780 both competitive with the other leading channels, and beats a projection of the early Run 2  
2781 result (from luminosity scaling) by 30 (40) %. This represents a significant improvement in  
2782 the analysis strategy, and sets the stage for a very promising set of  $HH$  results, both from  
2783 the full Run 2 combination and looking towards Run 3. Though an excess is seen for values  
2784 of  $\kappa_\lambda \geq 5$ , such an excess is demonstrated to be due to the low mass regime, where  $b\bar{b}b\bar{b}$  has  
2785 limited sensitivity.

2786 With the contributions of this thesis work, the  $b\bar{b}b\bar{b}$  channel remains one of the leading  
2787  $HH$  channels in sensitivity. With further increases in luminosity, as well as development of  
2788 even more advanced analysis techniques (see, e.g., Appendix B), the future is bright for  $HH$   
2789 at the LHC.

2790

## BIBLIOGRAPHY

- [1] S. Gasiorowski and H. Gray, *Fast Calorimeter Simulation in ATLAS*, EPJ Web Conf. **245** (2020) 02002. 7 p, URL: <https://cds.cern.ch/record/2756298> (cit. on pp. xxi, 59).
- [2] ATLAS Collaboration, *Search for pair production of Higgs bosons in the  $b\bar{b}b\bar{b}$  final state using proton–proton collisions at  $\sqrt{s} = 13$  TeV with the ATLAS detector*, JHEP **01** (2019) 030, arXiv: [1804.06174 \[hep-ex\]](https://arxiv.org/abs/1804.06174) (cit. on pp. xxii, 79, 88, 98, 105, 167, 172).
- [3] *Search for resonant pair production of Higgs bosons in the  $b\bar{b}b\bar{b}$  final state using pp collisions at  $\sqrt{s} = 13$  TeV with the ATLAS detector*, tech. rep., All figures including auxiliary figures are available at <https://atlas.web.cern.ch/Atlas/GROUPS/PHYSICS/CONFNOTES/ATL-CONF-2021-035>: CERN, 2021, URL: [http://cds.cern.ch/record/2777861](https://cds.cern.ch/record/2777861) (cit. on pp. xxii, 152).
- [4] A. Shmakov et al., *SPANet: Generalized Permutationless Set Assignment for Particle Physics using Symmetry Preserving Attention*, 2021, arXiv: [2106.03898 \[hep-ex\]](https://arxiv.org/abs/2106.03898) (cit. on p. xxiii).
- [5] D. M. Reiman, J. Tamanas, J. X. Prochaska, and D. Ďurovčíková, *Fully probabilistic quasar continua predictions near Lyman- $\alpha$  with conditional neural spline flows*, 2020, arXiv: [2006.00615 \[astro-ph.CO\]](https://arxiv.org/abs/2006.00615) (cit. on p. xxiii).
- [6] *A New Map of All the Particles and Forces*, <https://www.quantamagazine.org/a-new-map-of-the-standard-model-of-particle-physics-20201022/>, Accessed: 2021-07-23 (cit. on pp. 3, 27).
- [7] J. D. Jackson, *Classical electrodynamics; 2nd ed.* Wiley, 1975 (cit. on p. 2).

- 2813 [8] M. Thomson, *Modern particle physics*, Cambridge University Press, 2013, ISBN: 978-1-
- 2814 107-03426-6 (cit. on pp. 2, 48).
- 2815 [9] M. Srednicki, *Quantum Field Theory*, Cambridge Univ. Press, 2007 (cit. on p. 2).
- 2816 [10] M. Gell-Mann, *A schematic model of baryons and mesons*, Physics Letters **8** (1964)
- 2817 214, ISSN: 0031-9163, URL: <https://www.sciencedirect.com/science/article/pii/S0031916364920013> (cit. on p. 11).
- 2818 [11] G. Zweig, *An  $SU_3$  model for strong interaction symmetry and its breaking; Version 1*, tech. rep., CERN, 1964, URL: <https://cds.cern.ch/record/352337> (cit. on p. 11).
- 2819 [12] O. W. Greenberg, *Spin and Unitary-Spin Independence in a Paraquark Model of*
- 2820 *Baryons and Mesons*, Phys. Rev. Lett. **13** (20 1964) 598, URL: <https://link.aps.org/doi/10.1103/PhysRevLett.13.598> (cit. on p. 11).
- 2821 [13] M. Y. Han and Y. Nambu, *Three-Triplet Model with Double  $SU(3)$  Symmetry*, Phys.
- 2822 Rev. **139** (4B 1965) B1006, URL: <https://link.aps.org/doi/10.1103/PhysRev.139.B1006> (cit. on p. 11).
- 2823 [14] F. L. Wilson, *Fermi's Theory of Beta Decay*, American Journal of Physics **36** (1968)
- 2824 1150, eprint: <https://doi.org/10.1119/1.1974382>, URL: <https://doi.org/10.1119/1.1974382> (cit. on p. 14).
- 2825 [15] *The Nobel Prize in Physics 1979*, <https://www.nobelprize.org/prizes/physics/1979/summary/>, Accessed: 2021-07-23 (cit. on p. 15).
- 2826 [16] F. Englert and R. Brout, *Broken Symmetry and the Mass of Gauge Vector Mesons*, Phys. Rev. Lett. **13** (9 1964) 321, URL: <https://link.aps.org/doi/10.1103/PhysRevLett.13.321> (cit. on p. 20).
- 2827 [17] P. W. Higgs, *Broken Symmetries and the Masses of Gauge Bosons*, Phys. Rev. Lett. **13** (16 1964) 508, URL: <https://link.aps.org/doi/10.1103/PhysRevLett.13.508> (cit. on p. 20).
- 2828
- 2829
- 2830
- 2831
- 2832
- 2833
- 2834
- 2835
- 2836
- 2837

- 2838 [18] G. S. Guralnik, C. R. Hagen, and T. W. B. Kibble, *Global Conservation Laws and*  
 2839 *Massless Particles*, Phys. Rev. Lett. **13** (20 1964) 585, URL: <https://link.aps.org/doi/10.1103/PhysRevLett.13.585> (cit. on p. 20).
- 2841 [19] ATLAS Collaboration, *Observation of a new particle in the search for the Standard*  
 2842 *Model Higgs boson with the ATLAS detector at the LHC*, Phys. Lett. B **716** (2012) 1,  
 2843 arXiv: [1207.7214 \[hep-ex\]](https://arxiv.org/abs/1207.7214) (cit. on p. 20).
- 2844 [20] CMS Collaboration, *Observation of a new boson at a mass of 125 GeV with the CMS*  
 2845 *experiment at the LHC*, Phys. Lett. B **716** (2012) 30, arXiv: [1207.7235 \[hep-ex\]](https://arxiv.org/abs/1207.7235)  
 2846 (cit. on p. 20).
- 2847 [21] S. Weinberg, *A Model of Leptons*, Phys. Rev. Lett. **19** (21 1967) 1264, URL: <https://link.aps.org/doi/10.1103/PhysRevLett.19.1264> (cit. on p. 25).
- 2849 [22] ATLAS Collaboration, *Search for the  $HH \rightarrow b\bar{b}b\bar{b}$  process via vector-boson fusion*  
 2850 *production using proton–proton collisions at  $\sqrt{s} = 13$  TeV with the ATLAS detector*,  
 2851 JHEP **07** (2020) 108, arXiv: [2001.05178 \[hep-ex\]](https://arxiv.org/abs/2001.05178) (cit. on pp. 31, 78, 105, 197, 199),  
 2852 Erratum: JHEP **01** (2021) 145.
- 2853 [23] G. Branco et al., *Theory and phenomenology of two-Higgs-doublet models*, Physics  
 2854 Reports **516** (2012) 1, Theory and phenomenology of two-Higgs-doublet models,  
 2855 ISSN: 0370-1573, URL: <http://www.sciencedirect.com/science/article/pii/S0370157312000695> (cit. on pp. 32, 33).
- 2857 [24] K. Agashe, H. Davoudiasl, G. Perez, and A. Soni, *Warped gravitons at the CERN*  
 2858 *LHC and beyond*, Phys. Rev. D **76** (3 2007) 036006, URL: <https://link.aps.org/doi/10.1103/PhysRevD.76.036006> (cit. on pp. 32, 33).
- 2860 [25] A. Carvalho, *Gravity particles from Warped Extra Dimensions, predictions for LHC*,  
 2861 2018, arXiv: [1404.0102 \[hep-ph\]](https://arxiv.org/abs/1404.0102) (cit. on pp. 32, 33, 171).

- 2862 [26] ATLAS Collaboration, *Combination of searches for Higgs boson pairs in pp collisions*  
 2863 at  $\sqrt{s} = 13 \text{ TeV}$  with the ATLAS detector, *Phys. Lett. B* **800** (2020) 135103, arXiv:  
 2864 1906.02025 [hep-ex] (cit. on pp. 33, 36, 78, 175).
- 2865 [27] P. D. Group et al., *Review of Particle Physics*, *Progress of Theoretical and Experimental*  
 2866 *Physics* **2020** (2020), 083C01, ISSN: 2050-3911, eprint: <https://academic.oup.com/ptep/article-pdf/2020/8/083C01/34673722/ptaa104.pdf>, URL: <https://doi.org/10.1093/ptep/ptaa104> (cit. on p. 35).
- 2869 [28] T. van Ritbergen and R. G. Stuart, *On the precise determination of the Fermi coupling*  
 2870 *constant from the muon lifetime*, *Nuclear Physics B* **564** (2000) 343, ISSN: 0550-3213,  
 2871 URL: [http://dx.doi.org/10.1016/S0550-3213\(99\)00572-6](http://dx.doi.org/10.1016/S0550-3213(99)00572-6) (cit. on p. 35).
- 2872 [29] S. Dawson, A. Ismail, and I. Low, *What's in the loop? The anatomy of double Higgs*  
 2873 *production*, *Physical Review D* **91** (2015), ISSN: 1550-2368, URL: <http://dx.doi.org/10.1103/PhysRevD.91.115008> (cit. on p. 35).
- 2875 [30] A. M. Sirunyan et al., *Measurement of the top quark Yukawa coupling from  $t\bar{t}$  kinematic*  
 2876 *distributions in the dilepton final state in proton-proton collisions at  $\sqrt{s}=13 \text{ TeV}$* ,  
 2877 *Physical Review D* **102** (2020), ISSN: 2470-0029, URL: <http://dx.doi.org/10.1103/PhysRevD.102.092013> (cit. on p. 35).
- 2879 [31] S. Dawson, S. Dittmaier, and M. Spira, *Neutral Higgs-boson pair production at hadron*  
 2880 *colliders: QCD corrections*, *Physical Review D* **58** (1998), ISSN: 1089-4918, URL:  
 2881 <http://dx.doi.org/10.1103/PhysRevD.58.115012> (cit. on pp. 37, 197).
- 2882 [32] S. Borowka et al., *Higgs Boson Pair Production in Gluon Fusion at Next-to-Leading*  
 2883 *Order with Full Top-Quark Mass Dependence*, *Physical Review Letters* **117** (2016),  
 2884 ISSN: 1079-7114, URL: <http://dx.doi.org/10.1103/PhysRevLett.117.012001>  
 2885 (cit. on pp. 37, 197).

- 2886 [33] J. Baglio et al., *Gluon fusion into Higgs pairs at NLO QCD and the top mass*  
 2887 *scheme*, The European Physical Journal C **79** (2019), ISSN: 1434-6052, URL: <http://dx.doi.org/10.1140/epjc/s10052-019-6973-3> (cit. on pp. 37, 197).
- 2889 [34] D. de Florian and J. Mazzitelli, *Higgs Boson Pair Production at Next-to-Next-to-*  
 2890 *Leading Order in QCD*, Physical Review Letters **111** (2013), ISSN: 1079-7114, URL:  
 2891 <http://dx.doi.org/10.1103/PhysRevLett.111.201801> (cit. on pp. 37, 197).
- 2892 [35] D. Y. Shao, C. S. Li, H. T. Li, and J. Wang, *Threshold resummation effects in Higgs*  
 2893 *boson pair production at the LHC*, Journal of High Energy Physics **2013** (2013), ISSN:  
 2894 1029-8479, URL: [http://dx.doi.org/10.1007/JHEP07\(2013\)169](http://dx.doi.org/10.1007/JHEP07(2013)169) (cit. on pp. 37,  
 2895 197).
- 2896 [36] D. de Florian and J. Mazzitelli, *Higgs pair production at next-to-next-to-leading*  
 2897 *logarithmic accuracy at the LHC*, 2015, arXiv: [1505.07122 \[hep-ph\]](https://arxiv.org/abs/1505.07122) (cit. on pp. 37,  
 2898 197).
- 2899 [37] M. Grazzini et al., *Higgs boson pair production at NNLO with top quark mass effects*,  
 2900 Journal of High Energy Physics **2018** (2018), ISSN: 1029-8479, URL: [http://dx.doi.org/10.1007/JHEP05\(2018\)059](http://dx.doi.org/10.1007/JHEP05(2018)059) (cit. on pp. 37, 197).
- 2902 [38] J. Baglio et al., *gg → HH: Combined uncertainties*, Physical Review D **103** (2021),  
 2903 ISSN: 2470-0029, URL: <http://dx.doi.org/10.1103/PhysRevD.103.056002> (cit. on  
 2904 pp. 37, 197).
- 2905 [39] F. Dulat, A. Lazopoulos, and B. Mistlberger, *iHixs 2 — Inclusive Higgs cross sections*,  
 2906 Computer Physics Communications **233** (2018) 243, ISSN: 0010-4655, URL: <http://dx.doi.org/10.1016/j.cpc.2018.06.025> (cit. on p. 37).
- 2908 [40] ATLAS Collaboration, *Measurement prospects of the pair production and self-coupling*  
 2909 *of the Higgs boson with the ATLAS experiment at the HL-LHC*, ATL-PHYS-PUB-  
 2910 2018-053, 2018, URL: <https://cds.cern.ch/record/2652727> (cit. on p. 37).

- 2911 [41] D. de Florian, I. Fabre, and J. Mazzitelli, *Triple Higgs production at hadron colliders*  
 2912 *at NNLO in QCD*, Journal of High Energy Physics **2020** (2020), ISSN: 1029-8479, URL:  
 2913 [http://dx.doi.org/10.1007/JHEP03\(2020\)155](http://dx.doi.org/10.1007/JHEP03(2020)155) (cit. on p. 37).
- 2914 [42] A. Papaefstathiou, T. Robens, and G. Tetlamatzi-Xolocotzi, *Triple Higgs boson*  
 2915 *production at the Large Hadron Collider with Two Real Singlet scalars*, Journal of  
 2916 High Energy Physics **2021** (2021), ISSN: 1029-8479, URL: [http://dx.doi.org/10.1007/JHEP05\(2021\)193](http://dx.doi.org/10.1007/JHEP05(2021)193) (cit. on p. 37).
- 2918 [43] T. Robens, T. Stefaniak, and J. Wittbrodt, *Two-real-scalar-singlet extension of the*  
 2919 *SM: LHC phenomenology and benchmark scenarios*, The European Physical Journal C  
 2920 **80** (2020), ISSN: 1434-6052, URL: <http://dx.doi.org/10.1140/epjc/s10052-020-7655-x> (cit. on p. 37).
- 2922 [44] D. Egana-Ugrinovic, S. Homiller, and P. Meade, *Multi-Higgs boson production probes*  
 2923 *Higgs sector flavor*, Physical Review D **103** (2021), ISSN: 2470-0029, URL: <http://dx.doi.org/10.1103/PhysRevD.103.115005> (cit. on p. 37).
- 2925 [45] CERN, *CERN’s accelerator complex*, <https://home.cern/science/accelerators/accelerator-complex>, Accessed: 27 July 2021 (cit. on p. 39).
- 2927 [46] *Letter of Intent for the Phase-II Upgrade of the ATLAS Experiment*, (2012) (cit. on  
 2928 p. 40).
- 2929 [47] H.-L. Project, *The HL-LHC project*, <https://hilumilhc.web.cern.ch/content/hl-lhc-project>, Accessed: 16 August 2021 (cit. on p. 40).
- 2931 [48] J. Pequenao, “Computer generated image of the whole ATLAS detector”, 2008, URL:  
 2932 <https://cds.cern.ch/record/1095924> (cit. on p. 41).
- 2933 [49] ATLAS Collaboration, *The ATLAS Experiment at the CERN Large Hadron Collider*,  
 2934 *JINST* **3** (2008) S08003 (cit. on p. 42).

- 2935 [50] J. Pequenao and P. Schaffner, “How ATLAS detects particles: diagram of particle  
 2936 paths in the detector”, 2013, URL: <https://cds.cern.ch/record/1505342> (cit. on  
 2937 p. 43).
- 2938 [51] ATLAS Collaboration, *ATLAS Insertable B-Layer: Technical Design Report*, ATLAS-  
 2939 TDR-19; CERN-LHCC-2010-013, 2010, URL: <https://cds.cern.ch/record/1291633> (cit. on p. 44), Addendum: ATLAS-TDR-19-ADD-1; CERN-LHCC-2012-009,  
 2940 2012, URL: <https://cds.cern.ch/record/1451888>.
- 2941 [52] B. Abbott et al., *Production and integration of the ATLAS Insertable B-Layer*, JINST  
 2942 **13** (2018) T05008, arXiv: [1803.00844 \[physics.ins-det\]](https://arxiv.org/abs/1803.00844) (cit. on p. 44).
- 2943 [53] A. Outreach, “ATLAS Fact Sheet : To raise awareness of the ATLAS detector and  
 2944 collaboration on the LHC”, 2010, URL: <https://cds.cern.ch/record/1457044>  
 2945 (cit. on p. 46).
- 2946 [54] ATLAS Collaboration, *Performance of the ATLAS trigger system in 2015*, Eur. Phys.  
 2947 J. C **77** (2017) 317, arXiv: [1611.09661 \[hep-ex\]](https://arxiv.org/abs/1611.09661) (cit. on p. 47).
- 2948 [55] ATLAS Collaboration, *The ATLAS Collaboration Software and Firmware*, ATL-SOFT-  
 2949 PUB-2021-001, 2021, URL: <https://cds.cern.ch/record/2767187> (cit. on p. 47).
- 2950 [56] S. Forte and S. Carrazza, *Parton distribution functions*, 2020, arXiv: [2008.12305](https://arxiv.org/abs/2008.12305)  
 2951 [hep-ph] (cit. on p. 51).
- 2952 [57] P. Nason, *A New method for combining NLO QCD with shower Monte Carlo algorithms*,  
 2953 JHEP **11** (2004) 040, arXiv: [hep-ph/0409146 \[hep-ph\]](https://arxiv.org/abs/hep-ph/0409146) (cit. on pp. 52, 82).
- 2954 [58] S. Frixione, P. Nason and C. Oleari, *Matching NLO QCD computations with parton  
 2955 shower simulations: the POWHEG method*, JHEP **11** (2007) 070, arXiv: [0709.2092](https://arxiv.org/abs/0709.2092)  
 2956 [hep-ph] (cit. on pp. 52, 82).
- 2957 [59] S. Alioli, P. Nason, C. Oleari, and E. Re, *A general framework for implementing NLO  
 2958 calculations in shower Monte Carlo programs: the POWHEG BOX*, JHEP **06** (2010)  
 2959 043, arXiv: [1002.2581 \[hep-ph\]](https://arxiv.org/abs/1002.2581) (cit. on pp. 52, 82).
- 2960

- [60] J. Alwall et al., *The automated computation of tree-level and next-to-leading order differential cross sections, and their matching to parton shower simulations*, Journal of High Energy Physics **2014** (2014), URL: [https://doi.org/10.1007/jhep07\(2014\)079](https://doi.org/10.1007/jhep07(2014)079) (cit. on pp. 52, 81).
- [61] J. Bellm et al., *Herwig 7.0/Herwig++ 3.0 release note*, The European Physical Journal C **76** (2016), URL: <https://doi.org/10.1140/epjc/s10052-016-4018-8> (cit. on pp. 52, 81).
- [62] M. Bähr et al., *Herwig++ physics and manual*, The European Physical Journal C **58** (2008) 639, URL: <https://doi.org/10.1140/epjc/s10052-008-0798-9> (cit. on pp. 52, 81).
- [63] T. Sjöstrand et al., *An introduction to PYTHIA 8.2*, Computer Physics Communications **191** (2015) 159, ISSN: 0010-4655, URL: <https://www.sciencedirect.com/science/article/pii/S0010465515000442> (cit. on pp. 52, 82).
- [64] D. J. Lange, *The EvtGen particle decay simulation package*, Nucl. Instrum. Meth. A **462** (2001) 152 (cit. on pp. 52, 81).
- [65] S. Höche, *Introduction to parton-shower event generators*, 2015, arXiv: [1411.4085 \[hep-ph\]](https://arxiv.org/abs/1411.4085) (cit. on p. 53).
- [66] S. Agostinelli et al., *Geant4—a simulation toolkit*, Nuclear Instruments and Methods in Physics Research Section A: Accelerators, Spectrometers, Detectors and Associated Equipment **506** (2003) 250, ISSN: 0168-9002, URL: <https://www.sciencedirect.com/science/article/pii/S0168900203013688> (cit. on p. 54).
- [67] P. Calafiura, J. Catmore, D. Costanzo, and A. Di Girolamo, *ATLAS HL-LHC Computing Conceptual Design Report*, tech. rep., CERN, 2020, URL: <https://cds.cern.ch/record/2729668> (cit. on p. 54).

- 2985 [68] A. Collaboration, *Computing and Software - Public Results*, <https://twiki.cern.ch/twiki/bin/view/AtlasPublic/ComputingandSoftwarePublicResults>, Accessed:  
 2986  
 2987 27 July 2021 (cit. on p. 55).
- 2988 [69] HEPiX, *Benchmarking*, <https://w3.hepix.org/benchmarking.html>, Accessed: 17  
 2989 August 2021 (cit. on p. 55).
- 2990 [70] ATLAS Collaboration, *The ATLAS Simulation Infrastructure*, *Eur. Phys. J. C* **70**  
 2991 (2010) 823, arXiv: [1005.4568 \[physics.ins-det\]](https://arxiv.org/abs/1005.4568) (cit. on pp. 54, 81).
- 2992 [71] ATLAS Collaboration, *The new Fast Calorimeter Simulation in ATLAS*, ATL-SOFT-  
 2993 PUB-2018-002, 2018, URL: <https://cds.cern.ch/record/2630434> (cit. on pp. 56–  
 2994 58).
- 2995 [72] ROOT, *TPrincipal Class Reference*, <https://root.cern.ch/doc/master/classTPrincipal.html>, Accessed: 27 July 2021 (cit. on p. 56).
- 2996  
 2997 [73] M. Aharrouche et al., *Energy linearity and resolution of the ATLAS electromagnetic*  
 2998 *barrel calorimeter in an electron test-beam*, *Nuclear Instruments and Methods in*  
 2999 *Physics Research Section A: Accelerators, Spectrometers, Detectors and Associated*  
 3000 *Equipment* **568** (2006) 601, ISSN: 0168-9002, URL: <http://dx.doi.org/10.1016/j.nima.2006.07.053> (cit. on p. 57).
- 3001  
 3002 [74] ATLAS Collaboration, *Evidence for prompt photon production in pp collisions at*  
 3003  $\sqrt{s} = 7 \text{ TeV}$  *with the ATLAS detector*, ATLAS-CONF-2010-077, 2010, URL: <https://cds.cern.ch/record/1281368> (cit. on p. 58).
- 3004  
 3005 [75] D. P. Kingma and M. Welling, *Auto-Encoding Variational Bayes*, 2014, arXiv: [1312.6114 \[stat.ML\]](https://arxiv.org/abs/1312.6114) (cit. on p. 59).
- 3006  
 3007 [76] G. Aad et al., *Topological cell clustering in the ATLAS calorimeters and its performance*  
 3008 *in LHC Run 1*, *The European Physical Journal C* **77** (2017), ISSN: 1434-6052, URL:  
 3009 <http://dx.doi.org/10.1140/epjc/s10052-017-5004-5> (cit. on pp. 62, 64).

- 3010 [77] A. Ghosh and A. Collaboration, *Deep generative models for fast shower simulation*  
 3011 *in ATLAS*, Journal of Physics: Conference Series **1525** (2020) 012077, URL: <https://doi.org/10.1088/1742-6596/1525/1/012077> (cit. on p. 65).
- 3012  
 3013 [78] R. Di Sipio, M. F. Giannelli, S. K. Haghight, and S. Palazzo, *DijetGAN: a Generative-  
 3014 Adversarial Network approach for the simulation of QCD dijet events at the LHC*,  
 3015 Journal of High Energy Physics **2019** (2019), ISSN: 1029-8479, URL: [http://dx.doi.org/10.1007/JHEP08\(2019\)110](http://dx.doi.org/10.1007/JHEP08(2019)110) (cit. on p. 65).
- 3016  
 3017 [79] ATLAS Collaboration, *Jet reconstruction and performance using particle flow with*  
 3018 *the ATLAS Detector*, Eur. Phys. J. C **77** (2017) 466, arXiv: [1703.10485](https://arxiv.org/abs/1703.10485) [hep-ex]  
 3019 (cit. on pp. 67, 80).
- 3020 [80] ATLAS Collaboration, *Topological cell clustering in the ATLAS calorimeters and*  
 3021 *its performance in LHC Run 1*, Eur. Phys. J. C **77** (2017) 490, arXiv: [1603.02934](https://arxiv.org/abs/1603.02934)  
 3022 [hep-ex] (cit. on p. 67).
- 3023 [81] ATLAS Collaboration, *Variable Radius, Exclusive- $k_T$ , and Center-of-Mass Subjet*  
 3024 *Reconstruction for Higgs( $\rightarrow b\bar{b}$ ) Tagging in ATLAS*, ATL-PHYS-PUB-2017-010, 2017,  
 3025 URL: <https://cds.cern.ch/record/2268678> (cit. on pp. 67, 196).
- 3026 [82] M. Cacciari, G. P. Salam, and G. Soyez, *The anti- $k_T$  jet clustering algorithm*, Journal  
 3027 of High Energy Physics **2008** (2008) 063, ISSN: 1029-8479, URL: <http://dx.doi.org/10.1088/1126-6708/2008/04/063> (cit. on p. 67).
- 3028  
 3029 [83] G. P. Salam, *Towards jetography*, The European Physical Journal C **67** (2010) 637,  
 3030 ISSN: 1434-6052, URL: <http://dx.doi.org/10.1140/epjc/s10052-010-1314-6>  
 3031 (cit. on p. 67).
- 3032 [84] A. J. Larkoski, G. P. Salam, and J. Thaler, *Energy correlation functions for jet*  
 3033 *substructure*, Journal of High Energy Physics **2013** (2013), ISSN: 1029-8479, URL:  
 3034 [http://dx.doi.org/10.1007/JHEP06\(2013\)108](http://dx.doi.org/10.1007/JHEP06(2013)108) (cit. on p. 68).

- 3035 [85] A. Collaboration, *Configuration and performance of the ATLAS b-jet triggers in Run*  
 3036 *2*, 2021, arXiv: [2106.03584 \[hep-ex\]](https://arxiv.org/abs/2106.03584) (cit. on p. 71).
- 3037 [86] ATLAS Collaboration, *ATLAS b-jet identification performance and efficiency mea-*  
 3038 *surement with  $t\bar{t}$  events in pp collisions at  $\sqrt{s} = 13$  TeV*, *Eur. Phys. J. C* **79** (2019)  
 3039 **970**, arXiv: [1907.05120 \[hep-ex\]](https://arxiv.org/abs/1907.05120) (cit. on pp. 70, 80, 146).
- 3040 [87] ATLAS Collaboration, *Topological b-hadron decay reconstruction and identification*  
 3041 *of b-jets with the JetFitter package in the ATLAS experiment at the LHC*, ATL-  
 3042 PHYS-PUB-2018-025, 2018, URL: <https://cds.cern.ch/record/2645405> (cit. on  
 3043 p. 73).
- 3044 [88] R. Frühwirth, *Application of Kalman filtering to track and vertex fitting*, *Nuclear*  
 3045 *Instruments and Methods in Physics Research Section A: Accelerators, Spectrometers,*  
 3046 *Detectors and Associated Equipment* **262** (1987) 444, ISSN: 0168-9002, URL: <https://www.sciencedirect.com/science/article/pii/0168900287908874> (cit. on  
 3047 p. 73).
- 3049 [89] ATLAS Collaboration, *Identification of Jets Containing b-Hadrons with Recurrent*  
 3050 *Neural Networks at the ATLAS Experiment*, ATL-PHYS-PUB-2017-003, 2017, URL:  
 3051 <https://cds.cern.ch/record/2255226> (cit. on p. 74).
- 3052 [90] *Expected performance of the 2019 ATLAS b-taggers*, <http://atlas.web.cern.ch/>  
 3053 *Atlas/GROUPS/PHYSICS/PILOTS/FTAG-2019-005/*, Accessed: 2021-07-14 (cit. on  
 3054 p. 76).
- 3055 [91] ATLAS Collaboration, *Search for Higgs boson pair production in the  $b\bar{b}WW^*$  decay*  
 3056 *mode at  $\sqrt{s} = 13$  TeV with the ATLAS detector*, *JHEP* **04** (2019) 092, arXiv: [1811.04671 \[hep-ex\]](https://arxiv.org/abs/1811.04671) (cit. on p. 78).
- 3058 [92] ATLAS Collaboration, *A search for resonant and non-resonant Higgs boson pair*  
 3059 *production in the  $b\bar{b}\tau^+\tau^-$  decay channel in pp collisions at  $\sqrt{s} = 13$  TeV with the*

- 3060        *ATLAS detector*, Phys. Rev. Lett. **121** (2018) 191801, arXiv: [1808.00336 \[hep-ex\]](#)  
 3061        (cit. on p. 78), Erratum: Phys. Rev. Lett. **122** (2019) 089901.
- 3062        [93] ATLAS Collaboration, *Search for Higgs boson pair production in the  $WW^{(*)}WW^{(*)}$*   
 3063        *decay channel using ATLAS data recorded at  $\sqrt{s} = 13 \text{ TeV}$* , JHEP **05** (2019) 124,  
 3064        arXiv: [1811.11028 \[hep-ex\]](#) (cit. on p. 78).
- 3065        [94] ATLAS Collaboration, *Search for Higgs boson pair production in the  $\gamma\gamma b\bar{b}$  final state*  
 3066        *with 13 TeV pp collision data collected by the ATLAS experiment*, JHEP **11** (2018)  
 3067        040, arXiv: [1807.04873 \[hep-ex\]](#) (cit. on p. 78).
- 3068        [95] ATLAS Collaboration, *Search for Higgs boson pair production in the  $\gamma\gamma WW^*$  channel*  
 3069        *using pp collision data recorded at  $\sqrt{s} = 13 \text{ TeV}$  with the ATLAS detector*, Eur. Phys.  
 3070        J. C **78** (2018) 1007, arXiv: [1807.08567 \[hep-ex\]](#) (cit. on p. 78).
- 3071        [96] ATLAS Collaboration, *Reconstruction and identification of boosted di- $\tau$  systems in*  
 3072        *a search for Higgs boson pairs using 13 TeV proton–proton collision data in ATLAS*,  
 3073        JHEP **11** (2020) 163, arXiv: [2007.14811 \[hep-ex\]](#) (cit. on p. 78).
- 3074        [97] ATLAS Collaboration, *Search for non-resonant Higgs boson pair production in the*  
 3075         *$b\bar{b}\ell\nu\ell\nu$  final state with the ATLAS detector in pp collisions at  $\sqrt{s} = 13 \text{ TeV}$* , Phys.  
 3076        Lett. B **801** (2020) 135145, arXiv: [1908.06765 \[hep-ex\]](#) (cit. on p. 78).
- 3077        [98] ATLAS Collaboration, *Search for Higgs boson pair production in the two bottom quarks*  
 3078        *plus two final state with in pp collisions at  $\sqrt{s} = 13 \text{ TeV}$  with the ATLAS detector*,  
 3079        ATLAS-CONF-2021-016, 2021, URL: <https://cds.cern.ch/record/2759683> (cit. on  
 3080        pp. 78, 169, 173).
- 3081        [99] CMS Collaboration, *Search for production of Higgs boson pairs in the four b quark*  
 3082        *final state using large-area jets in proton–proton collisions at  $\sqrt{s} = 13 \text{ TeV}$* , JHEP **01**  
 3083        (2019) 040, arXiv: [1808.01473 \[hep-ex\]](#) (cit. on p. 78).
- 3084        [100] *Search for Higgs boson pair production in the four b quark final state*, tech. rep., CERN,  
 3085        2021, URL: <https://cds.cern.ch/record/2771912> (cit. on p. 78).

- 3086 [101] CMS Collaboration, *Combination of Searches for Higgs Boson Pair Production in*  
 3087 *Proton–Proton Collisions at  $\sqrt{s} = 13 \text{ TeV}$* , Phys. Rev. Lett. **122** (2019) 121803, arXiv:  
 3088 [1811.09689 \[hep-ex\]](https://arxiv.org/abs/1811.09689) (cit. on p. 78).
- 3089 [102] G. Bartolini et al., *Performance of the ATLAS b-jet trigger in  $p\ p$  collisions at  $\sqrt{s} =$*   
 3090 *13 TeV*, tech. rep. ATL-COM-DAQ-2019-150, CERN, 2019, URL: <https://cds.cern.ch/record/2688819> (cit. on p. 81).
- 3091 [103] ATLAS Collaboration, *Luminosity determination in  $pp$  collisions at  $\sqrt{s} = 13 \text{ TeV}$  using the ATLAS detector at the LHC*, ATLAS-CONF-2019-021, 2019, URL: <https://cds.cern.ch/record/2677054> (cit. on pp. 81, 146).
- 3092 [104] J. Butterworth et al., *PDF4LHC recommendations for LHC Run II*, J. Phys. G **43**  
 3093 (2016) 023001, arXiv: [1510.03865 \[hep-ph\]](https://arxiv.org/abs/1510.03865) (cit. on pp. 82, 147).
- 3094 [105] T. Head et al., *scikit-optimize/scikit-optimize: v0.5.2*, version v0.5.2, 2018, URL: <https://doi.org/10.5281/zenodo.1207017> (cit. on p. 89).
- 3095 [106] A. Carvalho et al., *Higgs pair production: choosing benchmarks with cluster analysis*,  
 3096 *Journal of High Energy Physics* **2016** (2016) 1, ISSN: 1029-8479, URL: [http://dx.doi.org/10.1007/JHEP04\(2016\)126](http://dx.doi.org/10.1007/JHEP04(2016)126) (cit. on p. 101).
- 3097 [107] A. Rogozhnikov, *Reweighting with Boosted Decision Trees*, *Journal of Physics: Conference Series* **762** (2016) 012036, ISSN: 1742-6596, URL: <http://dx.doi.org/10.1088/1742-6596/762/1/012036> (cit. on p. 106).
- 3098 [108] G. V. Moustakides and K. Basioti, *Training Neural Networks for Likelihood/Density*  
 3099 *Ratio Estimation*, 2019, arXiv: [1911.00405 \[eess.SP\]](https://arxiv.org/abs/1911.00405) (cit. on p. 106).
- 3100 [109] T. Kanamori, S. Hido, and M. Sugiyama, *A Least-Squares Approach to Direct Im-*  
 3101 *portance Estimation*, J. Mach. Learn. Res. **10** (2009) 1391, ISSN: 1532-4435 (cit. on  
 3102 p. 106).

- 3110 [110] A. Andreassen and B. Nachman, *Neural networks for full phase-space reweighting*  
 3111 and parameter tuning, *Physical Review D* **101** (2020), ISSN: 2470-0029, URL: <http://dx.doi.org/10.1103/PhysRevD.101.091901> (cit. on p. 107).
- 3113 [111] S. Fort, H. Hu, and B. Lakshminarayanan, *Deep Ensembles: A Loss Landscape Per-*  
 3114 *spective*, 2020, arXiv: [1912.02757 \[stat.ML\]](https://arxiv.org/abs/1912.02757) (cit. on p. 108).
- 3115 [112] B. Efron, *Bootstrap Methods: Another Look at the Jackknife*, *Ann. Statist.* **7** (1979) 1,  
 3116 URL: <https://doi.org/10.1214/aos/1176344552> (cit. on p. 138).
- 3117 [113] ATLAS Collaboration, *Jet energy scale and resolution measured in proton–proton*  
 3118 *collisions at  $\sqrt{s} = 13\text{ TeV}$  with the ATLAS detector*, (2020), arXiv: [2007 . 02645](https://arxiv.org/abs/2007.02645)  
 3119 [[hep-ex](#)] (cit. on p. 146).
- 3120 [114] G. Avoni et al., *The new LUCID-2 detector for luminosity measurement and monitoring*  
 3121 *in ATLAS*, *JINST* **13** (2018) P07017. 33 p, URL: <https://cds.cern.ch/record/2633501> (cit. on p. 146).
- 3123 [115] D. de Florian et al., *Handbook of LHC Higgs Cross Sections: 4. Deciphering the Nature*  
 3124 *of the Higgs Sector*, CERN Yellow Reports: Monographs, 869 pages, 295 figures, 248 ta-  
 3125 bles and 1645 citations. Working Group web page: <https://twiki.cern.ch/twiki/bin/view/LHCPhysics/>  
 3126 CERN, 2016, URL: <https://cds.cern.ch/record/2227475> (cit. on p. 147).
- 3127 [116] A. L. Read, *Presentation of search results: the CLs technique*, *Journal of Physics G:*  
 3128 *Nuclear and Particle Physics* **28** (2002) 2693, ISSN: 0954-3899 (cit. on p. 163).
- 3129 [117] G. Cowan, K. Cranmer, E. Gross, and O. Vitells, *Asymptotic formulae for likelihood-*  
 3130 *based tests of new physics*, *The European Physical Journal C* **71** (2011), ISSN: 1434-6052  
 3131 (cit. on p. 163).
- 3132 [118] E. Gross and O. Vitells, *Trial factors for the look elsewhere effect in high energy*  
 3133 *physics*, *The European Physical Journal C* **70** (2010) 525, ISSN: 1434-6052, URL:  
 3134 <http://dx.doi.org/10.1140/epjc/s10052-010-1470-8> (cit. on p. 167).

- 3135 [119] *Summary of non-resonant and resonant Higgs boson pair searches from the AT-*  
 3136 *LAS experiment*, tech. rep., All figures including auxiliary figures are available at  
 3137 <https://atlas.web.cern.ch/Atlas/GROUPS/PHYSICS/PUBNOTES/ATL-PHYS-PUB->  
 3138 2021-031: CERN, 2021, URL: <http://cds.cern.ch/record/2777013> (cit. on pp. 175–  
 3139 177).
- 3140 [120] A. Sherstinsky, *Fundamentals of Recurrent Neural Network (RNN) and Long Short-*  
 3141 *Term Memory (LSTM) network*, *Physica D: Nonlinear Phenomena* **404** (2020) 132306,  
 3142 ISSN: 0167-2789, URL: <http://dx.doi.org/10.1016/j.physd.2019.132306> (cit. on  
 3143 p. 201).
- 3144 [121] M. Zaheer et al., *Deep Sets*, 2018, arXiv: [1703.06114 \[cs.LG\]](https://arxiv.org/abs/1703.06114) (cit. on p. 201).
- 3145 [122] J. Zhou et al., *Graph Neural Networks: A Review of Methods and Applications*, 2021,  
 3146 arXiv: [1812.08434 \[cs.LG\]](https://arxiv.org/abs/1812.08434) (cit. on p. 201).
- 3147 [123] A. Vaswani et al., *Attention Is All You Need*, 2017, arXiv: [1706.03762 \[cs.CL\]](https://arxiv.org/abs/1706.03762)  
 3148 (cit. on p. 201).
- 3149 [124] I. Goodfellow, Y. Bengio, and A. Courville, *Deep Learning*, <http://www.deeplearningbook.org>, MIT Press, 2016 (cit. on p. 202).
- 3151 [125] K. P. Murphy, *Machine learning: a probabilistic perspective*, 2012 (cit. on p. 202).
- 3152 [126] I. Kobyzev, S. Prince, and M. Brubaker, *Normalizing Flows: An Introduction and*  
 3153 *Review of Current Methods*, *IEEE Transactions on Pattern Analysis and Machine*  
 3154 *Intelligence* (2020) **1**, ISSN: 1939-3539, URL: <http://dx.doi.org/10.1109/TPAMI.2020.2992934> (cit. on p. 207).
- 3156 [127] L. Dinh, J. Sohl-Dickstein, and S. Bengio, *Density estimation using Real NVP*, 2017,  
 3157 arXiv: [1605.08803 \[cs.LG\]](https://arxiv.org/abs/1605.08803) (cit. on p. 208).
- 3158 [128] C. Durkan, A. Bekasov, I. Murray, and G. Papamakarios, *Neural Spline Flows*, 2019,  
 3159 arXiv: [1906.04032 \[stat.ML\]](https://arxiv.org/abs/1906.04032) (cit. on p. 208).

- 3160 [129] F. Pedregosa et al., *Scikit-learn: Machine Learning in Python*, Journal of Machine  
3161 Learning Research **12** (2011) 2825 (cit. on p. 210).

3162

## Appendix A

3163

### OVERVIEW OF OTHER $b\bar{b}b\bar{b}$ CHANNELS

3164 The results discussed above have been developed in conjunction with (1) a boosted channel  
 3165 for the resonant search and (2) a vector boson fusion (VBF) channel for the non-resonant  
 3166 search. Detailed discussions of these two channels are beyond the scope of this thesis, though  
 3167 a combined set of resolved and boosted results are presented below. The VBF results are not  
 3168 included in this thesis, but much of this thesis work has been useful in the development of  
 3169 that result. For completeness, both analyses are therefore summarized here.

3170 *A.0.1 Resonant: Boosted Channel*

3171 The boosted analysis selection targets resonance masses from 900 GeV to 5 TeV. In such  
 3172 events,  $H$  decays have a high Lorentz boost, such that the  $b\bar{b}$  decays are very collimated. The  
 3173 resolved analysis fails to reconstruct such  $HH$  events, as the  $R = 0.4$  jets start to overlap.

3174 The boosted analysis instead reconstructs  $H$  decays as large radius,  $R = 1.0$  jets, with  
 3175 corresponding  $b$ -quarks identified with variable radius subjets, that is jets with a radius that  
 3176 scales as  $\rho/p_T$ , the  $p_T$  is that of the jet in question, and  $\rho$  is a fixed parameter, here chosen  
 3177 to be 30 GeV, which is optimized to maintain truth-level double  $b$ -labeling efficiency across  
 3178 the full range of Higgs jet  $p_T$  [81].

3179 Due to limited boosted  $b$ -tagging efficiency and to maintain sensitivity even when  $b$ -jets  
 3180 are highly collimated, the boosted analysis is divided into three categories based on the  
 3181 number of  $b$ -tagged jets associated to each large radius jet:

- 3182 • 4 $b$  category: two  $b$ -tagged jets in each
- 3183 • 2 $b - 1$  category: two  $b$ -tagged jets in one, one in the other

- 3184     •  $1b - 1$  category: one  $b$ -tagged jet in each

3185     The analysis then proceeds in each of these categories.

3186     The resolved and boosted channels are combined for resonance masses from 900 GeV to  
 3187     1.5 TeV inclusive. To keep the channels statistically independent, the boosted channel vetoes  
 3188     events passing the resolved analysis selection.

3189     A.0.2 *Non-resonant: VBF Channel*

3190     The vector boson fusion channel is considered for the non-resonant search, and builds off of  
 3191     the work developed in [22]. While the sensitivity is in general much more limited than the  
 3192     gluon-gluon fusion analysis due to the much smaller production cross section (1.726 fb at  $\sqrt{s}$   
 3193     = 13 TeV [31–38]), VBF is sensitive to a variety of Beyond the Standard Model physics, both  
 3194     complementary and orthogonal to the theoretical scope of gluon-gluon fusion. Representative  
 3195     Feynman diagrams are shown in Figure A.1.

3196     The VBF channel proceeds very similarly to the ggF, with the primary differences being  
 3197     the kinematic selections and the categorization, which are impacted by the presence of two  
 3198     *VBF jets*, resulting from the two initial state quarks. The ggF channel result presented here  
 3199     includes a veto on VBF events, such that if events pass the full VBF selection, they are not  
 3200     included in the set of events considered for the ggF result.

3201     Beginning with the assumption of four  $HH$  jets and two VBF jets, the VBF channel first  
 3202     requires an event to have a minimum six jets. The VBF jets are reconstructed as the two jets  
 3203     with the highest di-jet invariant mass,  $m_{jj}$ , out of the set of all non-tagged jets in the event.  
 3204     If no such pair exists (i.e., there are less than two non-tagged jets), the event is placed in the  
 3205     ggF channel. To reduce the number of background events, three cuts are then applied, VBF  
 3206     jets are required to have  $\Delta\eta > 3$  and a combined invariant mass of  $m_{jj} > 1000$  GeV.  $HH$   
 3207     jets are identified as in the ggF channel, and the vector sum of the  $p_T$  of the  $HH$  and VBF  
 3208     jets is required to be less than 65 GeV. The remainder of the analysis proceeds similarly to  
 3209     the ggF channel, and events failing any stage of this selection are considered for ggF.

<sub>3210</sub> Note that the background estimation for the VBF channel is inherited from the resonant  
<sub>3211</sub> and ggF analyses, a significant additional contribution of this thesis work.

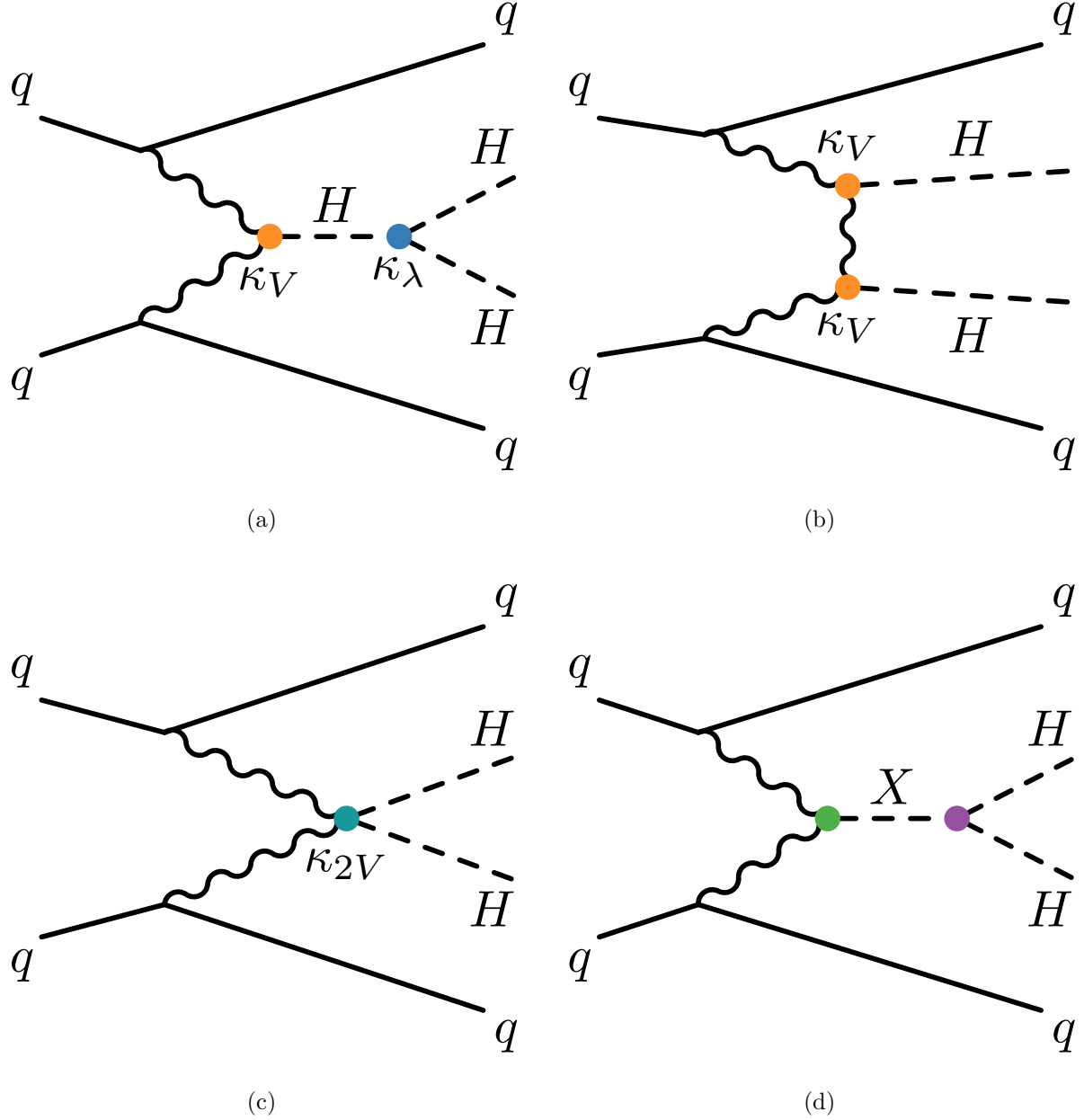


Figure A.1: Representative Feynman diagrams for the VBF channel. While this channel may be used for both resonant and non-resonant searches [22], this thesis work was developed concurrently with a focused non-resonant search. In addition to variations of the trilinear coupling,  $\kappa_\lambda$ , VBF is sensitive to various Higgs couplings to vector bosons, namely  $\kappa_V$  and  $\kappa_{2V}$ , attached to  $VVH$  and  $VVHH$  vertices respectively.

3212

## Appendix B

3213

### FUTURE IDEAS FOR $HH \rightarrow b\bar{b}b\bar{b}$

3214 The searches presented in this thesis make use of a large suite of sophisticated techniques,  
 3215 selected through careful study and validation. During this process, a variety of interesting  
 3216 directions for the  $HH \rightarrow b\bar{b}b\bar{b}$  analysis were explored by this thesis author, in collaboration  
 3217 with a few others<sup>1</sup>, but were not used due to a variety of constraints. Two such interesting  
 3218 directions are presented here, with the hope of encouraging further exploration of these  
 3219 techniques in future work.

3220 **B.1 pairAGraph: A New Method for Jet Pairing**

3221 As discussed in Chapter 7, one of the main problems to solve is the pairing of  $b$ -jets into  
 3222 Higgs candidates. Figure 7.1 demonstrates that the choice of the pairing method, while  
 3223 important for achieving good reconstruction of signal events, also significantly impacts the  
 3224 structure of non- $HH$  events, leading to various biases in the background estimate. Evaluation  
 3225 of the pairing method therefore must take both of these factors into account. While some  
 3226 advantages have been presented in respective contexts for the pairing methods considered in  
 3227 this thesis, it is motivated to explore further improvements to this important component of  
 3228 the analysis.

3229 To that end, we note that all of the pairing methods considered here share a common  
 3230 feature: four jets are selected, and the pairing is some discrimination between the available  
 3231 three pairings of these four jets. For the methods used in this analysis, the jet selection  
 3232 proceeds via a simple  $p_T$  ordering, with  $b$ -tagged jets receiving a higher priority than non-

---

<sup>1</sup>Notably Nicole Hartman (SLAC), who spearheaded much of the development and proof of concept work, in collaboration with Michael Kagan and Rafael Teixeira De Lima.

3233 tagged jets.

3234 With the advent of a variety of machine learning methods for dealing with a variable number  
 3235 of inputs (e.g. recurrent neural networks [120], deep sets [121], graph neural networks [122],  
 3236 and transformers [123]), a natural place to improve on the pairing is to consider more than  
 3237 just four jets. The pairing and jet selection is then performed simultaneously, allowing for  
 3238 the incorporation of more event information in the pairing decision and the incorporation of  
 3239 jet correlation structure in the jet selection.

3240 In practice, the majority of  $HH \rightarrow b\bar{b}b\bar{b}$  events have either four or five jets which pass the  
 3241 kinematic preselection, and any gain from this additional freedom would come from events  
 3242 with greater than or equal to five jets. However, this five jet topology is particularly exciting  
 3243 for scenarios such as events with initial state radiation (ISR), in which the  $HH \rightarrow 4b$  jets are  
 3244 offset by a single jet with  $p_T$  similar in magnitude to that of the  $HH \rightarrow 4b$  system. Such  
 3245 events have explicit event level information which is not encoded with the inclusion of only  
 3246 the  $HH \rightarrow 4b$  jets, and are pathological if the ISR jet happens to pass  $b$ -tagging requirements.

3247 Additionally, with the use of lower tagged regions for background estimation and alternate  
 3248 signal regions, this extra flexibility in jet selection may provide a very useful bias – since the  
 3249 algorithm is trained on signal, the selected jets for the pairing will be the most “4b-like” jets  
 3250 available in the considered set.

3251 For the studies considered here, a transformer [123] based architecture is used. This is  
 3252 best visualized by considering the event as a graph with jets corresponding to nodes and edges  
 3253 corresponding to potential connections – for this reason, we term this algorithm “pairAGraph”.  
 3254 The approach is as follows: each jet,  $i$ , is represented by some vector of input variables,  $\vec{x}_i$ ,  
 3255 in our case the four-vector information,  $(p_T, \eta, \phi, E)$  of each jet, plus information on the  
 3256  $b$ -tagging decision. A multi-layer perceptron (MLP) is used to create a latent embedding,  
 3257  $\mathbf{h}(\vec{x}_i)$ , of this input vector.

To describe the relationship between various jets in the event, we then define a vector  $\vec{z}_i$

for each jet as

$$\vec{z}_i = \sum_j w_{ij} \mathbf{h}(\vec{x}_j) \quad (\text{B.1})$$

3258 where  $j$  runs over all jets in the event (including  $i = j$ ), the  $w_{ij}$  can be thought of as edge  
 3259 weights, and  $\mathbf{h}(\vec{x}_j)$  is the latent embedding for jet  $j$  mentioned above.

Within this formula, both  $\mathbf{h}$  and the  $w_{ij}$  are learnable. To learn an appropriate latent mapping and set of edge weights, we define a similarity metric corresponding to each possible jet pairing:

$$\vec{z}_{1a} \cdot \vec{z}_{1b} + \vec{z}_{2a} \cdot \vec{z}_{2b} \quad (\text{B.2})$$

3260 where subscripts  $1a$  and  $1b$  correspond to the two jets in pair 1,  $2a$  and  $2b$  to the jets in pair  
 3261 2 for a given pairing of four distinct jets.

3262 This similarity metric is calculated for all possible pairings, which are then passed through  
 3263 a softmax [124] activation function, which compresses these scores to between 0 and 1 with  
 3264 sum of 1, lending an interpretation as probability of each pairing.

3265 In training, the ground truth pairing is set by *truth matching* jets to the  $b$ -jets in the  $HH$   
 3266 signal simulation – a jet is considered to match if it is  $< 0.3$  in  $\Delta R$  away from a  $b$ -jet in the  
 3267 simulation record. Given this ground truth, a cross-entropy loss [125] is used on the softmax  
 3268 outputs, and  $w_{ij}$  and  $\mathbf{h}$  are updated correspondingly. Training in such a way corresponds to  
 3269 updating  $w_{ij}$  and  $\mathbf{h}$  to maximize the similarity metric for the correct pairing.

3270 In evaluation, the pairings with a higher score (and therefore higher softmax output)  
 3271 given the trained  $h$  and  $w_{ij}$  therefore correspond to the pairings that are most “HH-like”.  
 3272 The maximum over these scores is therefore the pairing used as the predicted result from the  
 3273 algorithm.

3274 Because the majority of  $HH \rightarrow b\bar{b}b\bar{b}$  events have either four or five jets, it was found to  
 3275 be sufficient to only consider a maximum of 5 jets. Consideration of more is in principle  
 3276 possible, but the quickly expanding combinatorics leads to a rapidly more difficult problem.  
 3277 The jets considered are the five leading jets in  $p_T$ . Notably, this set of jets may include jets  
 3278 which are not  $b$ -tagged, even for the nominal 4 $b$  region – therefore events with 4  $b$ -tagged jets

3279 are not required to use all of them in the construction of Higgs candidates, in contrast to the  
 3280 other algorithms used in this thesis.

3281 A comparison of the pairAGraph jet selection with the baseline selection used in Chapter  
 3282 7 is considered in Table B.1 for the MC16a Standard Model non-resonant signal. As a  
 3283 reminder, the baseline selection orders jets by  $p_T$ , selecting first the highest  $p_T$   $b$ -tagged jets  
 3284 (according to the  $b$ -tag region definition) and then the highest  $p_T$  non-tagged jets. The first  
 3285 four jets in this ordering are used.

3286 For the comparison presented in Table B.1, only the leading five jets are considered in  
 3287 applying both algorithms in order to compare results on more equal footing. The numbers  
 3288 shown are the percent of the time that the correct jets are selected for the Higgs candidates  
 3289 by each algorithm, given that the correct jets fall within these leading five jets, where “correct”  
 3290 here means truth matched to the corresponding  $b$ -quarks. pairAGraph demonstrates a slight  
 3291 improvement over the baseline for  $4b$ , which widens when considering lower  $b$ -tag categories.  
 3292 Given that four  $b$ -quarks are present in all of these categories, this suggests that pairAGraph  
 3293 is able to recover information in the case of, e.g., mis-tagged jets.

3294 Table B.2 compares the  $HH$  pairing accuracy of a few different pairing algorithms for  
 3295 the Standard Model signal. Notably, pairAGraph demonstrates a higher pairing accuracy  
 3296 immediately after paring, but all methods are quite comparable after the full analysis selection.

3297

3298 As mentioned in Chapter 7, though the pairing is quite important for signal events, it also  
 3299 must be applied to events in data, where the overwhelming majority of events do not contain  
 3300  $HH$ . Though in general, pairing methods select for an  $HH$ -like topology, the additional  
 3301 flexibility of pairAGraph to choose which jets enter the candidate  $HH$  system provides an  
 3302 additional handle to shape the kinematics of events in data. Examples of this impact are  
 3303 seen in Figures B.1 and B.2, which compare the  $2b$  and  $4b$  distributions of  $p_T$  of the  $HH$   
 3304 candidate system between BDT pairing and pairAGraph pairing before and after reweighting.  
 3305  $HH$   $p_T$  was chosen as it is a variable which demonstrates both a large difference between  
 3306  $2b$  and  $4b$  and a residual mis-modeling after reweighting. As can be seen in Figure B.1, the

<b>4b correct jets</b>	96.7%	96.0%
<b>3b+1 loose correct jets</b>	96.3%	95.2%
<b>3b correct jets</b>	91.6%	83.2%

Table B.1: Percent of the time that the correct jets are selected for the Higgs candidates by each algorithm, given that the correct jets fall within the set of considered jets, where “correct” here means truth matched to the corresponding  $b$ -quarks. Only the leading five jets are considered in the assessment of both algorithms. Definitions of the  $4b$  and  $3b + 1$  loose categories are as described in Section 7.1, where  $3b$  requires three  $b$ -tagged jets and the fourth jet is untagged. pairAGraph demonstrates a slight improvement over the baseline for  $4b$ , which widens when considering lower  $b$ -tag categories. Given that four  $b$ -quarks are present in all of these categories, this suggests that pairAGraph is able to recover information in the case of, e.g., mis-tagged jets.

	After Pairing	After Full Selection
$D_{HH}$	71.8%	93.6%
$\min \Delta R$	69.7%	94.7%
pairAGraph	78.4%	94.2%

Table B.2: Pairing accuracy evaluated for the Standard Model signal (MC16a), comparing  $D_{HH}$  and  $\min \Delta R$  (discussed in Chapter 7) with pairAGraph trained on the Standard Model signal. Numbers are shown both immediately after pairing and after the full analysis selection. pairAGraph demonstrates a 7-8% higher accuracy than the other algorithms immediately after pairing, but all methods are quite comparable after the full analysis selection.

3307 *2b* and *4b* distributions are more similar before reweighting with pairAGraph. Figure B.2  
 3308 further shows that the residual mis-modeling after reweighting is reduced, along with the  
 3309 corresponding uncertainty. While this is not fully conclusive, it provides a hint that the jets  
 3310 chosen for the *2b* event *HH* candidate system may be more “*4b-like*” than the jets chosen  
 3311 with the baseline selection.

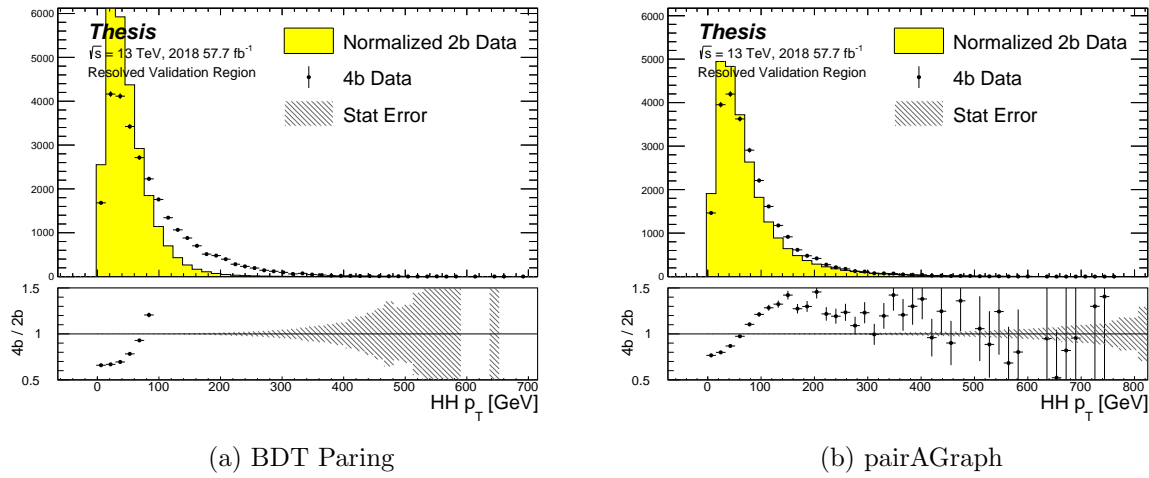


Figure B.1: Comparison of distributions of  $HH p_T$  in the 2018 resonant validation region before reweighting for BDT pairing (left) and pairAGraph (right).  $HH p_T$  is a variable with a large difference between *2b* and *4b*, but the relative shapes seem to be more similar for pairAGraph than for BDT paring, corresponding to the hypothesis that pairAGraph chooses more “*4b-like*” jets.

## 3312 **B.2 Background Estimation with Mass Plane Interpolation**

3313 The choice of a pairing algorithm that results in a smooth mass plane (such as  $\min \Delta R$ )  
 3314 opens up a variety of options for the background estimation. While the method based on  
 3315 reweighting of *2b* events used for this thesis performs well and has been extensively studied  
 3316 and validated, it also relies on several assumptions. In particular, the reweighting is derived

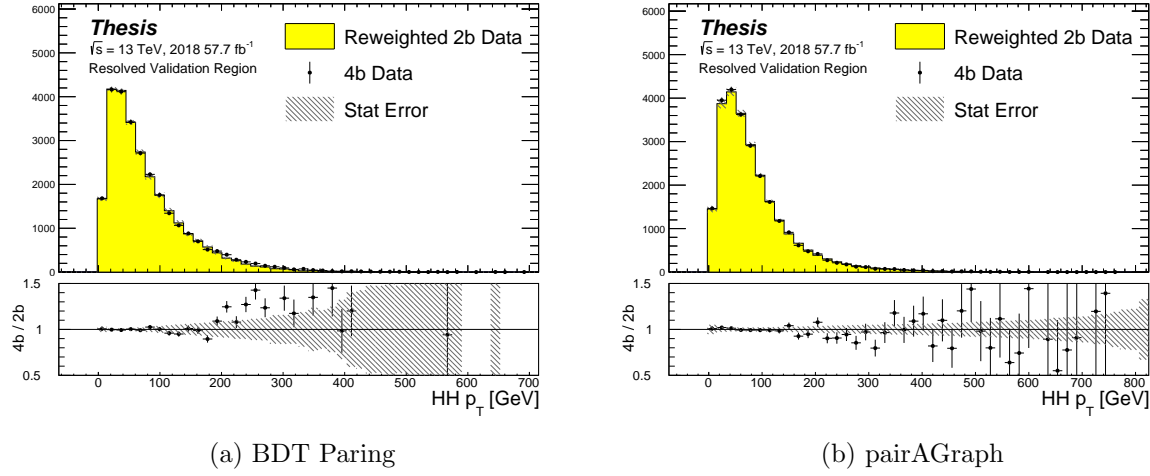


Figure B.2: Comparison of distributions of  $HH p_T$  in the 2018 resonant validation region after reweighting for BDT pairing (left) and pairAGraph (right).  $HH p_T$  is a variable with a large difference between  $2b$  and  $4b$ , and the reweighted agreement in the high  $p_T$  tail is significantly improved with pairAGraph, with a corresponding reduction in the assigned bootstrap uncertainty in that region.

3317 between e.g.,  $2b$  and  $4b$  events *outside* of the signal region and then applied to  $2b$  events *inside*  
 3318 the signal region, with the assumption that the  $2b$  to  $4b$  transfer function will be sufficiently  
 3319 similar in both regions of the mass plane. An uncertainty is assigned to account for the bias  
 3320 due to this assumption, but the extrapolation in the mass plane is never explicitly treated in  
 3321 the nominal estimate. While the approach of reweighting  $2b$  events within the signal region  
 3322 does have the advantage of incorporating explicit signal region information (that is, the  $2b$   
 3323 signal region events), the importance of the extrapolation bias motivates consideration of  
 3324 a method that operates within the  $4b$  mass plane. This additionally removes the reliance  
 3325 on lower  $b$ -tagging regions, allowing for the use of, e.g.  $3b$  triggers, and future-proofing the  
 3326 analysis against trigger bandwidth constraints in the low tag regions.

3327 The pairAGraph pairing method discussed in the previous section was developed concur-

3328 rently with these studies and demonstrates good properties for an interpolated estimate (as  
3329 shown below), and is therefore used in the following.

The method considered here relies on the following: for a given vector of input variables (event kinematics, etc),  $\vec{x}$ , the joint probability in the  $HH$  mass plane may be written as:

$$p(\vec{x}, m_{H1}, m_{H2}) = p(\vec{x}|m_{H1}, m_{H2})p(m_{H1}, m_{H2}) \quad (\text{B.3})$$

3330 by the chain rule of probability. This means that the full dynamics of events in the  $HH$  mass  
3331 plane may be described by (1) the conditional probability of considered variables  $\vec{x}$ , given  
3332 values of  $m_{H1}$  and  $m_{H2}$ , and (2) the density of the mass plane itself.

3333 We present here an approach which uses normalizing flows [126] to model the conditional  
3334 probabilities of events in the mass plane and Gaussian processes to model the mass plane  
3335 density. These models are trained in a region around, but not including, the signal region,  
3336 and the trained models are then used to construct an *interpolated* estimate of the signal  
3337 region kinematics. This approach therefore explicitly treats event behavior within the mass  
3338 plane, avoiding the concerns associated with a reweighted estimate. Validation of such a  
3339 method, as well as assessing of closure and biases of the method, may be done in alternate  
3340  $b$ -tagging or kinematic regions, notably the now unused  $2b$  region, results of which are shown  
3341 below.

### 3342 B.2.1 Normalizing Flows

Normalizing flows model observed data  $x \in X$ , with  $x \sim p_X$ , as the output of an invertible, differentiable function  $f : X \rightarrow Z$ , with  $z \in Z$  a latent variable with a simple prior probability distribution (often standard normal),  $z \sim p_Z$ . From a change of variables, given such a function, we may write

$$p_X(x) = p_Z(f(x)) \left| \det \left( \frac{d(f(x))}{dx} \right) \right| \quad (\text{B.4})$$

3343 where  $\left( \frac{d(f(x))}{dx} \right)$  is the Jacobian of  $f$  at  $x$ .

3344 The problem of normalizing flows then reduces to (1) choosing sets of  $f$  which are both  
3345 tractable and sufficiently expressive to describe observed data, and (2) optimizing associated

3346 sets of functional parameters on observed data via maximum likelihood estimation using  
 3347 the above formula. Sampling from the learned density is done by drawing from the latent  
 3348 distribution  $z \sim p_Z$  (cf. inverse transform sampling) – the corresponding sample is then  
 3349  $x \sim p_X$  with  $x = f^{-1}(z)$ .

3350 A standard approach to the definition of these  $f$  is as a composition of affine transfor-  
 3351 mations (e.g. RealNVP [127]), that is, transformations of the form  $\alpha z + \beta$ , with  $\alpha$  and  $\beta$   
 3352 learnable parameter vectors. This can roughly be thought of as shifting and squeezing the  
 3353 input prior density in order to match the data density. However, this has somewhat  
 3354 limited expressivity, for instance in the case of a multi-modal density.

This work thus instead relies on neural spline flows [128] in which the functions considered are monotonic rational-quadratic splines, which have an analytic inverse. A rational quadratic function has the form of a quotient of two quadratic polynomials, namely,

$$f_j(x_i) = \frac{a_{ij}x_i^2 + b_{ij}x_{ij} + c_{ij}}{d_{ij}x_i^2 + e_{ij}x_i + f_{ij}} \quad (\text{B.5})$$

3355 with six associated parameters ( $a_{ij}$  through  $f_{ij}$ ) per each piecewise bin  $j$  of the spline and  
 3356 each input dimension  $i$ . This is explicitly more flexible and expressive than a simple affine  
 3357 transformation, allowing, e.g., the treatment of multi-modality via the piecewise nature of  
 3358 the spline.

3359 The rational quadratic spline is defined on a set interval. The transformation outside of  
 3360 this interval is set to the identity, with these linear tails allowing for unconstrained inputs.  
 3361 The boundaries between bins of the spline are set by coordinates called *knots*, with  $K + 1$   
 3362 knots for  $K$  bins – the two endpoints for the spline interval plus the  $K - 1$  internal boundaries.  
 3363 The derivatives at these points are constrained to be positive for the internal knots, and  
 3364 boundary derivatives are set to 1 to match the linear tails.

3365 The bin widths and heights are learnable ( $2 \cdot K$  parameters) as are the internal knot  
 3366 derivatives ( $K - 1$  parameters), and these  $3K - 1$  outputs of the neural network are sufficient  
 3367 to define a monotonic rational-quadratic spline which passes through each knot and has the  
 3368 given derivative value at each knot.

3369 In the context of the  $HH \rightarrow 4b$  analysis, a neural spline flow is used to model the four  
 3370 vector information of each Higgs candidate, conditional on their respective masses. The  
 3371 resulting flow is therefore five dimensional, with inputs  $x = (p_{T,H1}, p_{T,H2}, \eta_{H1}, \eta_{H2}, \Delta\phi_{HH})$ ,  
 3372 where the ATLAS  $\phi$  symmetry has been encoded by assuming  $\phi_{H1} = 0$ . Conditional variables  
 3373  $m_{H1}$  and  $m_{H2}$  are not modeled by the flow, but “come along for the ride”. A standard normal  
 3374 distribution in 5 dimensions is used for the underlying prior. Modeling of the four vectors  
 3375 was chosen in order to reduce bias from modeling  $m_{HH}$  directly.

3376 The trained flow model then gives a model for  $p(x|m_{H1}, m_{H2})$  which may be sampled  
 3377 from to reconstruct distributions of  $HH$  kinematics given values of  $m_{H1}$  and  $m_{H2}$ .

3378 *B.2.2 Gaussian Processes*

3379 The second piece of this background estimate is the modeling of the mass plane density,  
 3380  $p(m_{H1}, m_{H2})$ . This is done using Gaussian process regression – note that a similar procedure  
 3381 is used to define a systematic in the boosted  $4b$  analysis. Generally, Gaussian processes  
 3382 are a collection of random variables in which every finite collection of said variables is  
 3383 distributed according to a multivariate normal distribution. For the context of Gaussian  
 3384 process regression, what we consider is a Gaussian process over function space, that is, for a  
 3385 collection of points,  $x_1, \dots, x_N$ , the space of corresponding function values,  $(f(x_1), \dots, f(x_N))$   
 3386 is Gaussian process distributed, that is, described by an  $N$  dimensional normal distribution  
 3387 with mean  $\mu$ , covariance matrix  $\Sigma$ .

3388 For a single point, this would correspond to a function space described entirely by a  
 3389 normal distribution, with various samples from that distribution yielding various candidate  
 3390 functions. For multiple points, a covariance matrix describes the relationship between each  
 3391 pair of points – correspondingly, it is represented via a *kernel function*,  $K(x, x')$ . As, in  
 3392 practice,  $\mu$  may always be set to 0 via a centering of the data, the kernel function fully defines  
 3393 the considered family of functions.

The considered family of functions describes a Bayesian *prior* for the data. This prior  
 may be conditioned on a set of training data points  $(X_1, \vec{y}_1)$ . This conditional *posterior* may

then be used to make predictions  $\vec{y}_2 = f(X_2)$  at a set of new points  $X_2$ . Because of the Gaussian process prior assumption,  $\vec{y}_1$  and  $\vec{y}_2$  are assumed to be jointly Gaussian. We may therefore write

$$\begin{pmatrix} \vec{y}_1 \\ \vec{y}_2 \end{pmatrix} \sim \mathcal{N} \left( \begin{pmatrix} 0 \\ 0 \end{pmatrix}, \begin{pmatrix} K(X_1, X_1) & K(X_1, X_2) \\ K(X_1, X_2) & K(X_2, X_2) \end{pmatrix} \right) \quad (\text{B.6})$$

3394 where we have used that the kernel function is symmetric and assumed prior mean 0.

By standard conditioning properties of Gaussian distributions,

$$\vec{y}_2 | \vec{y}_1 \sim \mathcal{N}(K(X_2, X_1)K(X_1, X_1)^{-1}\vec{y}_1, K(X_2, X_2) - K(X_2, X_1)K(X_1, X_1)^{-1}K(X_1, X_2)) \quad (\text{B.7})$$

3395 which is the sampling distribution for a Gaussian process given kernel  $K$ . In practice, the  
3396 mean of this sampling distribution is used as the function estimate, with an uncertainty from  
3397 the predicted variance at a given point.

The choice of kernel function has a very strong impact on the fitted curve, and must therefore be chosen to express the expected dynamics of the data. A common such choice is a radial basis function (RBF) kernel, which takes the form

$$K(x, x') = \exp \left( -\frac{d(x, x')^2}{2l^2} \right) \quad (\text{B.8})$$

3398 where  $d(\cdot, \cdot)$  is the Euclidean distance and  $l > 0$  is a length scale parameter. Conceptually, as  
3399 distances  $d(x, x')$  increase relative to the chosen length scale, the kernel smoothly dies off –  
3400 further away points influence each other less.

3401 Coming back to our case of the mass plane, the procedure runs as follows:

- 3402 1. A binned 2d histogram of the blinded mass plane is created in a window around the  
3403 “standard” analysis regions. Bins which have any overlap with the signal region are  
3404 excluded.
- 3405 2. A Gaussian process is trained using the bin centers, values as training points. The  
3406 scikit-learn implementation [129] is used, with RBF kernel with anisotropic length scale  
3407 ( $l$  is dimension 2). The length scale is initialized to  $(50, 50)$  to cover the signal region,

3408 and optimized by minimizing the negative log-marginal likelihood on the training data,  
 3409  $-\log p(\vec{y}|\theta)$ . Training data is centered and scaled to mean 0, variance 1, and a statistical  
 3410 error is included in the fit.

- 3411 3. The Gaussian process is then used to predict the density  $p(m_{H1}, m_{H2})$  in the signal  
 3412 region. This may then be sampled from via an inverse transform sampling to generate  
 3413 values  $(m_{H1}, m_{H2})$  according to the density (specifically, according to the mean of the  
 3414 Gaussian process posterior). Though in principle the Gaussian process sampling is not  
 3415 limited to bin centers, this is kept for simplicity, with a uniform smearing applied within  
 3416 each sampled bin to approximate the continuous estimate, namely, if a bin is sampled  
 3417 from, the returned value is drawn uniformly at random within the sampled bin.
4. The sampling in the previous step can be arbitrary – to set the overall normalization,  
 a Monte Carlo sampling of the Gaussian process is done to approximate the relative  
 fraction of events predicted both inside ( $f_{in}$ ) and outside ( $f_{out}$ ) of the signal region,  
 within the training box. The number of events outside of the signal region ( $n_{out}$ ) is  
 known, therefore, the number of events inside of the signal region,  $n_{in}$ , may be estimated  
 as

$$n_{in} = \frac{n_{out}}{f_{out}} \cdot f_{in}. \quad (\text{B.9})$$

3418 Note that the Monte Carlo sampling procedure is simply a set of samples of the Gaussian  
 3419 process from uniformly random values of  $m_{H1}, m_{H2}$ , and is the most convenient approach  
 3420 given the irregular shape of the signal region.

3421 This procedure results in a generated set of predicted  $m_{H1}, m_{H2}$  values for signal region  
 3422 background events, along with an overall yield prediction.

### 3423 B.2.3 The Full Prediction

3424 Given the normalizing flow parametrization of  $p(x|m_{H1}, m_{H2})$  and the Gaussian process  
 3425 generation of  $(m_{H1}, m_{H2}) \sim p(m_{H1}, m_{H2})$  and prediction of the signal region yield, all of the

3426 pieces are in place to construct an interpolation background estimate. Namely

- 3427 1. Gaussian process sampled ( $m_{H1}, m_{H2}$ ) values are provided to the normalizing flow to
  - 3428 predict the other variables for the Higgs candidate four-vectors. These are used to
  - 3429 construct the  $HH$  system (notably  $m_{HH}$ ).
- 3430 2. These final distributions are normalized according to the predicted background yield.

3431 *B.2.4 Results*

3432 All of the following results use the pairAGraph pairing algorithm, and reweighted results use  
3433 the region definitions from the resonant analysis.

3434 The Gaussian process sampling procedure is trained on a small fraction (0.01) of  $2b$  data  
3435 to mimic the available  $4b$  statistics. This fraction of  $2b$  data is blinded, and the prediction of  
3436 the estimate trained on this blinded region may then be compared to real  $2b$  data in the signal  
3437 region. The predictions for signal region  $m_{H1}$  and  $m_{H2}$  individually are shown in Figure B.3,  
3438 and the resulting mass planes are compared in Figure B.4. Good agreement is seen.

3439 The  $4b$  region is kept blinded for this work, meaning that a direct comparison of the  
3440 Gaussian process estimate in the  $4b$  signal region is not done. However, a Gaussian process is  
3441 trained on the blinded  $4b$  region and compared to the corresponding reweighted  $2b$  estimate,  
3442 trained per the nominal procedures from the analyses above. The predictions for signal  
3443 region  $m_{H1}$  and  $m_{H2}$  individually are shown in Figure B.5, compared to both the control and  
3444 validation region derived reweighting estimates, and the resulting signal region mass planes  
3445 are compared in Figure B.6. The estimates are seen to be compatible.

3446 The Gaussian process estimate may then be used as an input to the normalizing flow  
3447 estimate to form a complete background estimate. Figure B.7 shows such an estimate for the  
3448 subsampled  $2b$  signal region. Results for the prediction of the normalizing flow with inputs of  
3449 real  $2b$  signal region  $m_{H1}$  and  $m_{H2}$  are compared to the results of using Gaussian process  
3450 predicted  $m_{H1}$  and  $m_{H2}$ , and are seen to be consistent, demonstrating the above closure of

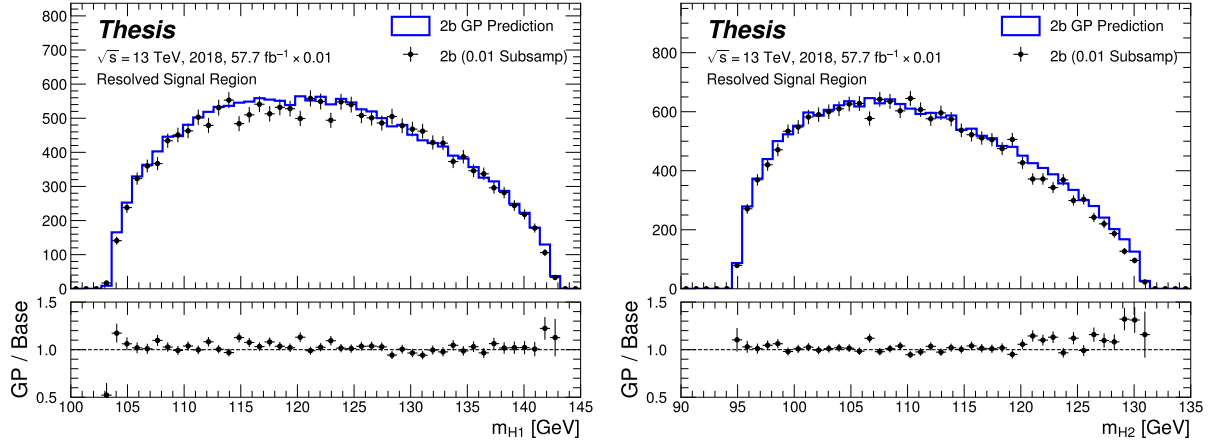


Figure B.3: Gaussian process sampling prediction of marginals  $m_{H_1}$  and  $m_{H_2}$  for  $2b$  signal region events compared to real  $2b$  signal region events for the 2018 dataset. Good agreement is seen. Only a small fraction (0.01) of the  $2b$  dataset is used for both training and this final comparison to mimic  $4b$  statistics.

3451 the Gaussian process prediction. Reasonable agreement with real  $2b$  signal region data is  
 3452 seen.

3453 Figure B.8 demonstrates the application of this process to the  $4b$  region, closely following  
 3454 how such an estimate would be used in the  $HH \rightarrow b\bar{b}b\bar{b}$  analysis. As the  $4b$  signal region  
 3455 is kept blinded for these studies, no direct evaluation is made, but results are compared to  
 3456 a resonant control region derived reweighting. Both signal region predictions are seen to  
 3457 be comparable, though there are some systematic differences. However, only the nominal  
 3458 estimates are compared here, with assessment of uncertainties on the interpolated estimate  
 3459 left for future work.

### 3460 B.2.5 Outstanding Points

3461 While good performance is demonstrated from the nominal interpolated background estimate,  
 3462 various uncertainties must be assigned according to the various stages of the estimate. These

3463 notably include

3464 • Assessing a statistical uncertainty on the normalizing flow training (cf. bootstrap  
3465 uncertainty).

3466 • Propagation of the Gaussian process uncertainty through the sampling procedure.

3467 • Validation of the resulting estimate and assessment of necessary systematic uncertainties  
3468 (e.g. from validation region non-closure).

3469 These are all quite tractable, but some, especially the choice of an appropriate systematic  
3470 uncertainty, are certainly not obvious and require detailed study. In this respect, the  
3471 reweighting validation work of the non-resonant analysis is certainly quite useful as a starting  
3472 place in terms of the available regions and their correspondence to the nominal  $4b$  signal  
3473 region.

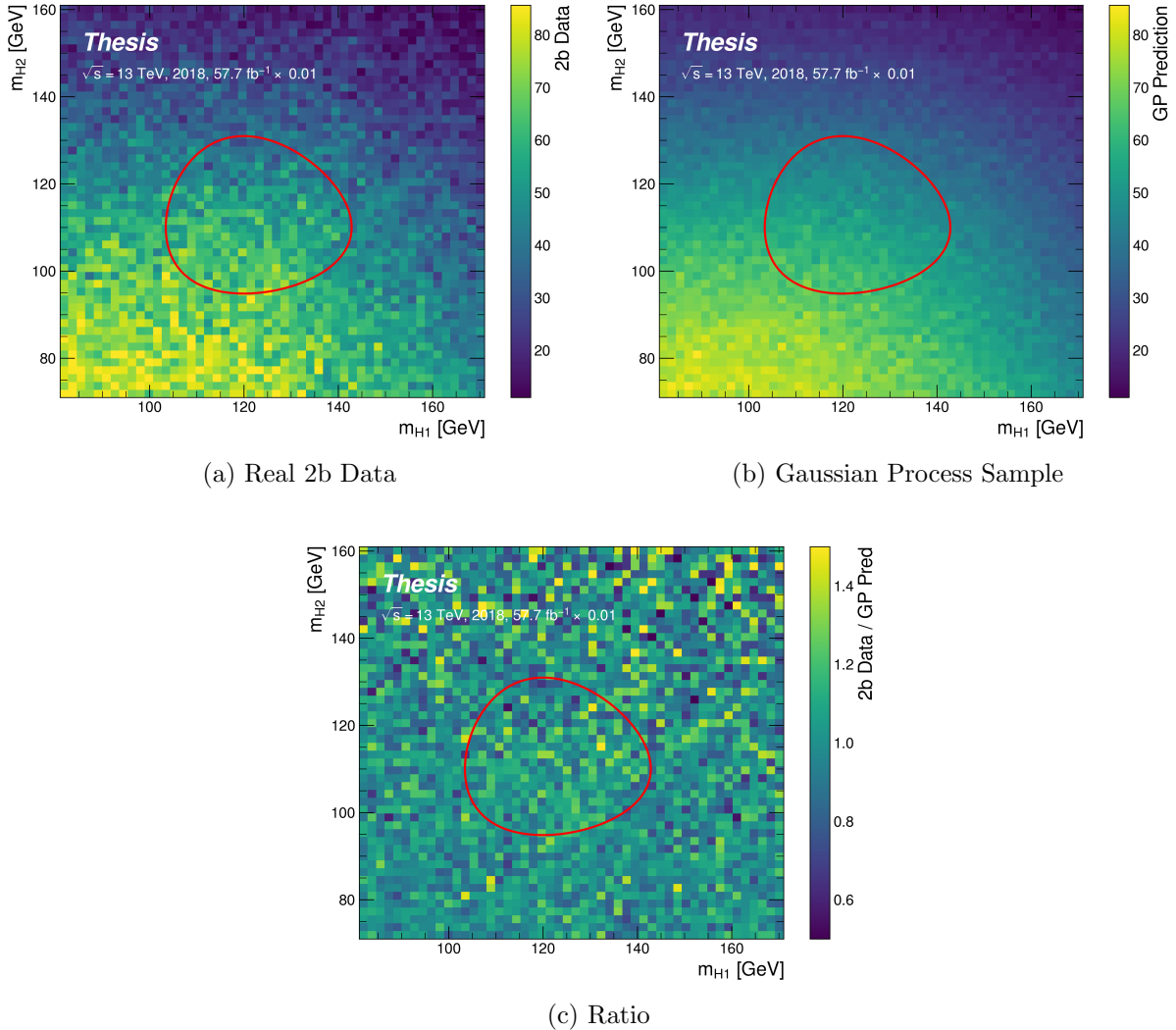


Figure B.4: Gaussian process sampling prediction for the mass plane compared to the real  $2b$  dataset for 2018. Only a small fraction (0.01) of the  $2b$  dataset is used for both training and this final comparison to mimic  $4b$  statistics. Good agreement is seen.

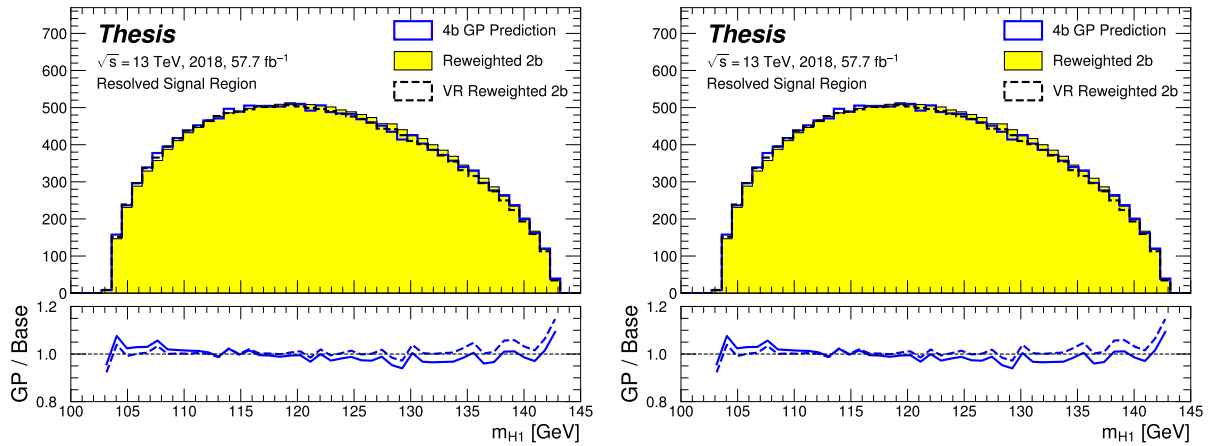


Figure B.5: Gaussian process sampling prediction of marginals  $m_{H1}$  and  $m_{H2}$  for 4b signal region events compared to both control and validation reweighting predictions. While there are some differences, the estimates are compatible.

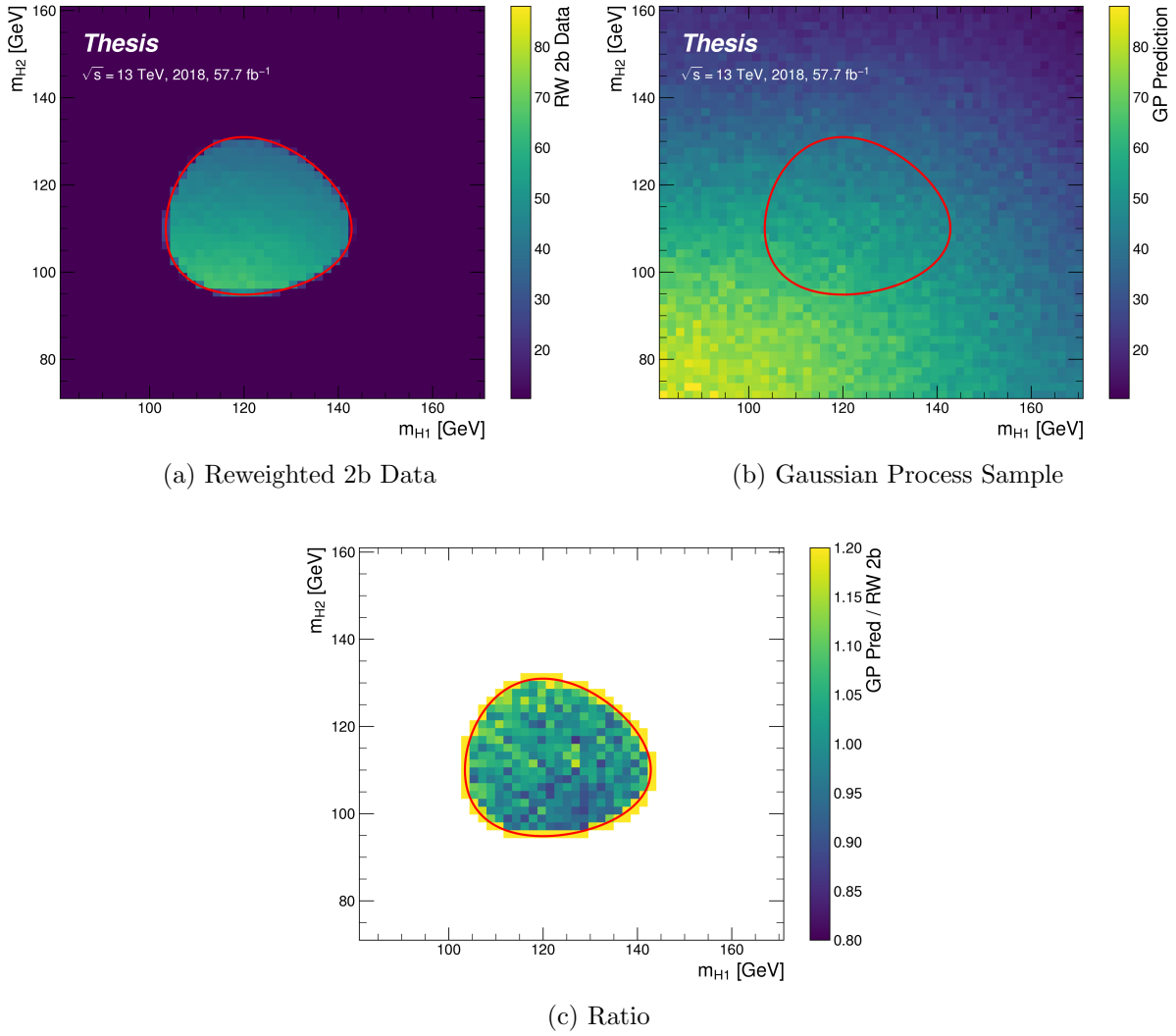


Figure B.6: Gaussian process sampling prediction for the  $4b$  mass plane compared to the reweighted  $2b$  estimate in the signal region. Both estimates are compatible.

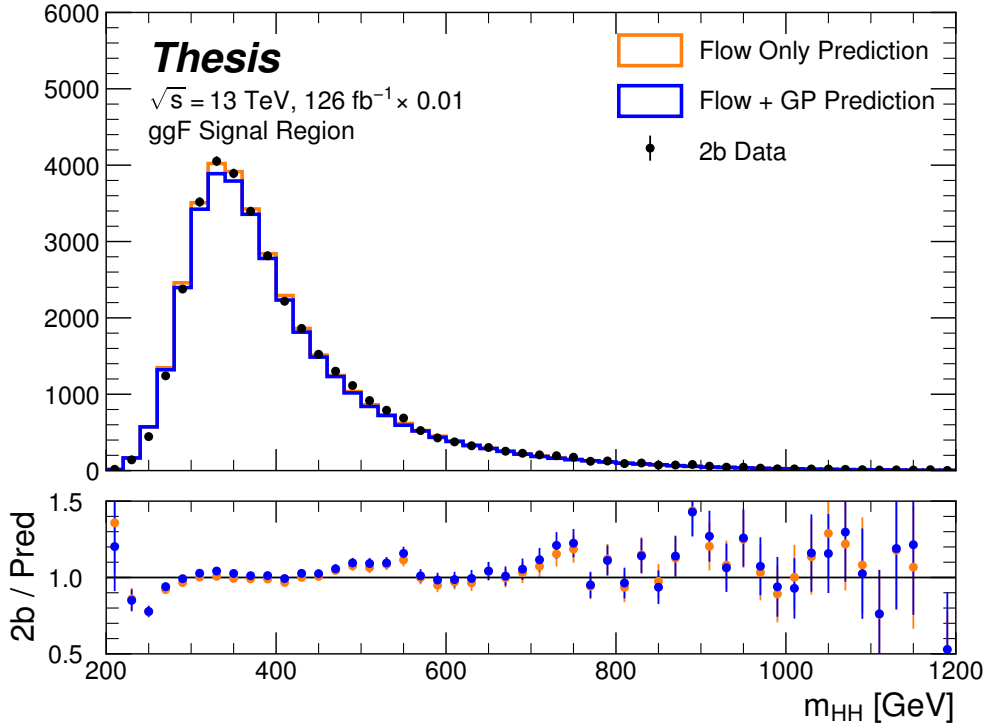


Figure B.7: Comparison of the interpolation background estimate with real 2b data in the signal region. Only 1 % of 2b data is used in order to mimic 4b statistics, and results are presented here summed across years. The “Flow Only” prediction uses samples of actual 2b signal region data for the input values of  $m_{H_1}$  and  $m_{H_2}$ , whereas the “Flow + GP” prediction uses samples following the Gaussian process procedure above, more closely mimicking a the full background estimation procedure. The two predictions are quite comparable, demonstrating the closure of the Gaussian process estimate, and the predicted  $m_{HH}$  shape agrees well with 2b data. Only 2b statistical uncertainty is shown.

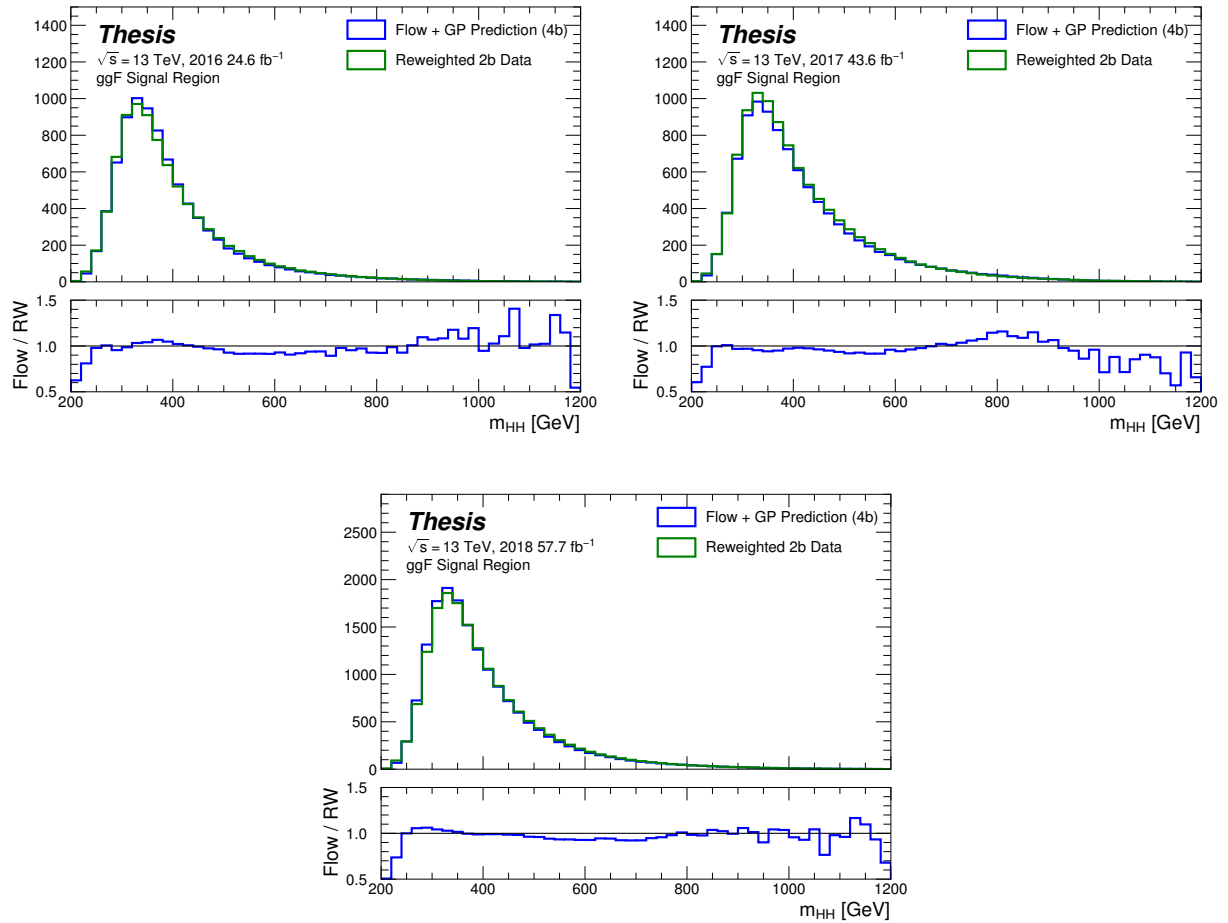


Figure B.8: Comparison of the interpolation background estimate in the  $4b$  signal region with the control region derived reweighted 2b estimate, shown for each year individually. Results are generally similar, within around 10 %.

3474

## Appendix C

3475

### KINEMATIC REWEIGHTING FOR THE 2018 VALIDATION REGION

3476

3477 The impact of this control region derived reweighting in the validation region for the  
3478 2018 dataset is shown in Figures C.1 through C.9 for the resonant search and Figures C.10  
3479 through C.18 for 4b and Figures C.19 through C.27 for 3b1l for the non-resonant search. 2018  
3480 is chosen because it is the largest subset of the data on which the year-by-year reweighting is  
3481 trained. Generally good agreement is seen, though there are differences due to the application  
3482 of the reweighting outside of the training region. As noted above, the bimodal structure in  
3483  $m_{H_1}$  for the non-resonant search is due to the definition of the validation region.

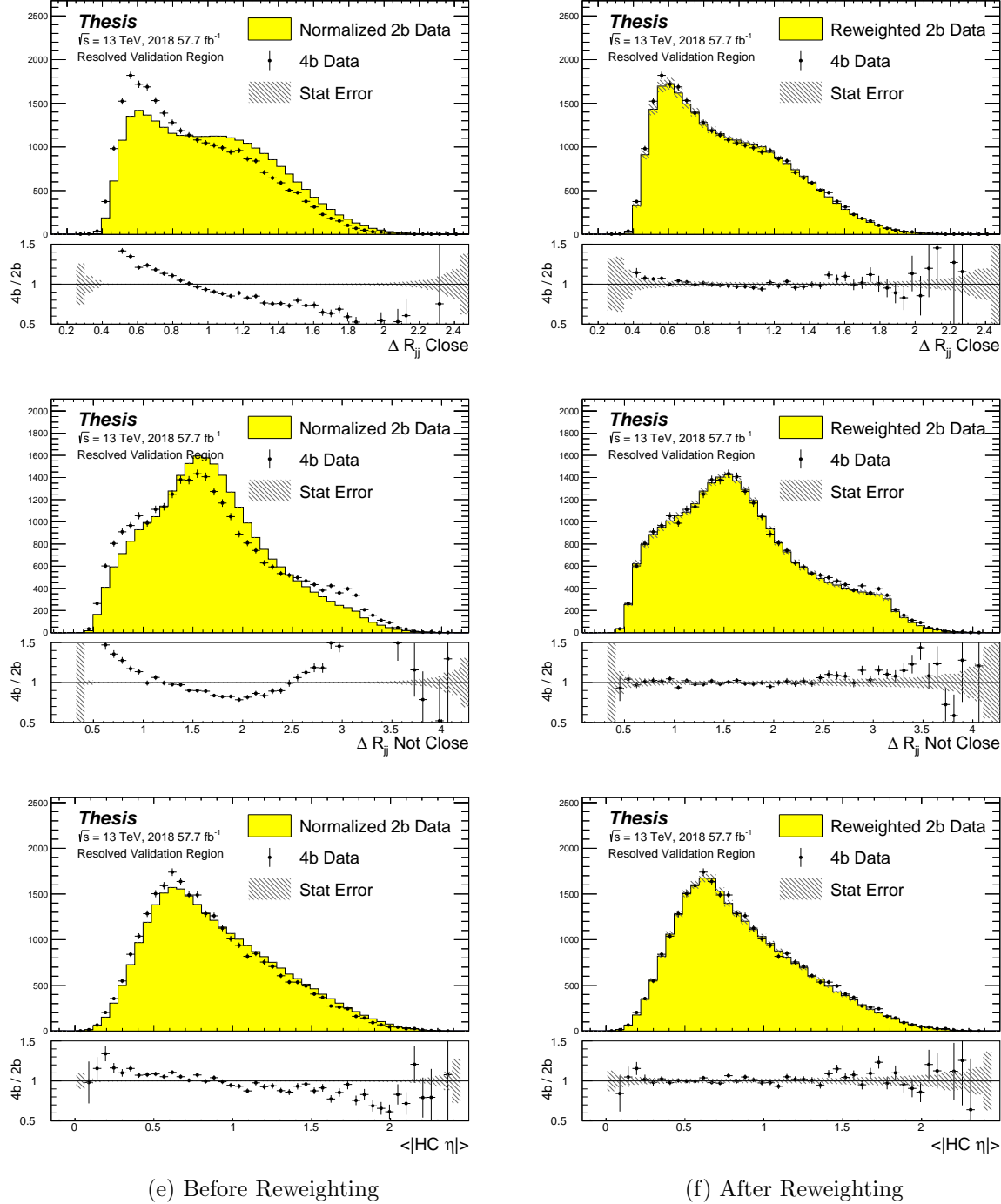


Figure C.1: **Resonant Search:** Distributions of  $\Delta R$  between the closest Higgs Candidate jets,  $\Delta R$  between the other two, and average absolute value of HC jet  $\eta$  before (left) and after (right) CR derived reweighting for the 2018 Validation Region.

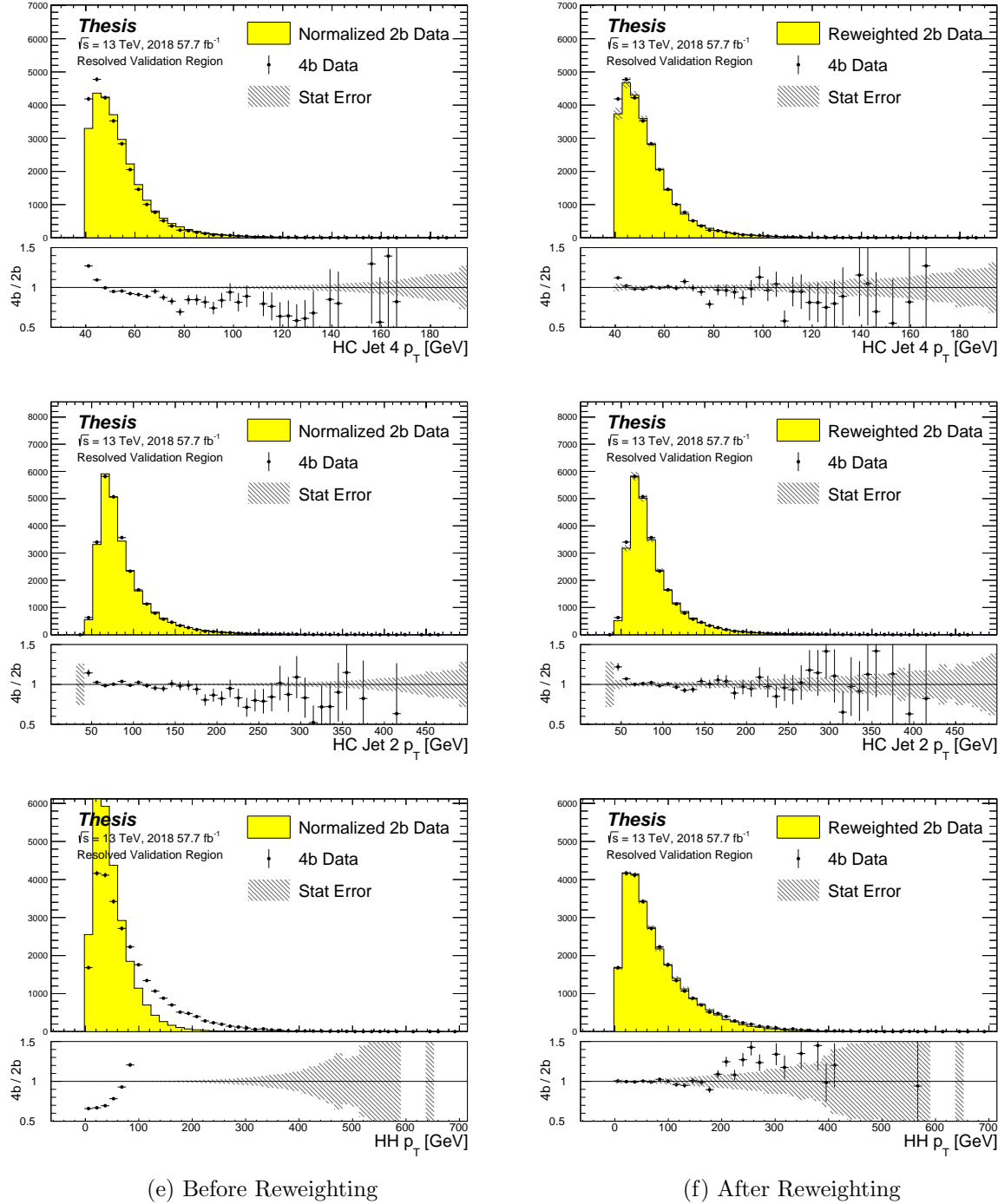


Figure C.2: **Resonant Search:** Distributions of  $p_T$  of the 2nd and 4th leading Higgs Candidate jets and the  $p_T$  of the di-Higgs system before (left) and after (right) CR derived reweighting for the 2018 Validation Region.

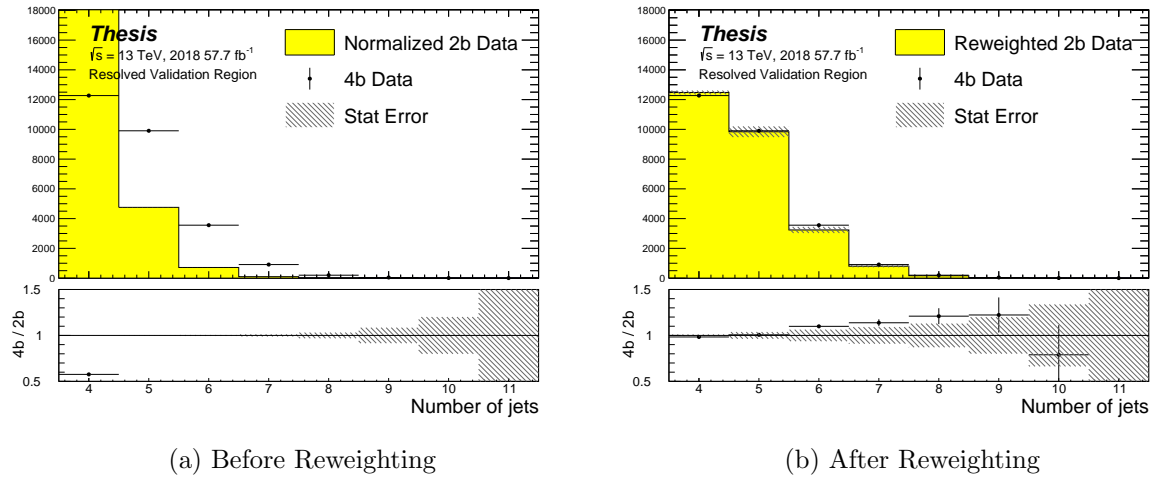


Figure C.3: **Resonant Search:** Distributions of the number of jets before (left) and after (right) CR derived reweighting for the 2018 Validation Region. A minimum of 4 jets is required in each event in order to form Higgs candidates.

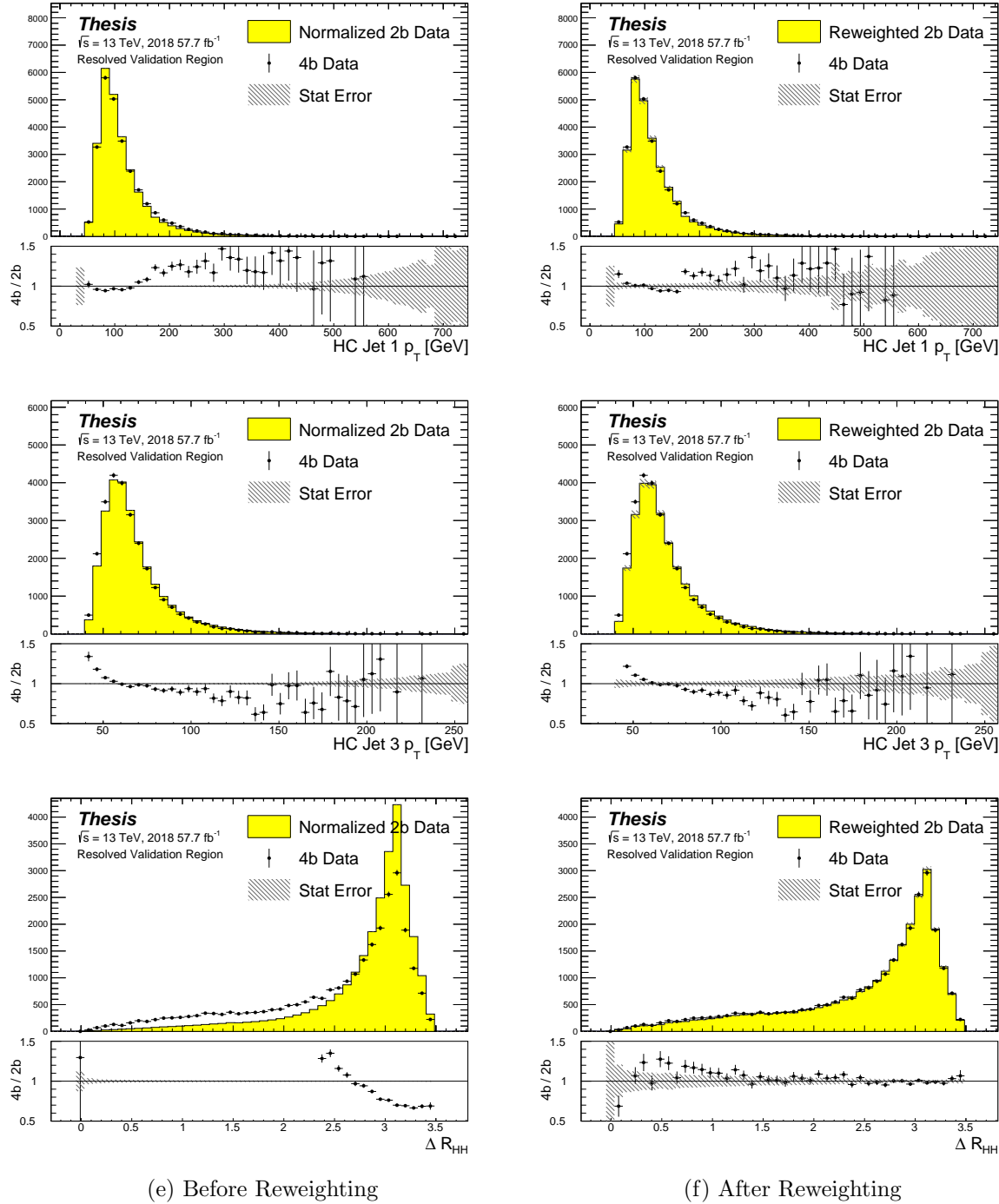


Figure C.4: **Resonant Search:** Distributions of  $p_T$  of the 1st and 3rd leading Higgs Candidate jets and  $\Delta R$  between Higgs candidates before (left) and after (right) CR derived reweighting for the 2018 Validation Region.

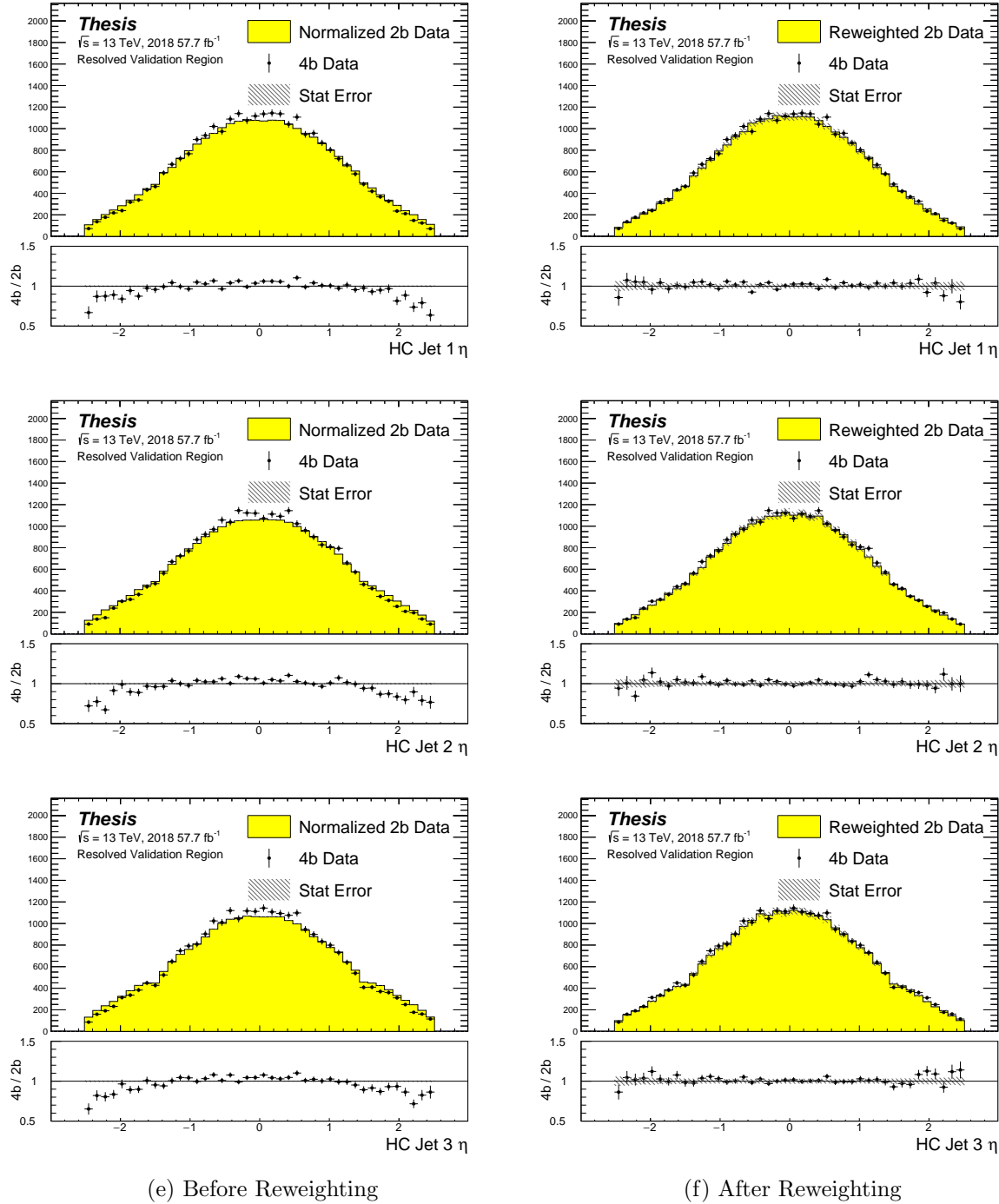


Figure C.5: **Resonant Search:** Distributions of  $\eta$  of the 1st, 2nd, and 3rd leading Higgs Candidate jets before (left) and after (right) CR derived reweighting for the 2018 Validation Region.

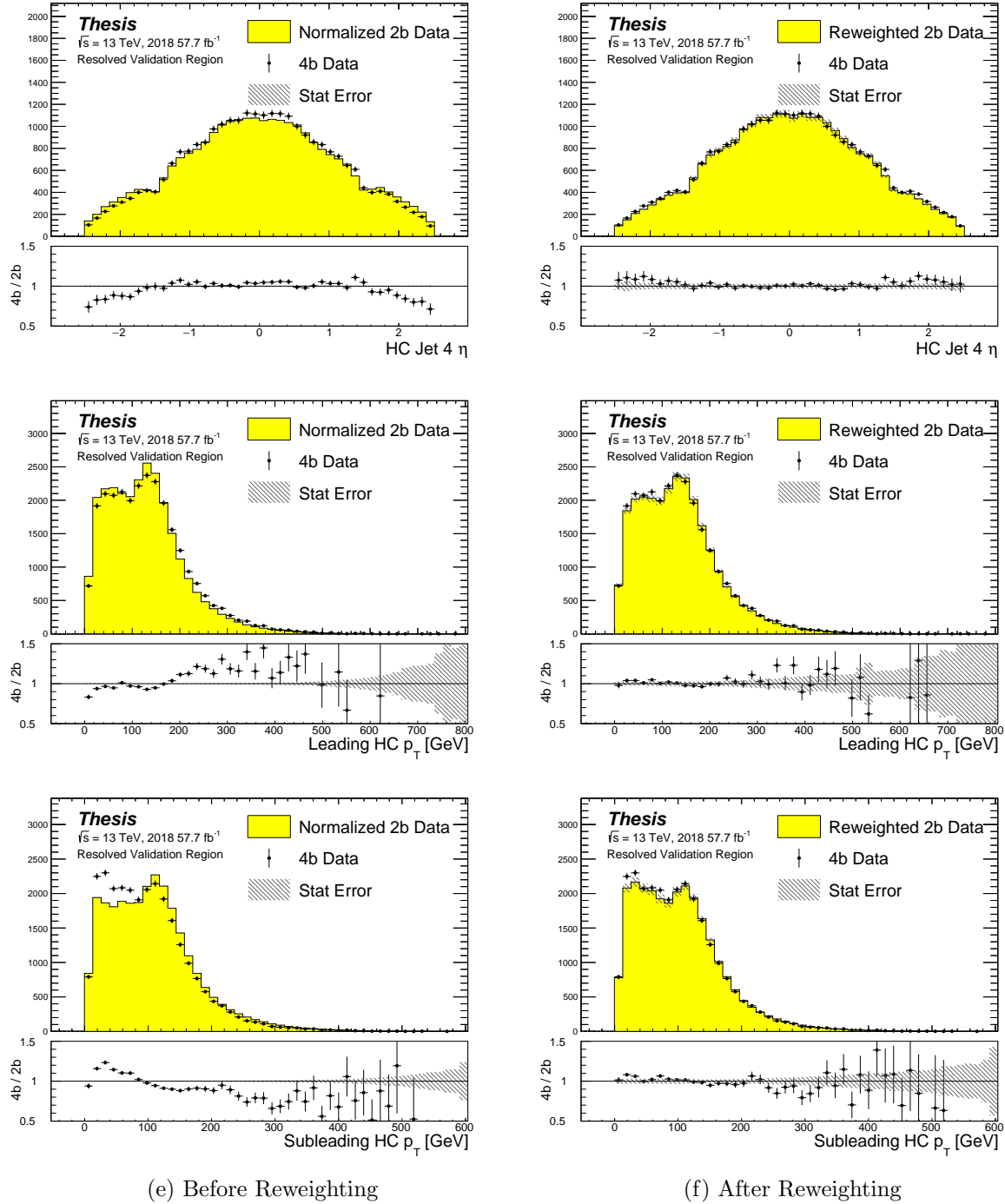


Figure C.6: **Resonant Search:** Distributions of  $\eta$  of the 4th leading Higgs Candidate jet and the  $p_T$  of the leading and subleading Higgs candidates before (left) and after (right) CR derived reweighting for the 2018 Validation Region.

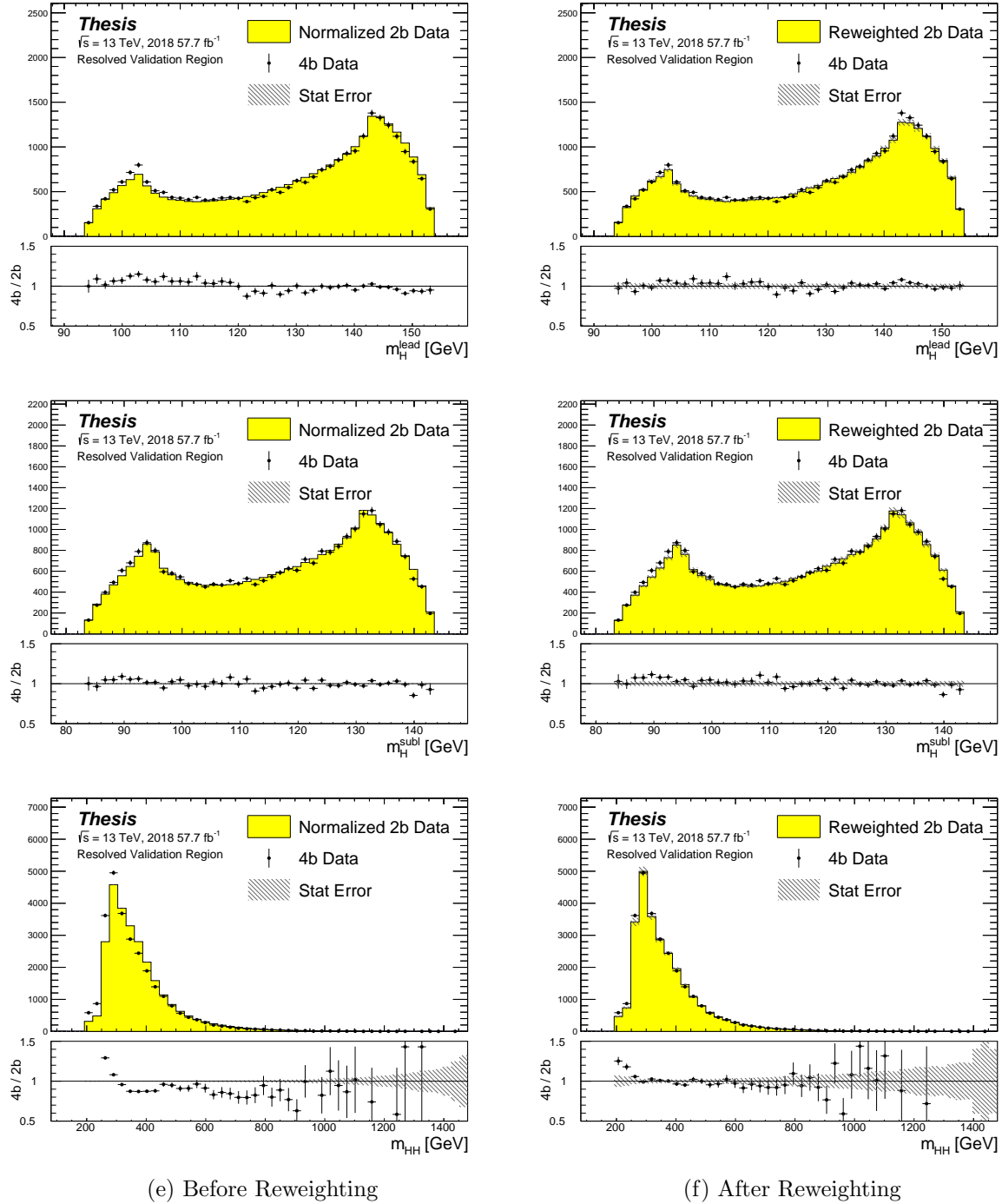


Figure C.7: **Resonant Search:** Distributions of mass of the leading and subleading Higgs candidates and of the di-Higgs system before (left) and after (right) CR derived reweighting for the 2018 Validation Region.

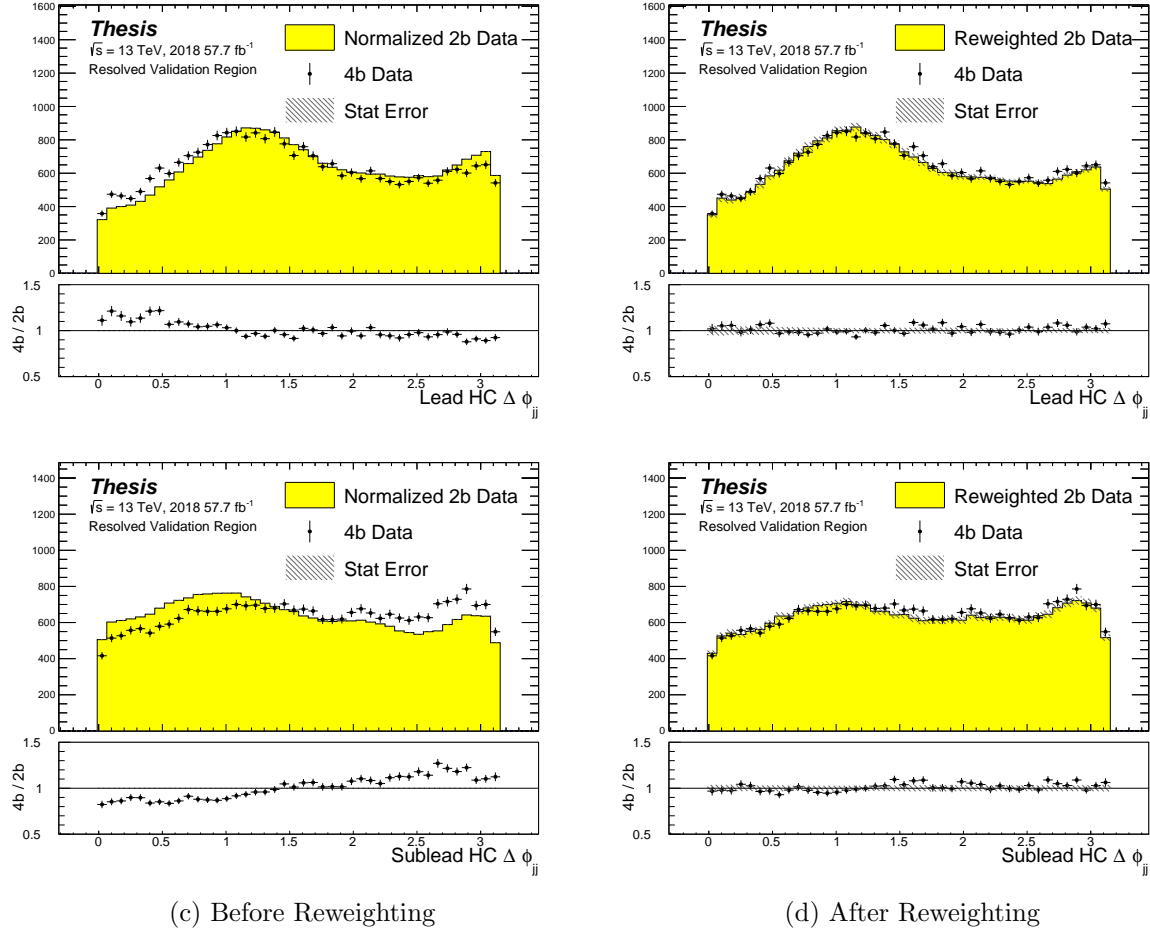


Figure C.8: **Resonant Search:** Distributions of  $\Delta\phi$  between jets in the leading and sub-leading Higgs candidates before (left) and after (right) CR derived reweighting for the 2018 Validation Region.

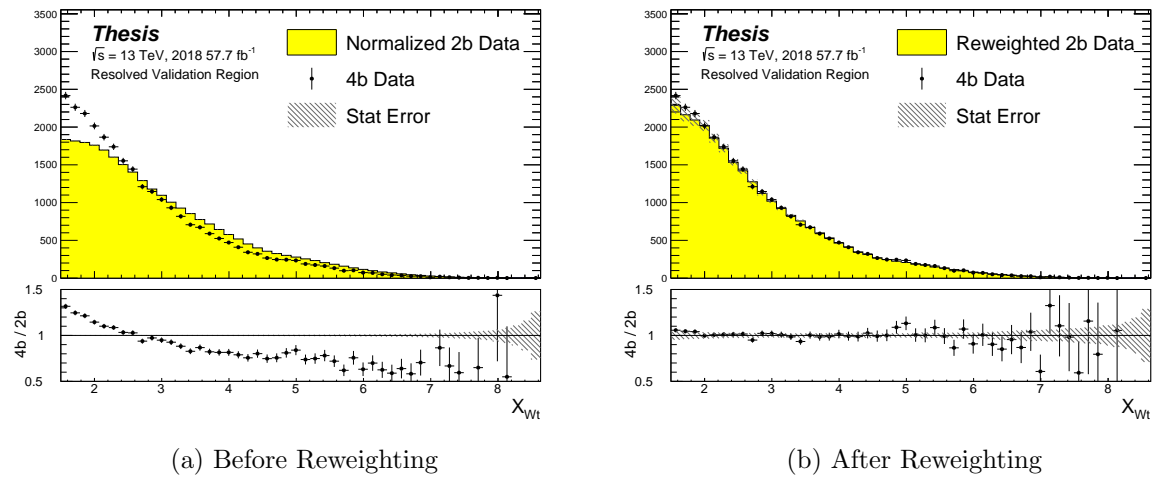


Figure C.9: **Resonant Search:** Distributions of the top veto variable,  $X_{Wt}$ , before (left) and after (right) CR derived reweighting for the 2018 Validation Region. Reweighting is done after the cut on this variable is applied

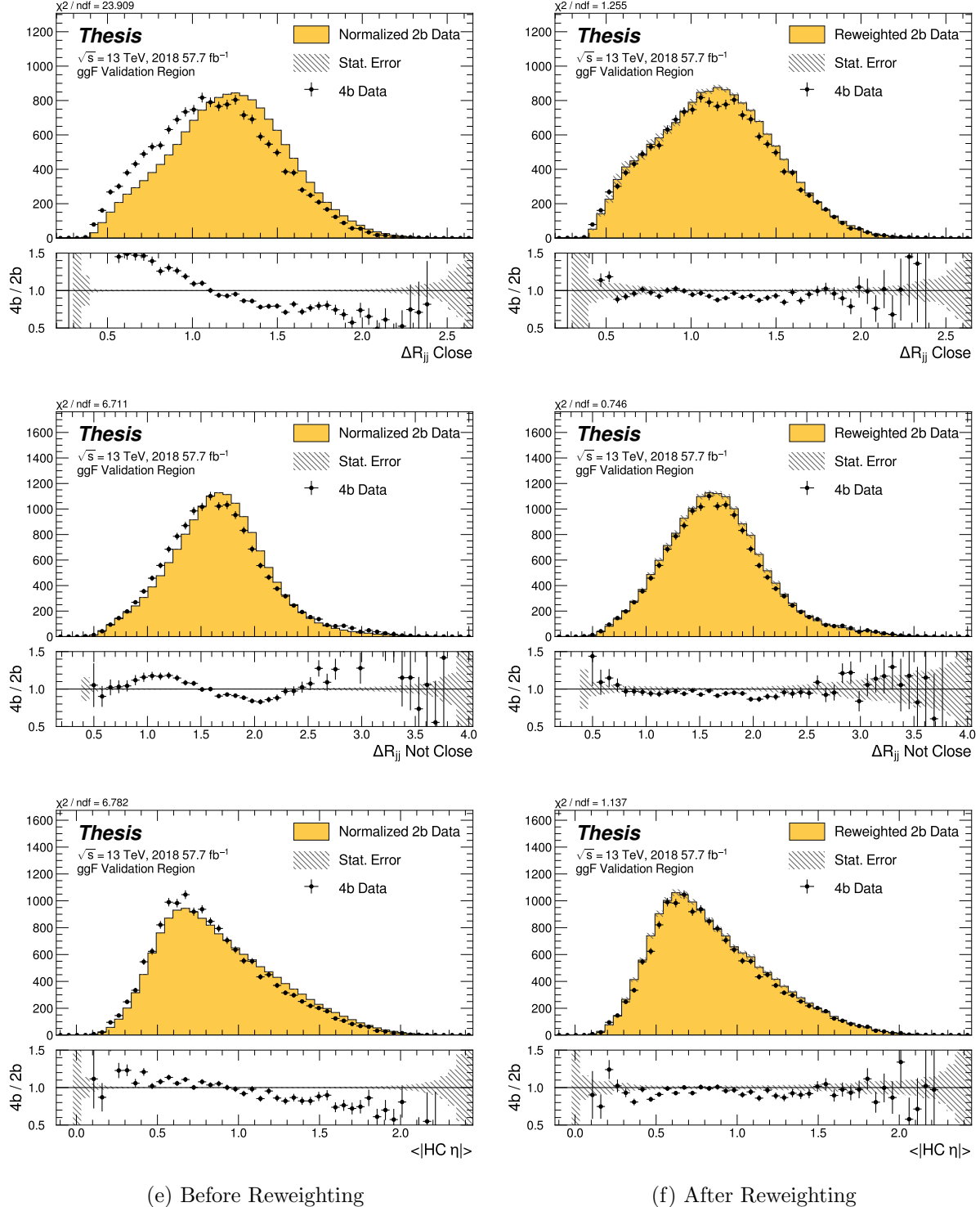


Figure C.10: **Non-resonant Search (4b):** Distributions of  $\Delta R$  between the closest Higgs Candidate jets,  $\Delta R$  between the other two, and average absolute value of HC jet  $\eta$  before (left) and after (right) CR derived reweighting for the 2018 4b Validation Region.

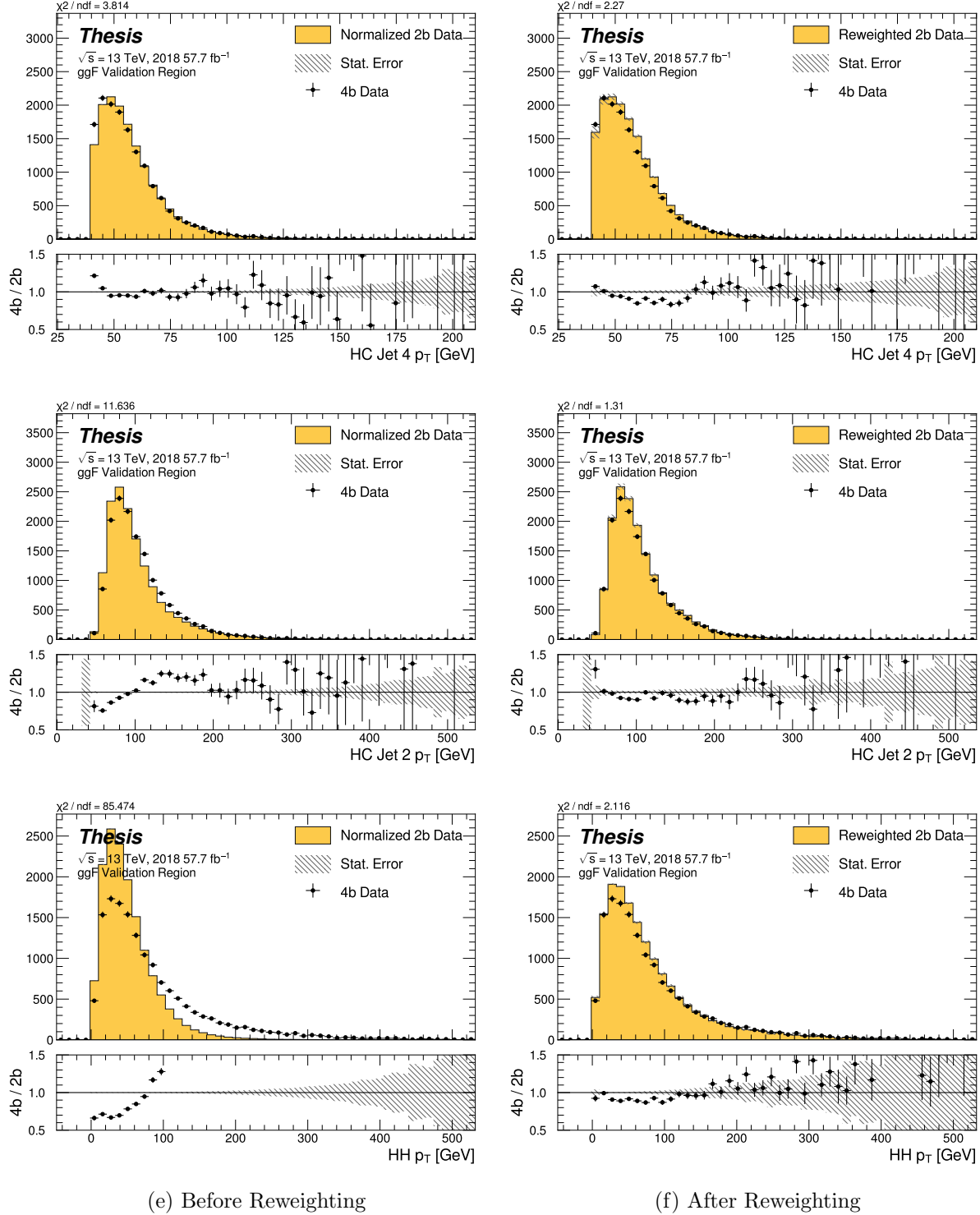


Figure C.11: **Non-resonant Search (4b):** Distributions of  $p_T$  of the 2nd and 4th leading Higgs Candidate jets and the  $p_T$  of the di-Higgs system before (left) and after (right) CR derived reweighting for the 2018 4b Validation Region.

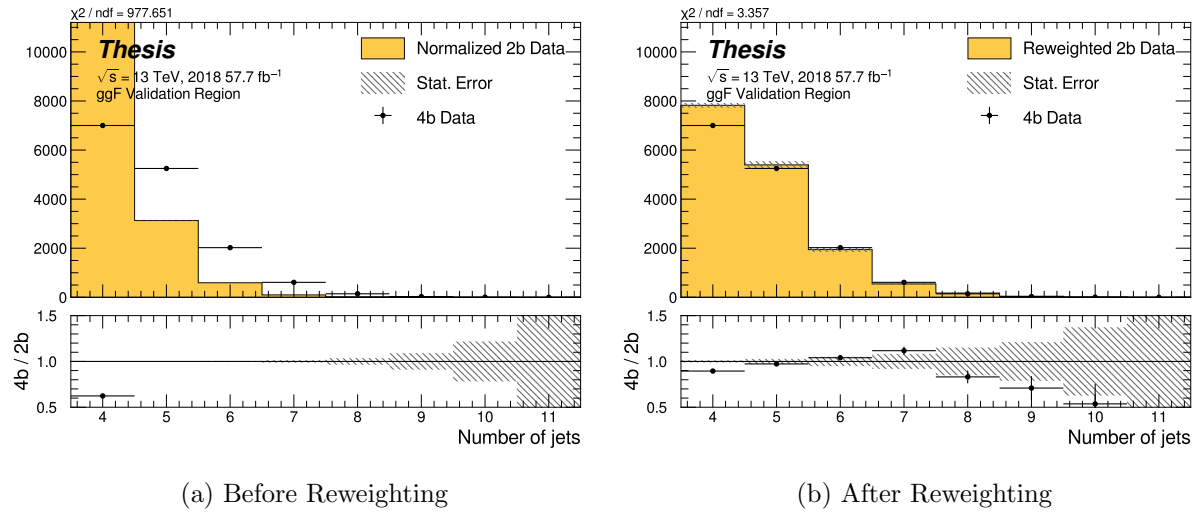


Figure C.12: **Non-resonant Search (4b):** Distributions of the number of jets before (left) and after (right) CR derived reweighting for the 2018 4b Validation Region. A minimum of 4 jets is required in each event in order to form Higgs candidates.

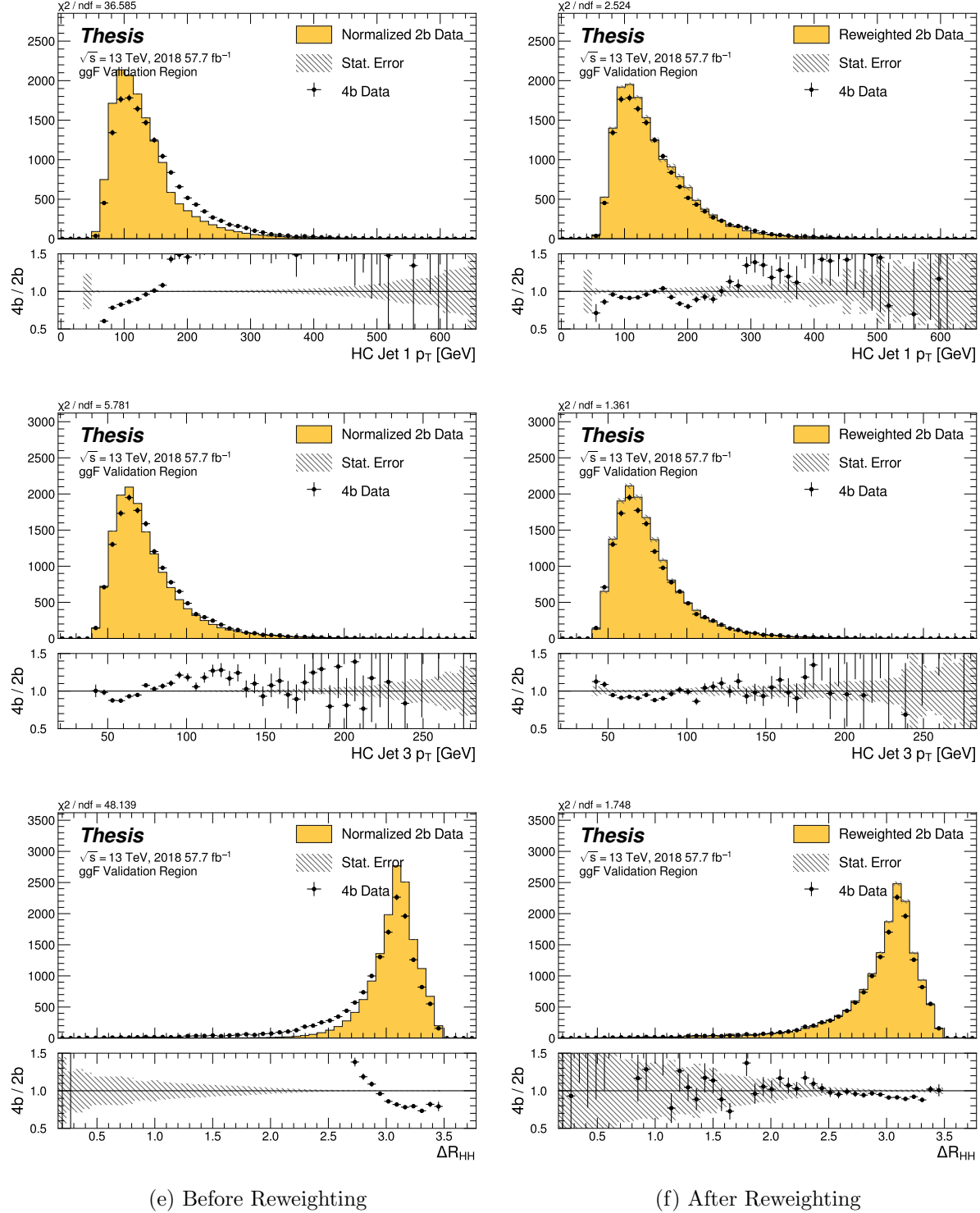


Figure C.13: **Non-resonant Search (4b):** Distributions of  $p_T$  of the 1st and 3rd leading Higgs Candidate jets and  $\Delta R$  between Higgs candidates before (left) and after (right) CR derived reweighting for the 2018 4b Validation Region.

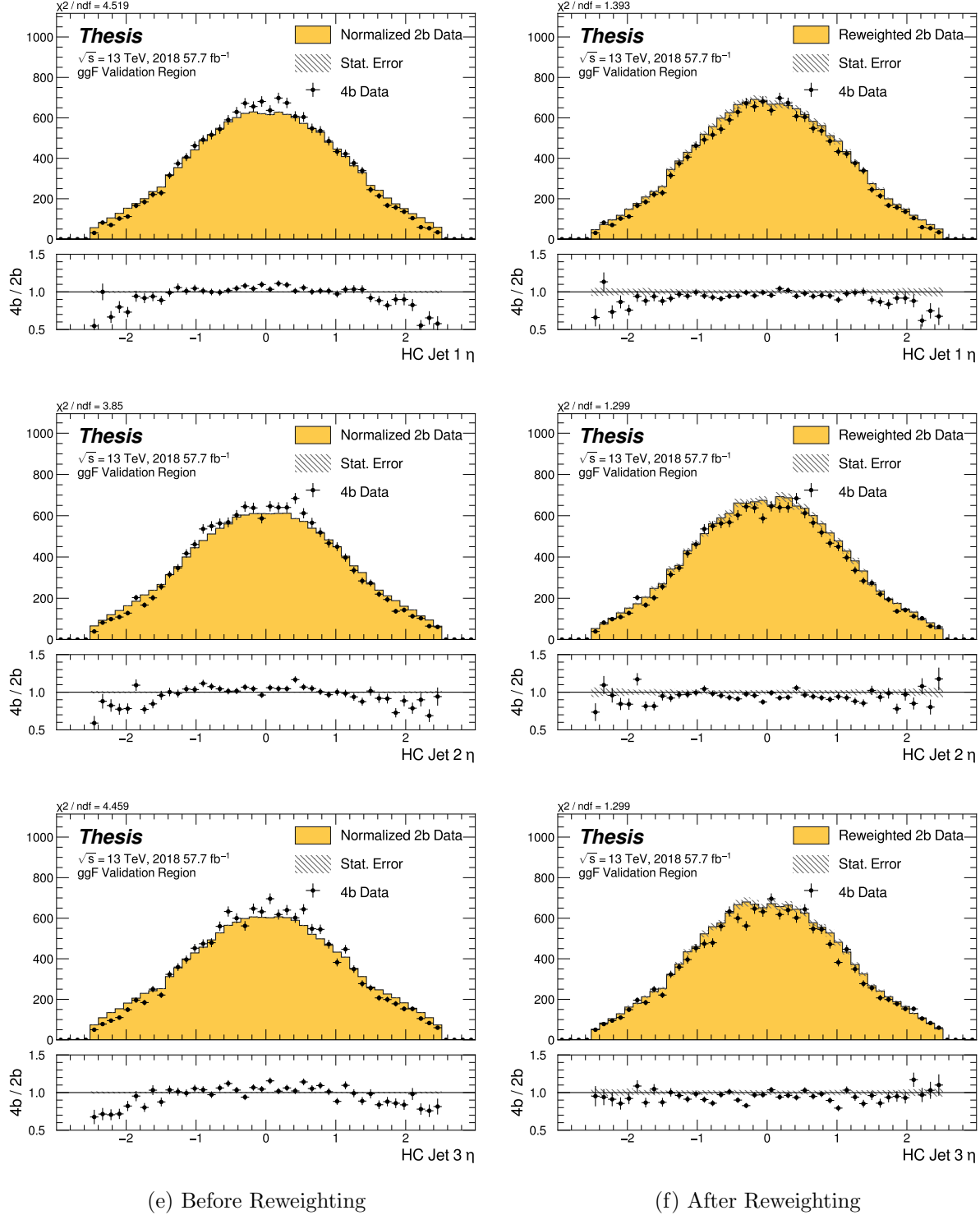


Figure C.14: **Non-resonant Search (4b):** Distributions of  $\eta$  of the 1st, 2nd, and 3rd leading Higgs Candidate jets before (left) and after (right) CR derived reweighting for the 2018 4b Validation Region.

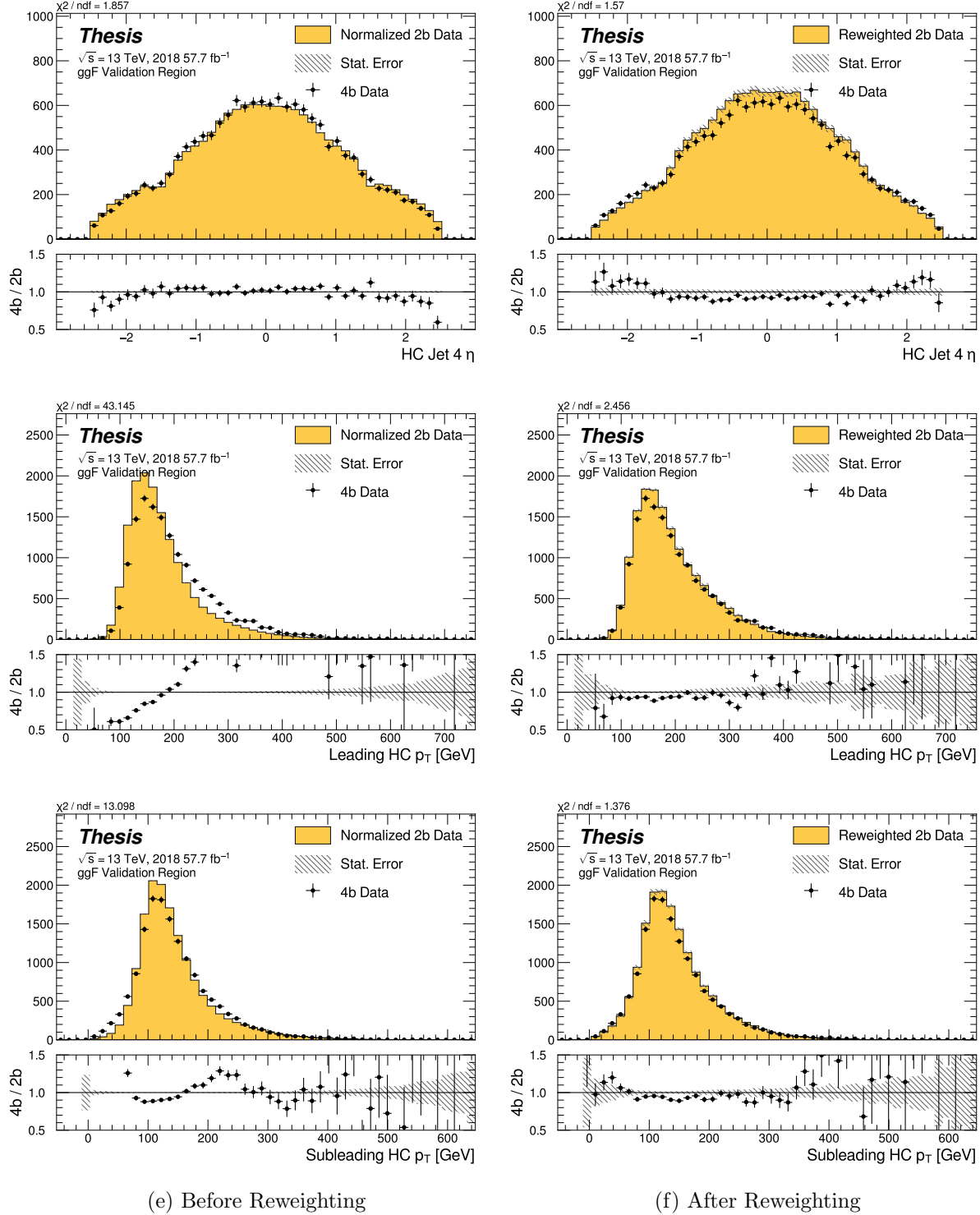


Figure C.15: **Non-resonant Search (4b):** Distributions of  $\eta$  of the 4th leading Higgs Candidate jet and the  $p_T$  of the leading and subleading Higgs candidates before (left) and after (right) CR derived reweighting for the 2018 4b Validation Region.

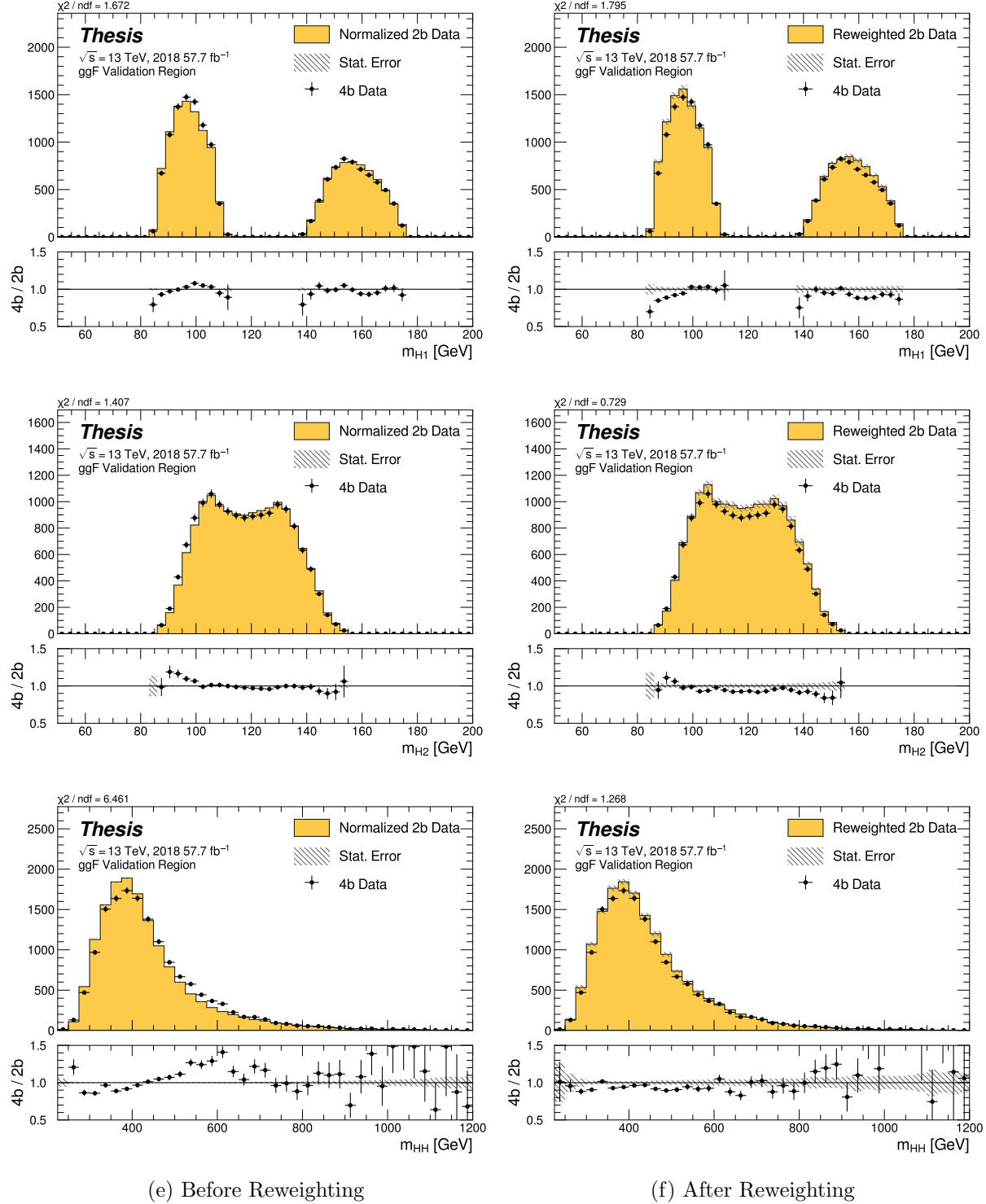


Figure C.16: **Non-resonant Search (4b):** Distributions of mass of the leading and sub-leading Higgs candidates and of the di-Higgs system before (left) and after (right) CR derived reweighting for the 2018 4b Validation Region.

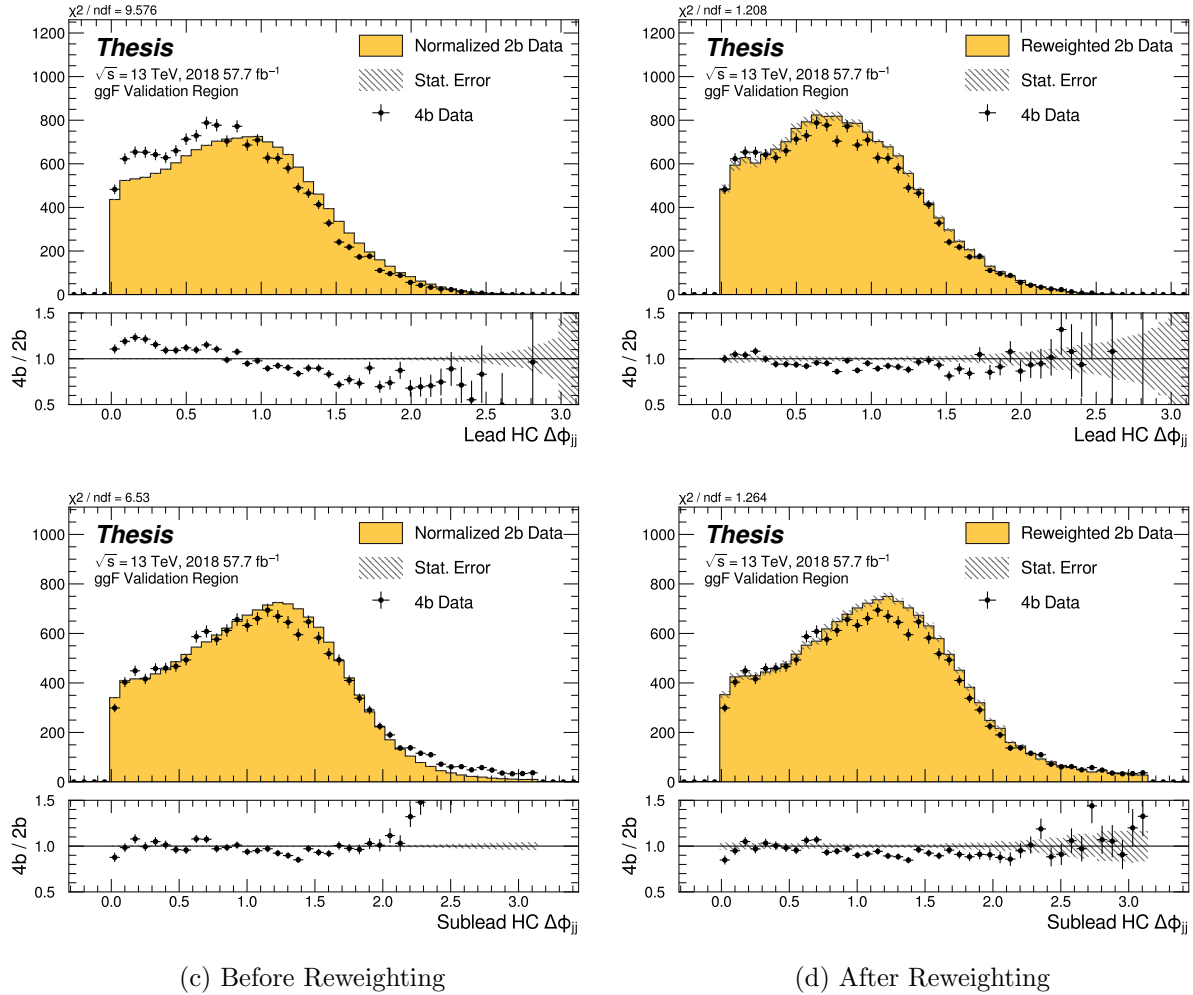


Figure C.17: **Non-resonant Search (4b):** Distributions of  $\Delta\phi$  between jets in the leading and subleading Higgs candidates before (left) and after (right) CR derived reweighting for the 2018 4b Validation Region.

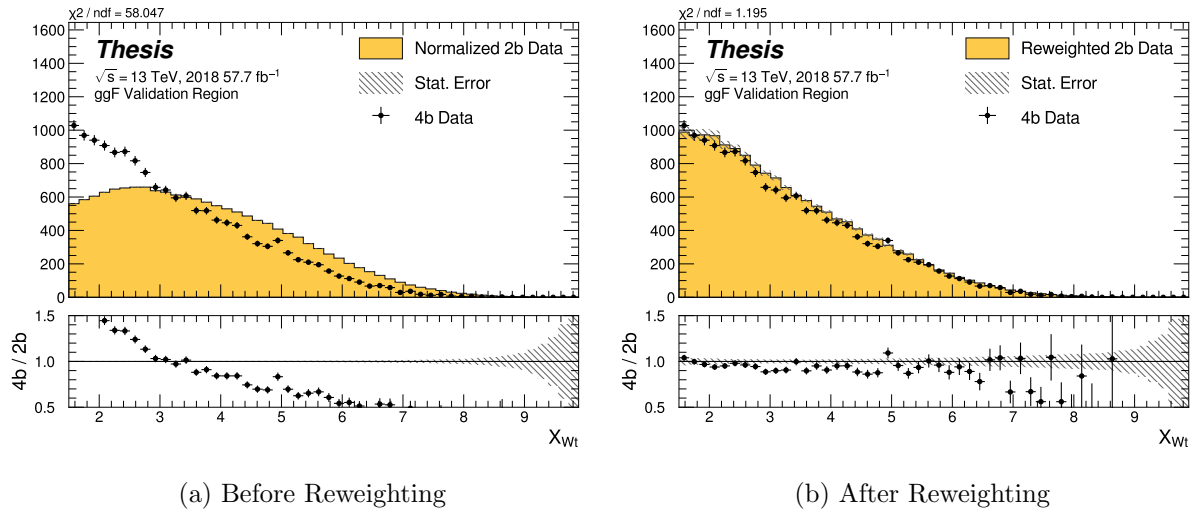


Figure C.18: **Non-resonant Search (4b):** Distributions of the top veto variable,  $X_{Wt}$ , before (left) and after (right) CR derived reweighting for the 2018 4b Validation Region. Reweighting is done after the cut on this variable is applied.

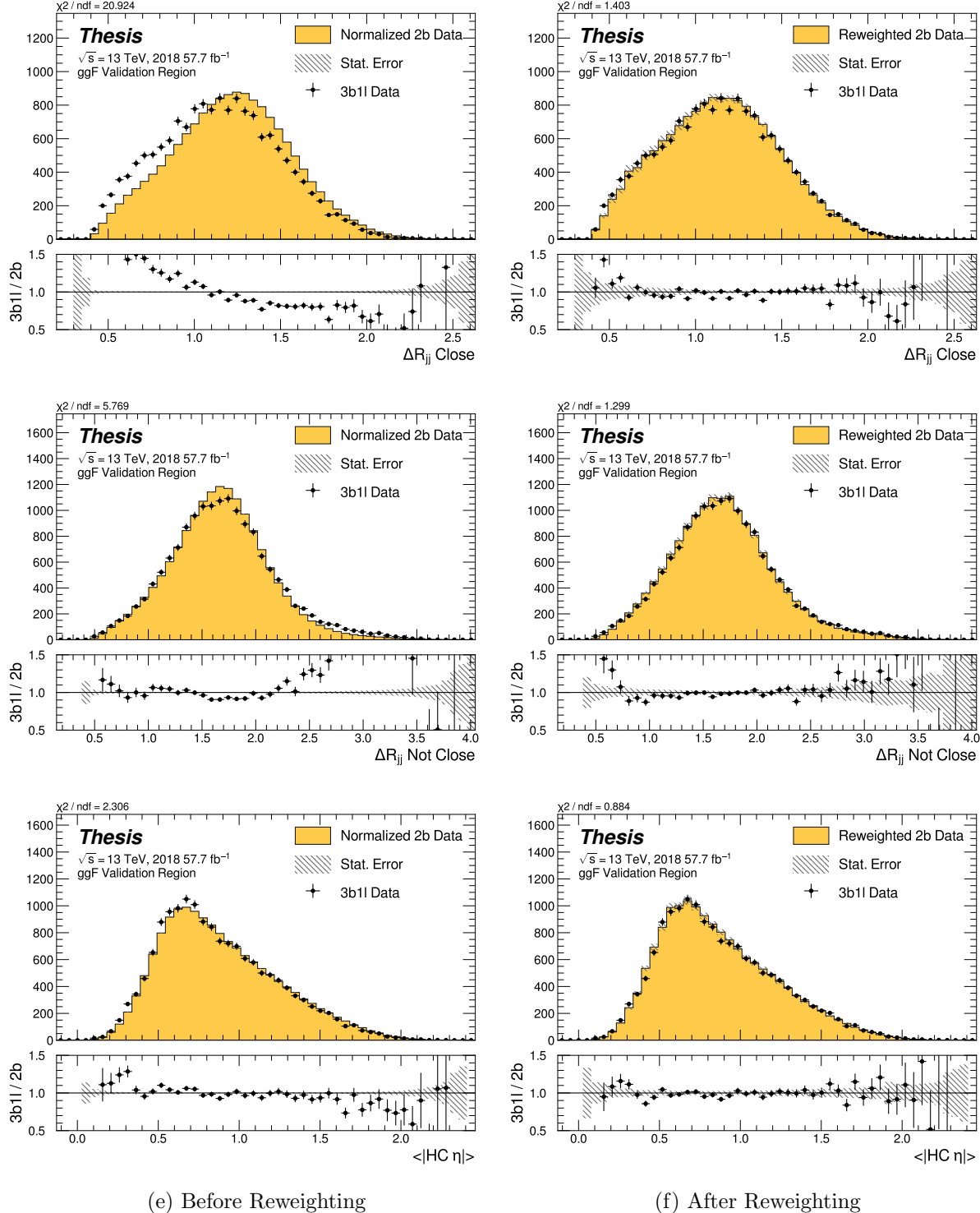


Figure C.19: **Non-resonant Search (3b1l):** Distributions of  $\Delta R$  between the closest Higgs Candidate jets,  $\Delta R$  between the other two, and average absolute value of HC jet  $\eta$  before (left) and after (right) CR derived reweighting for the 2018 3b1l Validation Region.

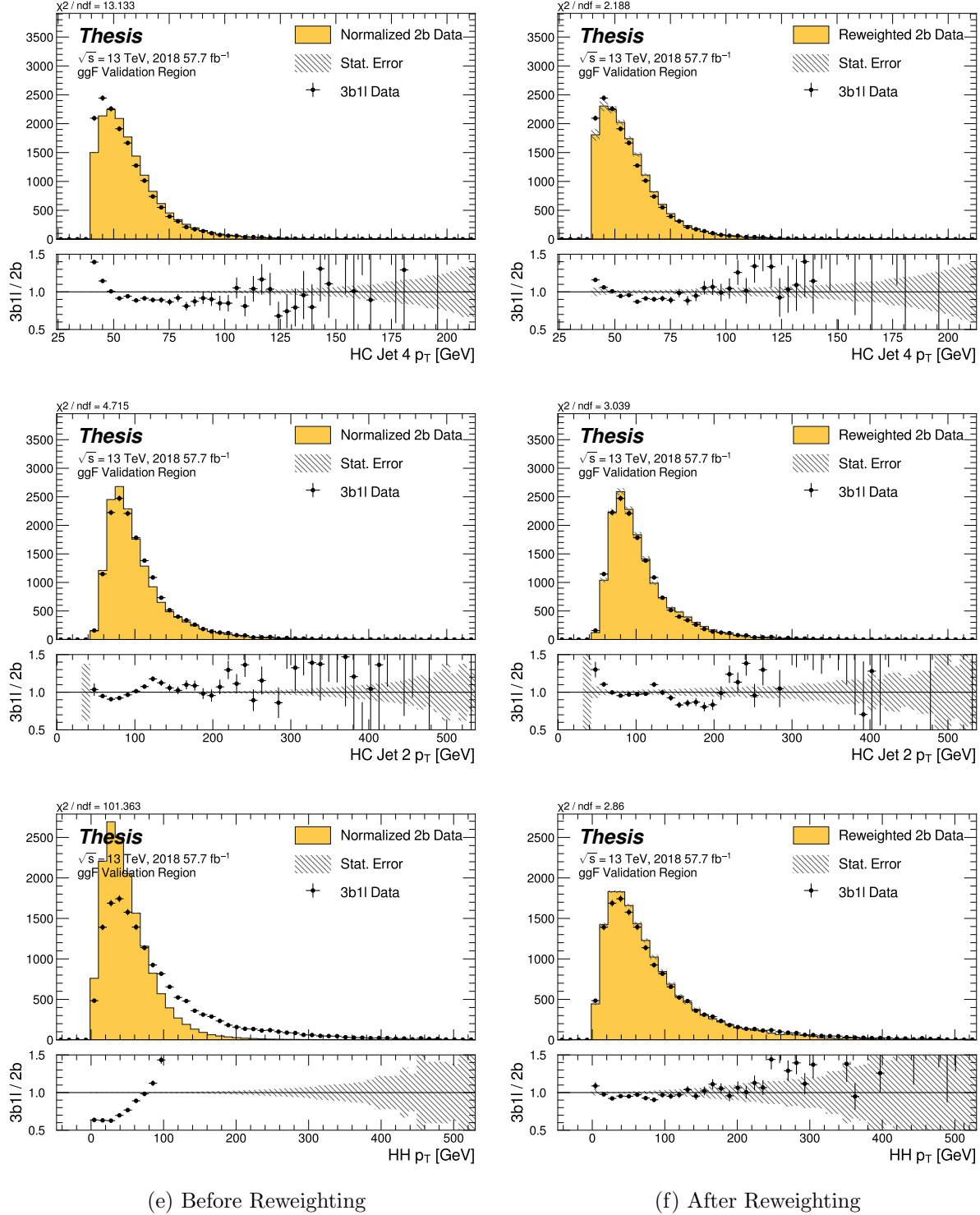


Figure C.20: **Non-resonant Search (3b1l):** Distributions of  $p_T$  of the 2nd and 4th leading Higgs Candidate jets and the  $p_T$  of the di-Higgs system before (left) and after (right) CR derived reweighting for the 2018 3b1l Validation Region.

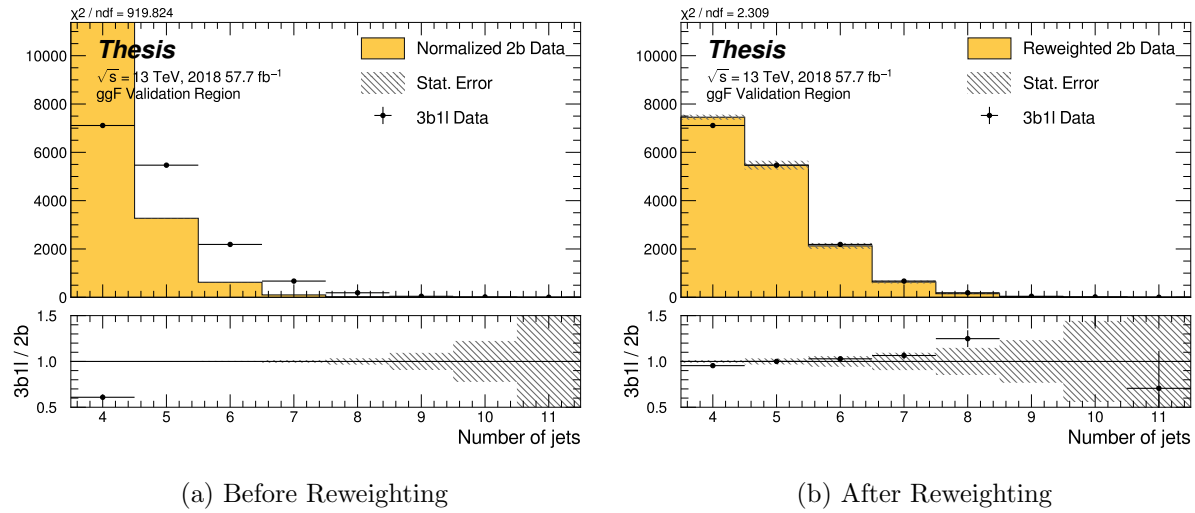


Figure C.21: **Non-resonant Search (3b1l):** Distributions of the number of jets before (left) and after (right) CR derived reweighting for the 2018 3b1l Validation Region. A minimum of 4 jets is required in each event in order to form Higgs candidates.

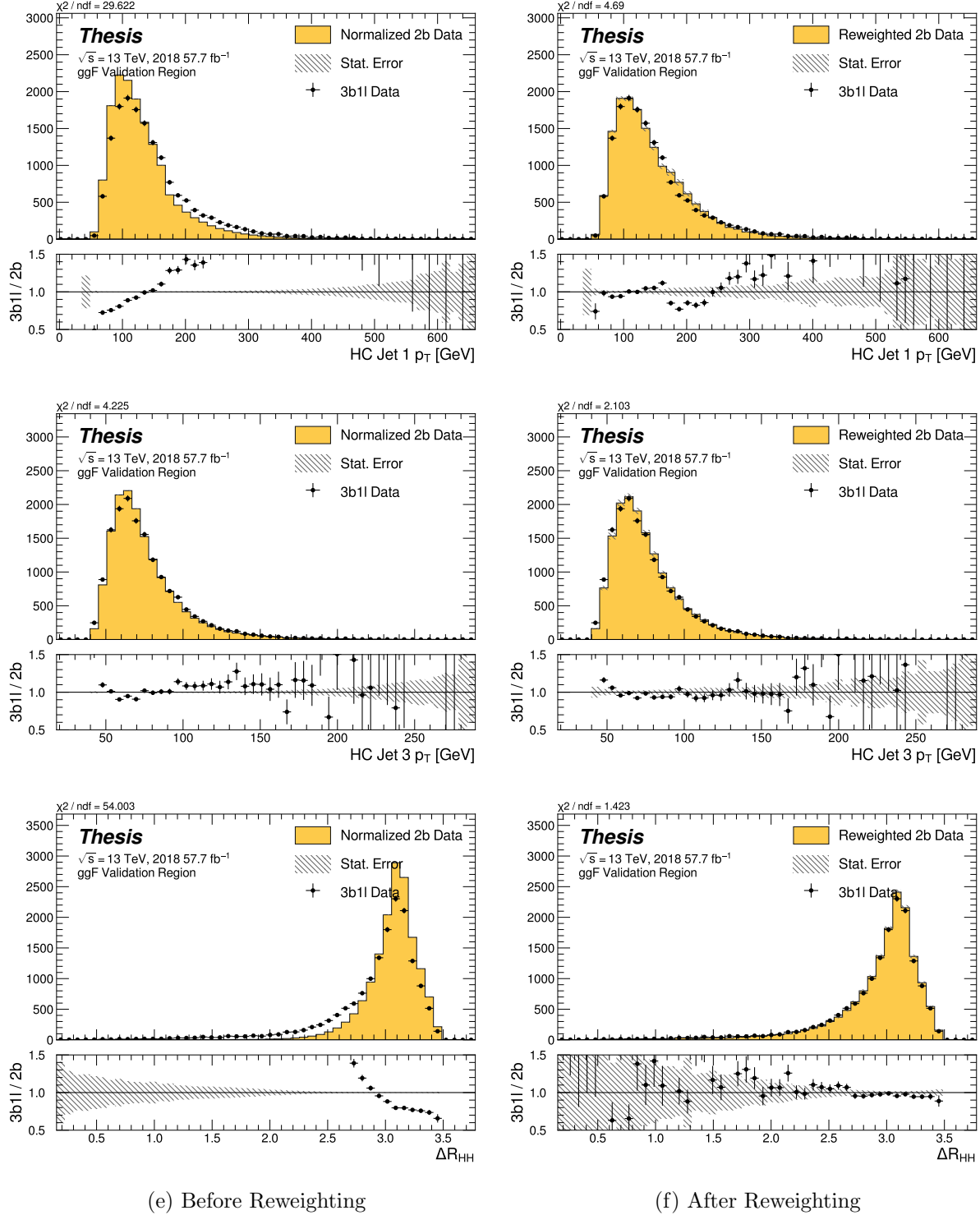


Figure C.22: **Non-resonant Search (3b1l):** Distributions of  $p_T$  of the 1st and 3rd leading Higgs Candidate jets and  $\Delta R$  between Higgs candidates before (left) and after (right) CR derived reweighting for the 2018 3b1l Validation Region.

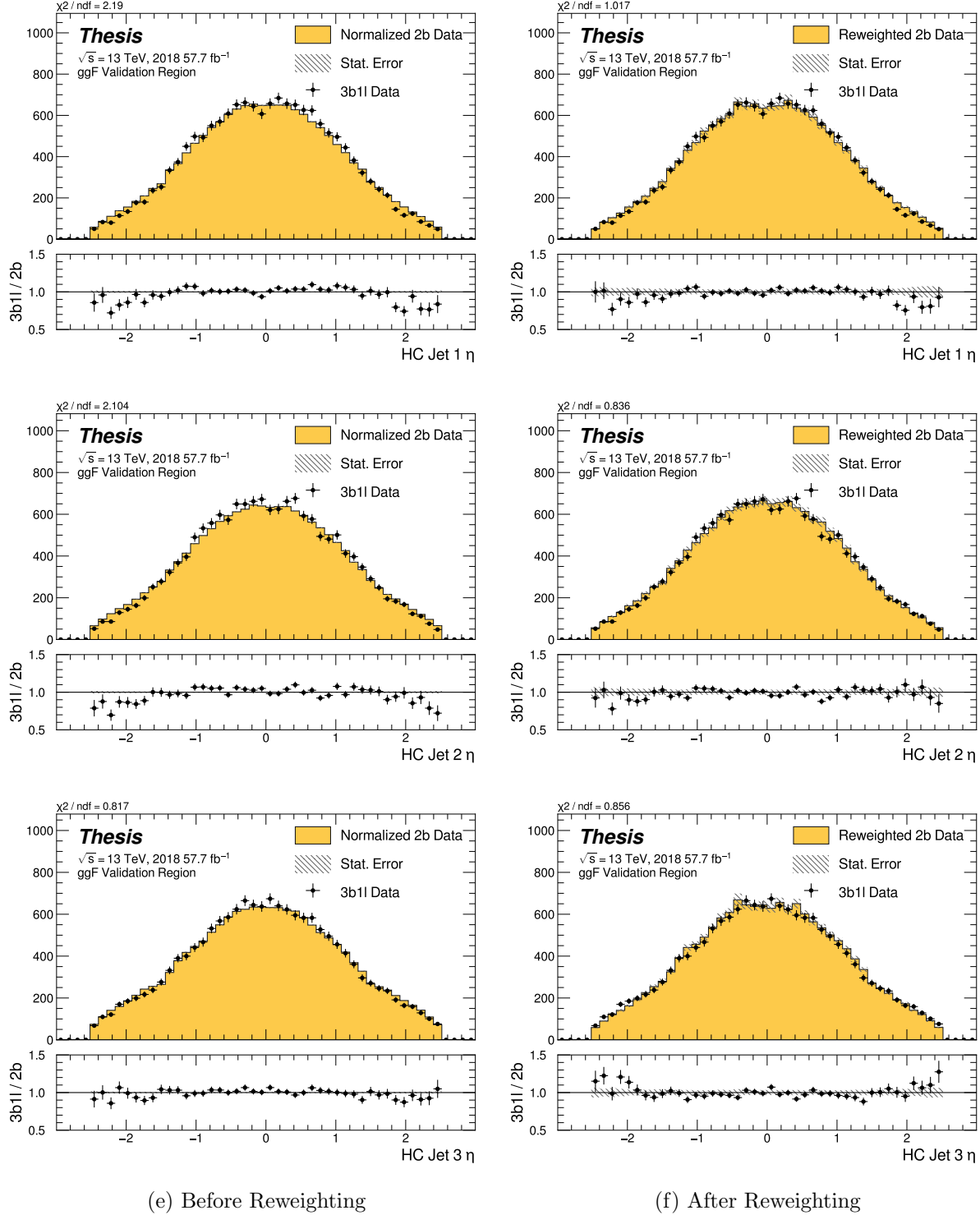


Figure C.23: **Non-resonant Search (3b1l):** Distributions of  $\eta$  of the 1st, 2nd, and 3rd leading Higgs Candidate jets before (left) and after (right) CR derived reweighting for the 2018 3b1l Validation Region.

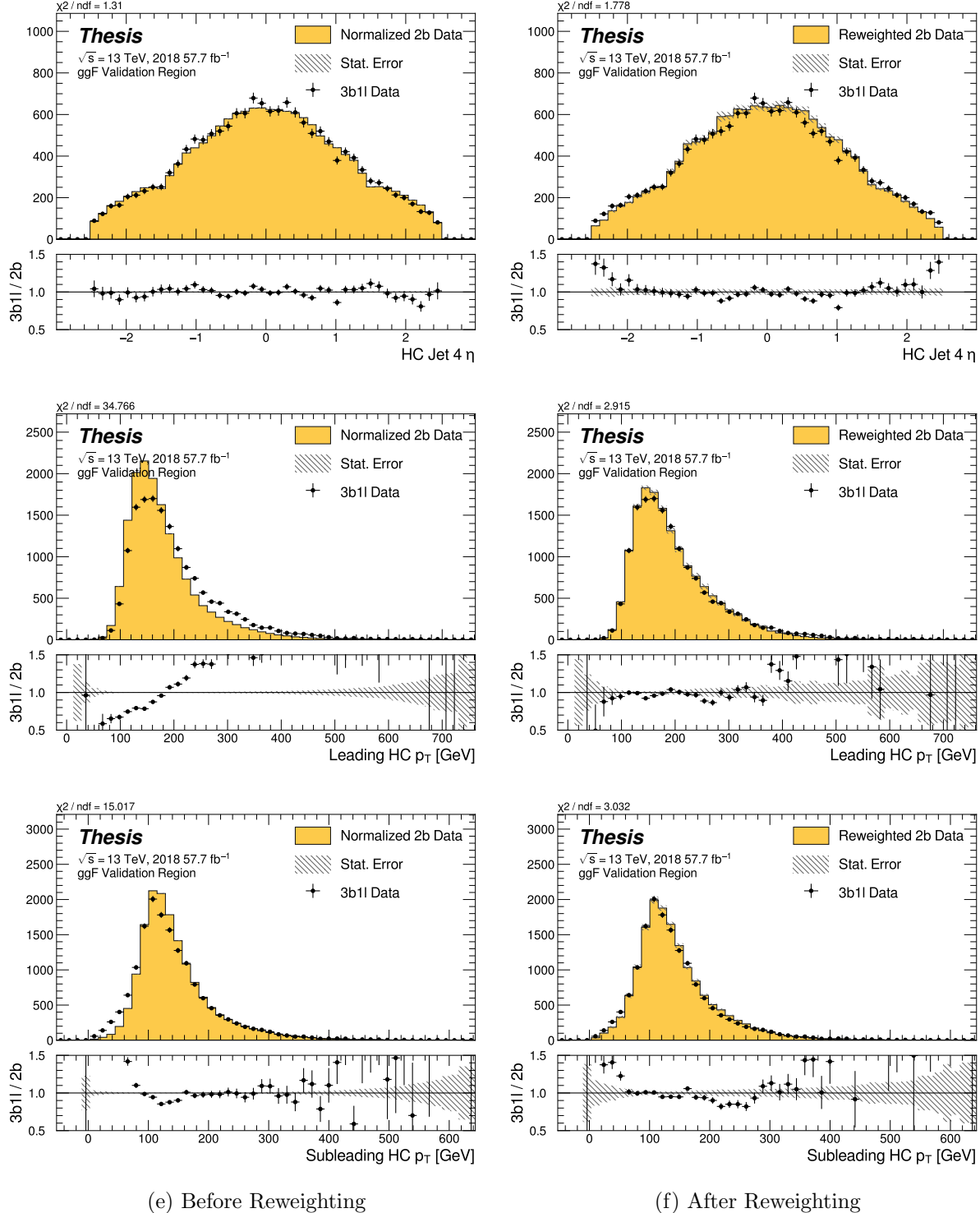


Figure C.24: **Non-resonant Search (3b1l):** Distributions of  $\eta$  of the 4th leading Higgs Candidate jet and the  $p_T$  of the leading and subleading Higgs candidates before (left) and after (right) CR derived reweighting for the 2018 3b1l Validation Region.

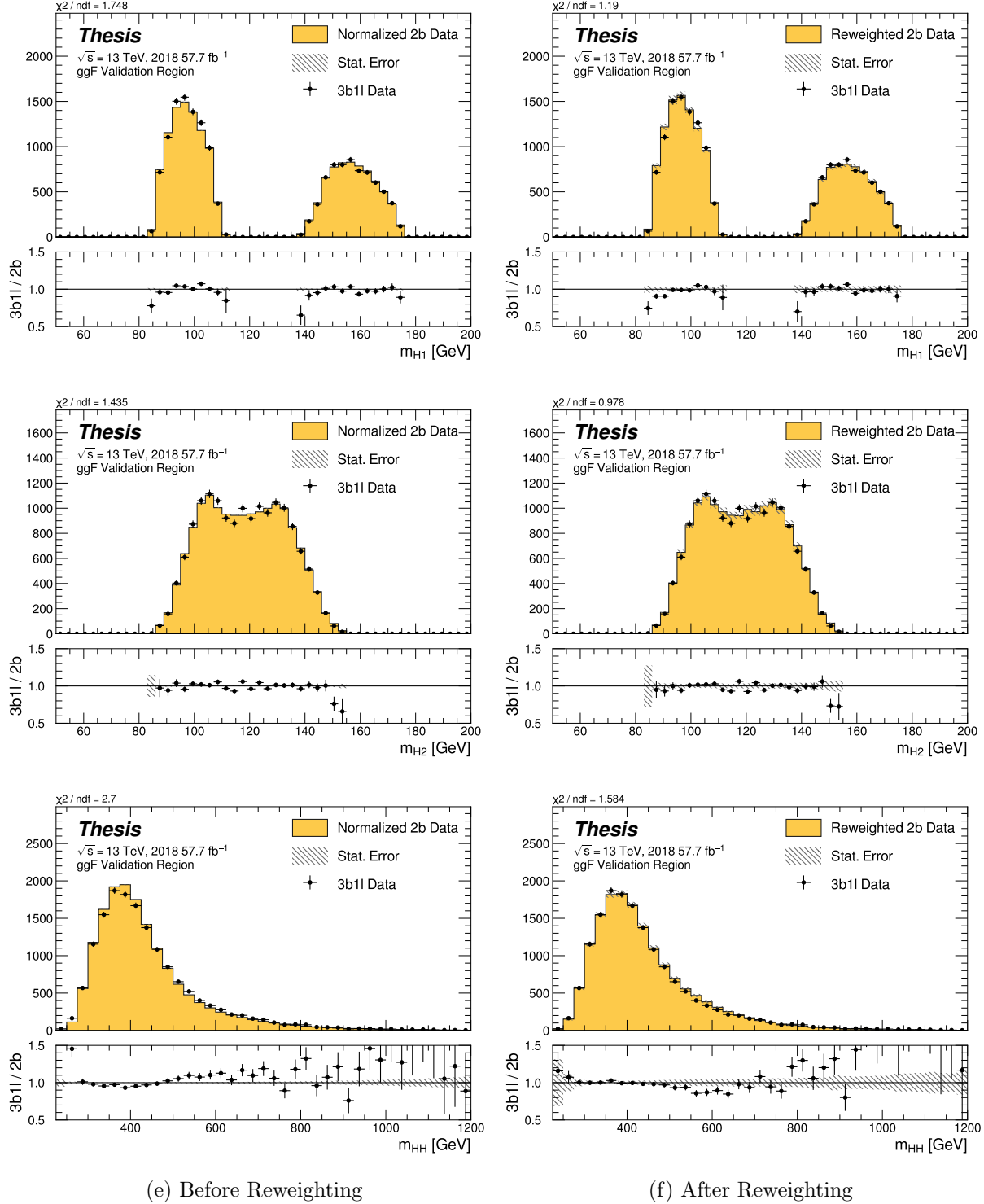


Figure C.25: **Non-resonant Search (3b1l):** Distributions of mass of the leading and subleading Higgs candidates and of the di-Higgs system before (left) and after (right) CR derived reweighting for the 2018 3b1l Validation Region.

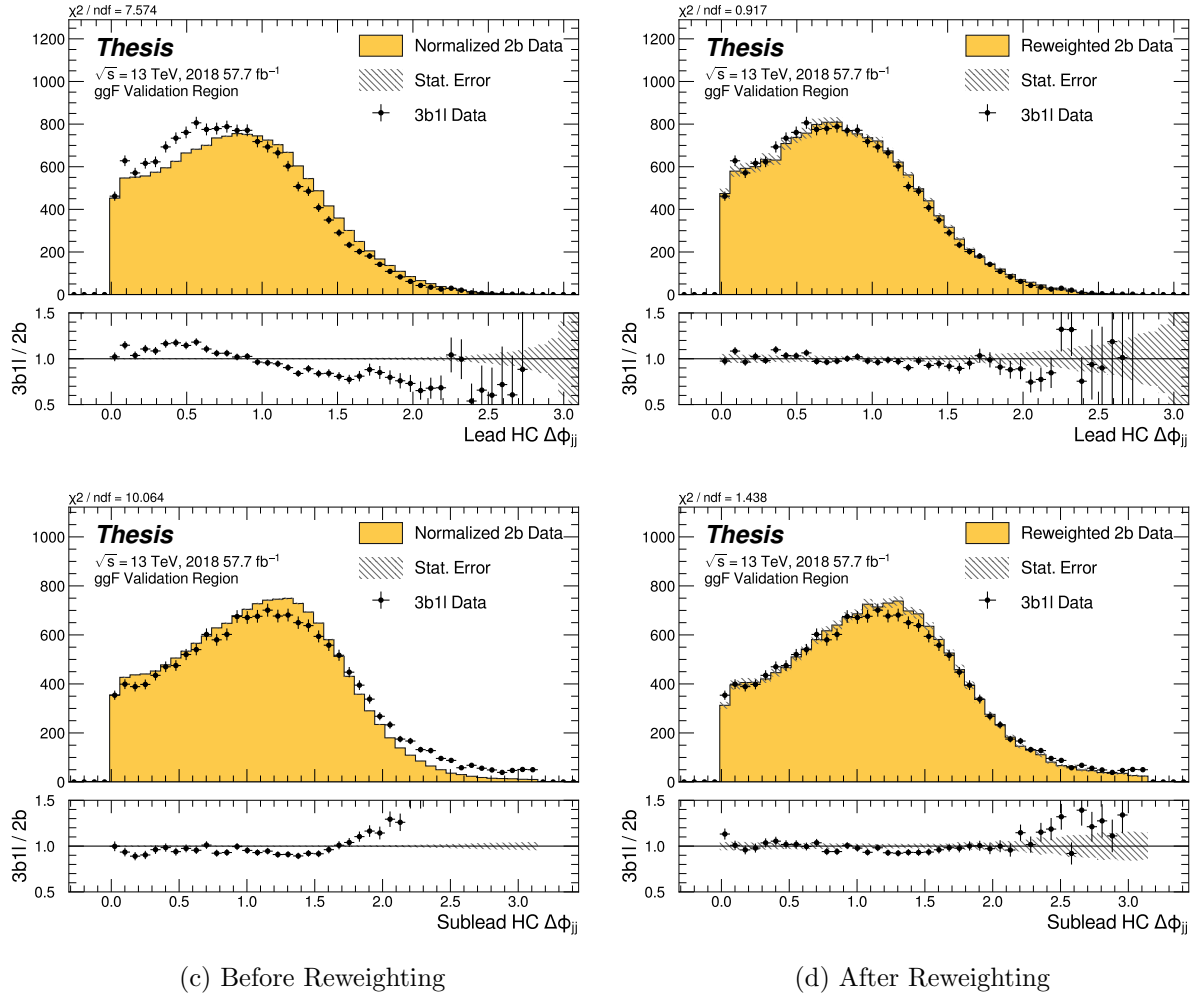


Figure C.26: **Non-resonant Search (3b1l):** Distributions of  $\Delta\phi$  between jets in the leading and subleading Higgs candidates before (left) and after (right) CR derived reweighting for the 2018 3b1l Validation Region.

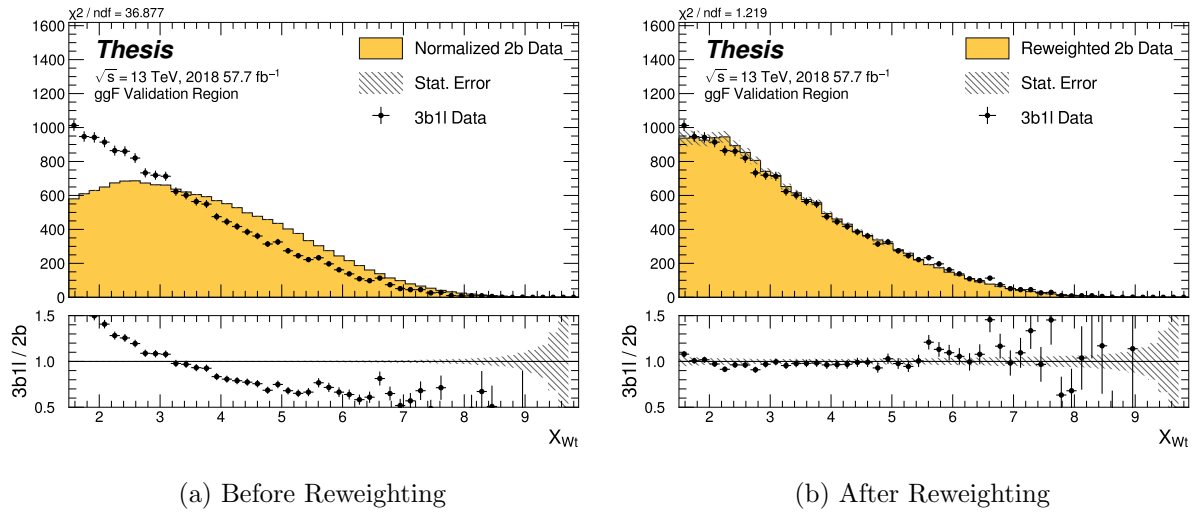


Figure C.27: **Non-resonant Search (3b1l):** Distributions of the top veto variable,  $X_{Wt}$ , before (left) and after (right) CR derived reweighting for the 2018 3b1l Validation Region. Reweighting is done after the cut on this variable is applied.